THE Na | NASICON INTERFACE IN SODIUM SOLID-STATE BATTERIES

EDOUARD L. P. QUÉREL

2022

Department of Materials
Imperial College London

A thesis submitted in part fulfilment of
the requirements for the degree of
Doctor of Philosophy

Declaration

I hereby declare that this thesis and the work reported within is a product of my own original research. Information derived from sources beyond this work has been duly acknowledged and referenced.

Edouard L. P. Quérel, 2022

Summary and organization of this thesis

In the last decade, solid-state batteries (SSB) have attracted scientific interest by virtue of their predicted superiority in terms of energy density and safety in comparison to conventional Li-ion batteries. The defining characteristic of SSBs is that their electrolyte is not a liquid but a solid. Solid electrolytes could, in theory, unlock many of the limitations imposed by liquid electrolytes regarding the choice of electrode materials. In particular, substantial energy density gains could be obtained from employing high capacity alkali metal negative electrodes instead of carbonaceous ones. Among the broad family of solid electrolytes, inorganic oxide solid electrolytes (ISEs) often display a good balance between a high room temperature ionic conductivity and a wide electrochemical stability window. This thesis brings the challenges of combining alkali metal electrodes with ISEs in SSBs under special focus. For this, a model system where a Na^+ conducting ISE of the NaSICON family ($Na_{3.4}Zr_2Si_{2.4}P_{0.6}O_{12}$, NZSP) interfaces with Na metal electrodes will be studied. This thesis more specifically explores how the reactions occurring at metal|ISE interfaces can affect the power performance and longevity of SSBs.

After briefly introducing the general context explaining why new generations of batteries with higher energy densities and safety are awaited, the benefits of Na-SSBs will be outlined in **Chapter 1**. **Chapter 2** introduces the theoretical background on ionic mobility in crystalline ISEs. A review of the pre-existing literature regarding processes affecting metal|ISE interfaces is provided in **Chapter 3**, at the end of which the scope and originality of this study are clarified. These first three chapters, serving as a prologue, are followed by a description of the experimental methods employed in this study (**Chapter 4**).

The first chapter of results of this thesis (**Chapter 5**) focuses on the synthesis of NZSP solid electrolytes and the characterization of their structure, microstructure, and elec-

trochemical performances. In **Chapter 6**, relations between the surface chemical composition of NZSP pellets and the Na|NZSP interface resistance of symmetrical cells are investigated. An important discovery from this chapter, exposed thanks to a combination of surface characterization and first principle calculations, is that a thin sodium phosphate layer terminates the surface of thermally treated NZSP samples and improves their electrochemical performances. **Chapters 7** and **8** investigate the stability of Na|NZSP interfaces: Chapter 7 reveals that impurities contained in Na metal electrodes can poison the Na|NZSP interface and could play a pivotal (and often neglected) role in the aging dynamics of cells; Chapter 8 probes the electrochemical stability (in that context, the ability to withstand reduction) of NZSP in contact with contaminant free Na metal via an *operando* XPS experiment. Finally, the last two chapters of this thesis look at challenges affecting the Na|NZSP interface under cycling conditions: **Chapter 9** looks at the formation of interfacial pores during stripping and the impact this has on the critical current density that symmetrical cells can withstand; **Chapter 10** introduces two interface design strategies to increase the power density of SSBs.

Dedicated to the loving memory of Thérèse Deléage (1923-2021)

Acknowledgements

I joined Imperial in 2016 for what I initially thought would be a one year MSc program. Little did I know back then that I would end up doing a PhD and stay in London for an extra four years. I have enjoyed every stage of the journey and am grateful towards so many people who have helped me along the way.

My deepest thanks go to my supervisor, Dr. Ainara Aguadero, who welcomed me in her group when I joined Imperial for my MSc and convinced me of continuing my studies with a PhD. I must thank Ainara for providing me with countless opportunities to develop as an independent researcher, and for transmitting her passion and scientific rigour to me. I am particularly grateful for her guidance, continuous encouragements, and friendship over my time in London. I would also like to express my gratitude towards my co-supervisor, Dr. Sam Cooper, whose scientific enthusiasm has been a continuous source of inspiration.

The Electroceramics laboratory has been an extremely supporting group and I thank all its members for their benevolence in the labs, and loyalty to Friday drinks. I owe special thanks to: Prof. Stephen Skinner, for the countless administrative and lab issues he helped me solve; Rowena, Federico, and Andrea, for having taught me so much when I had just started my PhD; Zonghao, and Ieuan, for legendarily having accepted to help me proof-read my manuscript; Nick, Fiona, George, Daisy, and Mat, among other things for having helped me stay fit over the years through all that climbing, running, and yoga.

I had the privilege of having access to world-class experimental facilities in the Department of Materials at Imperial College London. I am grateful to Drs. Richard Chater, Mahmoud Ardakani, Cati Ware and Richard Sweeney for having shared their scientific knowledge with me. Special thanks go to Dr. Gwilherm Kerherve for having helped me so many times troubleshoot issues with our XPS instrument. Thanks are also due to the administrative and workshop staff who provided a precious support during my time in the department.

I am very grateful to Drs. Qianli Ma and Frank Tietz who welcomed me at Forschungszen-

trum Jülich and trained me on their solid-electrolyte synthesis protocol, allowing me to considerably speed up my research progress.

The financial support for this work was provided by the Engineering and Physical Sciences Research Council (EPSRC) and Shell Global Solutions International B.V. I thank our collaborators at Shell, in particular Drs. Peter Klusener and Nicola Menegazzo, for fruitful discussions during our regular meetings.

I would also like to thank Profs. Robert Weatherup and John Kilner, for having accepted to examine my work despite their numerous solicitations.

To my friends (from high school, university, and flatmate), thanks for watching over my mental health by keeping me distracted from work all these years! Thanks to Fabio for being so present during the write-up months of my thesis, they would undeniably have been more stressful without him.

Finally, I want to thank my family for their ever loving support in all my academic adventures. Je vous embrasse fort!

Edouard

Dissemination

Journal articles and reviews

1. E. Quérel, I. Seymour, A. Cavallaro, Q. Ma, F. Tietz, and A. Aguadero. "The role of NaSICON surface chemistry in stabilizing fast-charging Na metal solid-state batteries." *Journal of Physics: Energy*, 2021
2. R. Brugge, I. Seymour, E. Quérel, F. Pesci, A. Aguadero. "Wetting in All-Solid-State Batteries: Local Interfacial Structures and Electronic Properties." *Materials Advances, under review*, 2022
3. E. Quérel, N. Williams, S. Skinner, A. Aguadero. "New insights into an *operando* protocol for the XPS analysis of metal|ISE interphases in solid-state batteries." *in preparation*
4. E. Quérel, A. Aguadero. "The poisoning of Na metal|NaSICON interfaces from impurities contained in Na metal electrodes." *in preparation*

Book Chapter

5. E. Quérel, A. Aguadero. Chapter "Sodium solid-state batteries" in the book "Sodium-ion batteries: materials, characterization, and technology." *Wiley*, 2022

Conference proceedings

2021 Talk **E-MRS Spring Meeting (online)**
"An in-situ formed sodiophilic layer on the surface of NaSICON electrolytes enables fast charging Na metal all-solid-state batteries"

2020 Poster **The Power of Interfaces (London), Best poster**
"The origin of high interfacial resistance in Na metal All-Solid-State Batteries: untangling surface chemistry and interface contact effects"

Poster **Postdoc Symposium of the Dpt. Materials (Imperial College London), Best cross-disciplinary poster**
"The origin of high interfacial resistance in Na metal All-Solid-State Batteries: untangling surface chemistry and interface contact effects"

2019 Poster **Solid State Ionics (Pyeongchang), Best poster**
"Achieving low Area Specific Resistance in Na metal All-Solid-State Batteries : the importance of surface chemistry at the Na metal|NaSICON interface"

Poster **International Conference on Electroceramics (Lausanne)**
"Achieving low Area Specific Resistance in Na metal All-Solid-State Batteries : the importance of surface chemistry at the Na metal|NaSICON interface"

Talk **STFC early career researcher conference (Abingdon)**
"Reduction of the Na metal/NaSICON interfacial resistance by thermal etching"

2018 Talk **Solid Oxide Interfaces for Fast Ion Transport, annual meeting (Tokyo)**
"Na metal/NaSICON all-solid-state batteries: stability of the anode|electrolyte interface"

Poster **International conference on Na batteries (Saint-Malo)**
"Observation of degradation effects at the Na metal|$Na_{3+nx}M_xZr_{2-x}Si_2PO_{12}$ electrolyte interface"

Poster **3rd Bunsen Colloquium on solid-state batteries (Frankfurt)**
"Observation of degradation effects at the Na metal|$Na_{3+nx}M_xZr_{2-x}Si_2PO_{12}$ electrolyte interface"

Contents

List of Figures

List of Tables

Acronyms/Nomenclature

General

ISE	Inorganic solid electrolyte
LLZO	$Li_7La_3Zr_2O_{12}$
NZSP	$Na_{3.4}Zr_2Si_{2.4}P_{0.6}O_{12}$
SEI	Solid electrolyte interphase
SSB	Solid-state battery

Technical terms (grouped by technique)

EIS	Electrochemical impedance spectroscopy
FRA	Frequency response analyser
GB	Grain boundaries
Ea	Activation energy (eV)
$\overline{Z}$	Impedance (Ω)
ω	characteristic frequency (Hz)
τ	relaxation time (s)
σ_i and σ_e	Ionic and electronic conductivity (S cm^{-1})
C_{GB}	Grain boundary capacitance (F)
$R_{Na\|NZSP}$ or R_{int}	Na|NZSP interface resistance (Ω)
T	temperature (K or °C)
$\eta_{Na\|NZSP}$	interface overpotential (V)
F	Faraday constant, 96.48533×10^3 s A mol^{-1}
k_B	Boltzman constant, 8.61733×10^{-5} eV K^{-1}

XPS	X-ray photoelectron spectroscopy
BE, KE	Binding energy, Kinetic energy (eV)
BP, SP	Bulk plasmon, Surface plasmon
FG	Flood Gun
FWHM	Full width at half maximum (eV)
IMFP, λ	Inelastic mean free path
LA	Asymmetric Lorentzian (XPS line shape)
LF	Finite Lorentzian (XPS line shape)
h	Planck constant, 4.13567x10^{-15} eV Hz^{-1}
ν	frequency (Hz)

DFT	Density Functional Theory
EDX	Energy dispersive X-ray spectroscopy
LEIS	Low Energy Ion Scattering
SEM	Scanning electron microscopy
XRD	X-ray diffraction

Chapter 1

Introduction

1.1 General context

In a new report released in August 2021, the International Panel on Climate Change (IPCC) reiterated their call for immediate actions to deeply reduce greenhouse gases emissions in order to respect the ambition of the Paris Agreement of limiting global warming to 1.5 °C in comparison to pre-industrial levels.[1] The report highlights that the actions taken in the seven years since the Paris Agreement was signed are not sufficient to put the world on the fast-paced decarbonization trajectory it requires.

In the United Kingdom (UK) as well as in most developed countries, two sectors are predominantly responsible for a large part of our emissions at an individual level: these are the sectors of electricity production and transport which are still heavily reliant on

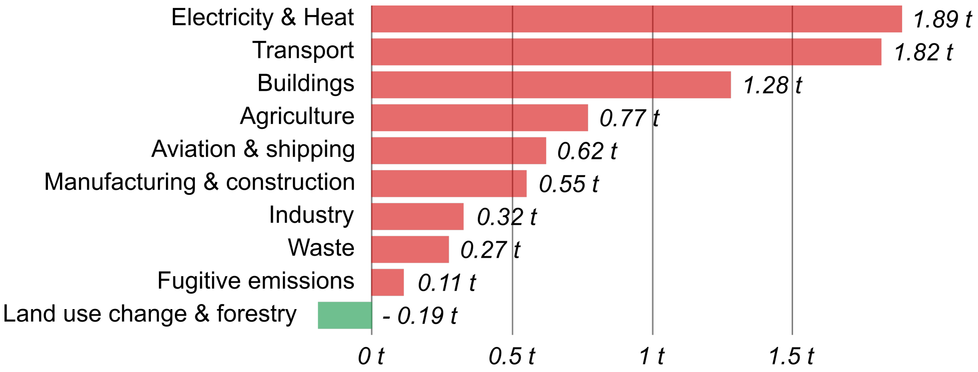

Figure 1.1: Per capita CO_2 emissions by sector in the United Kingdom in 2016. Average emissions by sector in tonnes per person per year. Adapted from [2]

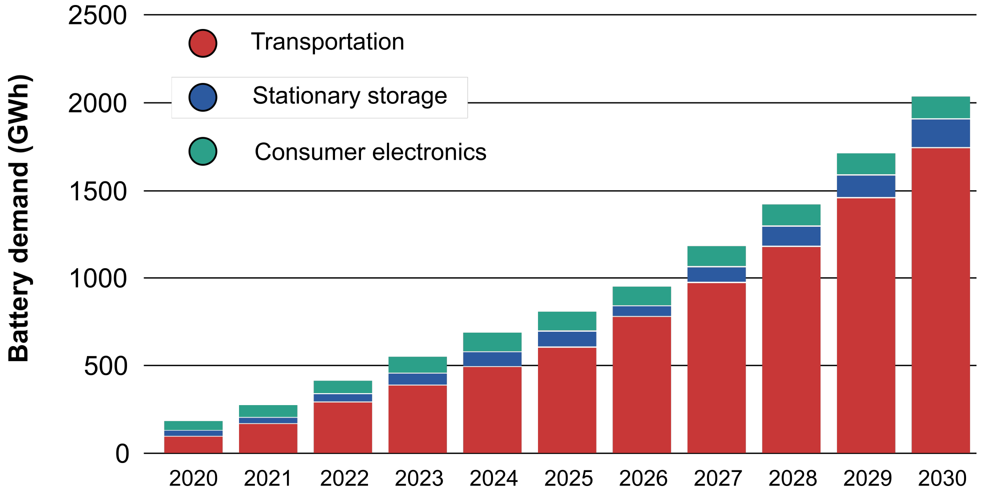

Figure 1.2: Projected global battery demand from 2020 to 2030, by application. Adapted from [3]

the combustion of fossil fuels (see Figure 1.1). Decarbonizing these sectors and shifting away from fossil fuels requires finding new efficient ways of storing energy: for the grid, stationary storage will enable more renewable energy production sources (such as wind or photovoltaic farms) to be implanted by guaranteeing a continuous power supply even when wind does not blow or sun does not shine; for the transportation sector, new energy storage solutions can replace fossil fuels in cars, buses (and possibly at some point aviation) and reduce the emissions associated to these journeys.

Thanks to their high energy density, electrochemical energy storage technologies (and in particular rechargeable batteries) are well set to play a major role in that transformation. Thereby, from a market mainly focused around portable electronics between the 1990s and early 2000s, the battery industry has shifted in the past decade to more high power and energy intensive applications such as grid-scale stationary storage or electric vehicles (EVs). This has transformed the industry and led to a dramatic increase in production volumes: from an annual demand of about 185 GWh in 2020, some projections indicate that demand could reach 2,035 GWh by 2030 with EVs becoming the dominant market share (see Figure 1.2).[3] This projected explosion of the demand for Li-ion batteries is a good sign that the transition is occurring and that it could happen fast. The question which needs to be asked is whether this transition will have the desired impact on the protection of our climate and our ecosystems.

The commercialization of the first Li-ion cell in 1991 boosted a lot of industry and research interest around the Li-ion battery technology. The development of Li-ion batteries has led other battery technologies based on Na, Mg or Ca charge carriers to be momentarily disregarded. Currently, the vast majority of batteries are based on a Li-ion architecture with a very similar chemistry consisting of graphite negative electrodes and transition metal oxide positive electrodes. The positive electrodes of high energy density Li-ion batteries often contain Ni, Mn and Co in a certain ratio (the so-called "NMC" cathodes). Most Li-ion batteries are assembled with an organic liquid electrolyte typically consisting of a lithium salt ($LiPF_6$) dissolved in a mixture of ethylene and dimethyl carbonate (EC:DMC).

Despite its proven technical efficacy, the scale-up of this battery chemistry to the levels projected in Figure 1.2 would pose serious environmental and ethical problems which could counteract the benefits of abandoning fossil fuels. Limited and geographically constrained resources for the raw elements constituting Li-ion batteries (for instance Li or Co) means that mining will become even more intensive and polluting on local environments: to date, Chile holds almost half of the known global reserves of Li[4], and over half of cobalt is sourced from the Democratic Republic of Congo.[5] The refinement of raw minerals to produce battery grade reactants will also have a significant environmental impact if it is conducted in countries with an a low penetration of renewable energy sources in their energy mixes. The conditions of extraction of minerals essential to batteries (for instance Co) in some part of the world are also becoming severely criticized.[6, 7, 8, 9] These environmental and ethical issues urge the scientific community to develop cell chemistries relying on more sustainable and abundant elements.

1.2 Beyond-Li battery chemistries

Among other charge carriers which could be used in batteries, sodium offers the advantage of being much more abundant than lithium in the earth crust - 23,000 ppm versus 17 ppm for lithium.[10] Replacing lithium with a more abundant and globally available resource such as sodium could have environmental, geopolitical, and economical benefits. The price of Na batteries is predicted to be lower than that of Li ones by virtue of the abundance of sodium (which makes it a cheap precursor), but also because copper current collectors could be replaced by aluminium ones on the negative electrode side of cells (yielding substantial savings). Besides the charge carrier, the other elements entering the composition of the electrolyte or electrode material will also need to be carefully selected to minimize the environmental impact of batteries.[10]

In comparison to Li, Na is a heavier atom and has a higher reduction potential (-2.71 V versus the standard hydrogen electrode, against -3.04 V for lithium). Thus, it is often claimed that sodium batteries should be targeted for stationary storage applications as their energy density will not compete with that of lithium batteries. Technologies such as the sodium sulfur (Na-S) or ZEBRA batteries are actually already powering our grids.[11] Developed a few decades ago, these systems work at high temperatures and rely on a Na^+ conducting ceramic solid electrolyte and molten electrodes. Recent models including all the active and inactive components of cells suggest that the energy density of some Na cell chemistries (particularly solid-state batteries) could also compete with their Li counterparts on other applications such as transportation.[12]

1.3 Solid-state batteries

Solid-state batteries (SSB) are predicted to outperform liquid electrolyte batteries in four key areas of performance: energy density, power density, longevity, and safety. These predicted performances come from several attributes which are discussed in this section. We note that some of these objectives might be mutually self-excluding depending on the choice of ISE and electrode materials of a specific SSB.

Energy density

Much of the scientific interest surrounding SSBs is motivated by the energy density increase that they could provide in comparison to Li-ion and Na-ion batteries. The energy density of a cell can be expressed in gravimetric ([W h kg^{-1}]) or volumetric ([W h L^{-1}]) terms. The gravimetric energy density E of a cell is given by equation 1.1 and depends on its capacity Q and cell potential V_0.

$$E = Q.V_0 = \frac{n.F}{3600.M_W}.V_0 \tag{1.1}$$

The formula which can be used to calculate the capacity of an electrode is developed in the right part of Equation 1.1, with n the number of electrons exchanged per cycle per formula unit, F the Faraday constant (in [s A mol^{-1}]), and M_W the molar mass of the electrode material considered (in [g mol^{-1}]). The factor 3600 is to ensure that the capacity is expressed in hours and not in seconds.

The highest gravimetric energy densities for Li-ion and Na-ion batteries are currently around 260 Wh kg^{-1}, and 120-150 Wh kg^{-1} respectively.[13] In comparison, some Na-SSBs

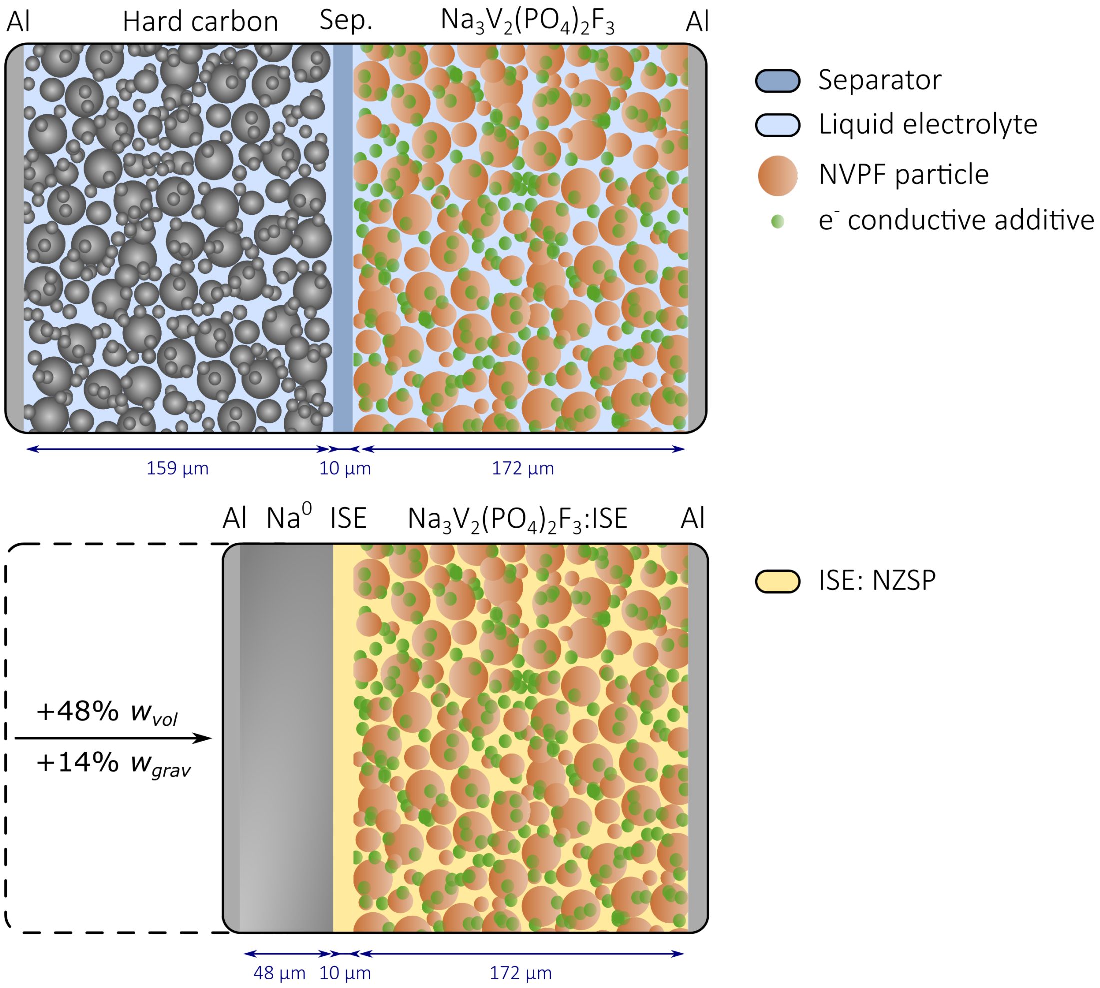

Figure 1.3: Schematic representation of a Na-ion battery and a Na metal SSB with an areal capacity of 5 mAh cm^{-2}. The Na-ion battery is constituted of a hard carbon anode (with a specific capacity of 300 mAh g^{-1} and a density of 1.5 g cm^{-3})[13], a separator and a $Na_3V_2(PO_4)_2F_3$ cathode (NVPF, with a specific capacity of 130 mAh g^{-1} and a density of 3.17 g cm^{-3}).[14] The hard carbon and NVPF electrodes include a 30 vol.% porosity.[12] For the gravimetric energy density calculations, the electrolyte and separator were assumed to contribute to 18 wt.% of the total cell weight (excluding current collectors and cell casing).[15] The Al current collectors were not included in the calculation. The Na metal SSB is constituted of a Na^0anode (spec. capacity 1166 mAh g^{-1} and density 0.97 g cm^{-3}), an ISE and a $Na_3V_2(PO_4)_2F_3$:ISE composite cathode. The cell is represented here in the charged state (*i.e.* the anode is completely sodiated). A 10 vol.% excess capacity was added to the Na^0 anode to avoid complete delamination at the end of discharge. For the gravimetric energy density calculations, the density of $Na_{3.4}Zr_2Si_{2.4}P_{0.6}O_{12}$ was taken for the ISE (3.3 g cm^{-3})[16] and the cathode composite was considered to be 70 vol.% NVPF and 30 vol.% $Na_{3.4}Zr_2Si_{2.4}P_{0.6}O_{12}$. Although represented on the schematic, the weight contribution of an electronically conductive additive in the cathode composite model was not included.

chemistries could theoretically reach 400 Wh kg^{-1} at the cell level.[12] The large volumetric and gravimetric energy density of SSBs originates, at the cell level, from the use of next generation electrodes. On the anode side, the substitution of carbonaceous electrodes by metallic ones (Na^0) would provide a large increase in capacity. Na metal has a specific capacity of 1,166 mAh g^{-1} in comparison to around 300 mAh g^{-1} for hard carbons (the negative electrode commonly used in Na-ion batteries).[13] The integration of metallic anodes in Li-ion or Na-ion cells has been the subject of numerous studies in the past decades but is unfortunately plagued by the dendritic plating of Li/Na even at moderate charging rates when the electrolyte is liquid.[17] In addition to being a safety hazard, the uncontrolled plating of alkali metal in liquid electrolyte cells also results in fast capacity fading because the decomposition of the electrolyte upon contact with freshly plated metal immobilizes charge carriers to form an interphase. In comparison, early computational models predicted that ISEs above a certain toughness would be impenetrable to metallic dendrites and thus enable the use of metallic anodes.[18] Section 3.4 will show that these early predictions were not confirmed experimentally and that metal filaments can, in some cases, still penetrate ISEs.

As schematically illustrated in Figure 1.3, replacing a hard carbon anode by a Na metal one would reduce the anode volume by more than two thirds. Thus, just by employing Na metal instead of hard carbon on the anode, volumetric energy density gains of around 48 % at the cell level can be expected. Regarding the gravimetric energy density, expected gains are more moderate because ISEs are dense relative to liquid electrolytes. For instance, in the calculation presented in Figure 1.3, a $Na_{3.4}Zr_2Si_{2.4}P_{0.6}O_{12}$ electrolyte (with a density of 3.3. g cm^{-3}) was employed. With the parameters detailed in the figure legend, a theoretical gravimetric energy density gain of 14 wt.% was calculated in comparison to a Na-ion cell with the same cathode and same areal capacity loading. A more significant improvement of up to 27 wt.% can be expected if a less dense electrolyte is used (such as the closo-borate $Na_2B_{12}H_{12}$ which has a density of 1.63 g cm^{-3}). These estimations are based on theoretical energy density calculations and it is important to note that experimental energy densities are often much lower than the theoretical ones. Whether experimental cells will outperform liquid electrolyte ones to the extent predicted by theoretical calculations (or even exceed it) remains to be proven.

To date, most experimental alkali metal SSBs are assembled in a charged state by pressing a film of metallic Na (respectively Li) on the anode interface of a solid electrolyte. An excess of Na metal is typically included to prevent the full depletion of the anode upon discharge. A 10 % excess Na metal would be considered a commercially acceptable value, although most experimental cells to date use much larger Na excesses.[19] In "anode-free" cell architectures, cells are assembled as cathode|ISE half-cells with the cathode completely sodiated (lithiated, respectively). In this type of cells, the metallic anode is formed *in-situ* during the first charge cycle of the battery. The removal of any excess alkali metal increases the energy density of such cells slightly. In addition, the manufacturing of “anode free” SSBs would be safer and cheaper alternative to handling hazardous alkali metal films whose surface get passivated extremely fast if the atmosphere is not perfectly moisture and oxygen free.

In parallel to the improvements on the anode side, the integration of high-voltage cathodes is another path to increase the energy density of cells, provided that the ISE has a large enough electrochemical stability window (see section 3.2).

Looking at the cell stack, further improvements in energy density can be obtained by minimizing the volume fraction of inactive cell components (electrolyte, current collectors, cell casing, etc.). Celgard separators commonly used in liquid electrolyte cells are already extremely thin ($\approx 10\ \mu$m) which makes it difficult to leverage any energy density improvements from the substitution of the liquid electrolyte by an ISE. In fact, the larger density of solid electrolytes in comparison to liquid ones comes with a gravimetric energy density penalty. Matching the thickness of Celgard separators and producing 10 μm thick fully dense ISE films is a manufacturing challenge, yet not an impossible one.[20]

The stacking of individual cells is an area where SSBs offer interesting architectural benefits. The absence of liquids in SSBs makes it possible to stack cells in series with the anode of one cell and the cathode of another cell connected to the same current collector. Thus, high voltage cell stacks can be obtained and the volume fraction of cell casing and current collectors minimized. An example of such bipolar stacking is illustrated in Figure 1.4.

Finally, the presence of a sophisticated temperature management system in SSB battery packs is not essential as most ISEs are stable in a wide range of temperatures. The low activation energy for ion migration of some ISEs also mean that their electrochemical performances are preserved over a wide range of operating temperatures. The simplification of the thermal management system in SSB battery packs constitutes another area where significant energy density gains could be achieved in comparison to conventional battery packs.

Power density

The rate at which a battery can be charged/discharged (its C-rate) defines its power

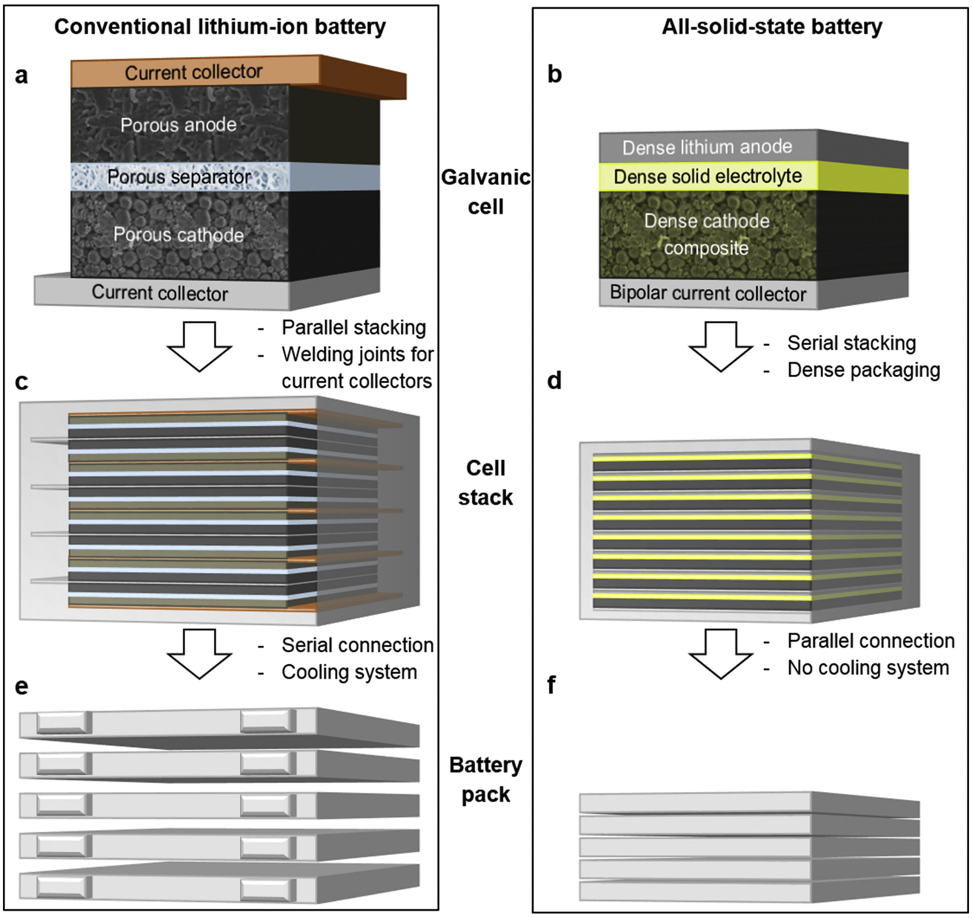

Figure 1.4: SSBs are expected to leverage energy density gains at several scales from individual cells, to cell stacks and even battery packs. Reproduced with permission from [21]

density. The rate capability of a battery is affected both by the electrolyte's ionic conductivity and by the kinetic limitations of redox processes at the electrodes. The ionic conductivity of ISEs in the temperature range targeted for SSBs was initially a limiting factor in their performance. But the ionic conductivity of ISEs has been considerably increased in the last decade and numerous ISEs are now competitive with organic liquid electrolytes, even at room temperature (in the 10^{-3}-10^{-2} S cm^{-1} range, see Figure 3.2). These fast-conducting ISEs are either newly discovered families of ISEs (such as sulfides, halides or closo-borates), or already established ISEs (oxides) whose ionic conductivity was incrementally improved over time. The immobilization of the anionic framework in solid electrolytes is also very advantageous because no bulk polarization occurs even at high C-rates. Besides ISEs, polymer electrolytes are another class of solid electrolytes but, to date, the ionic conductivity of dry polymers is insufficient (typically below 10^{-5} S cm^{-1} at room temperature) for them to be considered in practical applications.[22]

The main limitation to increase C-rates in conventional batteries is safety. The insertion/removal of Na^+ ions in an electrode material is a kinetically limited process. If a battery is operated at a C-rate exceeding the current density that an electrode material can accept at its state of charge (SoC), the expected reaction (intercalation, conversion) might be accompanied by additional parasitic redox processes (plating). For instance, the charging rate of Li^+ ions in Li_xC_6 (graphite, commonly used in Li-ion batteries) must be slowed down towards the end of charge to prevent unwanted Li metal plating at the surface of graphite.[23] The plating of Li metal could have catastrophic consequences if a dendrite were to grow through the separator and short-circuit the cell.

In contrast, alkali metal SSBs approach the question of metal plating with a radically different perspective: by design, metal plating is the fundamental mechanism by which charging occurs. Therefore, there is, in theory, no limit to the charging rate that SSBs could be operated at. To date, only molten anode solid-state batteries operating at high temperatures have achieved exceptionally high charging current densities (see for instance, Landmann et al. who cycled a Na|Na-β-β"-alumina|Na symmetrical cell at 1000 mA cm^{-2} for a cumulative plating of 10 Ah cm^{-2} at 250 °C [24]). It remains to be proven if such performances could be obtained at room temperature. One of the main challenges limiting the critical current density (the maximum current density that ISEs can withstand before failing, typically by short-circuiting) of SSBs at room temperature is non-homogeneous plating/stripping of Na at the metal|ISE interface (see sections 3.3 and 3.4 for more details). Still, some recent studies suggest that the road will not be long before Na metal-SSBs with oxide ISEs can be operated at current densities exceeding 10 mA cm^{-2} in commercial cells (see for instance Bay et al.[25]).

Safety

With large battery packs becoming ubiquitous in electromobility and stationary storage applications and the risk of pack failure scaling with its number of cells, guaranteeing a higher level of safety becomes a central key-selling point. Therefore, the absence of flammable organic solvents in SSBs is often presented as their main advantage. The intrinsic safety of SSBs is often demonstrated by penetration tests where cells are cut open with a pair of scissors in air without starting a fire.

The good thermal stability of ISEs is also a significant advantage because a careful temperature control of the battery pack will not be crucial in SSBs. If the ISE is penetrated by a metal dendrite over the course of its life, the implication would not be as catastrophic as they can be in liquid electrolyte cells (in liquid electrolyte cells, dendrites create thermal hot spots because of Joule heating which can be the starting point for thermal runaway).[26]

Despite these safety advantages, SSBs are however not 100% risk free. A risk of explosion exists in cells employing Na metal as the negative electrode if the alkali metal is exposed to water (or even atmospheric moisture). The release of toxic H_2S gas by sulfide electrolytes when exposed to air is another safety concern.[27]

Long-term stability

The hope that all SSBs would have a long cycle life has, in part, been fuelled by the impressive performance of some the first micro batteries which have been built with ISEs. The superior performance of one of these lithium micro batteries is illustrated in Figure 1.5 from a study published in 2015.[28] The capacity retention for the solid-state cell exceeded 90% after 10,000 cycles at a 5C rate which, in comparison to reference liquid electrolyte cells, was a major improvement.

Some of these hopes have been dampened by transitioning from micro to macro batteries and by integrating ISEs with higher ionic conductivities. Among other degradation

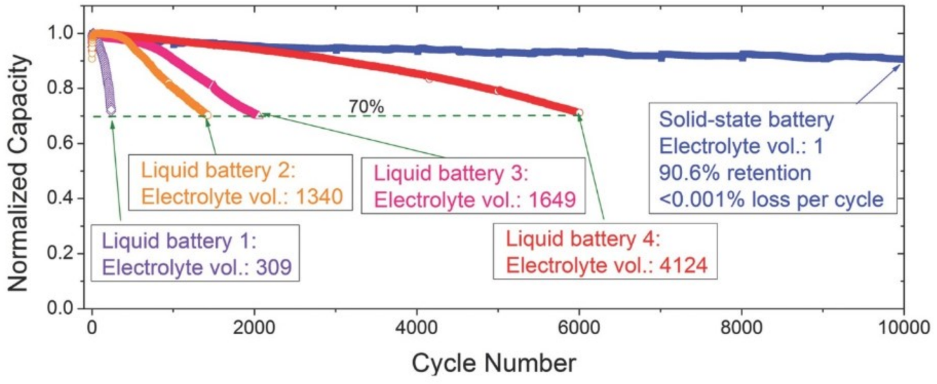

Figure 1.5: Comparison of the long-term performance of a micro solid-state battery versus reference liquid electrolyte batteries. The micro solid-state battery shows a much better capacity retention over 10,000 cycles in comparison to liquid electrolyte cells. The micro solid-state battery was composed of a Li metal anode, a LiPON inorganic solid electrolyte and a $LiNi_{0.5}Mn_{1.5}O_4$ cathode. For the liquid batteries, the anode and cathodes were the same and the electrolyte was a 1.2 M $LiPF_6$ dissolved in EC:DMC (the volume of the electrolyte was varied for cells 1 to 4). Reproduced with permission from [28].

phenomena, the electrochemical stability window of some fast-conducting ISEs is not as wide as initially expected (see section 3.2) making their interface with candidate electrodes unstable.

Notwithstanding, it is still very likely that solutions will be found to stabilize electrode|ISE interfaces and the objective of SSBs with minimal capacity fading is not a fantasy. For instance, one clear advantage of using a solid electrolyte instead of a liquid one is that it could efficiently prevent "cross-talk" (*i.e.* the poisoning of an electrode by the diffusion of elements from the other electrode). In addition, recent studies suggest that gas evolution from cathode particles at high state of charge might less severely affect SSBs than liquid electrolyte batteries.[29, 30]

1.4 The Na-SSB chemistry studied in this thesis

The experiments presented in this thesis were all conducted with NaSICON ceramic electrolytes of composition $Na_{3.4}Zr_2Si_{2.4}P_{0.6}O_{12}$ (referred throughout this work as NZSP) and with Na metal (Na^0) electrodes. The integration of cathodes into full SSB cells was not investigated as part of this work.

NZSP ceramics were selected because of their good electrochemical performances making them promising candidate ISEs for Na-SSBs. In Chapter 2, the theoretical background required to understand the good ionic conductivity of NZSP ceramics will be introduced. The performance of NZSP versus other Na-ISEs is compared in section 3.2 (Figure 3.2).

The decision to dedicate this thesis to the fundamental description of the Na|NZSP interface was motivated by the relative absence of studies focusing on Na|ISE interfaces in the literature in comparison to Li|ISE ones. Chapter 3 reviews the challenges affecting metal|ISE interfaces identified in the literature.

Chapter 2

Theoretical background on ionic mobility in solids

A candidate ISE should possess the following attributes:[31] (1) its electronic conductivity should be low (typically below 10^{-9} S cm^{-1}); (2) its ionic conductivity must be high across its operating temperature range to minimize ohmic losses under cycling conditions (typically in the 10^{-3} - 10^{-2} S cm^{-1} range, to be on par with liquid electrolytes); (3) its transference number t_i for the mobile cation should be very close to unity: $t_\mathrm{i} = \sigma_\mathrm{i}/\sigma \approx 1$; (4) its electrochemical stability window (the voltage window across which the electrolyte is inert, neither oxidized nor reduced) should be as wide as possible, allowing the use of alkali metal negative electrodes and high voltage positive electrodes; (5) it should be easily processable as dense and homogeneous films (with a target thickness in the range of 10-100 μm).

This section aims to describe the fundamental theory of ionic transport in ISEs. The transport of mobile charge carrier in ISEs is very different than in liquid electrolytes but shares the same conceptual framework as ionic mobility in electrode materials. The understanding of ionic mobility in crystalline lattices draws on concepts related to solid-state physics (crystallography, defect chemistry, diffusion…) and electrochemistry. For additional theoretical background on these topics, we invite readers to refer to the following reference textbooks and articles.[32, 33, 34] In addition, several excellent reviews on the design of superionic conductors have been published in recent years and inspired some of the graphs included in this section.[31, 35, 36]

ISEs are typically polycrystalline materials and the ion migration mechanisms will differ depending on the length scale of interest. The mechanisms of ionic migration at the atom scale in perfect crystalline lattices will be presented first. The impact of grain boundaries or pores on the ionic conductivity are discussed in section 2.4.

2.1 Anion and mobile cation sublattices

Inorganic solid electrolytes represent a broad family of materials with a diverse range of anion chemistries (oxides, sulfides and selenides, halides, borates,…) and crystal structures. What unites these materials is the general mechanism of ionic migration at the atom scale in their crystalline lattices.

The backbone of Li^+ and Na^+-ISEs is their anion sublattice which is typically composed of polyanionic moieties. Figure 2.1 shows the crystal structure of Na^+-ISEs from three different polyanion families. As an example, the polyanionic moieties of the sulfide β-Na_3PS_4 are $(PS_4)^{3-}$ tetrahedra, and for the closo-borate $Na_2B_{12}H_{12}$ they are $(B_{12}H_{12})^{2-}$ cages. The anion sublattice of β-Na_3PS_4 and $Na_2B_{12}H_{12}$ forms a body centered cubic (BCC) arrangement.

Interpenetrated in this anion sublattice, another sublattice is defined by the special arrangement of mobile cations (*i.e.* Na^+ ions in our case). In Li or Na-ISEs, mobile cations typically occupy tetrahedrally or octahedrally coordinated crystallographic sites: Na^+ ions tend to occupy octahedral sites whereas Li^+ ions (which have a smaller ionic radii) can also occupy tetrahedral sites.

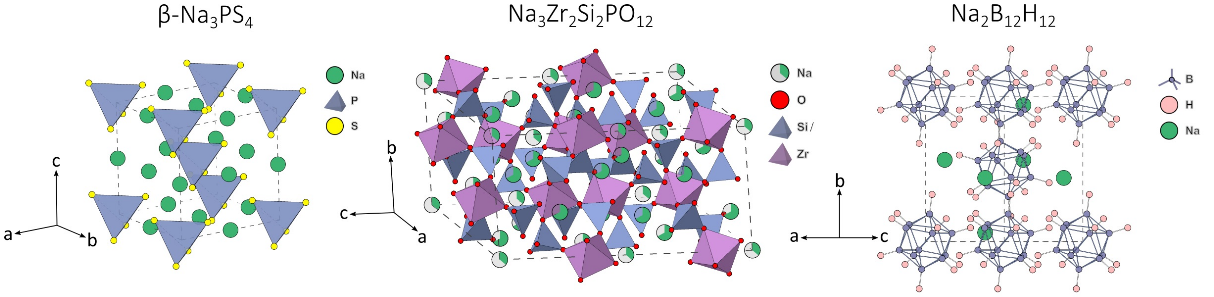

Figure 2.1: Crystal structures of three ISEs from different anionic families. The backbone of ISEs is composed of polyanionic moieties: $(PS_4)^{3-}$ in blue for β-Na_3PS_4; $(ZrO_6)^{8-}$ in purple, and $(PO_4)^{3-}$ and $(SiO_4)^{4-}$ in blue for $Na_3Zr_2Si_2PO_{12}$; $(B_{12}H_{12})^{2-}$ for $Na_2B_{12}H_{12}$. The spatial arrangement of these polyanionic moieties results in different crystal structures: bcc for β-Na_3PS_4 and $Na_2B_{12}H_{12}$, rhombohedral $R\overline{3}c$ for $Na_3Zr_2Si_2PO_{12}$. The partial occupancies of the two crystallographic sites available to Na in rhombohedral $Na_3Zr_2Si_2PO_{12}$ are represented using a pie chart notation.

The energy landscape that a mobile cation experiences as it diffuses through an ISE is determined by the various sites that it occupies on its migration path and the energy barriers between these sites (see section 2.2). The potential energy of the mobile cation sites depends on their bonding environment. Importantly, equivalent crystallographic sites will have the same energy. In the absence of electrostatic repulsions between nearest neighbor mobile cations, the sites with lowest energy will be preferentially filled.

Under certain conditions leading to a minimization of the overall crystal energy, some mobile cations can be pushed from the lowest energy sites to higher energy sites. This has the effect of leaving some crystallographic positions partially occupied (see the partial occupancies of Na in $Na_3Zr_2Si_2PO_{12}$ in Figure 2.1 for instance). As will be described in more details in section 2.3, an optimized concentration of vacancies in mobile cation sites is the origin for the superionic behaviour of numerous ISEs.

2.2 Ionic mobility in ISEs

Fundamental equations of electrical conductivity

The electrical conductivity of a crystal σ (a tensor) is related to the applied electric field E and the resulting current density i via Ohm's law if there is no gradient of charge carrier concentration:[34]

$$i = \sigma . E \tag{2.1}$$

To simplify the equations, the tensor form will not be kept in the following equations and ion migration will be assumed to occur in one dimension (along the x direction). The generalization to three dimensions will be reintroduced later.

Mobile charged particles in solids can be either ionic (cations, anions), or electronic (electrons and holes). The electrical conductivity of a solid is the sum of its electronic and ionic partial conductivities:

$$\sigma = \sigma_e + \sum_i \sigma_i \tag{2.2}$$

Under an applied electric field E, charge carriers move in a solid with a velocity v_i (more frequently expressed as their mobility $\mu_i = v_i/E$). The partial conductivity σ_i of the i^{th}

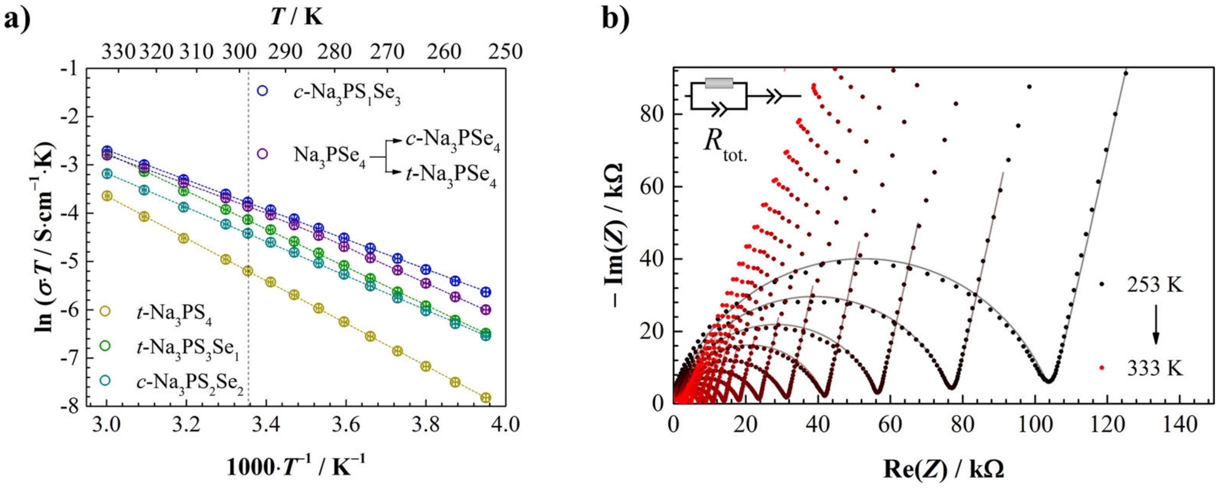

Figure 2.2: The Arrhenius type behaviour of the ionic conductivity of ISEs. (a) Representative Arrhenius plots of (HT)-$Na_3PS_{4\text{-}x}Se_x$ obtained via temperature dependent impedance spectroscopy. (HT) refers to the high temperature route which was employed for the synthesis of the material. “c” or “t” in the figure legend refer to the crystal structure of the phase (cubic or tetragonal). For Na_3PSe_4 a phase transition from cubic to tetragonal occurs below 270 K (marked by the vertical line). A subtle change in activation energy is associated with the phase transition. (b) Selected Nyquist plots of (HT)-Na_3PS_4 at varying temperatures. The Nyquist plots are fitted to the equivalent circuit in inset and the conductivity at each temperature is calculated in order to obtain the Arrhenius plot on the left. Reproduced with permission from [37].

charge carrier is related to its mobility μ_i, its concentration in the solid c_i, and its charge q_i by:

$$\sigma_i = c_i . q_i . \mu_i \tag{2.3}$$

The transport of ions is commonly a thermally activated diffusion process which can be described by a modified Arrhenius type equation:

$$\sigma_i = \frac{\sigma_i^0}{T} e^{-E_a/k_B T} \tag{2.4}$$

with σ_i^0 a pre-exponential factor, T the temperature (in K), E_a an activation energy (in eV) and k_B the Boltzmann constant (in eV K^{-1}). This relationship is only valid in temperature intervals where the phase is stable.

A general assumption which can often be made for ISEs is that their electrical conductivity is dominated by their ionic partial conductivity (because their electronic conductivity should be extremely low). The activation energy for ion migration E_a can therefore be obtained by measuring impedance spectra at various temperatures and linearly fitting the function $ln(\sigma T) = f(1/T)$ (see Figure 2.2 for an example and section 4.6 for information on how to fit the Nyquist plots of ISEs). If a phase transition occurs at a temperature T_t, and the migration mechanism is changed, two activation energies will be obtained (one for each phase stability domain in the regions $T < T_t$ and $T > T_t$).

At first sight, equations 2.3 and 2.4, which both describe the ionic conductivity of an ISE, seem to not be directly related. The link between these two equations is established in Appendix A, where the Arrhenius type relationship for the conductivity is derived from random walk theory with the assumption that the migration of mobile cations is non-correlated (which means that the individual elemental migration jumps are independent from all the previous jumps and can occur in all directions).[33] In the following sections, the migration pathways available to mobile cations will be presented (which will clarify the meaning of non-correlation) and common strategies to increase the ionic conductivity of SEs will be introduced.

Migration pathways in ISEs

At the atomic scale, mobile cations diffuse through an ISE by hopping between sites of the mobile cation sublattice. As previously described in section 2.1, the mobile cation sites have different energies depending on their bonding environment. In this section, two mobile cation sites will be considered: one “low energy” site and one “higher energy” site. Mobile cation sites can be either occupied or vacant.

Hopping between sites occurs via one of the following mechanism:[31] (1) **vacancy migration** whereby a cation from a low energy site hops to a neighboring vacant low energy site; (2) **interstitial migration** can occur when a cation in a higher energy site hops to a vacant higher energy site; (3) **correlated migration** (sometimes called concerted or interstitialcy migration) is a chain mechanism whereby a cation in a higher energy site knocks a neighboring cation located in a low energy site to a vacant higher energy site. The three scenarios are presented in Figure 2.3 alongside their schematic energy landscapes (*i.e.* the energy barriers that a cation has to overcome on its migration path). For the same migration path, correlated migration was demonstrated to lower the activation energy for migration in comparison to single-ion hops.[38] The energy landscape for single-ion migration can be calculated using the nudged elastic band method (NEB) within density functional theory (DFT)[39] or using pair potential methods.[40] For correlated migration energy landscapes, ab initio molecular dynamics (AIMD) simulations are required.[38, 41]

2.3 Designing superionic conductors

Increasing the ionic conductivity by increasing the defect concentration

One early step in the design of new ISE crystal structures is to ensure that the structure is thermodynamically stable at its operating temperature. Once a stable structure is found, its ionic conductivity can be estimated by calculations and measured experimentally by impedance spectroscopy. If the ionic conductivity of the newly designed ISE is not too low but also not in the range of interest for room temperature SSBs (around 10^{-3} to 10^{-2} S cm^{-1}), a common strategy to improve it is to increase the concentration of defects in the structure (*i.e.* maximizing the product c.(1-c) in equation A.7 in Appendix A).

An increase in the vacancy/interstitial concentration of mobile cations is typically achieved by substituting elements of the polyanionic sublattice with aliovalent elements (*i.e.* elements with a different oxidation state). Aliovalent substitutions result in a change of the anion sublattice charge which needs to be compensated by the mobile cation sublattice, either by creating vacancies or by accepting more Na^+ ions in the structure. A schematic example of an aliovalent substitution leading to a higher concentration of Na^+ ions is presented in Figure 2.4. On the left, a crystal composed of $(A)^{n-}$ polyanionic moieties is presented in its fully ordered state with its low energy crystallographic sites fully filled with cations (for instance Na^+ ions). As represented there, the crystal respects the charge neutrality rule. In the middle, the substitution of one $(A)^{n-}$ moiety by a $(B)^{(n+1)-}$ moiety (acceptor substitution) leaves a charge imbalance which needs to be compensated, for instance by an additional cation (with a charge +1) in a higher energy site. On the right, the presence of Na^+ ions in higher energy sites creates an electrostatic frustration and displace Na^+ ions from low energy to higher energy sites.

The family of NaSICON solid electrolytes can be taken as an example to illustrate how aliovalent substitutions can impact ionic conductivity and the occupancy of mobile cation sites. NaSICON phases exist in the compositional space described by the stoichiometry $Na_{1+x}Zr_2(SiO_4)_x(PO_4)_{3-x}$ ($0 \leq x \leq 3$).[42] This stoichiometric formula shows that $(PO_4)^{3-}$ tetrahedra can be substituted by $(SiO_4)^{4-}$ tetrahedra with a concomitant increase of the

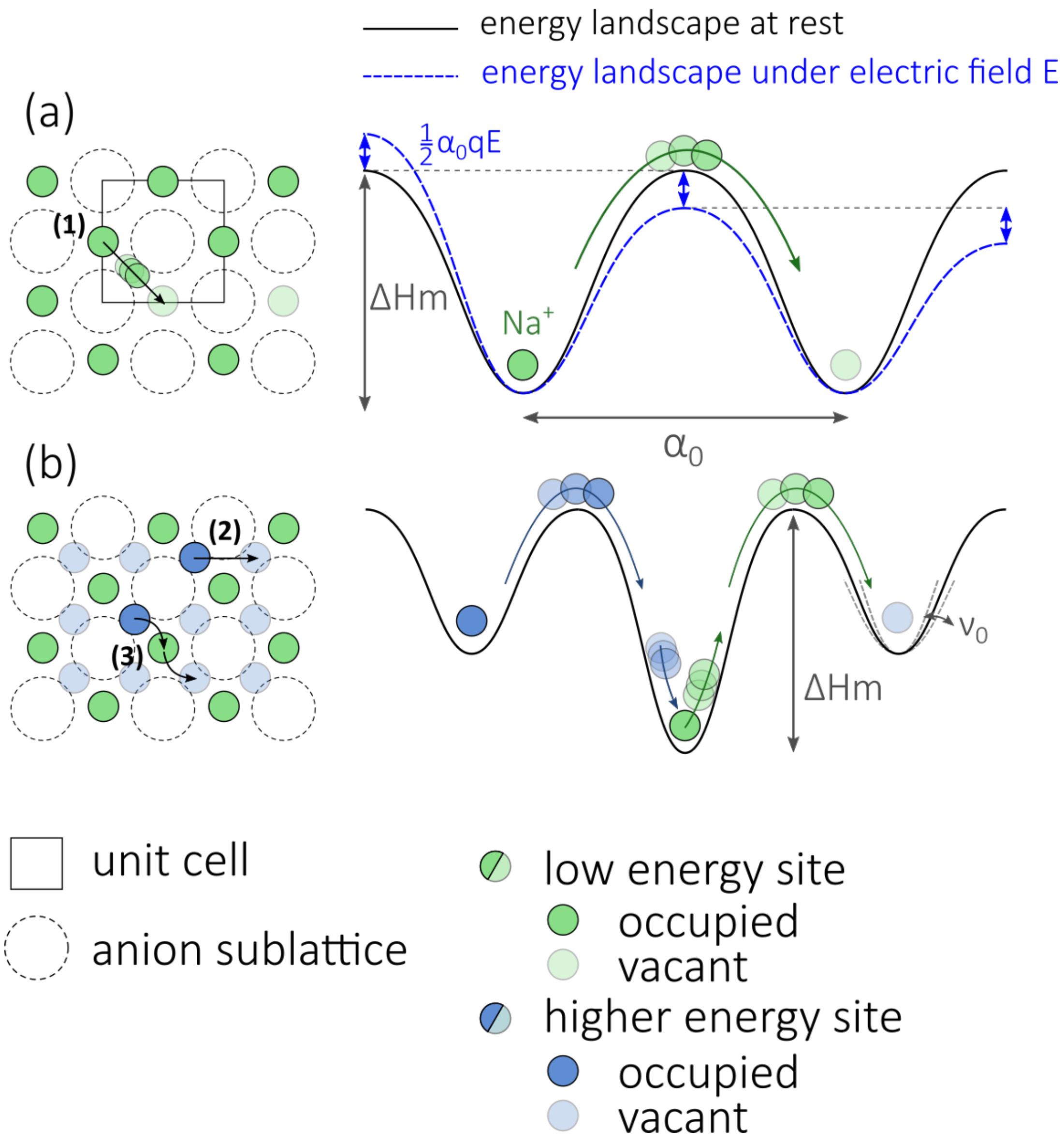

Figure 2.3: Cation migration mechanisms in ISEs. (a) Schematic 2D representation of a vacancy migration mechanism (1). In the static regime (self-diffusion), the vibration of a mobile cation in its crystallographic site may give it enough energy to hop to a neighboring vacant site by going over an energy barrier ΔHm (energy landscape represented with a solid line). The effect of applying an electric field on the energy landscape is also represented (dashed line). (b) 2D representations of an interstitial migration mechanism (2) and a correlated migration mechanism (3). The energy landscape represented corresponds to a correlated migration whereby a cation in a high energy site fills a low energy site by knocking a cation located there to a neighboring high energy site.

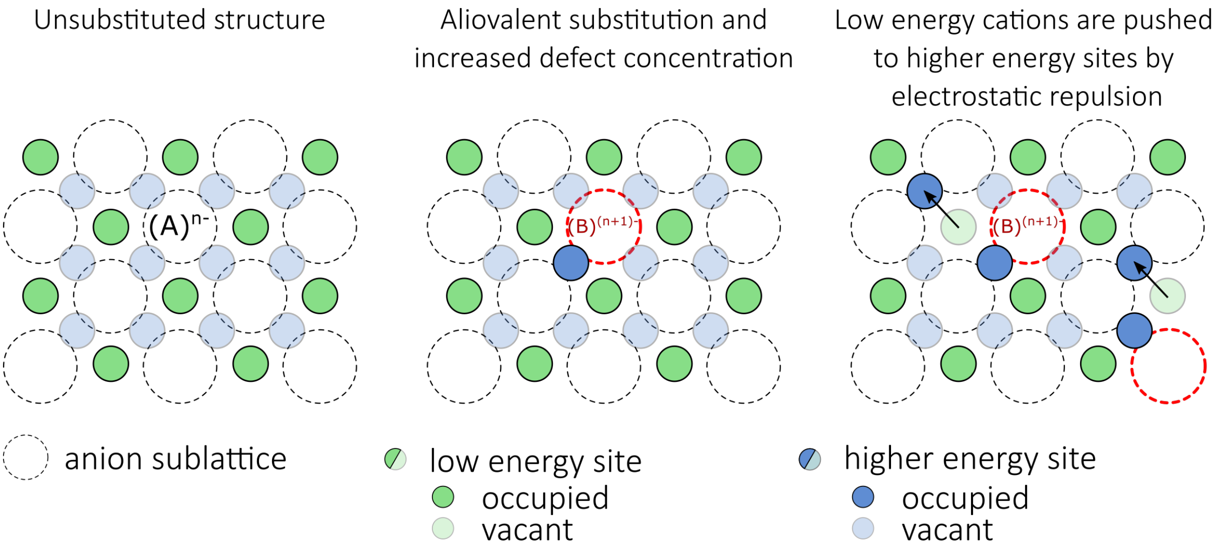

Figure 2.4: Schematic representation of the impact of aliovalent substitutions on charge carrier concentration and site distribution. The aliovalent substitution of a $(A)^{n-}$ moiety by a $(B)^{(n+1)-}$ is compensated by an additional mobile cation (which should be of charge +1 in this example to respect charge neutrality). In some cases, the addition of mobile cations in higher energy sites creates a local electrostatic frustration for neighboring cations in low energy sites; this frustration can be relaxed if the cations move to higher energy sites.

Na concentration to compensate the charge imbalance. As illustrated in Figures 2.5(a) and (b), the ionic conductivity can be increased by orders of magnitude in the $0 \leq x \leq 2.4$ region before dropping in the $2.4 \leq x \leq 3$ region. A recent study by Ma et al. (Figure 2.5(b)) focusing on the superionic region ($2 \leq x \leq 2.6$) revealed that a maximum ionic conductivity of 15.4 mS cm^{-1} (bulk conductivity at 25 °C) is reached for the composition $Na_{3.4}Zr_2Si_{2.4}P_{0.6}O_{12}$ ($x = 2.4$).[16]

Looking more closely at the partial occupancy of Na^+ ions in the structure reveals the fundamental reason for the superionic behaviour of the intermediate NaSICON compositions. For simplicity, only the rhombohedral phase of NaSICON (space group: $R\overline{3}c$) will be considered here, although a monoclinic phase (space group: $C2/c$) can also be stabilized in a certain compositional and temperature range. In the rhombohedral phase, Na^+ ions can occupy two sites (Na1 and Na2) whose positions are represented in Figure 2.1. The Na1 sites are lower in energy than the Na2 ones. For the two endmember structures ($Na_1Zr_2P_3O_{12}$ for x=0 and $Na_4Zr_2Si_3O_{12}$ for $x = 3$), these sites are either fully occupied or fully vacant: for $Na_1Zr_2P_3O_{12}$, Na1 sites are fully occupied and all Na2 sites are vacant; for $Na_4Zr_2Si_3O_{12}$, Na1 and Na2 sites are all fully occupied. The absence of

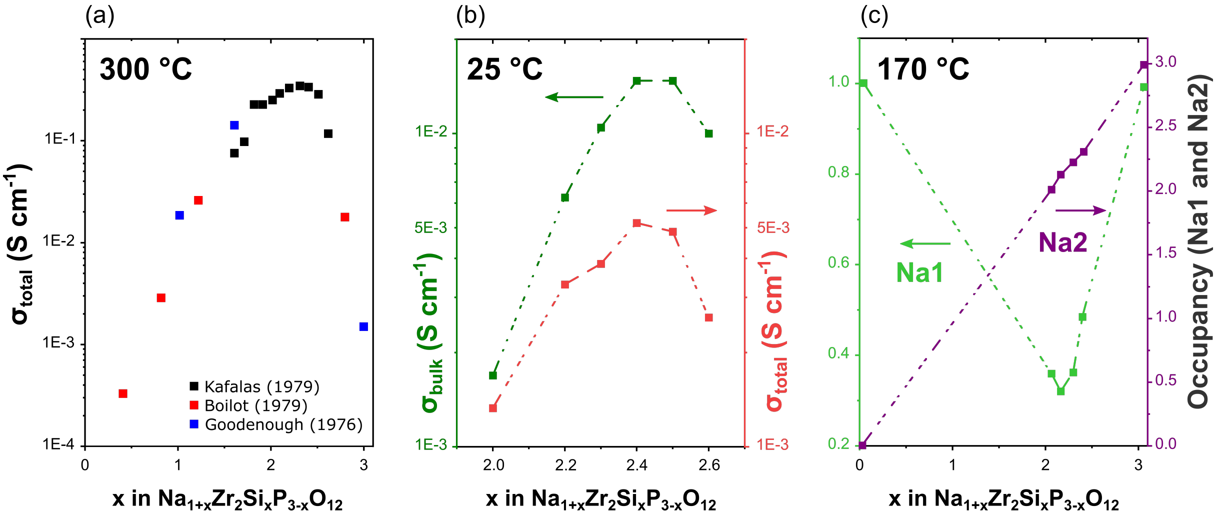

Figure 2.5: Aliovalent substitutions in the $Na_{1+x}Zr_2Si_xP_{3-x}O_{12}$ compositional space. (a) Total ionic conductivity at 300 °C as a function of NaSICON composition. The ionic conductivity can be increased by several orders of magnitude by the aliovalent substitution of P by Si (data digitized from Boilot et al.[43]). (b) Bulk (intragranular) and total ionic conductivities at 25 °C as a function of NaSICON composition in the superionic composition range ($2 \leq x \leq 2.6$) (data digitized from Ma et al.[16]). (c) Partial occupancies of Na sites determined by refinement of X-Ray diffraction data at 170 °C (data digitized from Boilot et al.[43])

defects in these structures explains their low ionic conductivities: at room temperature, their ionic conductivities are 4.50 10^{-6} S cm^{-1} for $Na_1Zr_2P_3O_{12}$ and 8.87 10^{-9} S cm^{-1} for $Na_4Zr_2Si_3O_{12}$.[44] In intermediate $Na_{1+x}Zr_2Si_xP_{3-x}O_{12}$ compositions, partial occupancies of the Na1 and Na2 sites creates disorder in the structure: as x increases, Na^+ ions are initially inserted in the only available sites (the Na2 sites). Above a certain concentration of Na^+ ions in Na2 sites, the occupation of Na1 sites becomes energetically unfavorable because of electrostatic repulsion from Na2 sites. A partial displacement of Na^+ ions from Na1 sites to vacant Na2 sites occurs (this is the situation described schematically on the right of Figure 2.4). As can be seen in Figure 2.5(c), the occupancy of Na1 sites reaches a minimum in the superionic region ($2 \leq x \leq 2.6$). For $x \geq 2.6$, as the concentration of vacant Na sites reduces, Na^+ ions start filling Na1 sites again. The addition of Na^+ ions in mobile cation sites past $x = 2.6$ reduces the overall concentration of defects. If the concentration of vacancies becomes too low (such as in $2.6 \leq x \leq 3$ region), Na^+ ions might not have a neighboring vacancy to hop to or a neighboring ion to knock to another position (assuming a correlated migration). If the defect concentration is too low, cations are essentially locked in position.

A similar aliovalent substitution strategy has been applied to increase the ionic conductivity of Na_3PS_4. In this case, the concentration of Na^+ ions can be increased by substituting P^{5+} by Si^{4+} (acceptor substitution)[45, 46] or the concentration of Na vacancies can be increased by substituting S^{2-} by Cl^- (donor substitution).[47, 48]

A paradox: why lowering the energy barrier for migration does not always result in a higher ionic conductivity?

From equations A.1 and A.7, we can see that minimizing the energy barrier for ion migration (ΔH_m) will increase the success rate for ion hopping ($\nu_\pm$) and thus increase the ISE's ionic conductivity (σ_i). Thus, designing ISEs with flat energy landscapes (*i.e.* with low ΔH_m) should be an objective. Yet, this strategy can be quite paradoxical because a lower ΔH_m will also result in a lower attempt frequency ν_0 (see Appendix A: $\nu_0 = \frac{1}{\alpha_0} \cdot \sqrt{\frac{2.\Delta H_m}{M}}$). Therefore, a balance needs to be found between low enough energy barriers (ΔH_m) and high enough attempt frequencies (ν_0). This problem is well studied in anion lattices with soft phonons such as sulfides.[37] In comparison to stiff oxide anion lattices, the migration energy barrier is typically lower in sulfide lattices. This can be partly attributed to: (1) the larger ionic radius of S^{2-} in comparison to O^{2-} which make mobile cation sites in sulfides bigger than in oxides; (2) the slightly weaker bonds in sulfide lattices mean that a lower strain energy is required to displace polyanions when cations pass through a migration bottleneck; and (3) the larger polarizability of S^{2-} ions in comparison to O^{2-} ions facilitates the dissociation of Na^+ ions from the anion lattice. Despite the low energy barrier for migration in sulfides, the lower attempt frequency explains why the ionic conductivities of Na conducting oxides and sulfides are analogous (with a few exceptions, see Figure 3.2).

Substitution strategies are also commonly used to widen the path for ion migration in ISEs and thus reduce ΔH_m. The energy barrier for migration can indeed be severely impacted by the size of the smallest bottleneck on the migration path of a Na^+ ion. If the anion lattice in which a Na^+ ion migrates is tightly packed, passing through a small bottleneck might require a large strain energy. Increasing the bottleneck size for ion migration can be achieved by substituting atoms of the anion sublattice with other atoms with a different ionic radius. In a survey study looking at the migration energies of over 100 different NaSICON compositions obtained by various substitution strategies, Guin et al. found that the activation energy for migration in NaSICON structures was correlated to the size of a bottleneck on the migration path of Na^+ ions.[44] An optimum ionic radius for substituent elements was provided in the study to minimize the migration energy.

Towards a more general concept of mobile cation frustration

A common point between the approaches consisting in increasing the concentration of mobile defects or reducing the energy barrier for migration is that they both impose frustration to the mobile cations at some level. More generally, all design strategies intended at creating a superionic behaviour in an ISE rely on frustrating mobile cations so that they are not locked in deep energy wells. Depending on the rigidity of the polyanionic framework, frustration strategies can be static or dynamic in nature.[36]

Static frustration can be structural, chemical or electrostatic. The substitution strategies described in the previous section impose for instance structural and electrostatic frustrations to the mobile cations. Cations are structurally frustrated if they have no site preference in a crystal. They are also frustrated in a mobile cation site if the size of the site exceeds their ionic radius because they will be loosely bonded to the coordinating anions. Electrostatic frustration occurs for instance when two cations cannot sit in two neighboring sites which leads to a redistribution of site occupancies (see Figure 2.4).

Dynamic frustration is created when the mobility of the anion framework forces cations to migrate. The idea of “mobile” anions might seem surprising since it was assumed from the beginning of this chapter that the anion framework is fixed in ISEs. The anion framework can indeed be considered immobile for long-range mobility but polyanions in some soft ISE lattices possess short-range vibrational and rotational mobility. Such vibrational and rotational mobility has been reported in the families of sulfide (such as in the Na_3PS_4 and related electrolytes) and closo-borate (such as $Na_2B_{12}H_{12}$ and related compounds) electrolytes.

The rotational mobility of polyanionic moieties (such as $(PS_4)^{3-}$ tetrahedra in Na_3PS_4) is often coined a “paddle-wheel” or “revolving door” mechanism. This terminology helps to visualize how the polyanions mobility transfers to a cationic mobility. The rotational disorder of the anion framework is even more pronounced in closo-borate electrolytes and can result in exceptional room temperature ionic conductivities of up to 70 mS cm^{-1} for the closo-carbaborate $Na_2(CB_{11}H_{12})(CB_9H_{10})$.[36] The anion dynamics for this compound was demonstrated to be even faster than the Na^+ diffusion at room temperature.[49] In such ISEs, the anion framework plays a crucial, dynamical role in fast cation migration. The ionic migration in these ISEs cannot be considered a purely non-correlated diffusive process because the ionic conductivity is greatly enhanced by the rotational/vibrational

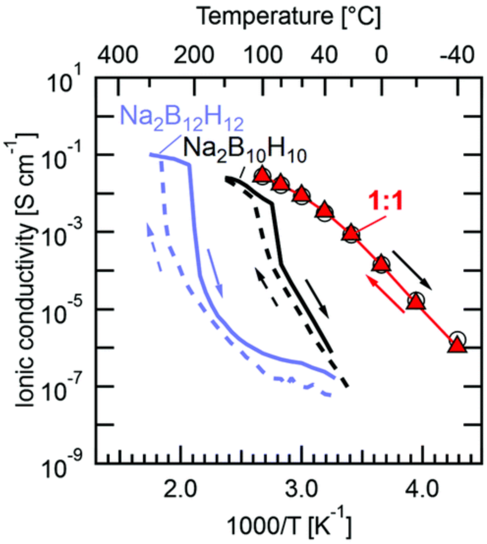

Figure 2.6: Example of a deviation from Arrhenius behaviour in closo-borate ISEs. For $Na_2B_{12}H_{12}$ and $Na_2B_{10}H_{10}$, a sharp drop in ionic conductivity is observed at their phase transition temperature and a hysteresis loop between cooling/heating of the sample is also noticed. A sharp phase transition is not observed for $Na_4(B_{12}H_{12})(B_{10}H_{10})$ (referred to as 1:1 on the figure) whose phase is stable even down to -40 °C and does not show any hysteresis. The conductivities of $Na_4(B_{12}H_{12})(B_{10}H_{10})$ cannot be fitted to a line which constitutes a deviation from perfect Arrhenius behaviour. Reproduced with permissions from [50].

mobility of the anions. Thus, a deviation from Arrhenius behaviour is typically observed in such ISEs: instead of a linear relationship between $ln(\sigma T)$ and $(1/T)$, a continuous change in the activation energy is observed across the analyzed temperature range (see Figure 2.6).[36]

2.4 Ionic conductivity at the micro/meso scale

In the previous sections, ionic migration has only been treated at the atom scale, that means, inside perfect single crystal lattices. But ISEs are typically polycrystalline, composed of grains (*i.e.* single crystals) held together by intergranular regions (also called grain boundaries, and sometimes complexions[51, 52, 53]). “Grain boundaries” can be a somewhat misleading terminology because the intergranular regions of ISEs can extend over several atomic planes in thickness. But because they are limited to only a few atomic planes in thickness, they can also not be considered as a “phase”. They can have different mechanical and chemical properties than the crystalline grains which is why the term "complexions" was coined to describe them. In oxide ISEs, which are usually densified via a high temperature sintering, intergranular regions frequently display a distinct chemical composition (they can act as a sink for elements)[54, 55, 56] and different mechanical properties (they are typically softer).

In oxide ISEs sintered at high temperatures, grain boundaries typically constitute chemical/structural heterogeneities on the migration path of mobile cations. Grain boundaries can act as obstacles for ionic diffusion which increases the resistance of macroscopic samples. An example of the resistive nature of grain boundaries is given in Figure 5.6 (section 5.2) where the total ionic conductivity of $Na_{3.4}Zr_2Si_{2.4}P_{0.6}O_{12}$ at 25 °C is three times lower than its bulk conductivity.[16] The difference in conductivity is associated to the presence of resistive grain boundaries in macroscopic $Na_{3.4}Zr_2Si_{2.4}P_{0.6}O_{12}$ samples whose microstructure is presented in Figure 2.7(a).[57] The impact of grain boundaries can be even more pronounced if the migration pathways are not isotropic in the ISE. This is the case for Na-β/β"-alumina for instance in which Na^+ ions migrate in 2D conduction planes. The conductivity of polycrystalline Na-β/β"-alumina is much lower than its bulk conductivity along the conduction planes because the Na^+ ions must follow a tortuous migration path.[58] It is important to note that some materials display a higher grain boundary conductivity than their bulk conductivity (typically alongside grain boundaries or in space charge layers next to grain boundaries).[59, 60, 61] For softer ISEs (such as sulfides or closo-borates), the impact of grain boundaries on the total ionic conductivity seem to be negligible in most cases.[62]

Another microstructural property of ISE pellets which should be controlled for fast ion migration is their density. Pores in macroscopic samples increase the tortuosity for ion migration and can be detrimental for the long-term operation of a cell (Na^+ ions might plate inside the pores instead of the anode interface during charge, see section 3.4). The density of ISE samples is typically reported as a fraction (the relative density) which can be obtained by dividing the experimentally measured density by the theoretical density of a single crystal of the same material. For soft ISEs which are densified by cold-pressing, the volume fraction of pores can be large. For instance, the relative density of cold-pressed t-Na_3PS_4 is around 80% and microscopic pores can be observed on the sample's surface as shown in Figure 2.7(b). For oxide ISEs, the densification of pellets is generally obtained via a high-temperature sintering step. The control of the sintering conditions is crucial to obtain highly dense, mechanically robust and fast ionically conducting pellets.[63] At the high temperatures required for these sintering steps, a partial evaporation of Na from the structure can occur and needs to be minimized to maintain a

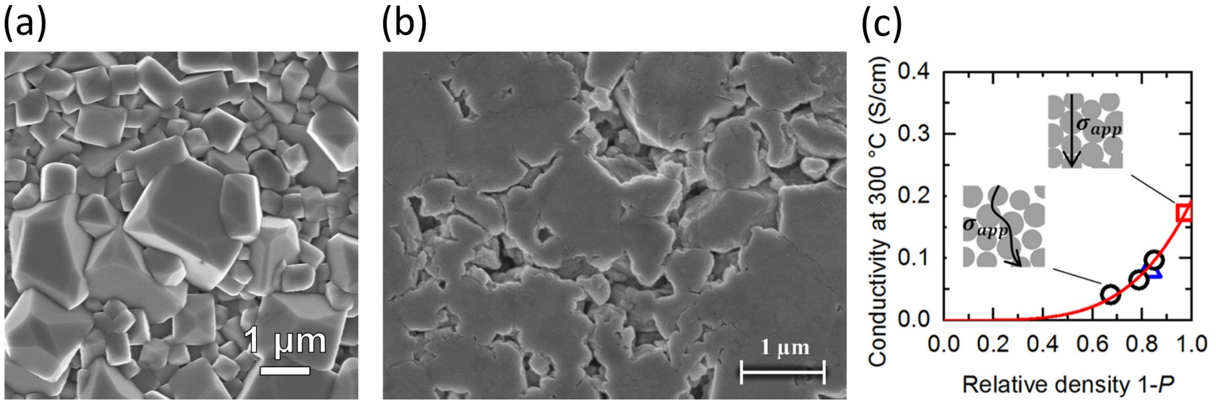

Figure 2.7: Microstructure of ISEs. (a) Sintered $Na_{3.4}Zr_2Si_{2.4}P_{0.6}O_{12}$ samples are dense but with very small grains which result in numerous grain boundaries. Reproduced with permission from [57]. (b) Cold pressed tetragonal Na_3PS_4 are more difficult to densify fully (80 % theoretical density in this study). Reproduced with permission from [62]. (c) The relationship between pellet density and the ionic conductivity of Na-β/β"-alumina samples. Reproduced with permission from [63].

good ionic conductivity performance.[64, 63] This problem is often mitigated by sintering the pellets in a bed of the mother ISE powder (which can act as an external source of Na during the sintering), or by adding a controlled excess of Na during the synthesis step. Other routes have been developed to counterbalance Na/Li loss in Na/Li-ISEs produced by thin film deposition.[65, 66] In oxide ISEs, the densification usually occurs via a liquid phase sintering. In a liquid phase sintering, the softening (or even partial melting) of the intergranular region creates a cohesive force pulling grains towards each other and helping their coalescence. Densification can also be promoted by using sinter aids. Sinter aids are phases which are mixed with the ISE powder and whose low melting point can activate a liquid phase sintering at high temperatures.[67] Figure 2.7(c) illustrates how higher ionic conductivities can be achieved by increasing the density of macroscopic ceramics using the example of Na-β/β"-alumina: in this study, the relationship between the pellet density and the ionic conductivity of Na-β/β"-alumina samples was fitted to Archie's law ($\sigma_{app} = \sigma_0.(1-P)^m$, where σ_{app} is the apparent conductivity of macroscopic samples, σ_0 is the conductivity of perfect crystals, P is the porosity fraction, and thus $(1-P)$ is the relative density).

Chapter 3

Literature review - Challenges at metal|ISE interfaces

This chapter offers an overview of the main degradation mechanisms known to affect alkali metal|ISE interfaces. A graphical summary of some of these interfacial challenges is provided in Figure 3.1. A degradation of the interface can either occur at rest (when no current is applied across the cell) or under cycling conditions. Although Figure 3.1 includes some degradation mechanisms occurring at cathode|ISE interfaces, these will not be discussed in this chapter as they were not studied in this thesis.

3.1 Metal|ISE interface resistance

To maximize the charge/discharge rate of a cell (its power performance), all its sources of internal resistance to ionic diffusion should be minimized. The overall ionic resistance of the electrolyte can be minimized by increasing its ionic conductivity or by making it thinner (see section 2.3). Another important contribution to the cell resistance comes from the transfer of Na^+ ions across the electrode|ISE interfaces. Depending on the choice of electrode and ISE materials and on the procedure employed to assemble the cell, interface resistances can vary by orders of magnitude. For example, a list of Na|NZSP interface resistances recently reported in the literature is provided in Table 3.1. The reported values of $R_{\mathrm{Na|NZSP}}$ vary from a few Ω cm^2 to over 10,000 Ω cm^2 for the most resistive ones. Extensive research on the subject has allowed a good understanding of the factors influencing the metal anode|ISE interface resistance to emerge.

Charge transfer at the interface between oxide ISEs (such as NaSICONs, Na-β/β"-

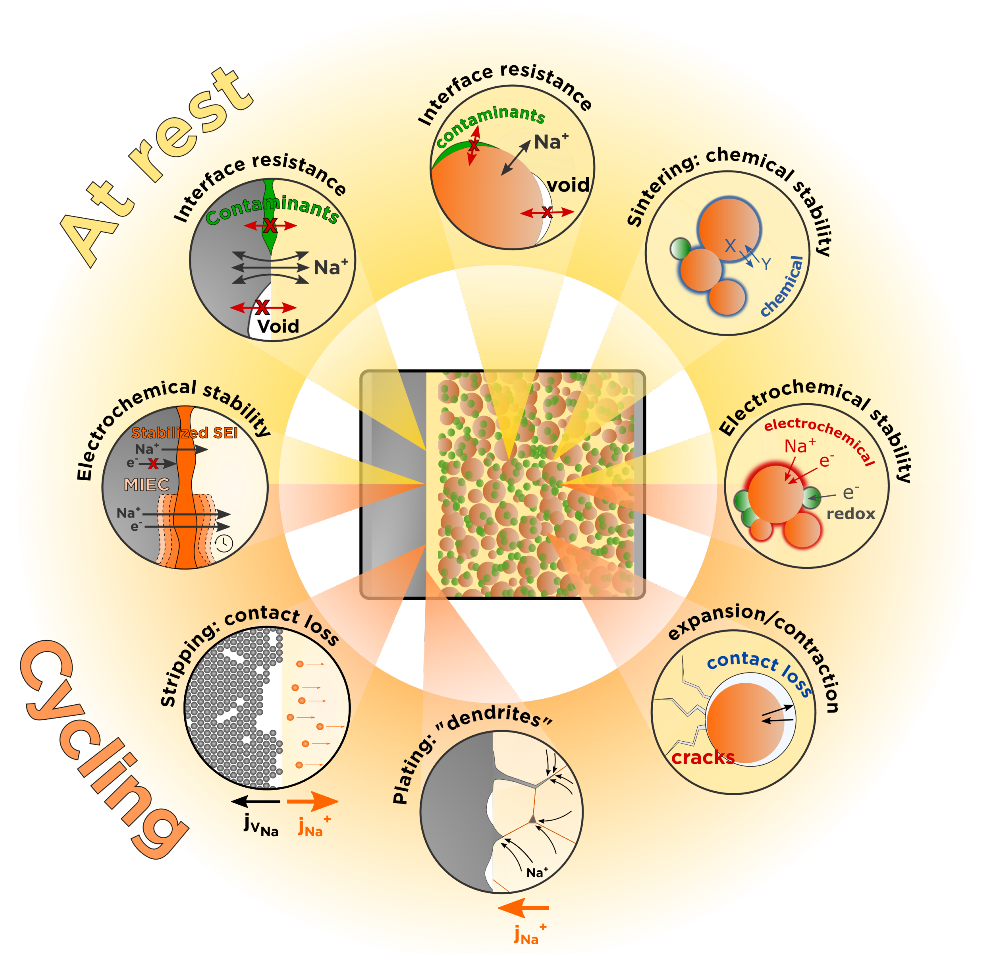

Figure 3.1: Schematic summary of challenges affecting electrode|ISE interfaces in SSBs. The issues affecting the metal|ISE and the ISE|cathode interfaces are grouped on the left/right respectively.

Al_2O_3, or LLZO) and alkali metal anodes has long been considered to be intrinsically sluggish because of the large interfacial resistances which were measured in the first experimental cells. But recent studies allowed to clarify that the charge transfer resistance at metal|ISE interfaces can, in fact, be as low as 0.1 Ω cm^2 at room temperature.[68, 57] The metal|ISE interface resistance can therefore be dominated by other resistive contributions than charge transfer. In other words, it is important to separate the charge transfer resistance (which only accounts for the resistance associated with the $Na^0_{anode} \leftrightarrow Na^+_{ISE} + e^-_{anode}$ transfer) from the interface resistance (which corresponds to the apparent sum of all interface processes with a resistive contribution, charge transfer being only one of them).

It is now well understood that the initial alkali metal|ISE interface resistance of a cell is predominantly affected by:

1. **Pores** resulting from improper contact between the metal anode and ISE during cell assembly.[69, 70] Pores at metal|ISE interfaces make certain areas inactive for charge transfer. This reduced area available for charge transfer creates a constriction resistance as the migration path of Na^+ ions is tortuous at the interface. Applying external pressure to the cell stack during cell assembly is an efficient solution to create an intimate contact between the metal anode and ISE and was demonstrated to minimize constriction resistance.[104] In the absence of adventitious contaminants or resistive interphases, a simple equation can be used to relate the impact of applying a force F on minimizing the constriction resistance R_{constr}:

   $$R_{constr} = \frac{\rho}{2}\sqrt{\frac{\pi.H_{Na}}{F}} \tag{3.1}$$

   where ρ is the resistivity of the ISE and H_{Na} is the Vickers hardness of Na metal (in the case of a Na metal SSB). As an example, Uchida et al. were able to reduce the Na|NaSICON interface resistance of their cells from 660 Ω cm^2 to 14 Ω cm^2 by applying a 30 MPa pressure during cell assembly.[70]

2. **Contaminants** which can be found on the ISE surface and/or the Na metal surface prior to cell assembly are a second interface resistive contribution.[71, 25, 72, 73, 74] Na metal is an extremely reactive specie and a passivation layer will always form on its surface even in the cleanest of gloveboxes. Some ISEs can also form a passivation layer on their surface because of a reaction with a gas phase or by reaction with a solvent if the samples are polished. One example is Na-β/β"-Al_2O_3 whose surface can get passivated by Na_2CO_3 and NaOH.[25] These surface contaminants can typically be decomposed with a short annealing step at high temperature. If the ISE is assembled after the annealing without exposing it to air (or even residual gases in glovebox atmospheres), the interface resistance can be lowered by orders of magnitude (for instance from $1.99x10^4$ Ω cm^2 to 8 Ω cm^2 for the Na-β/β"-Al_2O_3 interface).[25]

3. **Interphases** forming from the decomposition of the SE in contact with the metal anode can also increase the interface resistance. The types of interphases and strategies to prevent their formation will be presented in section 3.2

Pub.	**Stoich.**	**R_{int} (Ω cm^2)**	**C_{int} (10^{-7} F)**	**Surface treatment and Cell assembly**
Noguchi[75]	$NZSP_3$	17,000*	0.42	NR
Gao[76]	$NZSP_3$	13,100	NR	**Polishing**: 1200/2500 SiC **Annealing**: 1100 °C for 30 min in air **Cell assembly**: heated at 70 °C for 1 h in a furnace
Wang[77]	$NZSP_3$	340-1360 *	$\sim$ 1	NR
Yang[78]	$NZSP_3$	1402	0.53	**Polishing**: Yes **Annealing**: No **Cell assembly**: pressure and temperature (80 °C for 1 h)
Uchida[70]	$NZSP_3$	660	1.2	**Polishing**: 9/3 µm diamond paste **Annealing**: 1100 °C for 30 min in air **Cell assembly**: no pressure applied
Gao[76]	$NZSP_3$	636	NR	**Polishing**: 1200/2500 SiC **Annealing**: 450 °C for 2h in air **Cell assembly**: heated at 70 °C for 1 h in a furnace
Kehne[79]	NScZSP	578	4	**Polishing**: mirror polished with a solvent **Annealing**: 800 °C for 1 h in air **Cell assembly**: Na is cold pressed by hand
Ma[80]	NScZSP	175	12	**Polishing**: dry polished **Annealing**: no **Cell assembly**: Na is cold pressed by hand
Yang[78]	$NZSP_3$	101	1.3	**Polishing**: Yes **Annealing**: No **Cell assembly**: TiO_2 interlayer to improve wetting. Pressure and temperature (80 °C for 1 h)
Uchida[70]	$NZSP_3$	14	50-160	**Polishing**: 9/3 μm diamond paste **Annealing**: 1100 °C for 30 min in air **Cell assembly**: 30 MPa pressure
Ma[16]	$NZSP_{3.4}$	4.1	4.7	**Polishing**: no (as sintered) **Annealing**: no **Cell assembly**: Na is cold pressed by hand
Song[81]	NMgZSP	1.98*	NR	NR

Table 3.1: List of reported Na|NZSP interface resistances and associated surface treatments in recent literature. $NZSP_3=Na_3Zr_2Si_2PO_{12}$, $NZSP_{3.4}=Na_{3.4}Zr_2Si_{2.4}P_{0.6}O_{12}$, $NScZSP=Na_{3.4}Sc_{0.4}Zr_{1.6}Si_2PO_{12}$, $NMgZSP=Na_{3.1}Mg_{0.05}Zr_{1.95}Si_2PO_{12}$, NR = not reported, values followed by a star symbol (*) were calculated from data available in the article.

3.2 Electrochemical stability

Predicting, characterizing, and controlling the decomposition reactions which can occur at alkali metal|ISE interfaces constitute an important part of the current research on SSBs. The attention that these challenges receive is deserved because what is at stake is the preservation of the cells electrochemical performances in the long-term. The formation of new phases (called interphases) via an electrochemical reaction involves the participation of electrons e^- and ions between the anode and the ISE. These reactions are thermodynamically driven. In some cases, a reaction with a negative reaction energy may not occur if it is kinetically stabilized. Electrochemical reactions can occur during the assembly and/or cycling of cells. Selecting materials to produce a stable interface or engineer a stable interphase is key in guaranteeing the cells longevity. Failure to select appropriate materials can lead to large internal resistance growths (power density degradation), capacity fading (energy density degradation) and short-circuits (cycle life degradation).

Electrochemical stability window

The electrochemical stability window of an ISE is the voltage range that it can withstand without suffering redox decomposition. Together with the ionic conductivity, the stability window of an ISE is one of its most important characteristics. An ISE with a large stability window can be used in a high voltage cell, which is desirable for high energy density (see Equation 1.1). To speed up materials discovery, electrochemical stability windows are often theoretically estimated before materials synthesis and experimental measurements. For example, the calculated electrochemical stability windows (or voltage stability windows) of various Na conducting ISEs is presented in Figure 3.2.[82]

Theoretical predictions of voltage stability windows rely on first principles calculations based on density functional theory (DFT). In particular, two methods are widely used to estimate the voltage stability of ISEs.[88] The first method requires a prior knowledge of the set of phases that an ISE can decompose to at oxidative (when Na atoms tend to be extracted from the ISE lattice) or reductive (Na atoms tend to be inserted into the ISE lattice) potentials. To establish if an ISE is stable at a given voltage, the grand potentials Φ of each phases (ISE and decomposition phases) are calculated at this voltage (for information on how to calculate Φ, refer to [88]). The ISE will be stable at this voltage if its grand potential lies on the so-called “grand potential convex hull”. This operation is repeated over a range of different voltages until an oxidation and reduction limit are

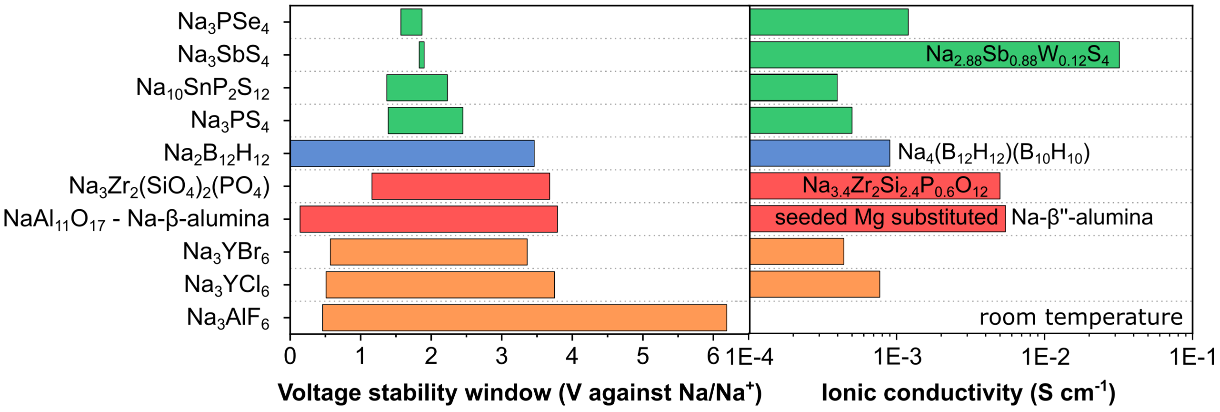

Figure 3.2: The voltage stability window and ionic conductivity of candidate Na-ISEs. For each phase, the ionic conductivities are the highest experimentally reported values to date. For some ISEs, a different stoichiometry is used for the ionic conductivity. Care was taken not to choose too distant stoichiometries which could have a different stability window than on the left panel. For instance, the ionic conductivity of $Na_4(B_{10}H_{10})(B_{12}H_{12})$ was preferred over $Na_4(CB_9H_{10})(CB_{11}H_{12})$ even if the latter one is much higher (70 mS cm^{-1}) because no data could be found at the time of writing on the thermodynamic stability window of the closo-carbaborate. The voltage stability windows were calculated in references [82, 83]. For the ionic conductivities, the following references were used: Na_3PSe_4 [84], $Na_{2.88}Sb_{0.88}W_{0.12}S_4$ [85], $Na_{10}SnP_2S_{12}$ [86], Na_3PS_4 [87], $Na_4(B_{12}H_{12})(B_{10}H_{10})$ [50], $Na_{3.4}Zr_2Si_{2.4}P_{0.6}O_{12}$ [16], seeded Mg-substituted Na-β-β"-alumina [58], Na_3YrCl_6 and Na_3YrBr_6 [83]

found. For example, the voltage stability windows presented in Figure 3.2 were calculated using this method. The voltage stability window predicted by this method is a worst-case scenario because the decomposition of an ISE into new phases at its oxidation/reduction limit often requires an activation energy which increases the voltage stability window by a certain overpotential. The second approach to predict the stability window of an ISE consists in calculating the potential at which a Na atom can be topotactically removed/added from/to an ISE structure. This second method does not consider the possible phases that an ISE can decompose to and therefore constitutes a purely thermodynamic calculation (no kinetic effects involved). This method provides an estimation for the widest voltage stability window.

The high voltage oxidation stability of an ISE is set by its inclination to give electrons at a given potential. The propensity of an atom to give an electron away is defined as its ionization energy. Atoms with a low ionization energy do not require much energy to give an electron away. Typically, the oxidation stability of an ISE is set by its anion framework. The trend from low to high oxidation stability goes as $N^{3-} < P^{3-} < H^{-} \ll S^{2-} < I^{-} < O^{2-} < Br^{-} < Cl^{-} \ll F^{-}$.[89] This rule of thumb can be verified in Figure 3.2 where, for instance, the oxidation stability of sulfides (with S^{2-} anions) is worse than that of oxides (with O^{2-} anions) and that of halides (with F^{-} or Cl^{-} anions). The oxidation of the ISE is typically studied at cathode|ISE interfaces. If an electronically conductive additive is used in the cathode composite, the oxidation of the ISE can also occur at the interfaces where the ISE is in contact with the additive.[88]

At low voltages, ISEs might be reduced if they are prone to accept electrons from the anode. Metallic anodes have very low voltages which very few ISEs are stable at. The reduction stability of an ISE is influenced by its non-mobile cations and the bond stiffness of the polyanionic framework.[31] Among the selected ISEs presented in Figure 3.2, only the closo-borate $Na_2B_{12}H_{12}$ is predicted to be stable at 0 V against Na/Na^+.

Figure 3.2 shows that there is no family of ISEs which surpasses others both in terms of ionic conductivity and voltage stability window. For instance, the good ionic conductivity of sulfides is counterbalanced by their narrower stability window. Inversely, the stability window of Na_3AlF_6 is very large but Na_3AlF_6 is a poor Na^+ ion conductor (so much so that its room temperature ionic conductivity has not been measured but is expected to be below 10^{-10} S cm^{-1}).[90]

Interface/interphase types

Electrode|ISE interfaces are typically separated into three types (schematically represented on Figure 3.3) depending on whether the interface is electrochemically stable or, if it is not, the stability of formed interphases. It is important to distinguish the terms “interface” - which refer to the area of contact between two phases - and “interphase” - which refer to the new phases which are produced at an interface from electrochemical reactions.

1. **Intrinsically stable and kinetically stabilized interfaces.** Intrinsically stable interfaces constitute the ideal case where the ISE and the electrode are thermodynamically stable with no driving force for reactions. Only a few metal|ISE interfaces are intrinsically stable (as seen on Figure 3.2). In some cases (such as the Na|Na-β/β"-alumina or the Li|LLZO interfaces), the theoretical decomposition potential of the ISE is so close to the metal’s potential that the interface can be kinetically

stabilized (*i.e.* the overpotential required for the ISE to decompose extends the voltage stability window of the ISE beyond the metal's potential).[91]

2. **Stable interphases.** This type of interface is obtained when the electrode and ISE react to form a stable solid electrolyte interphase (SEI) with negligible electronic conductivity, preventing further degradation. An ideal SEI will also have a good ionic conductivity to limit the internal resistance rise of the cell and maintain good power performance.

3. **Mixed ionic electronic conducting (MIEC) interphases.** This is the functional scenario which should be avoided. In this case, the interphase is both ionically and electronically conducting and results in the continuous decomposition of the ISE. This type of interphase is likely to form if the ISE contains metal or metalloid elements.[89] In this case, a protecting layer will be required to separate the electrode from the ISE.

In addition to the computational predictions previously mentioned, the stability of an interface can be assessed by several direct and/or indirect experimental techniques. The evolution of the cell resistance with time can reveal information about the nature of the interface (see Figure 3.3): if the interface is stable, the resistance should stay constant; if it forms a type 2 interface whose SEI is resistive, then the cell resistance will initially increase before reaching a plateau when the interphase is stabilized; if a type 3 interface is formed, the resistance will drop because the partial electronic conductivity of the interphase will dominate the total electrical conductivity of the cell.

Characterizing the growth-rate and chemical composition of interphases using direct experimental methods is challenging because interphases typically have a low volume fraction making them invisible to bulk characterization techniques, and they are often buried at distances exceeding the depth resolution of surface characterization techniques. Ingenious workarounds have however been developed to enable the characterization of interfaces in SSBs.

In-situ TEM studies are one of the direct observation techniques which can be used to assess the stability of interfaces. The experiments can be complex as they typically require to put in contact two thin lamellas of each phases inside the microscope using micro-manipulators.[93, 94] These studies provide interesting information about the growth kinetics of the interphase just after contact, and combined with electron energy

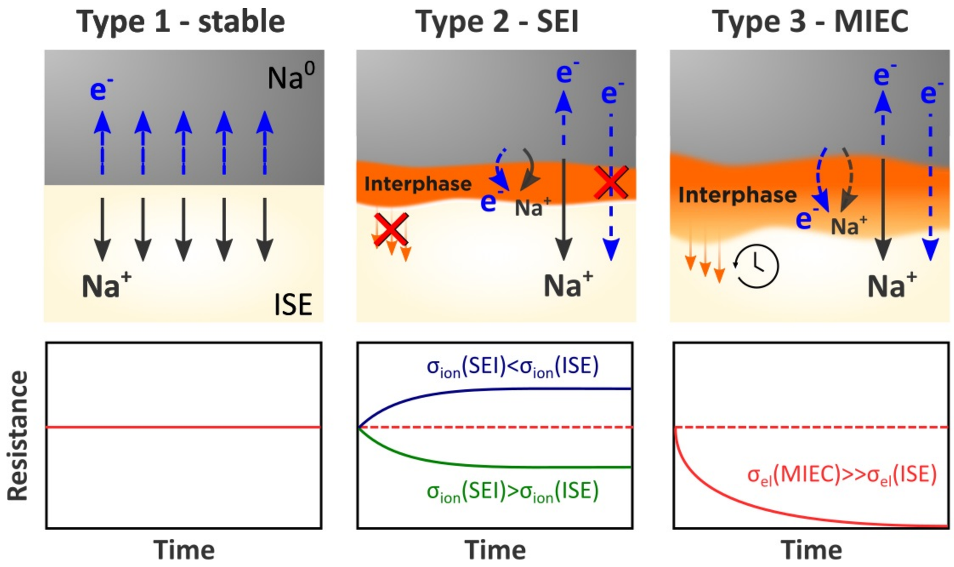

Figure 3.3: Types of interfaces between Na metal and ISEs and their expected cell resistance evolution with time. Adapted with permission from [92]

loss spectroscopy (EELS), the chemical composition of the interphase can also be investigated.

X-ray photoelectron spectroscopy (XPS) can also be used to study the chemical composition of interphases at metal|ISE interfaces. What comes to mind first when one wants to obtain information about the composition of the metal|ISE interphase, is to disassemble an aged cell, remove the metal electrode, and analyse the surface of the ISE which was in contact with the metal. Careful analysts will employ vacuum transfer modules to transfer the sample from the glovebox where the cell was disassembled to the XPS instrument. Yet, even this protected transfer to the spectrometer can influence the composition of the interphase (if the phases are highly reactive) and lead to a misinterpretation of the exact decomposition mechanism. *In-situ* and *in-operando* experiments have been developed to circumvent this issue and ensure that the chemical composition of the interphase is not affected by an exposition to an atmosphere.[95, 92, 96, 97] The *in-situ* strategies presented in Figure 3.4 rely either on custom-made XPS instruments with access to thin-film deposition chambers,[98] or on the clever engineering of a target holder enabling to deposit a thin film on a substrate using the Ar^+ sputter gun available in most XPS instruments.[95] Recently, Wood *et al.* also proposed a technique allowing to plate the metal electrode on the ISE surface by employing the charge compensating electron flood gun as a "virtual electrode" and whilst measuring the composition of the interphase *in operando*.[96] This

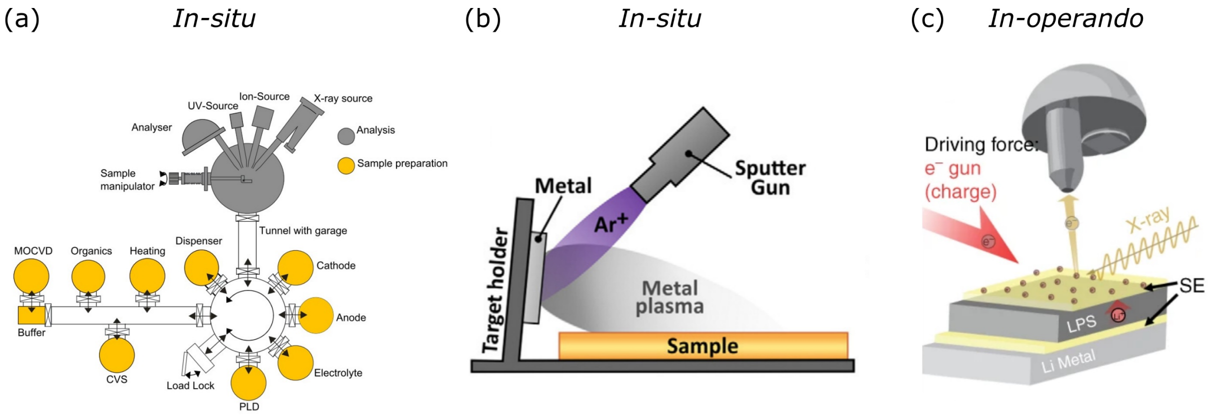

Figure 3.4: Three XPS solutions to study the stability of metal|ISE interfaces. (a) Custom XPS systems with deposition chambers connected under vacuum to the XPS chamber (the Daisy-Bat platform in Darmstadt).[98] (b) *In-situ* sputter deposition of a metal thin film inside a XPS.[95] (c) *In-operando* plating of a metal layer using the XPS charge compensating flood gun.[96]

last technique was adapted to study the stability of the Na|NZSP interface in this thesis and will be described in more details in Chapter 8.

Protecting/buffer layers and alloys

The only functionally viable interfaces for battery operation are type 1 and 2 interfaces. If the ISE and electrodes react to form a type 3 interface (MIEC), then a protective interlayer will be required. If the reaction products from a type 2 interface are ionically insulating and the interface has a large resistance, then a protective interlayer can also be considered. Two new interfaces are created when a interlayer/buffer layer is employed: an electrode|interlayer and an interlayer|ISE interface. Whilst it is not absolutely necessary that the interlayer forms stable interfaces (type 1), it is however crucial that they form a type 2 interface with ionically conductive interphases.

On the anode side, the protective layer should prevent the reduction of the electrolyte. The low electron affinity of N^{3-} and H^{-} anions make nitride, and hydride compounds generally stable against alkali metals and interesting options as protective layers.[99] This strategy was cleverly employed in a recent study to stabilize Na_3SbS_4 against reduction versus Na metal.[100] To form a protective interlayer *in-situ*, a two-step process was used. The Na_3SbS_4 samples were first exposed to humid air to form a hydrated $Na_3SbS_4.8H_2O$ compound on their surface. Upon contact with Na metal, the hydrated ISE reacted to form an electronically insulating but ionically conducting interphase composed of NaH and Na_2O. The stabilized Na_3SbS_4 was successfully cycled against Na metal even though the predicted reduction potential for the pristine phase is of 1.83 V (see Figure 3.2).

Whilst protective layers attempt to improve the stability of an ISE towards an electrode by extending its voltage stability window, another strategy consists in choosing electrodes whose potential already lies within the ISE stability region (or within the kinetic stability region). On the negative electrode side, preventing the reduction of ISEs which are unstable at 0 V against Na metal can be achieved by employing Na-M alloys (with M = Sn, Pb, Ge, or Si). In the case of Na-Sn alloys, the voltage varies between around 0.7 V (in the discharged state, Sn) to 0.1 V (in the charged state, $Na_{15}Sn_4$) vs Na/Na^+.[101] This strategy is commonly employed to prevent the anodic decomposition of sulfide ISEs.

3.3 Dynamics of metal|ISE interfaces under stripping

The discharge of metallic anodes is commonly referred to as stripping or electrodissolution. The terminology reflects the mechanism occurring at a metal|ISE interface during discharge. Under an anodic load, charge transfer occurs via the ionization of a metal atom located at the interface: $Na_{Na}(Na) + V'_{Na^+}(SE) \rightarrow Na^X_{Na^+}(SE) + V^X_{Na}(Na) + e'(Na)$ in Kröger-Vink notation. In this equation the transfer of a Na metal atom ($Na_{Na}(Na)$) to a vacant mobile cation site of the neighbouring ISE ($V'_{Na^+}(SE)$) creates a vacancy at the interface ($V^X_{Na}(Na)$) and liberates an electron $e'(Na)$. For simplicity, the previous equation assumes a vacancy migration mechanism, but a correlated migration could also be considered (see section 2.2). The interface can become morphologically unstable if metal vacancies are not annihilated quickly enough. For instance, at a current density of 2.5 mA cm^{-2} (corresponding to a 2 h discharge rate for a cell with an areal capacity of 5 mAh cm^{-2}), a 6 nm layer of Na metal is stripped from the interface every second. These vacancies need to be quickly eliminated to prevent the delamination of the metal|ISE interface. It must also be emphasized that this value is a lower limit, and that the depletion rate can be even faster if the electrodissolution is not uniform across the entire interface (constriction hotspots). The following sections aim to describe this issue in more details and include some established solutions to mitigate/prevent it.

Experimental evidence of interface contact loss during stripping

The accumulation of interfacial vacancies is a problem which was reported to affect many metal|ISE couples under stripping conditions (both in Na-SSBs and in Li analogues). The existence of interfacial pores in experimental systems has been demonstrated indirectly (using electrochemical methods)[69, 102] and directly (using in-situ X-ray computer tomography [103] and *ex-situ* SEM [103, 69, 68]). To demonstrate the accumulation of vacancies using electrochemical methods, Krauskopf *et al.* analysed the electrochemical response of a metal|ISE|metal symmetrical cell from which one metal electrode was stripped.[69] In the experiment presented in Figure 3.5, a small current density of 0.1 mA cm^{-2} is applied across the cell until the accumulation of interfacial voids at the stripped electrode creates a large constriction resistance resulting in a large overpotential. The overpotential increase occured at a critical stripping time t_0 of around t = 11 h. The overpotential was attributed to an increase in the cell's interface resistance by employing impedance spectroscopy (bottom of panel b). Two further studies making use of a reference electrode confirmed that the interface whose resistance increases is the stripped electrode interface and not the plated electrode one.[102, 103]

Further evidence of the existence of voids at the stripped interface were provided by *ex-situ* SEM studies. One example is presented in Figure 3.5 where microscopic voids can clearly be seen on the surface of the Li metal electrode after stripping.[69] In another study, cross-sections of cycled symmetrical cells were produced using an ultrasonic cutter

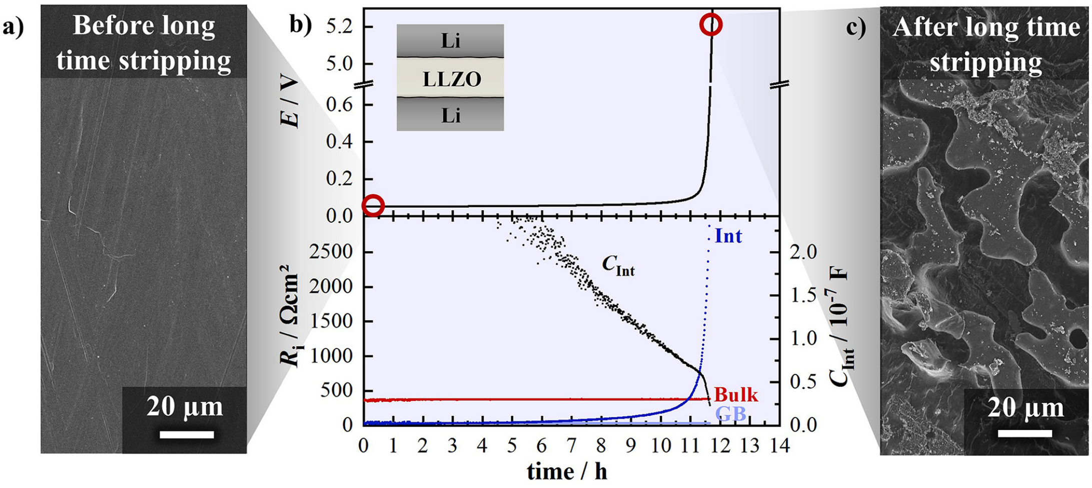

Figure 3.5: Pore coalescence at the Li|LLZO interface under stripping. Reproduced with permissions from [69].

which allowed to observe the voids without having to peel the metal foil off the ISE.[103] These experimental observations have led researchers to develop theoretical models to explain the nucleation and annihilation of interfacial vacancies. Some of these models are discussed in Appendix B.

Solutions to prevent void formation

Interlayers

Mathematical models discussed in Appendix B suggest that the coalescence of pores at metal|ISE interfaces can be stopped if the interfacial adhesion between the metal and ISE exceeds a certain value. If the interfacial adhesion between the metal and ISE is below this critical value for interfacial adhesion, then an interlayer can be used to promote adhesion. In most cases, the interlayer is not stable in contact with the metal anode and react to form an interphase. This reactivity is sought because it provides a driving force for spreading. Eventually, the reactivity of the alkali metal with the interlayer yields an intimate interfacial contact, a phenomenon which is called reactive wetting. A soon to be published review written in collaboration with Dr. Rowena Brugge, Dr. Ieuan Seymour, Dr. Federico Pesci and Dr. Ainara Aguadero will focus on various aspects of solid|solid wetting (details can be found in the Dissemination).

An important consideration which will dictate the choice of material for the interlayer is if the ISE is stable against reduction at 0 V vs Na/Na^+: if the ISE is not stable, then the interphase will have to be electronically insulating whereas a conductive interphase will be acceptable if the ISE is already stable at 0 V.

Despite the great popularity of reactive interlayers, very few studies have focused on their long-term morphological stability. Yet, a gradual dissolution of the interlayer in the bulk of the metal anode is strongly suggested by the few studies which did look at their long term stability.[104, 105, 106, 107] The dissociation of the interlayer from the interface, even if this occurs in several hundreds of hours, could cause a serious limitation to the use of this strategy to ensure metal|SE adhesion in the long term. As the elements of the interlayer diffuse in the metal electrode and ultimately form a diluted anode alloy, the driving force for maintaining good contact between the anode and SE could be lost. For this reason, interlayers were qualified as cell assembly "contact mediators" by Krauskopf *et al.*.[108]

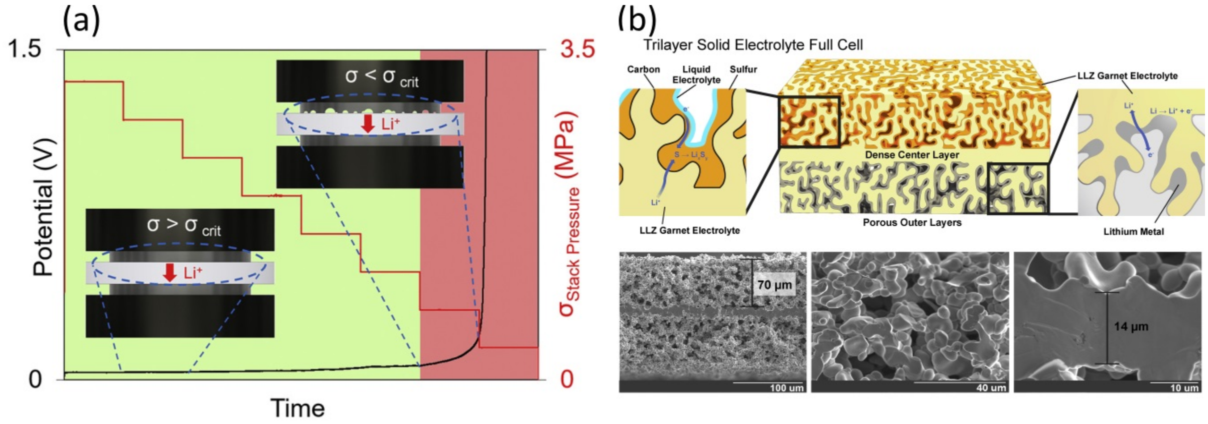

Figure 3.6: Solutions to prevent void formation. (a) The accumulation of interfacial vacancies can be prevented by applying pressure on the cell stack; below a certain critical pressure, the impact of pressure is not sufficient to annihilate the interfacial vacancies and a large overpotential is observed. Reproduced with permission from [102]. (b) a 3D architecture can be used to minimize the local current density at each infinitesimal interface area whilst maintaining a large apparent current density. Reproduced with permission from [20]

Pressure

It is still debated whether the application of an external pressure on cells to mechanically deform the metal anodes and maintain contact at the interface will be required in commercial cells. Applying large pressures during cell assembly was already demonstrated to efficiently lower the initial interface resistance [69] and increase the current density at which cells can be cycled without signs of pore formation (except if the ISE is not fully dense in which case pressure might drive Na metal to infiltrate pores).[103, 102] The critical pressure preventing void formation was estimated in Figure 3.6(a) by conducting an experiment during which the stack pressure applied on a symmetrical Li|LLZO |Li cells was gradually decreased (whilst continuously stripping the same Li electrode) until a large overpotential was observed.[102]

Oxide ISEs typically have large Young's moduli and can be considered non deformable at the pressures which are typically applied. In this case, the pressure is transferred entirely in the form of strain to the metal anode which deforms both elastically and plastically. It was also demonstrated that creep is an important deformation mechanism under cycling conditions for Li and even more for Na metal.[109] For softer ISEs (such as sulfides), the approximation of non-deformation of the ISE is not valid and more detailed mechanical models simulating the deformation of both the ISE and the metal anode are required.

The pressure-induced annihilation of interfacial vacancies comes from the combined effect of creep and plastic deformation.[109] To date, the pressures which are required to maintain the morphological stability of interfaces in Li metal SSBs are prohibitive for industrial applications. With that respect, preventing contact loss in Na metal SSBs should be facilitated by the softer nature of Na metal in comparison to Li metal. This is what is indeed observed experimentally, with several Na metal SSBs operated at charging rates one order of magnitude higher than state-of-the art Li-metal SSBs.[24, 25] This highlights the clear potential of Na metal SSBs for high power applications.

3D interfaces

Without external pressures to maintain contact at the interface, the vacancy diffusion model presented in Appendix B predicts that pores will form at a current density of 0.2 mA cm^{-2} or lower for Li|Li-ISE interfaces (the value will be higher for Na|Na-ISE interfaces due to faster vacancy diffusion in Na metal in comparison to Li metal).[69, 25] This model suggests that stripping at current densities in excess of 2 mA cm^{-2}, which would be required for high power applications, might not be possible with planar metal|ISE interfaces. To achieve high apparent (cell level) current densities while maintaining low local (interface level) current densities, “3D interfaces” have been designed (see Figure 3.6(b)). 3D interfaces refer to structures where the actual metal|ISE interface contact area is large versus its apparent area (the area that the interface would have if it was planar).[20] 3D interfaces are typically produced by melting or electroplating an alkali metal into the pores of an ISE scaffold. These porous ISE scaffolds can be produced by 3D printing [110], freeze-drying [111], or using a sacrificial pore former which can be decomposed during sintering (above 500-600 °C) [112]. The porous ISE scaffolds provide a pathway for ions to reach the alkali metal pockets. By virtue of the much larger actual contact area achieved in such architectures, a high apparent current density in the dense layer can be achieved while, at each infinitesimal interface area, the local current density remains small (thus mitigating pore coalescence).

3.4 Dynamics of metal|ISE interfaces under plating

The main obstacle preventing the use of alkali metal anodes in batteries liquid electrolyte is the inhomogeneous distribution of current fluxes during plating (charging) which can lead to a roughening of the interface. Protuberances at the interface act as current focusing hotspots and the preferential deposition of metal at these tips can ultimately lead to fast propagating dendrites with the risk of short-circuiting the cell.

It was initially thought that plating instabilities would not affect alkali metal SSBs because of the rigidity of solid electrolytes whose mechanical properties are quantified by their Young's (E) and shear (G) elastic moduli and by their fracture toughness (K_{IC}). An early model from Monroe and Newman predicted that polymer electrolytes with a shear modulus twice as high as that of Li metal would not be affected by Li metal penetration.[18] Whilst this criterion is easily met by ISEs, short-circuits at fast charging rates have been demonstrated to affect the vast majority of alkali metal SSBs. The maximum current density which a solid electrolyte can withstand before a short-circuit occurs is named the critical current density (CCD). The CCD of an ISE is conventionally evaluated on symmetrical metal|ISE|metal cells by monitoring their overpotential while the applied current density at each plating/stripping cycle is increased sequentially (see section 4.6). A sharp decrease in the overpotential is typically attributed to the penetration of the electrolyte by metal filaments and the change in the conductivity mechanism from ionic to electronic. At the time of writing, an exact terminology to qualify the metal growths penetrating solid electrolytes has not been established: studies often refer to them as "metal filaments", "Li/Na growths", "metal protrusions" or more frequently "dendrites" (although this terminology is misleading because of its association to a specific morphology in liquid electrolyte cells).

The penetration of Na metal through solid electrolytes has first been observed in the context of the NaS and ZEBRA batteries development from the 1970s.[116] It was found in an early study from Virkar and Viswanathan that both Na-β"-alumina and $Na_3Zr_2Si_2PO_{12}$ were penetrable by Na metal if its temperature was lower than its melting point.[117] More recently, the nucleation and growth (both cross-sectional and lateral) of Li metal

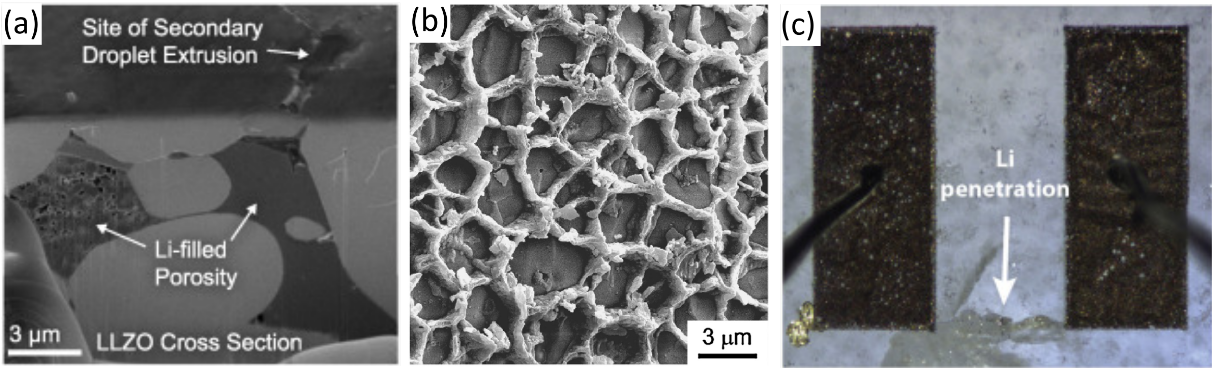

Figure 3.7: Metal penetration in ISEs. The nucleation sites can be: (a) surface pores [113]; (b) grain boundaries [114]; (c) through a grain [115]

across Li-ISEs has been directly observed through *in-situ* and *operando* microscopic studies by taking advantage of the translucent nature of some solid electrolytes (see Figure 3.7).[115, 118, 119] Ectopic metal growths have been observed at different locations in ISEs including: (1) interconnected pores, which can be present in insufficiently densified ISE samples [113]; (2) grain boundaries [114]; (3) through the bulk of ISE grains [115]; (4) inside isolated pores of the ISE [120, 121] (see Figure 3.7).

Most of the models of crack nucleation and propagation established to explain the degradation of Na-β"-alumina in NaS batteries are still in use today although they were initially developed with molten anodes in mind. In particular, the classification of ISE penetration failures into two modes remains valid for room temperature SSBs.[116] The difference between the two modes of failure relate to where the undesirable metal growth is initiated: in ***mode 1***, the metal penetration is initiated at the metal|ISE interface whilst in ***mode 2***, the penetration occurs at a defect site inside the ISE. A schematic illustrating these two failures modes and their driving forces is presented in Figure 3.8.

Mode 1 failures

Attributing the short-circuit of an ISE to a *mode 1* or *2* failure requires to analyse the cell before it short-circuits to locate where metal growths initiated. It cannot be unequivocal based on post-mortem techniques. For non-transparent ISEs where the metal growth mode cannot be directly observed using microscopy techniques, an ex-situ magnetic resonance imaging (MRI) technique based on ^{7}Li nuclear magnetic resonance (NMR) spectroscopy was recently presented as a powerful tool to spatially resolves the growth of Li^0 in a LLZO sample and attribute it to a *mode 1* growth.[122]

In *mode 1*, ISE failure by penetration is dictated by microstructural defects / inhomogeneities at the metal|ISE interface. A particular attention should therefore be dedicated to the processing of ISE membranes and metal|ISE interfaces. The driving force for nucleation of metal protrusions is preferential plating at interfacial current hotspots. The constriction of current lines to these hotspots can be of:

- **Morphological origin:** for instance, voids at the metal|ISE interface (whose presence can either be due to insufficient contact in as-assembled cells [69] or because of contact loss during a stripping cycle, see section 3.3 [103, 123]) will reduce the active area for metal plating and constrict the current to a few interfacial load bearing points; surface defects (cracks, protrusions, grain boundaries emerging to the surface) are also suspected to be preferential nucleation points.[119]

- **Chemical origin:** the partial coverage of the interface by ionically blocking secondary phases (either contaminants or a non-homogeneous distribution of resistive SEI phases) will have a similar current-flux diverting effect as interfacial voids; the distinct chemical composition of ISE grain boundary regions (which can act as sinks for elements during sintering) can make them prone to act as nucleation sites and propagation routes for metal growth;[54, 124] the mechanical softness of grain boundaries has also been proposed to act as a stress relief mechanism for metal|ISE interfaces under electrochemical load explaining the preferential plating of metal at these sites.[125]

The local current densities in hotspot regions can be extremely large because of this current focusing mechanism. The migration of vacancies inside the bulk of Na metal towards the interface can act as a relief mechanism but the fast kinetics of plating in constricted regions is often imbalanced (the Schmalzried and Janek diffusion model derived in Appendix B can be used to demonstrate that).[68, 102] This imbalanced localized flux of incoming atoms results in an electrochemical strain ($\epsilon_{electrochemical}$) which can initiate a crack. Although one could legitimately think that this strain would be mechanically dissipated in the direction of the softer solid (i.e. the alkali metal direction), a strong dependence of the mechanical properties of alkali metal on volume size (a nano volume of alkali metal has different properties to a macro volume) and strain-rate (the faster the plating rate the greater the stress concentration) partially explains how ductile metals can fracture tough solids if they locally accumulate in small volumes.[109] Once initiated, one mode of crack propagation is along the grain boundaries of an ISE. This propagation mode has been demonstrated to exist by ex-situ microscopic [114] and secondary ion mass spectrometry (SIMS) studies both in Li|Li-ISE and Na|Na-ISE systems.[54, 77] Several electro-chemo-mechanical models have been proposed to describe this propagation. More details can be found in the comprehensive reviews from Cao *et al.* and Krauskopf *et al.*.[126, 68]

If the nucleation of metal growth in *mode 1* failures is initiated at metal|ISE interface defect sites, what dictates if a crack will be formed and propagate are the mechanical properties of the alkali metal. One experimental parameter which can be tuned to change these mechanical properties and prevent crack formation is temperature. *Mode 1* failures can be largely mitigated by operating cells at higher temperature as demonstrated by numerous studies which observed a strong dependence of the CCD with temperature.[25, 127, 113] One of these studies focuses on the Na|Na-β"-alumina interface whose CCD can

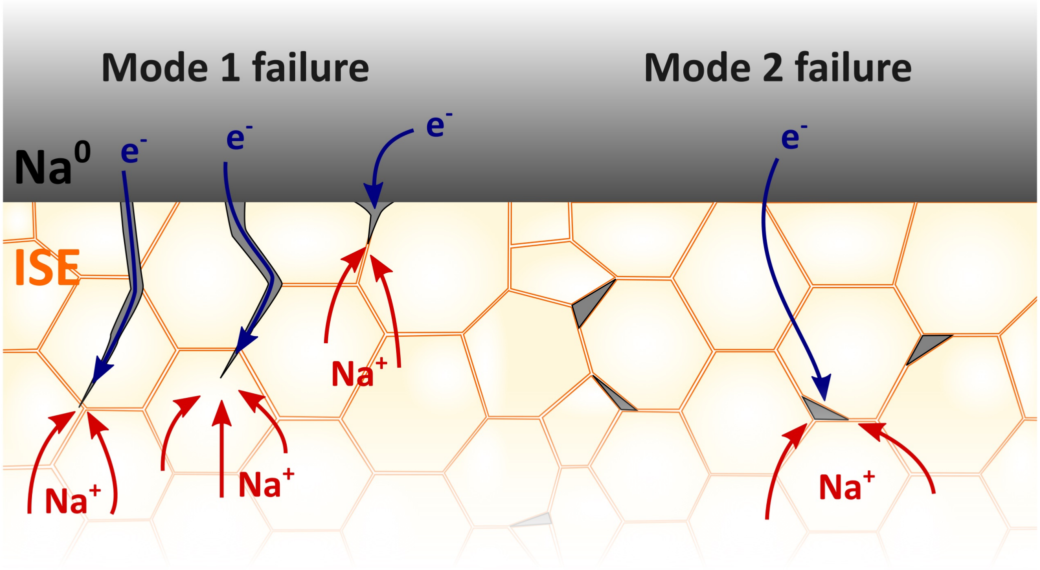

Figure 3.8: The two modes of metal growth through ISEs. In *mode 1*, metal filaments nucleate from the interface whereas in *mode 2*, pockets of Na metal can nucleate at defect sites inside the ISE if its electronic conductivity is too high.

reach 19 mA cm^{-2} at 60 °C.[25] This large CCD was attributed to the faster Na metal self-diffusion when the temperature is increased which facilitates the migration of plated Na atoms away from the interface and alleviates stress concentration. The role of fast diffusion in suppressing crack formation is even more pronounced when the temperature is elevated above the melting point of alkali metals (which drastically reduces their viscosity): in a recent study on the cycling performance of molten Na|Na-β"-alumina interfaces, short-circuits were not observed even at astonishingly high current densities of 2600 mA cm^{-2} (two orders of magnitude higher than for solid anodes).[24]

Stripping and plating cycles can impose two sorts of morphological instabilities to the metal|ISE interface: pore coalescence during stripping, and electrochemical stress on plating. Increasing the Na metal self-diffusivity by operating cells at a higher temperature promotes a good morphological stability of the interface both during plating and stripping. This creates a virtuous cycle as it is known that preventing the formation of interfacial voids on stripping cycles keeps the interface-active area to a maximum and minimize the risks of filament propagation due to current focusing (see section 3.3). Overall, a holistic approach to stabilize the interface under all cycling conditions needs to be adopted because stripping and plating instabilities are interdependent.

Mode 2 failures

This mode of metal nucleation can, at first, seem surprizing considering that the reduction of a mobile cation to a metallic atom requires the participation of an electron. *Mode 2* nucleation is therefore associated to the non-negligible electronic conductivity of some ISEs (especially when $\sigma_e > 10^{-12}$ S cm^{-1}).[120] The exact mechanism of *mode 2* failures is still debated, but the ISE microstructure is often suspected to explain its partial electronic conductivity. In particular, grain boundary regions are investigated as possible electronic pathways because of their distinct chemical composition and structural properties.[54, 128] The trapping of electrons on ISE surfaces (including inner pores) was also recently proposed as an explanation for *mode 2* metal growth.[129] Various electro-chemo-mechanical models of *mode 2* metal growth have been summarized in a recent review.[68]

Experimental evidence of the existence of *mode 2* metal growths in ISE was recently provided by operando TEM [128] and neutron depth profiling (NDP) [120, 130] experiments. More specifically, using NDP, Han *et al.* were able to measure an increase in the Li concentration in the bulk of a Li-ISE whilst cycling; as the concentration of mobile cation in an ISE can typically not change without breaking the charge neutrality condition, they associated the increase to the nucleation of metallic Li in the bulk of their Li-ISE. Combined with post-mortem microscopic studies which revealed the presence of isolated pockets of metal inside various ISEs,[121] it is becoming clearer that *mode 2* metal growths can affect ISEs. Unlike Li, the collision of neutrons with Na does not result in the formation of species which can be detected by NDP detectors which makes this technique unfortunately not adequate to study Na-SSBs.

It is important to note that grain boundaries are not always detrimental in all ISEs and can also suppress metal growth nucleation if they are electronically insulating. This was recently demonstrated for a Li-ISE electrolyte using a combination of transition electron microscopy (TEM), atom probe tomography (APT) and first principles calculations.[131]

Critical current density or critical overpotential for filament penetration?

The tolerance of an ISE to failure by filament penetration is typically tested by measuring its critical current density (CCD, more details in Section 4.6). In mode 1 failures

(Section 3.4), filament propagation in an ISE is often caused by a concentration of the ion flux to a few contact points at the interface. Whilst a potentiostat allows to control an *apparent* current density (set based on an apparent contact area), the *local* current densities could be much higher if the actual contact area is smaller (for instance if pores have accumulated at the interface). This is one of the issues with the concept of CCD which can underestimates the capability of a SE to withstand large current densities. Several groups have started to suggest that a better descriptor for the capability of an ISE to withstand filament propagation is the overpotential it can withstand before failing. The concept of a CCD can also misleadingly suggest that filament penetration is uniquely determined by the properties of the ISE and that the interface has no impact. In reality, a good interfacial contact can often solve all problems of dendrite penetration. As an example, the cycling of Na-ASSBs at a staggering current density of 2600 mA cm^{-2} was demonstrated by Landmann et al. by operating their cell above the melting point of Na^{0}and ensuring the interface was always perfectly wet by molten Na^0.[24]

3.5 Scope of this study

For SSBs to become industrially relevant, the power performance and longevity of devices should be improved. More specifically, metal|SE interfaces should be improved to enable fast charging of SSBs with capacities of 5 mAh cm^{-2} at current densities of 10 mA cm^2 (30 minutes charging).[19] The stability of metal|SE interface should also be improved to guarantee that devices will be able to withstand at least one thousand of cycles (i.e. $>$ 3 years of life for a cell).

This chapter summarized the conclusions of several studies focusing on challenges affecting metal|ISE interfaces which were published both before and over the course of this thesis. Some processes are starting to be well understood by the community, but theories and models presented here are still debated and require further studies. Besides, by virtue of the prevalence of studies focusing on Li-SSBs, most of the theories presented here were developed based on experiments employing Li|ISE interfaces; in most cases, it remains to be proven if Na|ISE interfaces behave similarly. The initial objectives of this study included:

- To develop new protocols to study interfaces in SSBs
- To compare the performance (interface resistance, voids, "dendrites", electrochemical stability,...) of Na|ISE interfaces with those of Li|ISE ones

- To identify possible new sources of degradation affecting Na|ISE interfaces
- And from the understanding developed, to optimize the performance and longevity of the Na|NZSP interface

Chapter 4

Experimental methods

This chapter provides an overview of the experimental techniques employed in this work.

NB: the synthesis described in this section is largely inspired by the protocol established by our collaborators in Forschungszentrum Jülich to whom I am particularly grateful for having accepted to share it with me.[16]

4.1 Synthesis and pellet processing

NZSP Synthesis

Since their discovery, various routes have been proposed to synthesize NaSICON phases. Reported routes include solid-state ones (for which the final phase is obtained via a combination of mechanical milling and high temperature calcination steps) and solution syntheses (where the precursors are homogeneously dissolved in a solution before the solvent is evaporated). Recently, our collaborators in Jülich have developed a hybrid synthesis route relying first on a solution synthesis followed by a mechanical milling step.[16] This solution-assisted solid-state synthesis is described in this section.

$Na_{3.4}Zr_2Si_{2.4}P_{0.6}O_{12}$was synthesized using $NaNO_3$ (Sigma Aldrich, 99 %), $ZrO(NO_3)_2$ (Sigma Aldrich, 99 %), $Si(OC_2H_5)_4$ (Sigma Aldrich, 99 %) and $NH_4H_2PO_4$ (Sigma Aldrich, 99.5 %) as precursor materials. One advantage of nitrate precursors is their good solubility in aqueous solutions. The downside is that their low decomposition temperature typically prevents them from being dried at high temperatures before a synthesis. To reduce water absorption from the precursor powders, all of them were stored in a dessicator (relative humidity around 5-10 %). Before each new synthesis, $NaNO_3$ and $NH_4H_2PO_4$ were dried overnight in a Büchi oven at 80 °C under rough vacuum. For the Zr precursor, a solution

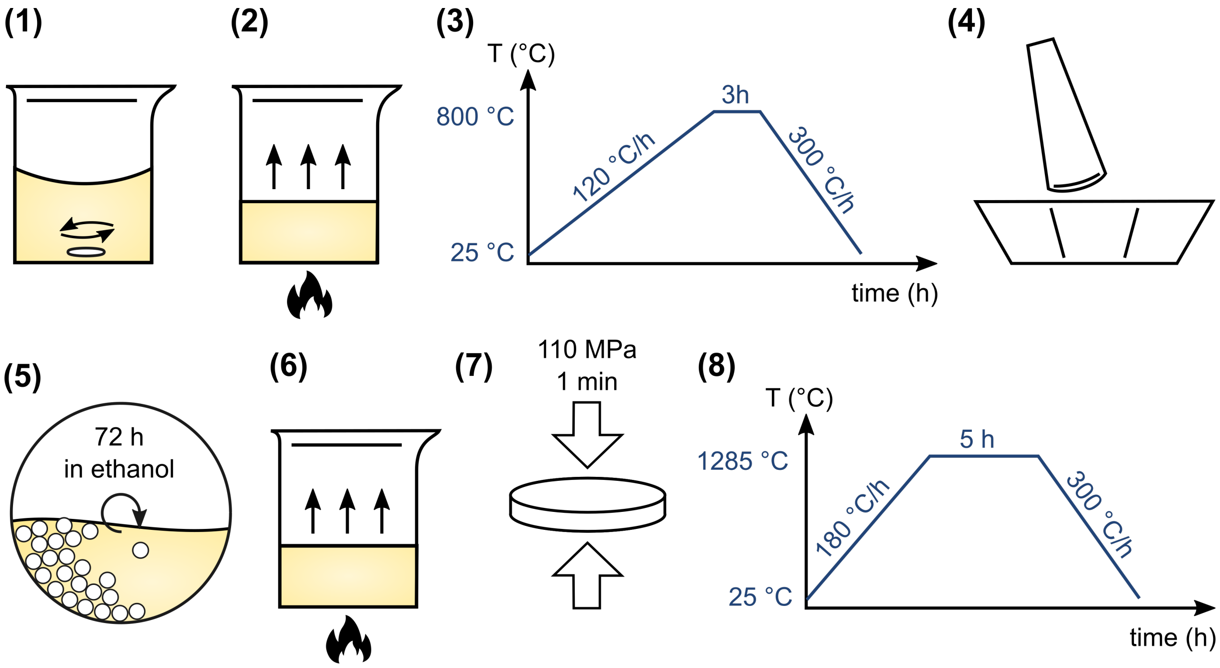

Figure 4.1: Steps of the NZSP synthesis. (1) Mixing of precursors in solution. (2) Solution vaporization. (3) Decomposition. (4) Hand milling. (5) Ball milling. (6) Ethanol vaporization. (7) Pellet pressing. (8) Sintering.

was prepared by dissolving $ZrO(NO_3)_2$ in water and the concentration of Zr in this solution was then measured. More precisely, the concentration of the solution was derived from the mass of the residual ZrO_2 powder obtained after decomposing the solution at a high temperature (a structural analysis of the residual powder by X-ray diffraction confirmed it was ZrO_2).

For the NZSP synthesis (**step 1** in Figure 4.1), stoichiometric amounts of $NaNO_3$ and the Zr-solution were first mixed together in a tall beaker. Concentrated HNO_3 was added while stirring to help with the dissolution of precursors. The volume of HNO_3 represented 5 % of the final volume of the solution once all precursors have been added (this typically corresponded to 20 mL of HNO_3 for a final volume of 400 mL for a synthesis of 20 g of NZSP). The liquid $Si(OC_2H_5)_4$ precursor was then added in stoichiometric proportions in the beaker and the solution was stirred until complete dissolution of all precursors (between one to two hours of stirring). Finally, $NH_4H_2PO_4$ was dissolved in a small volume of water before adding it to the main solution in the beaker still under magnetic stirring. The addition of $NH_4H_2PO_4$ resulted in the rapid formation of precipitates. The solution was then homogenized by stirring for one hour and dried on a hotplate at 80 °C inside a fume cupboard overnight (**step 2** in Figure 4.1).

The dried powder was then decomposed at 800 °C in air for 3 h with heating and cooling rates of 120 °C h^{-1} and 300 °C h^{-1} respectively (**step 3**). The obtained white powder was ground by hand in an agate mortar (**step 4**) and then ball-milled on a roller bench for 72 h in ethanol with zirconia balls (**step 5**). After 72 h, the NZSP powder was retrieved by vaporizing the ethanol (**step 6**). Pellet samples were pressed using a 13 mm diameter die under a pressure of 110 MPa/load of 1.5 T (**step 7**). Pellets were finally sintered in a Pt crucible (or alumina crucible lined with Pt foil) at 1285 °C for 5 h with heating and cooling rates of 180 °C h^{-1} and 300 °C h^{-1} (**step 8**). A Pt crucible was employed because the bottom of NZSP pellets otherwise fused to Al_2O_3 crucibles during sintering.

It was empirically found that adding an off-stoichiometric excess of $NaNO_3$ and $NH_4H_2PO_4$ during step (1) improved the purity, density and ionic conductivity of NZSP samples (see section 5.3). The Na and P precursors were added in excess in the ratio $Na_{3.4}Zr_2Si_{2.4}P_{0.6}O_{12}\cdot$ 1.5 % Na_3PO_4. The optimum ratio of 1.5 % was found to yield the best results (see section 5.3).

The relative density of NZSP pellets used in this study was estimated geometrically by measuring their mass on a scale and dimensions using a caliper. All the pellets used in this work had a relative density of 96 ± 2 %.

Pellet surface processing

Some NZSP pellets used in this work were polished after sintering with SiC pads (Struers, grit sizes: 500, 1200, 2400, 4000). For some samples, ethanol (VWR ethanol absolute >99.8 %) was used as a lubricating solvent. To remove surface residues after polishing, pellets were either sonicated in ethanol for 1 min or dusted with compressed air for dry polished samples.

Some polished NZSP samples were annealed in air after polishing in a muffle furnace at 900 °C, for 0.5 h with a 900 °C h^{-1} heating and cooling rate. The choice of the annealing temperature and heating/cooling rate was based on previous literature on the Li metal|LLZO interface for which it was demonstrated that a large improvement in interface resistance could be obtained using these annealing parameters.[54, 132]

NZSP samples nomenclature

The following nomenclature is used throughout the manuscript to distinguish the surface treatments that NZSP samples have received. The surface processing conditions are indicated in the subscript text at the right of the "NZSP" term. A pellet which has not received any treatment after sintering (*i.e.* as sintered), is referred to as $\mathrm{NZSP_{AS}}$. For polished pellets, the first part of the subscript text indicates if a polishing solvent was used ("EtOH" indicates ethanol was used for polishing, "dry" indicates no solvent was used during polishing), and the second part indicates the finest grit size of SiC pad with which the pellet was polished. For example, $\mathrm{NZSP_{EtOH500}}$ refers to a NZSP pellet which was polished down to a SiC pad grit size of 500 (rough polish) with ethanol as solvent. $\mathrm{NZSP_{dry4000}}$ refers to a pellet which was polished down with SiC pads of grit sizes 500/1200/2400/4000 (fine polish) without using a lubricating solvent. A post-polishing annealing step is indicated by the term "anneal" in the subscript. Finally, $\mathrm{NZSP_{Xsection}}$ refers to a sample which was snapped in half to analyze the chemical composition of the center of a pellet. Table 4.1 summarizes this nomenclature:

Sample name	**Polishing**		**Annealing**
	Solvent	Final SiC grit size	
$\mathrm{NZSP_{AS}}$			
$\mathrm{NZSP_{EtOH500}}$	EtOH	500	
$\mathrm{NZSP_{EtOH500\text{-}anneal}}$	EtOH	500	900 °C, air
$\mathrm{NZSP_{EtOH4000}}$	EtOH	4000	
$\mathrm{NZSP_{EtOH4000\text{-}anneal}}$	EtOH	4000	900 °C, air
$\mathrm{NZSP_{dry500}}$	Dry (no solvent)	500	
$\mathrm{NZSP_{dry4000}}$	Dry (no solvent)	4000	

Table 4.1: Nomenclature of NZSP samples according to their surface treatment

4.2 X-ray diffraction

Theory

X-Ray diffraction (XRD) is a non-destructive characterization technique providing structural information about crystalline samples. When a crystalline sample is illuminated by a X-ray source, the X-rays may be scattered at different depths by different atomic planes. XRD relies on the measurement of the intensity of scattered X-rays as a function of scattering angle. Depending on the angle at which X-rays are scattered, the waves will either interfere constructively if they are in phase, or destructively if they are out of phase (see Figure 4.2). The conditions required for X-rays to interfere constructively are defined by Bragg's law:

$$n\lambda = 2d_{hkl}sin(\theta) \tag{4.1}$$

where n is the order of the reflection (an integer number), λ is the wavelength of the source, and d_{hkl} is an interplanar spacing (any set of lattice planes can be indexed by its Miller indices hkl).

The interference pattern is collected by a X-Ray detector scanning a defined range of angles. The intensity of the reflections is plotted on a graph versus 2θ on the x-axis. The intensity is plotted in arbitrary units as the value measured by the detector depends on the time step defined in the experiment settings: a long time step allows to reduce noise and improve the quality of the data but might not always be necessary to correctly identify a compound. The position of the peaks as well as their intensity ratios are characteristic of a precise structure. If the crystal structure is known, it is easy to predict at which angles constructive interferences will be be observed from equation 4.1. The reverse operation (identifying a crystal structure from its X-ray diffractogram) is more complex because multiple phases with closely separated peaks can be present in experimental powder patterns, and solid samples can crystallize with a preferred orientation. References database have been built and can be used to identify samples (ICSD, Crystallography Open Database). Refinement of the data is commonly used to obtain further information on the crystal lattice parameters (see section 4.2).

In this work, XRD was mainly used to check the purity of NZSP syntheses. X-ray diffractograms were collected either on a Bruker D2 Phaser or a PANAlytical MPD in a Bragg-Brentano geometry with a Cu Kα source (λ = 1.5418 Å), typically in a 2θ range of 10-80 °, with a step size of 0.033 °and an integration time of 1 to 3 s/step. For pellet samples, the sample stage was spun during the acquisition to average the signal over more grain orientations.

Le Bail refinement

Comparing experimental XRD data to reference datasets visually can quickly reach its limits when the sample consists of complex crystal structures with low symmetry or when

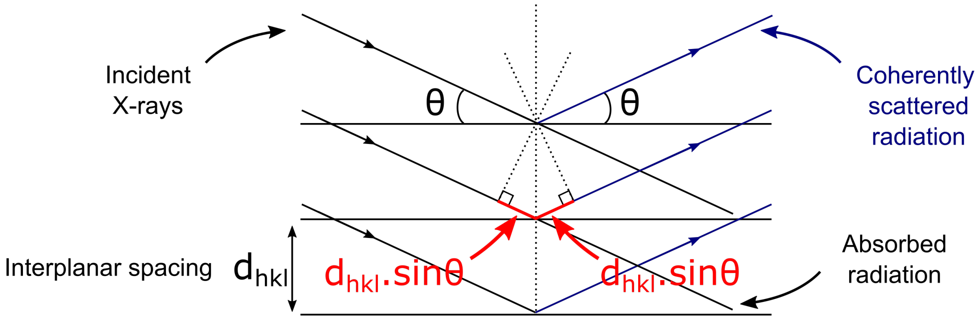

Figure 4.2: Fundamental principle of X-ray diffraction in a Bragg-Brentano geometry

it contains several phases with closely separated reflections. In such cases, more detailed information about the sample structure can be obtained by refining the parameters of synthetic crystal structure models to fit the experimental data. The eponymous Le Bail and Rietveld methods are refinement techniques based on least square minimization algorithms which refine a synthetic line profile until it matches the measured experimental diffractogram. The information which can be obtained from refinement include: the unit cell parameters, atomic coordinates, site occupancies, preferential orientation, strain, or phase fractions in multiphasic samples.

The Le Bail method[133] is a refinement algorithm which can be used to determine the phases present in sample. More specifically, the initial input model has to provide the space groups and approximate cell parameters of the phases which are expected to be found in the sample, and the algorithm then refines these cell parameters and the peak shapes to match the experimental data. The peak intensities are not refined in the Le Bail method. Instead, an arbitrary intensity is initially given to each peak which is then adapted after each least squares minimization iteration to yield the best fit.

In this work, patterns were fitted using the Le Bail method as implemented in the Fullprof software suite. A pseudo-Voigt peak shape function was used to fit the data. The quality of the refinement was assessed visually by plotting the difference between the calculated profile and the experimental data.

4.3 Scanning electron microscopy

Scanning Electron Microscopy (SEM) can be used to visualize the surface microstructure of samples. The technique relies on the detection of electrons escaping from a sample surface as a result of the illumination of the surface by a beam of accelerated primary

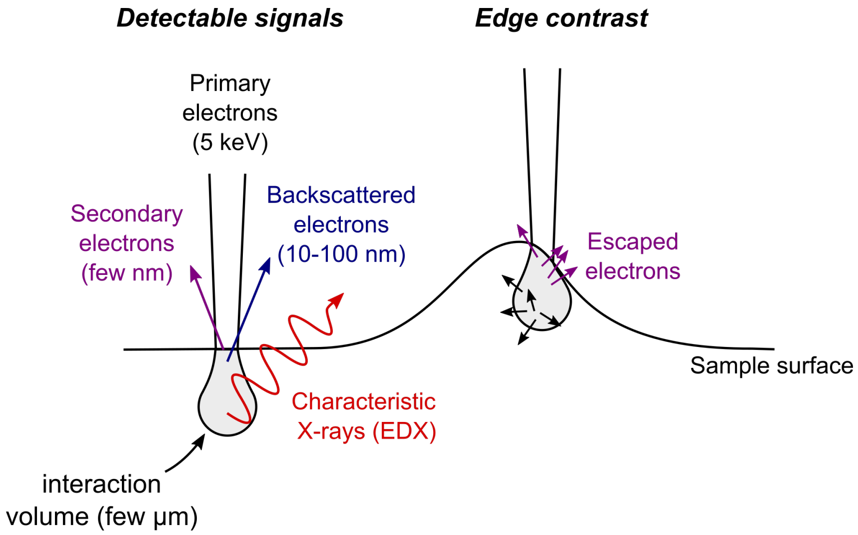

Figure 4.3: Signals produced from the interaction of a primary electron beam with a sample in a SEM. The figure also illustrates the concept of edge contrast.

electrons. SEM images are obtained by rastering the primary electron beam over an area of the sample surface and reconstructing the signal collected on the detector. Two types of electrons escaping from the surface are illustrated in Figure 4.3: (1) secondary electrons are low energy electrons emitted from the excitation of atoms by the high energy beam; (2) backscattered electrons are former primary electrons which penetrated a sample and whose trajectory following scattering events made them resurface and escape into vacuum. Because backscattered electrons have higher energy than secondary electrons, they can escape from a greater depth than secondary electrons. Thus, a SEM instrument operated in secondary electron mode typically gives information about the topography of a sample, whereas when it is operated in backscattered mode, it can provide compositional information about surface and subsurface features. The extreme surface sensitivity of the secondary electron mode make edges on the surface appear brighter, a phenomenon called edge contrast (the increased surface area around edges means that more secondary electrons can escape into the vacuum).

In addition to electrons, the interaction of the primary beam with the sample can also produce X-rays whose energy can be measured by a separate detector. The process leading to the emission of X-rays follows two steps: (1) a hole is produced in a core shell following the excitation of an atom by the primary beam; (2) to stabilize the excited atom, an electron from a higher energy shell fills the core hole and the difference in energy between the two levels can be released in the form of a X-ray. Thus, the X-ray energy is a signature of a particular nuclear transition and can be used to identify an element. The technique, known as Energy Dispersive X-ray spectroscopy (EDS or EDX), is employed to characterize the elemental composition of features on a surface. As the attenuation length of X-rays is longer than that of electrons, X-rays can be detected from the entire interaction volume. To analyze small features by EDX, the primary beam energy needs to be reduced to constrict the interaction volume.

In this work, SEM images were obtained using the in-lens detector of a Zeiss Leo Gemini 1525 at a working distance of 7 mm with an electron beam accelerating voltage of 5 kV and a 30 µm aperture. EDX spectra were measured with a x-act detector (Oxford Instrument) using the same beam excitation. A low accelerating voltage was chosen to ensure a reduced interaction volume and higher surface sensitivity. The low X-ray production rate was compensated by longer integration times.

4.4 X-ray photoelectron spectroscopy

Photoelectron spectroscopy (PES) is a group of surface characterization techniques relying on the photoelectric effect, whereby electrons are emitted by a surface upon its illumination by photons. Among the variety of PES techniques, X-Ray photoelectron spectroscopy (XPS) is probably the most popular thanks to the simplicity with which measurements can be acquired in modern instruments (such as the Thermo Fisher Kα instrument which was used throughout this work). XPS is a very valuable technique to get information on the electronic properties and the chemical environment of samples. The limited depth resolution (< 10 nm) of conventional soft XPS is a key attribute of the technique which makes it extremely well suited for analyzing surfaces but which can also complicate the analysis of buried layers underneath samples surfaces. As XPS is used extensively throughout this work, the technique is described in slightly greater detail than other experimental techniques.

Theory and instrumentation

In its most simplified form, the theory of photoemission can be broken down into the three elementary steps schematically represented in Figure 4.4(a):

1. Photoelectrons are **generated** within a solid from the excitation of electrons in certain atomic orbitals by incident X-rays. The energy of the photons $h\nu$ is transferred

to the photoelectrons and, depending on their core level of origin, these photoelectrons will have different initial kinetic energies.

2. the generated photoelectrons then **travel** through the solid. Some photoelectrons emitted close to the sample surface will reach it without suffering any inelastic collisions. These photoelectrons produce what is called the "primary structure" (see section 4.4). But most photoelectrons (especially those produced from layers deep below the surface) will encounter various scattering processes on their way to the surface through which some of their initial kinetic energy will be lost. These photoelectrons contribute to the continuous background of XPS spectra and to some defined features (*e.g.* plasmons, see section 4.4).

3. last, the photoelectrons which have reached the surface will be **emitted into the vacuum** of the instrument if they can overcome the sample's work function Φ_{sample}.

Assuming no energy loss affects them, primary photoelectrons escape in vacuum with a kinetic energy E'_{K} related to the binding energy of the atomic orbital (E_{B}), the photon energy ($h\nu$) and the sample work function (Φ_{sample}) via:

$$E'_{\text{K}} = h\nu - \Phi_{\text{sample}} - E_{\text{B}} \tag{4.2}$$

These energies are represented on an energy level diagram in Figure 4.4(b). If the sample is electronically conducting, then, once the sample is connected to the analyser, the Fermi levels of the sample and the analyser align (as represented in Figure 4.4(b)). The binding energy of atomic orbitals and the sample work function are referenced with regards to this Fermi level.

By definition, the work function of a material is the difference between its Fermi (E_{F}) and vacuum ($E_{\text{vac-sample}}$) levels. Physically, it corresponds to the minimum energy required to extract an electron out of the material into vacuum. The work function of a material can be affected by space charge potentials and/or surface potentials. Two materials are unlikely to have the same work function (like what is represented in Figure 4.4(b): $\Phi_{\text{sample}} \neq \Phi_{\text{analyser}}$). As a result of their work functions being different, the vacuum levels of the sample and the analyser are not aligned. A contact potential ($\Phi_{\text{contact}} = \Phi_{\text{sample}} - \Phi_{\text{analyser}}$) is thus generated between the sample and the analyser. The kinetic energy of photoelectrons reaching the detector (E_K) is referenced with regards to the vacuum level of the *analyser* (not the sample). From Figure 4.4(b), we can see that:

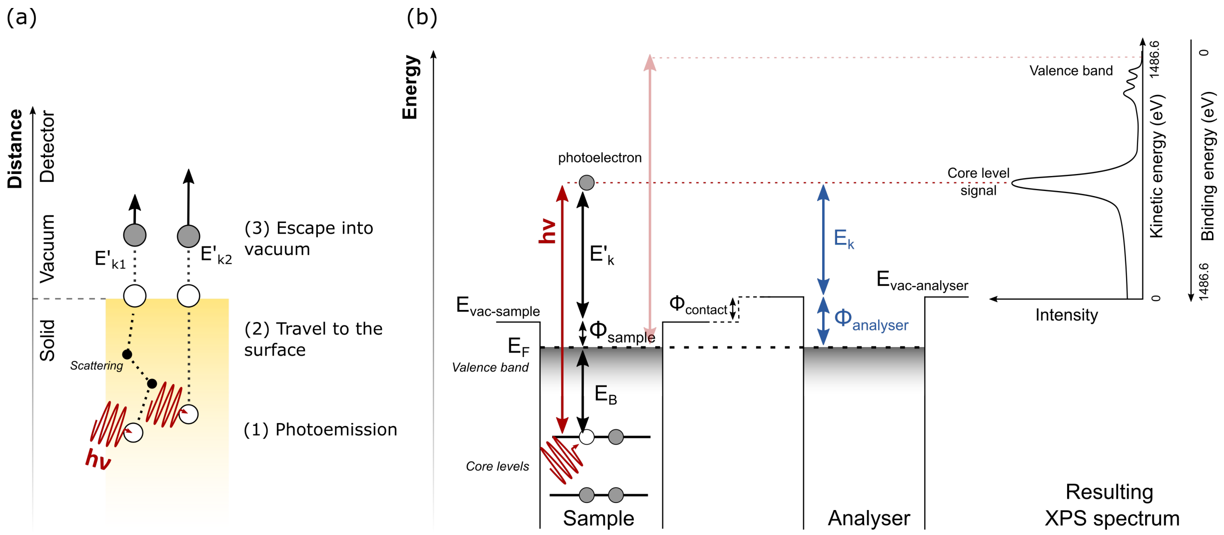

Figure 4.4: Fundamental principles of XPS. (a) The three steps of the photoemission process. The paths of both a secondary photoelectron (subject to inelastic scattering events) and of a primary photoelectron are represented with dashed lines. (b) Energy level diagram for the emission of a photoelectron suffering no scattering energy losses (i.e. a primary photoelectron) from an electronically conducting sample. The energies which can be measured by an XPS instrument are represented in blue.

$$E_\mathrm{K} = E'_\mathrm{K} - (\Phi_\mathrm{analyser} - \Phi_\mathrm{sample}) = h\nu - \Phi_\mathrm{sample} - E_\mathrm{B} - (\Phi_\mathrm{analyser} - \Phi_\mathrm{sample}) = h\nu - E_\mathrm{B} - \Phi_\mathrm{analyser} \tag{4.3}$$

Or rearranged as a binding energy:

$$E_\mathrm{B} = h\nu - E_\mathrm{K} - \Phi_\mathrm{analyser} \tag{4.4}$$

This equation is independent of Φ_sample which means that, for conductive samples, it is not necessary to know their work function to obtain the binding energies of specific atomic orbitals. Since E_K and Φ_analyser can be measured, equation 4.4 gives access to E_B. In practice however, Φ_analyser can be difficult to accurately measure. To remove this complexity, the binding energy scale of the instrument is regularly calibrated using the Fermi edge of metallic calibration standards (typically Au, Ag and Cu). Because metal surfaces have occupied states in their valence band up to $\mathrm{E_F}$, if the binding energy scale is shifted so that the kinetic energy of Fermi level electrons is set to $E_\mathrm{k} = h\nu$ then equation 4.4 simplifies to $E_\mathrm{B} = h\nu - E_\mathrm{K}$ which is independent of Φ_analyser.

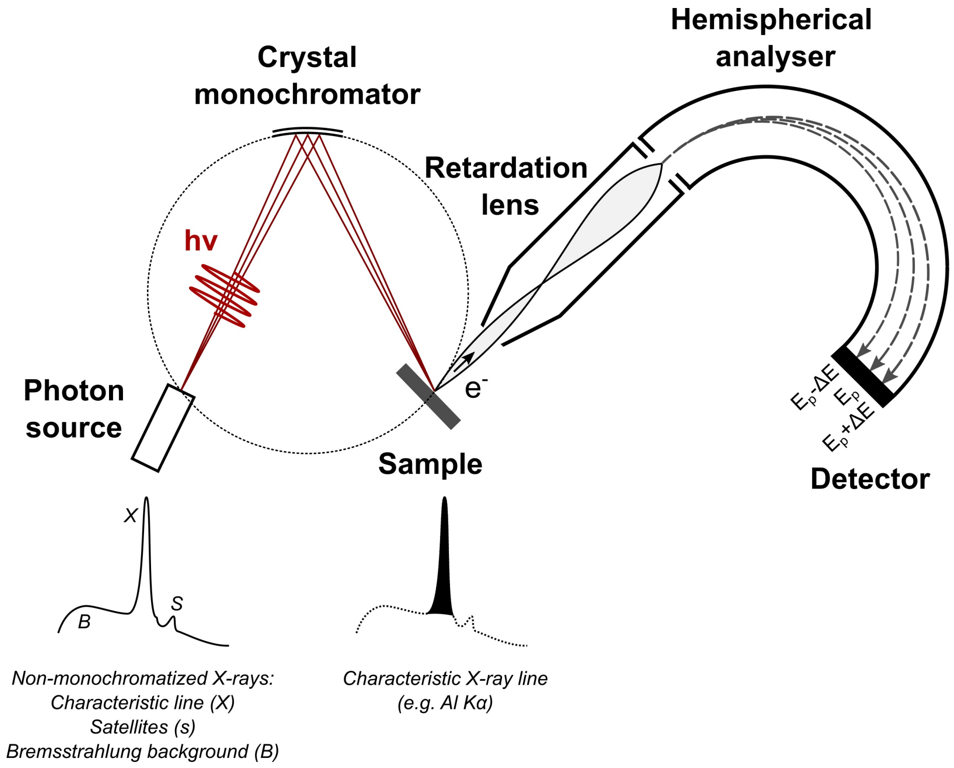

Figure 4.5: The main components of a monochromated XPS instrument. Inspired from [134].

The most common experimental set-up employed to acquire XPS data is presented in Figure 4.5. The first step is to produce a X-ray beam using a photon source (a X-ray gun in a laboratory based instrument, or a synchrotron source). For the XPS instrument used in this work, an Al Kα X-ray gun was employed. The crystal monochromator acts as a filter to remove the Bremstrahlung and satellite wavelengths from the photon source and obtain a narrow beam line width (Al Kα_1 with an energy $\lambda = 1486.70 \pm 0.05$ eV [135]). High-throughput XPS instruments are commonly set so that the monochromated beam hits the sample at an incidence angle of 54.7 ° from the surface normal (which is aligned with the entrance of the detector). Acquiring XPS data at this "magic" angle greatly simplifies data analysis because the asymmetry of the photoemission process (which is subshell dependent) does not need to be taken into account in quantitative analyses: at this collection angle, the relative intensities for photoelectrons emitted from different orbitals are equal to the relative intensities which would be obtained by integrating the photoelectron signals over all emission angles.[134] The ejected photoelectrons are then focused onto the entry slit of the analyser through a retardation lens. In addition to focusing the electron beam, the retardation lens reduces the kinetic energy of photoelectrons before they enter the hemispherical analyser. The analyser consists of two concentric hemispherical plates with a set potential between them. Only the photoelectrons entering the analyser at the pass energy E_p will have the right trajectory to hit the detector at the end of the analyser. Photoelectrons with a higher or lower kinetic energy than E_p will be deflected to the walls of the analyser before reaching the detector. By tuning the retarding voltage in the retardation lens, it is possible to selectively retard photoelectrons of a certain kinetic energy and only allow them to reach the detector. Thus, by sweeping the retarding voltage in the lens, a spectrum of all photoelectron kinetic energies can be constructed.

Spectral features

XPS analysis typically starts with the collection of a wide scan spectrum called a survey (typically from 0 to 1350 eV for our Thermo Fisher Kα instrument). The energy range accessible to an instrument depends on the excitation source. Survey spectra (such as Figure 4.6(a)) are usually given by intensity (counts per second) as a function of the binding energy. Historically, photoelectron spectra were displayed with kinetic energy on the x-axis. This convention was retained when the kinetic energy scale was replaced by the binding energy one which is why the x-axis of XPS spectra is typically plotted from high to low energies.

XPS spectra consist of several well-defined lines (peaks) superimposed on a continuous background signal. Survey spectra show all accessible lines including core levels, Auger lines, satellite structures and valence band. The features observed on a survey spectrum can be separated into a primary and secondary structure. The primary structure is constituted of photoelectrons which have not lost a significant amount of energy from photoemission to detection. The secondary structure are lines which are associated to photoelectrons having lost part of their initial kinetic energy on their journey to the sample surface.

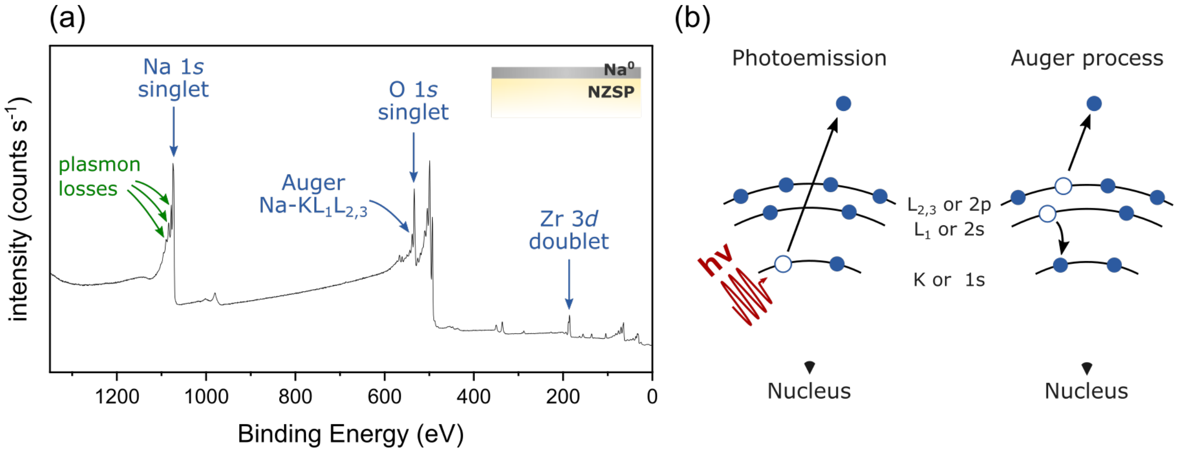

Figure 4.6: (a) Example of a XPS survey spectrum from a NZSP sample covered by a thin Na^0 overlayer. Some features corresponding to the primary and secondary structures are represented in blue and green respectively. (b) A $\mathrm{KL_1L_{2,3}}$ Auger photoelectron is an electron emitted from a $\mathrm{L_{2,3}}$ shell using the energy transferred by the relaxation of a $\mathrm{L_1}$ electron into a K core hole.

Primary structure

The main features in the primary structure of a XPS spectrum are the core level peaks (such as the Na 1*s*, O 1*s*, or Zr 3*d* peaks in Figure 4.6). These peaks are identified using spectroscopic notation nl_j where n is the principal quantum number (*e.g.* 1, 2, 3,...), l is the angular momentum (*e.g.* s, p, d,...) and j is the total angular momentum (*e.g.* 1/2, 3/2, 5/2,...). The total angular momentum is calculated as $j = |l + s|$ where s is the spin momentum ($s = \pm 1/2$). Table 4.2 gives a summary of the electron notations in XPS.

For s levels ($l = 0$), j only has one value (+1/2) and the obtained signal is a singlet. For other values of l, two values of j are obtained and two peaks are seen, referred to as a doublet. Because it is proportional to the expectation value $\left\langle \frac{1}{r^3} \right\rangle$ of the orbital (where r is the orbital radius)[136], the spin orbit splitting ΔE increases with increasing atomic number Z for a given atomic subshell (*e.g.* ΔE(Si 2p) = 0.6 eV < ΔE(P 2p) = 0.87 eV), and decreases with increasing l at a given n (*e.g.* ΔE(Zr 3d) = 2.40 eV < ΔE(Zr 3p) = 13.70 eV)[1]. The relative intensities of the two peaks making a doublet are determined by the ratio of their occupancy (see Table 4.3).

A second type of features observed in the primary structure of Figure 4.6(a) are Auger photoelectrons (for instance $\mathrm{Na\text{-}KL_1L_{23}}$). The emission of Auger photoelectrons occurs

---

[1] values for ΔE were extracted from the NIST XPS database

Quantum numbers				Spectroscopic	X-ray notation
n	l	s	j	notation (Core levels)	(Auger)
1	0	+1/2,-1/2	1/2	$1s_{1/2}$	K
2	0	+1/2,-1/2	1/2	$2s_{1/2}$	L1
2	1	-1/2	1/2	$2p_{1/2}$	L2
2	1	+1/2	3/2	$2p_{3/2}$	L3
3	0	+1/2,-1/2	1/2	$3s_{1/2}$	M1
3	1	-1/2	1/2	$3p_{1/2}$	M2
3	1	+1/2	3/2	$3p_{3/2}$	M3
3	2	-1/2	3/2	$3d_{3/2}$	M4
3	2	+1/2	5/2	$3d_{5/2}$	M5

Table 4.2: Spectroscopic and X-ray notations used in XPS

l	$j = \|l + s\|$	Degeneracy $(2j + 1)$	Area ratio
0, s	1/2	2	
1, p	1/2, 3/2	2, 4	1:2
2, d	3/2, 5/2	4, 6	2:3
3, d	5/2, 7/2	6, 8	3:4

Table 4.3: Doublet intensity ratios

when an atom is in an excited state following a X-ray photoemission event which produced a core hole: to bring the atom into a more neutral state, an electron from a higher atomic orbital will fill the core hole and the energy released by this transition forces an Auger electron to be emitted (see Figure 4.6(b)). By convention, Auger photoelectrons are expressed in X-ray notation. For instance, a $KL_1L_{2,3}$ Auger photoelectron is an electron emitted from a $L_{2,3}$ shell from the energy transferred by the relaxation of a L_1 electron into a K core hole.

Secondary structure - plasmons

The secondary structure is constituted of signals appearing because photoelectrons have lost a characteristic energy as they moved through the sample. Of specific interest to this thesis are secondary peaks formed from the excitation of plasmons in metals. Plasmons are collective oscillations of the sea of free electrons in a metal (an analogy with phonons - collective oscillations of the atoms within a crystal - can be made).[32] The characteristic energy lost to excite a plasmon resonance is in the order of a few eVs (5.85 eV for Na metal for instance). Photoelectrons having lost energy to excite plasmons resonances produce a series of peaks at integer multiples of the characteristic plasmon energy (E_{BP}) on the high BE side of a primary metal peak. For example in Figure 4.7(a) (data collected as part of this work), bulk plasmon losses are observed at integer multiples of 5.85 eV towards higher BE from the main Na^0 peak. Figure 4.7(a) also mentions the existence of surface plasmons which have a distinct characteristic energy E_{SP}. The characteristic energy of surface plasmons is theoretically $1/\sqrt{2}$ lower than that of bulk plasmons.[32] In Figure 4.7(a), the ratio $E_{BP}/E_{SP} = 1.47$ is close to the theoretical value. Additional plasmon resonances can also be seen at $n.E_{BP} + E_{SP}$ from the main Na^0 peak and correspond to the scenario where a photoelectron excites n bulk plasmons and a surface plasmon as it exits to the surface of the sample.

Finally, a distinction needs to be made between extrinsic and intrinsic plasmons: (1)

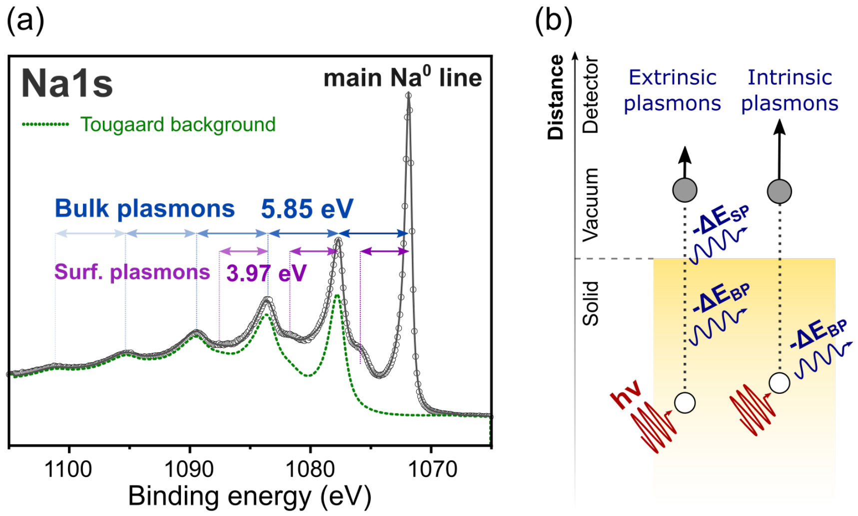

Figure 4.7: Plasmon losses. (a) Wide region Na 1*s* signal of a sputter-cleaned Na metal sample showing a series of plasmon losses. (b) Distinction between extrinsic and intrinsic plasmons.

extrinsic plasmons correspond to plasmons excited by photoelectrons away from the photoemission site as they travel through the metal; (2) intrinsic plasmons are plasmons excited at the photoemission site and simultaneously to the photoemission event (see Figure 4.7(b) for a schematic illustration). This distinction will be important for the selection of background functions which can model these inelastic losses (see Section 4.4).

Surface charging

The equations derived in section 4.4 are valid for conducting samples in electrical contact with the spectrometer. For insulating samples (such as the NZSP samples which will be studied in this thesis), the energy level diagram presented in Figure 4.4(b) needs to include two modifications:[137]

1. **surface charging:** in insulating samples, the photoemission process results in an accumulation of positive charges at and near the surface. The surface potential created from the charge buildup retards photoelectrons leaving the surface. The consequence for XPS spectra is that signals appear shifted to a higher binding energy than expected and have distorted shapes. Charging can also be non-uniform (*differential charging*), for instance when phases with different electronic properties coexist on a surface.[138] In this case, some core level lines will be shifted more than others.

2. **Fermi level referencing:** for conducting samples, the alignment of the Fermi levels of the sample and the spectrometer facilitate the determination of photoelectron BEs. For insulating samples, the situation is more complex as the Fermi levels do not align and the absence of a contact potential means that the photoelectron BE is no longer independent from the sample's work function. For insulating samples, the sample and spectrometer are referenced relative to their vacuum level.

Studying insulating samples by XPS requires to: (1) minimize surface charging during data acquisition which is typically achieved by employing a charge compensating flood gun; (2) apply a post-acquisition correction to shift the binding energy scale in order to align a selected signal of the XPS spectrum to a desired BE.[137] With a proper calibration of the BE scale, it should be possible to precisely identify chemical species from a database of references. Whilst some reference databases already exist (*e.g.* NIST XPS), the BEs reported for the same chemical specie sometimes vary by several eVs because the most appropriate technique to reference BE scales is still a debated topic.[139]

Referencing the BE scale using the C 1*s* peak of adventitious contaminants present on the surface of samples is still the most widely employed calibration technique. Despite its convenience, this way of referencing XPS spectra has generated criticism owing to the unknown composition and morphology of these adventitious species (which have led to a wide range of C 1*s* BE values being reported in the literature).[140] The preferred option for the BE calibration of XPS spectra in this thesis was to take an inner reference (an element common to all analysed surfaces and assumed to be in the same chemical environment for all of them) and assign it to a fixed position. Typically in this work, the Zr $3d_{5/2}$ peak of NZSP was fixed at 182.40 eV. With this calibration technique, relative chemical shifts between samples can be detected.

Regarding charge compensation during acquisition, most XPS instruments are equipped with flood guns whose role is to provide low energy electrons to the sample surface to neutralize positive charging on its surface. In instruments equipped with dual mode charge compensating flood guns, the neutralizing beam also includes a fraction of positive ions (such as Ar^+) to neutralize negative surface charging. Dual mode charge compensation has been found to be more efficient at preventing differential charging in modern instruments.[137] The ThermoFisher Kα instrument used in this thesis is equipped with dual mode charge compensation (e^- and Ar^+).[141]

Inelastic mean free path and cross-sections

For a sample that is homogeneous in the sampling volume, the intensity of a XPS line is proportional to:[142]

$$I \propto n\sigma\lambda T \tag{4.5}$$

where n is the concentration of the element in the sample, λ the inelastic mean free path, σ the photoionization cross-section of the analysed subshell (in cm^2), and T is a term combining several spectrometer parameters (such as the photon flux, illumination area or the instrument efficiency). The dependence of the IMFP and cross-sections terms towards the photon energy and atomic subshell are discussed in this section.

Inelastic mean free path

The surface sensitivity of XPS comes from the limited distance that photoelectrons can travel in a solid without suffering inelastic collisions.[143] The average distance that electrons with a given energy can travel between inelastic collisions in a solid is called the inelastic mean free path λ (IMFP). The IMFP should not be confused with two closely related concepts, the effective attenuation length (EAL), and the mean escape depth (MED).[144] The EAL is the average emission function decay length which was introduced to include the impact of elastic scattering events (no energy loss). The MED is the average depth (normal to the sample surface) from which photoelectrons escape. Because photoelectrons are not only emitted perpendicular to the surface normal, the MED is a function of the angle at which electrons where emitted relative to the surface normal. The discussions included in this thesis will only refer to the concept of IMFP. A conventionally accepted approximation is that 68 % of all photoelectrons come from within a depth of λ, and the majority (99.7 %) of photoelectrons come from a depth of 3λ.

The IMFP λ_m (in Å) of a photoelectron of energy E (in eV) in a solid can be conveniently estimated from a predictive formula derived by Tanuma, Powell, and Penn (the eponymous TPP-2M model)[145]:

$$\lambda_m(E) = \frac{E}{E_p^2\left[\beta ln(\gamma E) - \frac{C}{E} + \frac{D}{E^2}\right]} \tag{4.6}$$

with

$$\beta = -0.10 + 0.944({E_p}^2 + {E_g}^2)^{-1/2} + 0.069\rho^{0.1} \tag{4.7}$$

$$\gamma = 0.191\rho^{-1/2} \tag{4.8}$$

$$C = 1.97 - 0.91U \tag{4.9}$$

$$D = 53.4 - 20.8U \tag{4.10}$$

$$U = \frac{N_v\rho}{M} = \frac{{E_p}^2}{829.4} \tag{4.11}$$

and $E_p = 28.8\sqrt{N_v\rho/M}$ is the free-electron plasmon energy (in eV), N_v is the number of valence electrons per atom or molecule, E_g is the bandgap energy (in eV), ρ is the density (in g cm^{-3}) and M the atomic/molecular weight of the solid (in g mol^{-1}). Since $\lambda_m(E)$ depends on several parameters specific to the solid (N_v, ρ and M), a photoelectron emitted by a given elemental subshell will have different IMFPs depending on the compound it travels through. This effect can be seen in Figure 4.8(a): the IMFP is typically shorter for high density materials (W) in comparison to low density ones (PMMA).[143]

Photoionization cross-sections

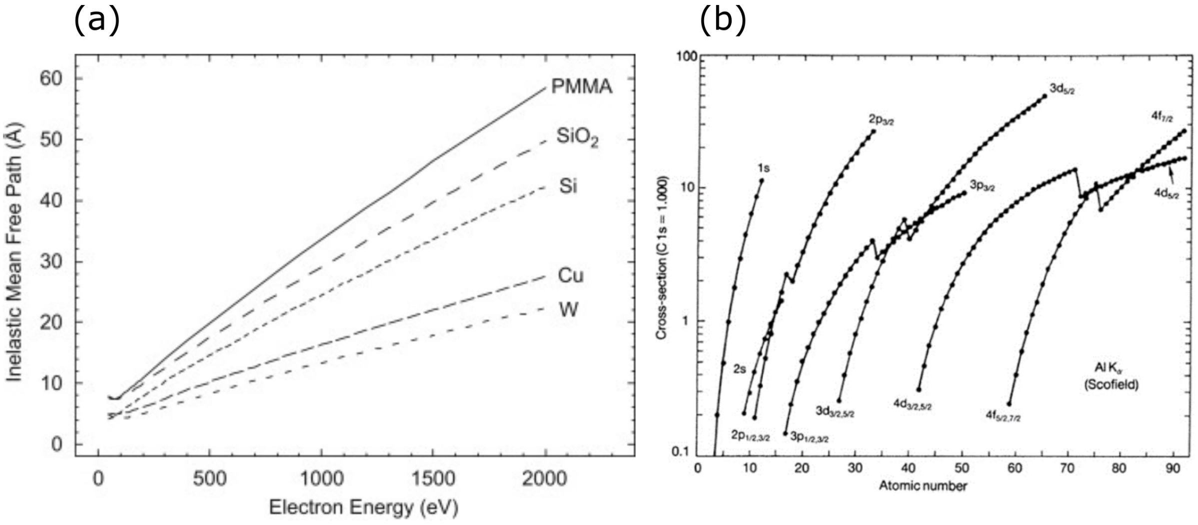

Figure 4.8: (a) IMFPs of photoelectrons travelling through various compounds calculated using the TPP-2M model. Reproduced with permission from [143] (b) Photoionization cross-sections for an Al Kα source normalized to the C 1s signal. After [146, 136].

Cross-sections reflect the probability that a photoionization event will occur in an atomic subshell under a given excitation energy. Theoretical photoionization cross-sections are tabulated.[146, 147] The manufacturers of XPS instruments also typically provide elemental cross-sections tables for their specific instrument. Theoretical cross-sections calculated by Scofield for the 1s to 4f subshells of elements with atomic numbers $0 \leq Z \leq 92$ are plotted in Figure 4.8(b).[146, 136] The cross-sections are represented relative to the C 1s cross-section (*i.e.* the y-axis consists of the ratio $\sigma_{A,i}/\sigma_{C1s}$, where A and i refer to a specific element and subshell). The cross-sections presented in Figure 4.8(b) are calculated for the energy of an Al Kα source (1486.6 eV). At higher photon energies, cross-sections are dramatically decreased. This is an important consideration to take into account in Hard X-ray XPS (HAXPES) experiments as the signal intensities will be decreased proportionally.[148]

In practice, photoionization cross-sections are used in the analysis of XPS data to select core level lines which will have a high enough intensity to extract meaningful information. They are also an essential normalization term for the calculation of atomic fractions when quantitatively analysing the composition of a surface.

Spectrum fitting - backgrounds

To extract quantitative information from a XPS spectrum, a synthetic surface model is refined using a least-square algorithm in order to replicate the raw XPS data. XPS fitting therefore requires to have a good prior understanding of the composition of a surface, as the input model for the fit needs to account for all the possible chemical environments that atoms on a surface could be found in. The synthetic model used to fit a core level is constituted of several peaks (one for each possible chemical environment) whose position, intensity, width and shape will be refined by the least square algorithm. For some peaks, additional constraints can be added: a typical example is that the area ratio of doublet peaks should be fixed.

The first step of XPS data fitting is to model the background level. The peaks of the synthetic surface model will then sit on top of this background function. The most common background functions available in XPS fitting softwares are the linear, Shirley, and Tougaard backgrounds (see Figure 4.9(a)).[149]

The most simple background function is the linear background which connects the two end points of a specified region by a line. A clear advantage of this background is its mathematical simplicity. However, this function lacks physical basis because the background of a XPS spectrum is intrinsically non-linear since it consists of scattered photoelectrons having randomly lost some of their KE as they travel though the solid.

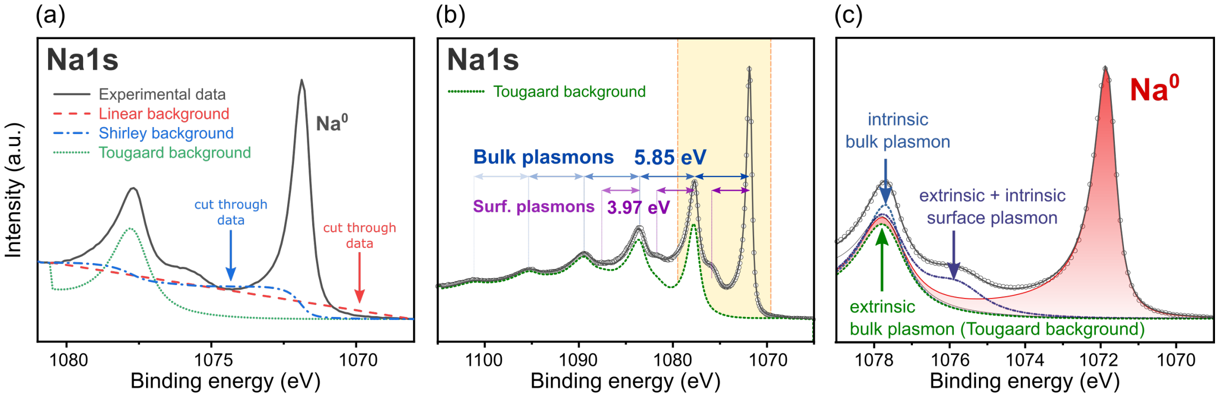

Figure 4.9: XPS Backgrounds. (a) Comparison of background functions for the same experimental data. (b) Wide scan Na 1*s* region of a Na metal sample showing the extent of the inelastic background below the main peak. The BE region used in other panels is highlighted in yellow. (c) The inelastic background model for Na metal includes extrinsic/intrinsic bulk and surface plasmons.

The Shirley function is a more evolved non-linear and iterative background. It relies on the assumption that, the higher the signal intensity, the more electrons are decelerated by inelastic events at the same time. Despite its advantages over the linear background, the Shirley background also has a limited physical basis. An example of its limitations is provided in Figure 4.9(a) for the Na 1s region of a pristine Na metal foil: the Shirley function intersects the measured data in one region, and fails to appropriately model the plasmon losses.

In contrast with the other two functions, the Tougaard background has a firm physical basis as it accounts for the initial energy distribution function (*i.e.* the measured spectrum) and inelastic electron scattering via a universal cross-section term. The three-parameter Tougaard background function $B_{Tougaard}$ is defined as:[149]

$$B_{Tougaard}(E) = B_1 \int_{E}^{E_{max}} \underbrace{J(E')}_{\text{spectral intensity}} \underbrace{\frac{E' - E}{[C + (E' - E)^2]^2 + D(E' - E)^2}}_{\text{cross section term}} dE' \tag{4.12}$$

where E is the binding energy, E_{max} is the high BE limit to the specified region, J is the energy distribution function, and C and D are parameters which are material specific and can be varied by the analyst during the fitting procedure. The factor B_1 is adjusted so that the background reaches the signal level in a region between 30 and 50 eV below the characteristic peak. The fact that a large BE range is required to appropriately model the inelastic background using a Tougaard function is a disadvantage of this function (since a large BE range considerably extends the acquisition time for high precision spectra). For instance, the Na 1s region of a Na metal sample has an inelastic background extending over 30 eV below the main peak. An appropriate model for the background therefore needs to extend over this entire region, like in Figure 4.9(b). In Figures 4.9(a) or (c), since a shorter range BE region is selected, the Tougaard function which accurately describes the inelastic background does not respect the boundary condition $B_{E_{max}} = I_{E_{max}}$.

Tougaard backgrounds as implemented in CasaXPS readily account for extrinsic plasmon losses as can be seen in Figure 4.9(b) (after calibration, the background function replicates the periodicity of the bulk plasmon losses).[150, 151] Interestingly, it can be noticed that although the Tougaard function models the background well in a region 15 eV below the main peak, a noticeable part of the plasmon peaks intensity is not captured by the Tougaard function as implemented in CasaXPS. This difference in intensity has been discussed in other publications (focusing on Al metal) and originates from the distinction between extrinsic and intrinsic plasmons.[150] Very recently, Gnacadja *et al.* have proposed a new background function combining these two contributions.[152] As this background function is not readily implemented in CasaXPS, the contribution from intrinsic plasmons was modelled by separate peaks in this thesis (see Figure 4.9(c)). These peaks (the first intrinsic bulk plasmon and first extrinsic+intrinsic surface plasmon) are part of the Na^0 background. The contribution of intrinsic plasmon losses drops significantly after the second bulk plasmon resonance and the Tougaard background function itself is sufficient. Previous XPS studies on Na metal did not employ a Tougaard background.[153]

Spectrum fitting - line shapes

Although the theoretical shape of XPS signals is Lorentzian in nature, some Gaussian character is observed in most XPS line shapes.[136] This Gaussian character translates into peaks with narrower peak base and wider tips than purely Lorentzian signals (see Figure 4.10). Several factors contribute to adding Gaussian character to XPS lines:[154] (a) the finite widths of slits and detector elements in the spectrometer; (b) some energy dispersion in the photon energy; (c) phonon broadening can affect the peak shape in samples above 0 K; (d) "disorder broadening" affects amorphous materials.

In practice, Voigt line shapes relying on a convolution of Gaussian and Lorentzian signal are conventionally used in softwares to fit symmetric core level lines. This type of line shape is for instance accessible in CasaXPS with the LA(α,β,m) function. The LA line shape is based on a generalized Lorentzian function whose sides can be raised to different powers to create asymmetry (this is the role of the variables α and β whose values can range from 0 to 900). Despite its name, the asymmetric Lorentzian (LA) line shape can also model symmetric peaks if its variables α and β are equal (for instance, the "Voigt" line shape in Figure 4.10 was obtained with a LA(α = β=1.53,243) function). The variable m in the function corresponds to the amount of Gaussian character introduced into the function by convolution.

Fitting XPS spectra becomes more challenging when the core level lines are asymmetric. Asymmetry is typically observed in the signal of metallic chemical species. More specifically, in conducting samples, a tail on the high BE side of peaks (lower KE) is observed due to the interaction of photoelectrons with valence electrons promoting them into the conduction band. An exact procedure to model asymmetric peaks in XPS is still debated. The only asymmetric peak shape with a theoretical basis is the Doniach-Sunjic (DS) one. However, a problem with the DS function is that its asymptotic form means it integrates

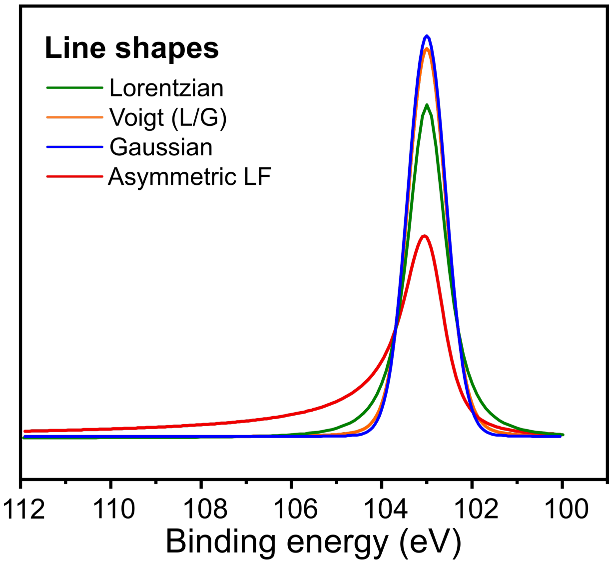

Figure 4.10: XPS line shapes. Example of line shapes employed in this thesis. The most frequently employed shape function is the symmetric LA(1.53,243) one. To fit asymmetric Na^0 peaks, a LF(0.58,1.15,200,50) line shape was employed.

to infinity. The extracted peak area is therefore dependent on the defined energy region. In a recent review, Major *et al.* propose a series of solutions to address the asymmetry problem, including the use of finite Lorentzian (LF) functions to overcome the problem of non-integrability of the DS function.[154] The LF(α,β,w,m) line shape shares the same mathematical backbone as the LA line shape with an added variable w. This line shape ensures that the peak tail reaches the baseline at a non too-distant energy from the peak centre. The extent of the tail away from the peak centre is controlled by the parameter w. An example of an asymmetric LF line shape is provided in Figure 4.10. For the reasons expressed above, this line shape was used to fit Na^0 peaks in Chapter 8.

XPS measurement conditions

The XPS analyses presented in Chapters 6 and 7 were collected at room temperature on a Thermo Fisher Scientific K-Alpha XPS system using a monochromated Al Kα source (1486.6 eV) operating at a power of 72 W (6 mA x 12 kV). The BE scale is regularly calibrated using Au, Ag, and Cu standards.[135] The analysis area is an ellipsoid of dimensions *ca.* 400 μm x 800 μm. The samples were mounted on the sample stage using conductive clips.

Survey spectra (averaged over 3 scans) were measured at a pass energy of 200 eV, a resolution of 0.5 eV and an integration time of 25 ms/point. Core level spectra were measured at a pass energy of 20 eV, a resolution of 0.1 eV and an integration time of 50 ms/point. The average number of scans for each narrow region scan varied from 30 for intense signals (Na 1*s* for instance) to 80 for lower intensity signals (P 2*p*). Sample charging was neutralized using a low energy electron flood gun (0.2 V, 100 μA). Results were fitted using the Avantage software (Thermo Fisher Scientific) or CasaXPS.

4.5 Low Energy Ion Scattering

Low energy ion scattering (LEIS) is one of the most sensitive technique to characterize the surface composition of samples. Unlike other surface sensitive techniques which typically provide an average signal from the first few nanometers of a sample (such as XPS), a LEIS spectrum gives information about the atomic composition of the outer atomic layer of a surface. LEIS can also deliver information about the atomic composition of sub-surface layers known as "in-depth" signals. LEIS relies on the binary collision between low energy primary ions (typically $^{4}\mathrm{He}^{+}$ or $^{20}\mathrm{Ne}^{+}$) and the elements present on the surface of a specimen. A LEIS spectrum shows the intensity of the collected signal as a function of the scattered ion energy. To simplify the syntax in this thesis, the peaks have been named according to the analyzed interacting atom (*e.g.* “the Na peak”) although it should be understood as scattered He^{+} ions which interacted with the respective surface atom.

The positions of the peaks observed in a LEIS energy spectrum are determined by the laws of conservation of energy and momentum and depend on the primary ions mass, the primary ions energy, the mass of the analyzed atomic species, and the detector acceptance angle according to:

$$E_f = k.E_0 = \left(\frac{cos\theta + \sqrt{r^2 - sin^2\theta}}{1 + r} \right)^2 .E_0 \tag{4.13}$$

with $r = \frac{m_{at}}{m_{ion}} \geq 1$, $\theta \geq 90°$, and k is called the kinematic factor. Some of the parameters included in Equation 4.13 can be found illustrated in Figure 4.11: in particular, θ is the scattering angle, α is the polar angle, $\Delta\Omega$ is the instrument acceptance angle, E_0 is the incident energy and E_f is the scattered energy.

Figure 4.11 illustrates the kinematics of LEIS in two situations: scattering from the outer surface layer, or scattering from deeper layers (in-depth). The figure shows that

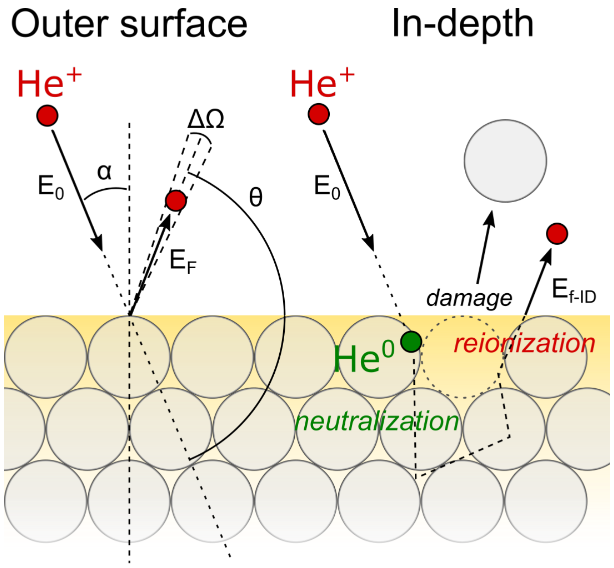

Figure 4.11: Fundamental principles of LEIS. The primary He^+ ions can either be scattered by the outer atomic layer or penetrate the sample and be back-scattered after having lost part of their initial energy.

primary ions penetrating the surface are typically neutralized. The neutralization is a consequence of the low energy of the primary ions and can also occur for ions scattering from the outer layer. The LEIS analyser can only detect charged particles, thus only the scattered ions (not the neutral particles) can give information about the sample composition. In-depth information is obtained from primary ions scattered from deep layers which either have not been neutralized, or have reionized as they exited the sample surface.[155] The figure also shows that, like any ion beam technique, the primary ion beam in LEIS can induce damage (sputtering) to the sample surface. This damage can however be limited in modern instruments which only require a low ion fluence for the analysis of surfaces. For the analysis of deeper layers in the sample, an Ar^+ ion sputter beam can be employed. A depth-profile is established by alternating analysis sequences (with the He^+ beam) and sputtering sequences (with the Ar^+ beam).

Equation 4.13 imposes that the mass of the analysed atom is larger than the mass of the primary ion. Thus a He^+ ion flux is typically used when light elements are expected to be found on a surface. Equation 4.13 is valid for purely elastic interactions between the primary ion and surface atoms. In practice, and especially when low primary energies are employed (*e.g.* 3 keV He^+ ion beams), inelastic energy losses can shift experimental peak maxima in LEIS spectra by up to 100 eV in comparison to theoretical (elastic) values.[156]

The elastic scattering energy is typically found to correspond to the high-energy onset of the peak.

The LEIS analyses presented in Chapter 6 were carried out with an Ion-ToF Qtac100 instrument by ION-TOF GmbH. The base pressure in the analysis chamber was $\approx 9\text{x}10^{-10}$ mbar. During the experiment, the chamber pressure increases to 10^{-8} mbar because of the noble gas flux from the ion source. For the measurements, a 3 keV $^4He^+$ ion beam was used. A He^+ ion source was chosen because of its high sensitivity to low mass atoms. The primary ion beam was aligned with the samples surface normal and the scattered ions were collected at an angle of 145 °. The primary ion beam was scanned on a sample surface area of 500×500 μm. To prevent charging effects due to the insulating nature of NaSICON samples, a low-energy electron flood gun (10 eV) was used.

Unfortunately, Na atoms in NaSICON samples suffered from preferential sputtering which is a typical instrumental artefact of sputtering techniques. More specifically, a Na peak could always be detected on non-sputtered surfaces but disappeared after one sputter cycle. Sodium depletion from Ar^+-bombarded silicate glass surfaces has already been reported.[157] An attenuation of the Na peak with increasing ion dose was also noticed even with the 3 keV He^+ ion analysis beam (see Figure 6.5 in Section 6.3 for example). Another possible hypothesis is that, because of their high mobility, a positive surface charging would repel Na^+ ions away from the outer surface of samples. Our collaborator Jaap Van den Berg at the University of Huddersfield was also unable to obtain a depth profile signal for Na by Medium Energy Ion Scattering (MEIS).

4.6 Electrochemical methods

Cell assembly

The cells studied in this thesis were all assembled in a symmetrical configuration (the two electrodes are the same). For cells employing blocking electrodes, a thin Au layer was sputtered on both sides of a pellet using a magnetron sputter coater (Q150T, Quorum Technologies Ltd, UK) with a sputtering current of 20 mA for 2 minutes, resulting in an Au layer of roughly 50 nm thickness.

For cells employing Na metal electrodes, these were freshly prepared for each new cell in an Ar-filled glovebox (see Figure 4.12). A clean piece of Na was cut from a rod (Na sticks, covered in film of protective hydrocarbon oil, 99%, Alfa Aesar, or Na cubes in oil, 99.9%, Sigma Aldrich) using a ceramic scalpel. The Na^0 chunk was then pressed flat

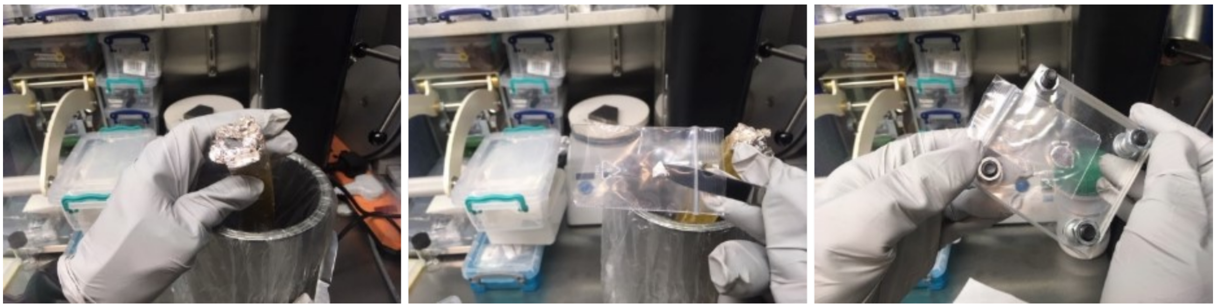

Figure 4.12: Na metal electrodes preparation. (left) a piece of Na^0 is cut from a rod; (center) the piece is placed in a LDPE; (right) the piece is pressed into a foil. Circular electrodes are then punched from the foil (not illustrated here).

in a LDPE plastic bag to a thickness of around 100–300 μm. Circular electrodes were then punched from this foil. Their surface was mechanically cleaned using the blade of a scalpel. The Na metal electrodes were then placed on both sides of a NZSP pellet and the Na|NZSP|Na stack was pressed with a uniaxial pressure of around 10 MPa. The applied pressure was measured using a KMM50-10 kN force sensor (inelta Sensorsysteme GmbH). Because the Na metal plastically deforms during cell assembly, the diameter of the Na metal electrodes was measured after the cell was pressed.

For electrochemical testing outside the glovebox, the cells were placed in either coin or pouch cells. For coin cells, the Na|NZSP|Na stack was sandwiched between two 0.5 mm stainless steel current collectors (also acting as spacers), a wave spring was added, and the full stack was crimped in a coin cell casing. All the coin cell casing parts were purchased from Hohsen Corp. or Tob New Energy Technology Co. For pouch cells, the current collectors (Ni tabs, Tob New Energy) were manually pressed against the Na metal electrodes. The cells were then placed in heat-sealable barrier bags (Agar Scientific) and hermetically sealed with an impact sealer.

Electrochemical Impedance Spectroscopy (EIS)

Theory

EIS is a spectroscopic technique employing small AC electric stimuli to resolve electrochemical processes occurring in a cell. The frequency response analyser (FRA) which is the instrument producing the electric stimulus and converting the output signal into an impedance, can be operated either in potentiostatic mode (the amplitude of the voltage is fixed and the current through the cell is measured), or in galvanostatic mode (the ampli-

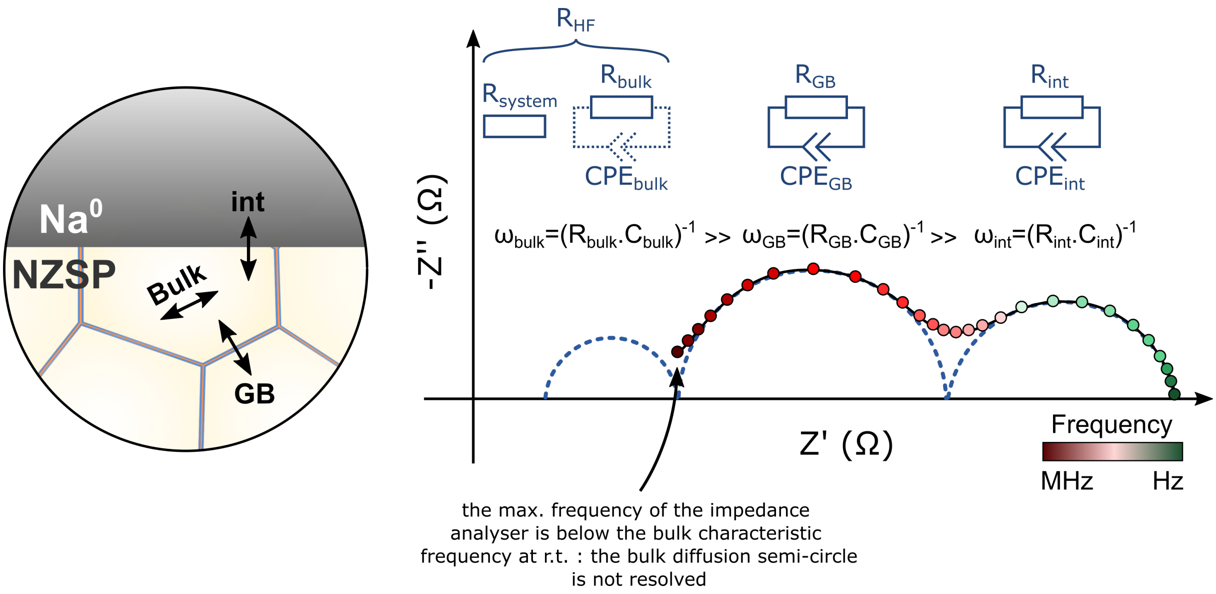

Figure 4.13: Nyquist plots in EIS. EIS can be used to identify electrochemical processes with different characteristic frequencies (*e.g.* bulk, GB, interface).

tude of the current is fixed). The input signal applied to the poles of the electrochemical system in potentiostatic EIS is a voltage sinusoid of fixed amplitude. The frequency of this sinusoid is sweeped from high frequencies to low frequencies. At each frequency, the amplitude and phase shift (ϕ) of the current passing through the FRA is measured and the complex impedance of the system ($\overline{Z}$) is calculated:

$$\overline{Z}(\omega) = \frac{\overline{V}(\omega)}{\overline{I}(\omega)} = Z' + i.Z" = |\overline{Z}|.e^{i.\phi} \tag{4.14}$$

where $Z' = Re(\overline{Z})$ and $Z" = Im(\overline{Z})$ are the real and imaginary part of the complex impedance, and $|\overline{Z}|$ and $\phi = arg(\overline{Z})$ are the magnitude and phase of $\overline{Z}$. The complex impedance of electrochemical cells is conventionally represented as Nyquist plots where $-Z"$ is plotted as a function of Z' (see Figure 4.13), or as Bode plots where $|\overline{Z}|$ and ϕ are plotted as a function of frequency.

Application to studying solid-state batteries

At the macroscopic scale, the ionic conductivity of ISEs is typically measured by electrochemical impedance spectroscopy (EIS) in a symmetrical cell configuration with blocking electrodes (for instance, a thin layer of Au can be sputtered on the surface of Na-ISEs, because Au does not alloy with Na). Special pressing dies with electronically insulating walls have also been developed to allow pressure dependent operando EIS measurements which can be particularly useful for softer ISEs densified by cold pressing.[158, 159] The ionic transport properties of macroscopic ISE samples can often be well described by the so-called brick-layer model for which more mathematical details can be found in a recent review.[160]

Nyquist plots of ISEs most generally feature one or several well-separated semi-circles (see Figure 4.13). Semi-circular features in Nyquist plots are the signature of diffusive processes entailing a resistive and capacitive component. Diffusion processes corresponding to different migration mechanisms (such as bulk diffusion or grain boundary diffusion) will typically have different characteristic frequencies ω (the inverse of ω is the relaxation time $\tau = 2\pi/\omega$). If the characteristic frequencies of the two (or more) processes are separated by several orders of magnitude, the corresponding semi-circles in a Nyquist plot will be well separated. Merging of semi-circles can occur if the characteristic frequencies of the different diffusion processes are too close to each other. In this case, advanced impedance data analyses (for instance a distribution of relaxation time analysis[161, 162]) can be used to deconvolute the different contributions to an impedance spectrum.

The ionic conductivity of an ISE is typically extracted from Nyquist plots by fitting the data using equivalent circuit modelling. Semi-circles are typically modelled using R-CPE elements consisting of a resistor in parallel with a CPE (constant phase element). Unlike a capacitor, a CPE is not associated to any physical process, but it is a useful mathematical operator to model non-perfect semi-circles in Nyquist plots. Semi-circles can appear to be depressed in the Nyquist plots of ISEs because macroscopic samples are composed of grain and grain boundaries (GB) of varying size and random orientation (unlike the brick-layer model). Instead of single characteristic frequency, the diffusion across grain and grain boundaries of varying size and orientation will lead to a distribution of characteristic frequencies. How narrowly ranged this distribution is will determine how distorted the apparent semi-circle in a Nyquist plot will be.[163]

Because a CPE is not representative of a physical process, it is more useful to convert the CPE parameters of a fit to express it as true capacitance. This true capacitance is calculated from the CPE parameters (Q and n) and the resistance of the process (R) using the Brug formula:

$$C = \frac{(Q.R)^{1/\mathrm{n}}}{R} \tag{4.15}$$

The characteristic frequency ω of a process can be calculated from impedance data by:

$$\omega = \frac{1}{R.C} = \frac{1}{\rho.\epsilon} \tag{4.16}$$

where R and C are the values obtained from fitting the Nyquist plot, and ρ (the resistivity, in Ω m) and ϵ (the permittivity, in F m^{-1}) are normalized values which do not depend on the sample dimensions (thickness and electrodes area). The bulk conductivity of a sample σ_{bulk} (typically expressed in S cm^{-1}) is obtained by:

$$\sigma_{\text{bulk}} = \frac{1}{R_{\text{bulk}}}.\frac{L}{A} = \frac{1}{\rho_{\text{bulk}}} \tag{4.17}$$

where R_{bulk} is the bulk resistance of the ISE (in Ω, extracted from the semi-circle corresponding to bulk diffusion), L is the pellet thickness (in cm), and A is the area of the electrodes (in cm^2).

The relative volume fraction of grain boundaries in a macroscopic pellet is typically small. To obtain the grain boundary conductivity, equation 4.17 needs to be modified because only a fraction of the distance travelled by mobile cations is travelled across grain boundaries. The distance fraction $\frac{L_{\text{GB}}}{L}$ (where L_{GB} is the distance travelled across grain boundaries and L is the pellet thickness) cannot be known *a priori*. A common solution is to use the ratio $\frac{C_{\text{bulk}}}{C_{\text{GB}}}$ (where C_{bulk} and C_{GB} are the fitted bulk and grain boundary capacitances) as a proxy for the ratio $\frac{L_{\text{GB}}}{L}$ assuming that the permittivity of the bulk and grain boundaries are the same. This gives:

$$\sigma_{\text{GB}} = \frac{1}{R_{\text{GB}}}.\frac{L}{A}.\frac{C_{\text{bulk}}}{C_{\text{GB}}} \tag{4.18}$$

In general, the characteristic frequencies of diffusion processes in ISEs are fast and require FRAs with fast excitation frequencies (at least in the MHz range for bulk diffusion processes). In some cases, bulk diffusion processes are so fast that they cannot even be resolved in the MHz range at room temperature (see Figure 4.13). Faster excitation frequencies (in the GHz range) can then be used to observe bulk diffusion at room temperature.[16] Alternatively, by going to lower temperatures, the diffusion processes can be significantly slowed down. As the temperature is reduced, the resistance associated with a diffusion process increases and its characteristic frequency is reduced. Lowering the temperature can therefore make the characteristic frequency of a process fall in the frequency range assessed by the impedance analyzer. For instance, for the NaSICON elecrolyte tested in Figure 5.6, only one semi-circle corresponding to grain boundary diffusion can be observed at 25 °C if the maximum excitation frequency is 3 MHz. But at

-100 °C, with the same excitation frequency of 3 MHz, a part of the bulk semi-circle can be resolved in the Nyquist plot.

The ionic conductivity of an ISE is typically obtained in a symmetrical cell with blocking electrodes (for instance Au). As blocking electrodes are inactive to charge transfer, a capacitive tail is typically observed at low frequencies (see Figure 5.6). Once the impedance of the ISE is understood in a cell with blocking electrodes, charge transfer active electrodes can be integrated. This multi-step process enables to deconvolute the contribution from each individual process contributing to the impedance of a cell. Ionic transport across Na metal|ISE interfaces typically give rise to a semi-circle response in Nyquist plots as well. Depending on the magnitude of the resistance of this process (see Chapter 6), the semi-circle might be resolved or not at room temperature.

Measurement settings

Impedance spectra were measured on a Solartron 1260 and a Biologic VMP-300 frequency response analyzers (FRAs) with an excitation amplitude of $V_{\mathrm{A.C.}} = 50$ mV. For the Solartron measurements, data points were collected in the frequency range of 13 MHz to 5 Hz (7 MHz to 1 Hz for the Biologic) with a logarithmic sampling at 20 points/decade. To minimize the signal to noise ratio, the frequency range was split into three sub-ranges (13 MHz–500 kHz, 500 kHz–500 Hz, 500 Hz–5 Hz) with varying integration times and delays (2 s integration and ten cycles delay; 1 sec integration and five cycles delay; 30 cycles integration and three cycles delay, respectively). The cell temperature was controlled via climate chambers: for temperature measurements across wide temperature ranges (for instance for Arrhenius plots), a Linkam Scientific THMS600 stage capable of heating to 600 °C and cooling to -100 °C (with liquid nitrogen) was employed; to maintain cells at a temperature of 25 °C for longer experiments, a constant climate chamber (Binder GmbH) was employed. Results were fitted using RelaxIS3 (Rhd instruments).

As impedance spectra were measured on two different FRAs, a difference in the systems' ohmic resistances was sometimes noticed (in fact, the ohmic resistance of the Solartron instrument was often shifting between two consecutive measurements). For samples measured with the Solartron, when the ohmic resistance was high, the spectra were shifted so that the high frequency intercept with the real axis corresponds to a NZSP bulk conductivity of 15 mS cm^{-1}.

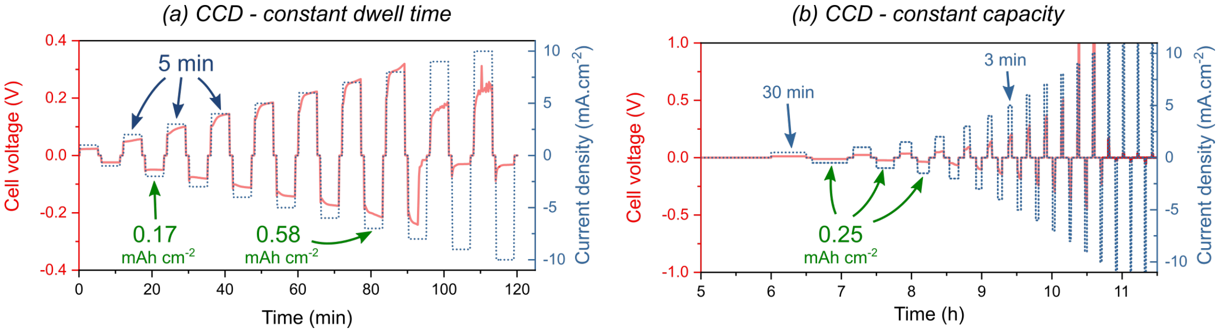

Figure 4.14: Example of a CCD measurement acquired with constant dwell times (a), or constant capacity at each cycle (b).

Cell cycling and Critical Current Density measurement

The properties of the Na|NZSP interface under cycling conditions have been probed in this work by using potentiostats in galvanostatic mode (constant current). Measurements were acquired with a SP240 potentiostat (Biologic) or with a 580 Battery Test System (Alvatek) in a two electrodes configuration and in floating mode (the counter electrode was not connected to the ground). The cell temperature was controlled via the same climate chambers as previously described (Linkam and Binder).

The measurement of critical current densities (CCD) will be mentioned in Chapter 9. CCD measurements have gained in popularity in the literature recently and are becoming the norm to evaluate the ability of metal|SE|metal symmetrical cells to withstand filament penetration during cycling. CCD measurements consist in cycling cells at gradually increasing current densities until a sudden drop in the voltage of cells is detected indicating a filament short-circuited the SE. Depending on the publication, the galvanostatic dwells at each current density are equal either in (i) duration, or (ii) capacity. The difference between the two modes of experiment are represented in Figure 4.14. In this thesis, the second mode of operation (constant capacity) will be preferred as it guarantees that, at each current density, the same amount of Na^0 is stripped/plated from/at the electrodes.

Chapter 5

Properties of NZSP ceramics

The aim of this chapter is to provide a structural, microstructural, and electrochemical characterization of the pristine NZSP pellets which are employed in cells in the following chapters. The synthesis of technologically-pertinent NZSP pellets needs to meet two important criteria: sintered pellets need to be highly dense to efficiently act as a separator, and pellets also need to be phase pure as large concentration of impurities can affect the electrochemical performance of the electrolyte. Optimizing the synthesis to produce pellets meeting these two criteria has been a long process. Instead of explaining this optimization chronologically, this chapter focuses first on the characterization of pristine NZSP samples, and then highlights some crucial steps of the synthesis to obtain high quality NZSP samples.

5.1 Structural and microstructural characterization of NZSP ceramics

Structural characterization

Foreword

Previous work from Ma *et al.* established that the composition with the highest ionic conductivity in the $Na_{1+x}Zr_2Si_xP_{3-x}O_{12}$ ($0 \leq x \leq 3$) compositional space is $Na_{3.4}Zr_2Si_{2.4}P_{0.6}O_{12}$.[16] For this reason, the $Na_{3.4}Zr_2Si_{2.4}P_{0.6}O_{12}$ composition was adopted for this project.

Despite having been discovered 40 years ago, the stability of the $Na_{3.4}Zr_2Si_{2.4}P_{0.6}O_{12}$ composition is still debated in the literature. A thermodynamic analysis using energetics from the Materials Project database predicts a decomposition of $Na_{3.4}Zr_2Si_{2.4}P_{0.6}O_{12}$ into the following phases:[164]

$$Na_{3.4}Zr_2Si_{2.4}P_{0.6}O_{12} = 0.4Na_3Zr_2Si_2PO_{12} + 0.8Na_2ZrSi_2O_7 + 0.2Na_3PO_4 + 0.4ZrO_2 \tag{5.1}$$

In another recent study, Deng *et al.* also predicted that the $Na_{3.4}Zr_2Si_{2.4}P_{0.6}O_{12}$ composition is metastable by building the $Na_{1+x}Zr_2Si_xP_{3-x}O_{12}$ phase diagram from first principles calculations.[165] Their phase diagram predicts a decomposition of the $Na_{3.4}Zr_2Si_{2.4}P_{0.6}O_{12}$ into $Na_3Zr_2Si_2PO_{12}$ and $Na_4Zr_2Si_3O_{12}$.

Experimentally, Ma *et al.* also found that their high ionic conductivity NZSP was actually a composite consisting of a monoclinic $C2/c$ phase and a rhombohedral $R\overline{3}cH$ phase.[16] Their powder XRD data was refined using two references from the ICSD corresponding to the NaSICON compositions $Na_3Zr_2Si_2PO_{12}$ (for the $C2/c$ phase) and $Na_{3.35}Zr_2Si_{2.35}P_{0.65}O_{12}$ (for the $R\overline{3}cH$ phase).

$Na_{3.4}Zr_2Si_{2.4}P_{0.6}O_{12}$ pellets are therefore unlikely to be single phase and a composite structure can be expected.

Powder XRD analysis

The crystal structure of pristine NZSP was analysed by collecting XRD data from NZSP powder obtained by crushing sintered pellets. Le Bail refinement results of the powder XRD data over a 2θ range of 10°- 80° are presented in Figure 5.1(a). A magnification on a region of interest is provided in Figure 5.1(b). The reference crystal structures used to refine the data are the same as the one reported previously by Ma *et al.*.[16] The three Le Bail refinements presented in Figure 5.1(a) have the same input XRD data but attempt to fit it to different crystal structures: two refinements assumed that the powder data came from a single phase (either the $R\overline{3}cH$ or $C2/c$ NaSICON phases) and one refinement used three phases for the fit (the $R\overline{3}cH$ and $C2/c$ phases and an impurity ZrO_2 phase).

Whilst it was possible to make the single phase fits converge, the three phases fit results in much lower residuals (lower χ^2 value). The improvements obtained by fitting the powder data to three phases instead of one are more clearly observed in the magnified Figure 5.1(b). A secondary ZrO_2 phase is often observed in sintered NaSICON samples. But the synthesis process adopted here results in a low concentration of ZrO_2 as indicated by the low intensity of the reflections attributed to the ZrO_2 phase (identified with stars in Figure 5.1). These results confirm that NZSP samples are composite structures consisting

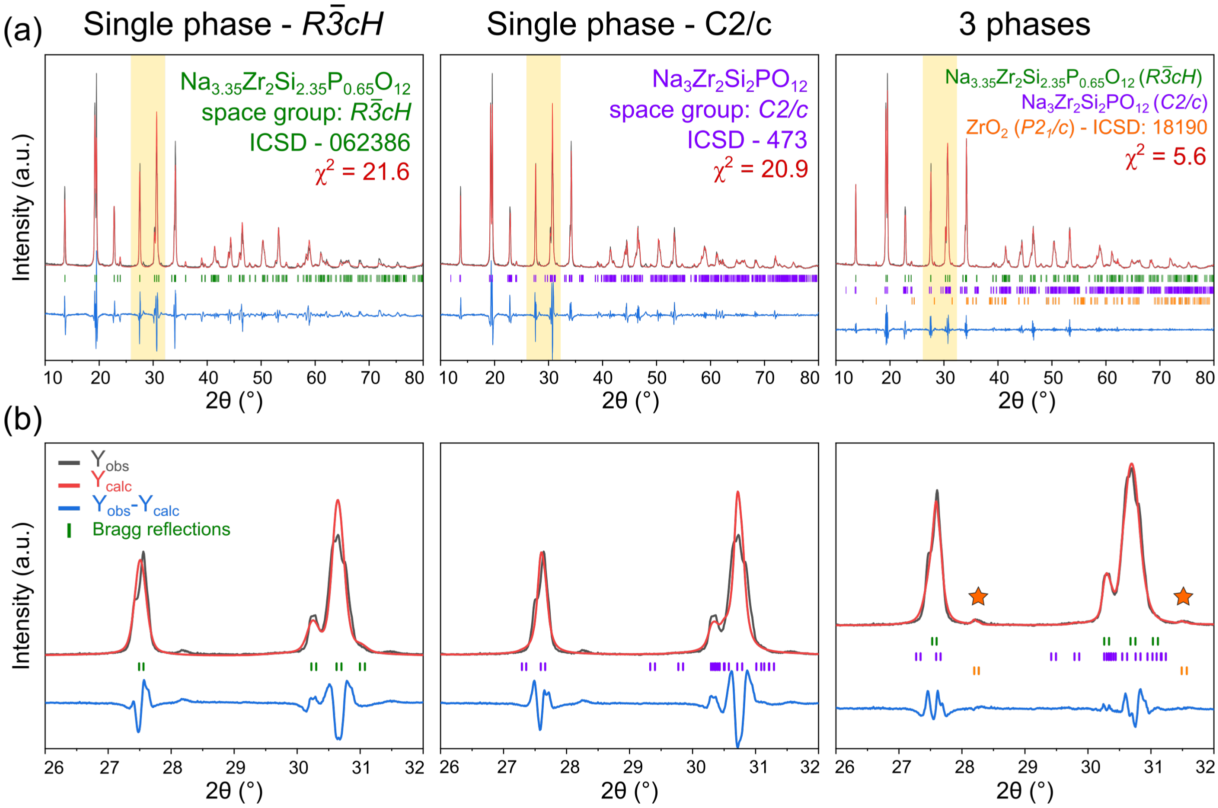

Figure 5.1: Crystal structure of pristine NZSP powders.(a) Comparison of the results of three Le Bail refinements on the same NZSP powder XRD data. The yellow box indicates the region which is magnified in panel (b). (b) Zoom on the 26°-32° region illustrating the improvement in the quality of the fit when three phases are employed.

of several phases. Future crystallographic studies will have to identify more precisely the exact nature and relative fraction of the phases present in NZSP pellets.

Comparison of powder and pellet XRD

Three diffractograms are compared in Figure 5.2. The bottom and middle ones (in red and grey) were obtained from the same sintered NZSP sample: the grey curve corresponds to the XRD data of NZSP in a pellet form, and the red curve correspond to the XRD data after the pellet was crushed into a powder. Differences in the intensities of peaks between these two diffractograms are subtle but noticeable even by visual comparison. The most noticeable difference is in the intensity of the reflections in the 18°-20° region. The reflection at 30.6 ° is also more intense for the pellet than for the powder.

The final diffractogram in Figure 5.2 was collected on a different NZSP pellet whose surface had been polished ($\mathrm{NZSP_{500EtOH}}$). Compared with $\mathrm{NZSP_{AS}}$, some small differences

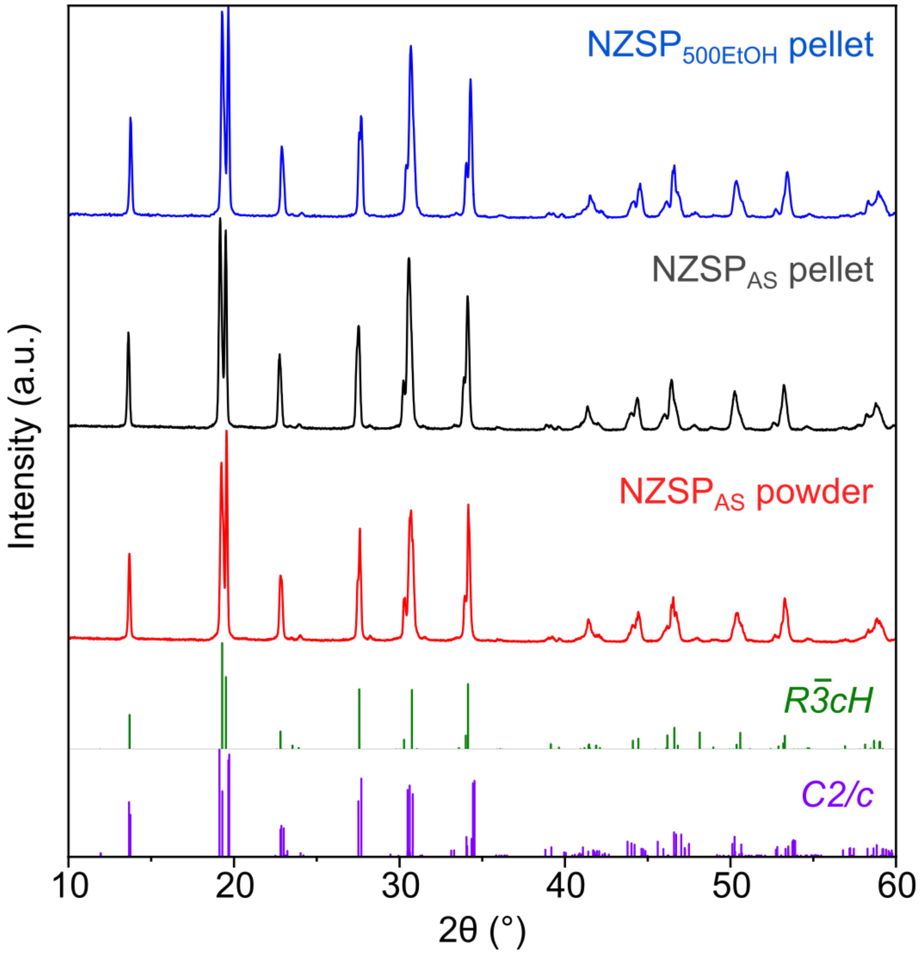

Figure 5.2: Comparison of XRD data from NZSP powder and two NZSP pellet samples. The same sample was used to produce the $NZSP_{AS}$ pellet and $NZSP_{AS}$ powder XRD data. The $NZSP_{500EtOH}$ pellet data was obtained with a different sample.

in the intensity of the reflections (especially in the 18°-20° region) can be noticed.

These differences in the intensities of peaks could suggest a preferential orientation of grains on the $NZSP_{AS}$ surface or an inhomogeneous distribution of the various phases across the NZSP pellet. For future work, we propose to investigate this phenomenon in more details and establish a mapping of the locations where the phases of the NZSP composite are present in solid samples.

Microstructural characterization

SEM characterization of NZSP surfaces

The surface microstructure of NZSP pellets is analysed by SEM in Figure 5.3. In this figure, the surface microstructures of an as sintered $\mathrm{NZSP_{AS}}$ pellet (images a, b, and c) and a polished $\mathrm{NZSP_{500EtOH}}$ pellet (images e, d, and f) are compared.

Image (a) shows that the surface of $\mathrm{NZSP_{AS}}$ pellets has no surface pores and that NZSP pellets are dense. Image (a) also confirms the composite nature of NZSP samples with regions which appear darker. These islands distributed on $\mathrm{NZSP_{AS}}$ surfaces are around 10 to 20 µm in diameter and their composition is investigated by EDX in the following section. Another view of these islands at grazing angle is presented in image (c). Image (b) shows that NZSP grains are small cubic grains with a size ranging from 200 nm to 2 µm.

Polishing sintered pellets has a large impact on the surface microstructure of pellets as can be seen from images (d), (e), and (f). Here, the pellet was only roughly polished with a 500 grit size SiC pad. Polishing leaves clearly observable trenches on the sample surface. The dark island-forming phase which was observed on the surface of $\mathrm{NZSP_{AS}}$ is no longer observed. Some contrast is observed on the images between amorphized regions (where polishing marks can be seen) and shallow pores of 10 to 40 µm in diameter at the bottom of which cubic NZSP grains can be seen. We suggest that these pores could be induced by the rough polishing which can rip grain-aggregates off the surface instead of cleaving them (this theory is developed in more details in section 6.5).

Composition of the island-forming phase on $\mathrm{NZSP_{AS}}$ surfaces

The composition of the island-forming phase observed on $\mathrm{NZSP_{AS}}$ surfaces in Figure 5.3 is analysed by EDX in Figure 5.4. To minimize the primary electron beam interaction volume and thus maximize surface sensitivity, a low accelerating voltage of 5 kV was used for this experiment. With this excitation energy, the Kα transitions of O, Na, Si and P could be detected as well as the Lα transition of Zr. Unfortunately, the proximity of the P Kα (2.01 keV) and Zr Lα (2.04 keV) lines complicates the identification of these elements. The EDX point analysis presented in Figure 5.4(a) indicates that the dark region (Spectrum 1, in orange) is composed of Na, O and possibly P. In contrast, the spectrum of the NZSP region (Spectrum 2, in green) displays a clear Si Kα transition and a broader signal around 2 keV which can be associated to the overlap of the P Kα and Zr Lα transitions. The line scan analysis presented in Figure 5.4(b) confirms that the island

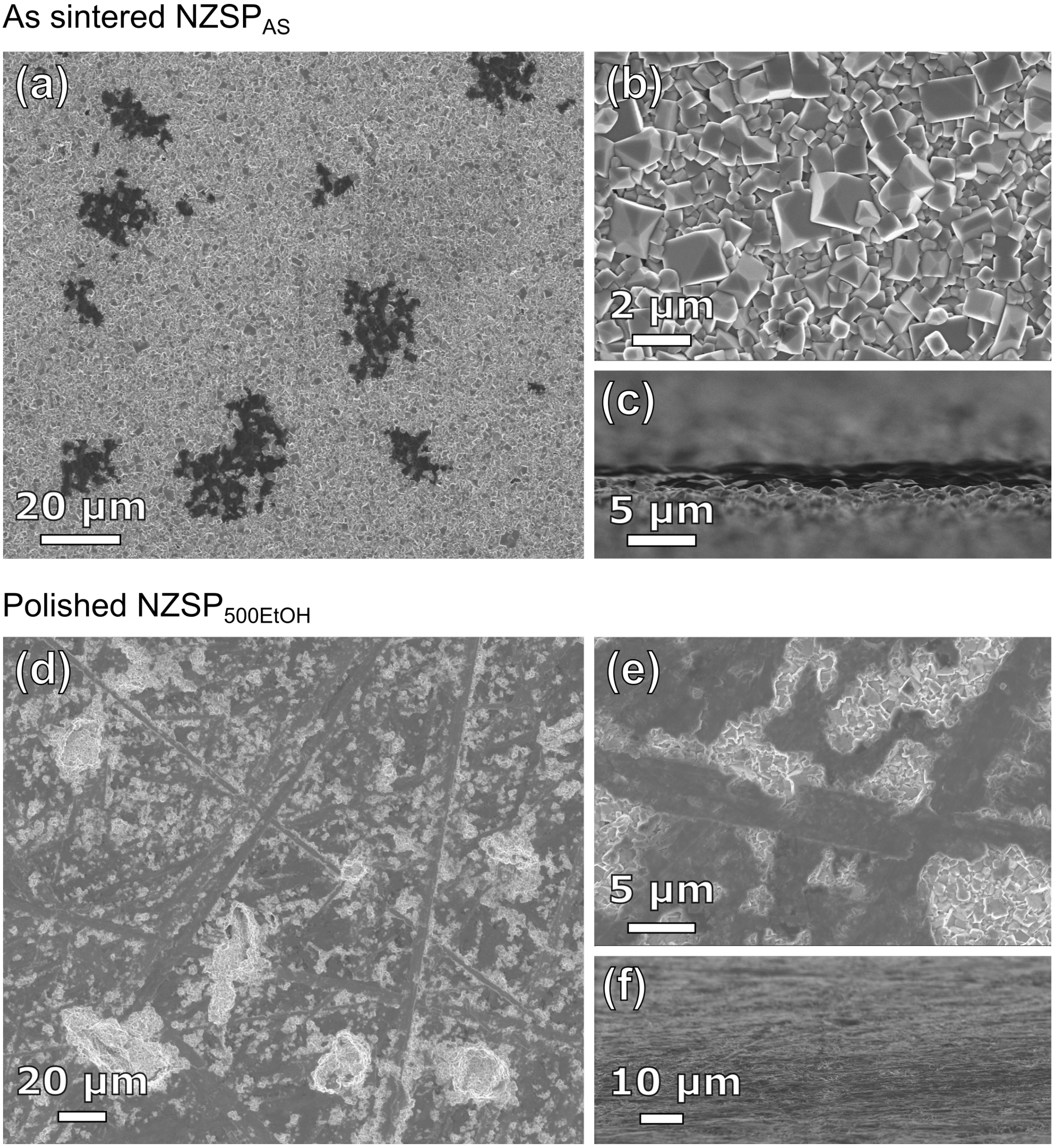

Figure 5.3: Comparison of the surface microstructures of a NZSP$_{AS}$ and a NZSP$_{500EtOH}$ pellet. NZSP$_{AS}$ sample: (a) Top view image. (b) Magnified top view image. (c) Grazing angle side view of a dark island region. **NZSP$_{500EtOH}$ sample**: (d) Top view image. (e) Magnified top view image. (f) Grazing angle side view.

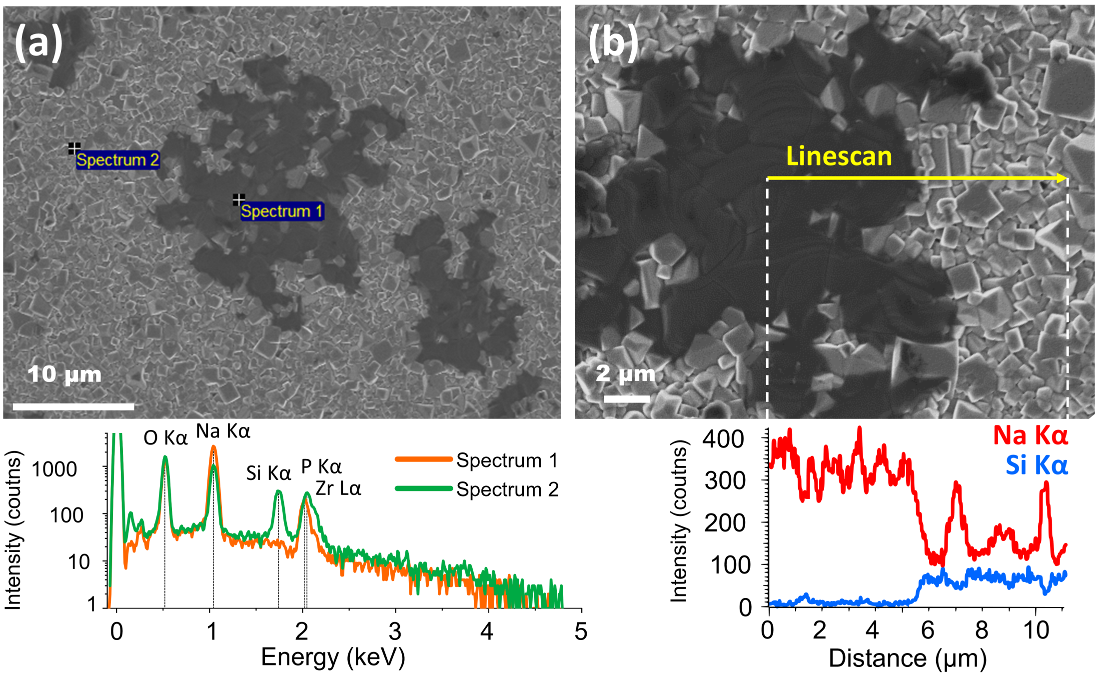

Figure 5.4: Comparison of the EDX signals emitted by the dark island-forming region and the NZSP region. (a) EDX point analysis comparing the signals of two points located either in the dark region (Spectrum 1) or in the NZSP region (Spectrum 2). (b) EDX analysis showing the changes in Na Kα and Si Kα signal intensities along a line (in yellow) scanning the surface from a dark region to the NZSP region.

phase contains no Si and has a higher atomic fraction of Na compared to the NZSP grain region.

Overall, the EDX analysis clearly indicates that the island-forming phase is free of Si and is enriched in Na. It also suggests that the phase is composed of P, although the overlap between the P and the Zr transitions introduces some uncertainty. These results suggest that the islands could be composed of a sodium phosphate phase. This suggestion will be corroborated in the next chapter (Chapter 6) where the surface composition of NZSP pellets is analysed in more detail.

Surface energies and grain shape

In this subsection, we investigate whether the very regular cuboidal shape of NZSP grains observed in Figure 5.3(b) is consistent with the predicted Wulff shape of the crystal. The Wulff shape of a crystal is the equilibrium shape obtained by minimizing the total surface free energy of a crystal in contact with another medium (*e.g.* air). It can be generated by calculating the surface energies of all the different possible facets of a crystal and finding out the grain shape with the overall minimum energy. The results presented here are only a brief summary of the computational study carried out by my colleague Dr. Ieuan Seymour. This Wulff shape analysis is included in this thesis because it will help to understand a DFT model discussed in section 6.4. More details on the calculations can be found in the article where these results were published.[57]

In the absence of an extensive DFT literature on the $Na_{1+x}Zr_2Si_xP_{3-x}O_{12}$ ($0 \leq x \leq 3$) family of materials, a first necessary step consisted in identifying the NaSICON facets with the highest probability of being formed. A decision was made to focus on the two end member compositions $NaZr_2P_3O_{12}$ (NZP) and $Na_4Zr_2Si_3O_{12}$ (NZS) to remove the complexity of handling partial occupancies in the Si/P site. The surface energies and structures of the $(1\bar{1}02)$, $(10\bar{1}4)$, (0003), and $(11\bar{2}0)$ planes of NZP and NZS are shown in Table 5.1 and in Figure 5.5.

Previous studies of phosphates and oxides have demonstrated that the cleavage of transition metal-O bonds results in high energy surfaces.[166, 167] For NZP and NZS, the $(1\bar{1}02)$ surface has the lowest energy, which is consistent with the fivefold coordination

Stoich.	Plane		Slab formula	Zr surface coord.	Surface energy (J m^{-2})
	Primitive	Conventional			
$NaZr_2P_3O_{12}$ (NZP)	(110)	$(1\bar{1}02)$	$Na_6Zr_{12}P_{18}O_{72}$	5	0.69
	(211)	$(10\bar{1}4)$	$Na_8Zr_{16}P_{24}O_{96}$	4	0.86
	$(10\bar{1})$	$(11\bar{2}0)$	$Na_6Zr_{12}P_{18}O_{72}$	5	1.15
	(111)	(0003)	$Na_8Zr_{16}P_{24}O_{96}$	3	0.97
$Na_4Zr_2Si_3O_{12}$ (NZS)	(110)	$(1\bar{1}02)$	$Na_{24}Zr_{12}Si_{18}O_{72}$	5	0.67
	(211)	$(10\bar{1}4)$	$Na_{32}Zr_{16}Si_{24}O_{96}$	4	0.88
	$(10\bar{1})$	$(11\bar{2}0)$	$Na_{24}Zr_{12}Si_{18}O_{72}$	5	1.26
	(111)	(0003)	$Na_{32}Zr_{16}Si_{24}O_{96}$	3	0.89

Table 5.1: Surface energy calculations of NZS and NZP

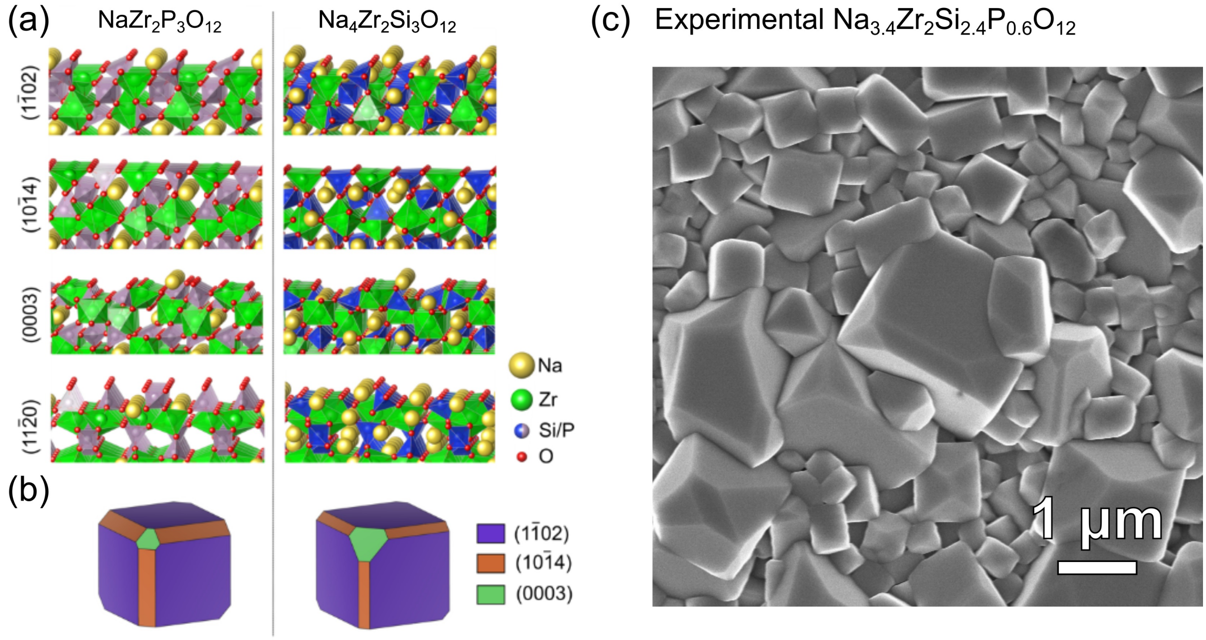

Figure 5.5: Wulff construction of two NaSICON phases. (a) Surface termination of the four low-energy facets of $NaZr_2P_3O_{12}$ and $Na_4Zr_2Si_3O_{12}$. (b) Corresponding Wulff shape calculated for the two phases. (c) Surface SEM image of a NZSP pellet showing grains with the same cuboidal shape.

of Zr (ZrO_5) on the surface in comparison to the $(10\bar{1}4)$ and (0003) planes which respectively leave Zr only fourfold and threefold coordinated. The $(11\bar{2}0)$ surface, which also has fivefold coordinated Zr on the surface, has a higher surface energy than the $(1\bar{1}02)$ plane as the surface PO_4/SiO_4 groups have a lower coordination with neighboring Na^+ ions. Although only a limited number of surface terminations have been investigated in this study, the significantly lower energy of the $\{1\bar{1}02\}$ family of planes relative to other surfaces for NZP/NZS would result in an approximately cubic morphology from a Wulff construction (see Figure 5.5(b)), which is consistent with the cubic morphology of grains observed experimentally in this work (see Figure 5.5(c)) and analogous NaSICON materials in other studies.[168, 169]

It can be seen from Table 5.1 that the $(1\bar{1}02)$ planes of NZP and NZS have similar surface energies (0.69 J m^{-2} and 0.67 J m^{-2}, respectively), even though the latter surface contains a larger number of undercoordinated Na^+ ions. The similarity between the different materials suggests that the nature of the tetrahedral Si^{4+} or P^{5+} ion has less of an impact on the surface energy than the coordination of the Zr^{4+} ion.

Overall, the Wulff construction was found to accurately describe the shape of sintered NZSP grains. It is therefore suggested that NZSP grains adopt this cuboidal shape to minimize the total surface free energy of the crystal during the sintering step. The faces of the NZSP cubes in sintered samples is likely to belong to the $\{1\bar{1}02\}$ family of planes. Another model built upon these results will be presented in Chapter 6. This other model investigates the impact on the surface energy of having a terminating layer of a different composition of the surface of NZSP grains.

5.2 Conductivity measurements

Ionic conductivity and activation energies

In this section, EIS is employed to measure the ionic conductivities of pristine NZSP pellets. For this, Au|NZSP|Au symmetrical cells are first employed. The gold blocking electrodes were deposited on the NZSP surfaces using a sputter deposition instrument. Nyquist plots of the Au|NZSP|Au symmetrical cell acquired at two different temperatures (25 °C and -100 °C) are presented in Figure 5.6(a).

At 25 °C (black curve), the characteristic frequency associated to Na^+ ion diffusion through the bulk of NZSP grains is very high and falls outside of the range which can be excited by our frequency response analyzer (its maximum frequency is 13 MHz). In a previous study, Ma *et al.* demonstrated that a GHz frequency response analyzer was required to resolve the bulk diffusion of Na^+ ions in NZSP pellets at room temperature.[16] In Figure 5.6, the bulk diffusion response was detected by lowering the temperature of the cell to -100 °C (blue curve). Lowering the temperature of the cell causes the characteristic frequencies of diffusive processes to drop (see section 4.6) making it possible to detect even the fastest ones with a MHz frequency response analyser. A capacitive tail is observed at

Temp (°C)	**σ_{bulk} (S cm^{-1})**	**C_{bulk} (F)**	**σ_{GB} (S cm^{-1})**	**C_{GB} (F)**	**σ_{tot} (S cm^{-1})**
25	7.0(±0.6) 10^{-3}	-	3.0(±0.3) 10^{-5}	1.4(±0.1) 10^{-9}	3.5(±0.3) 10^{-3}
-100	8.2(±0.7) 10^{-4}	6(±2) 10^{-12}	7.5(±0.7) 10^{-7}	1.45(±0.04) 10^{-9}	1.5(±0.1) 10^{-4}

Table 5.2: Ionic conductivities and capacitances of a NZSP pellet at 25 and -100 °C. Standard deviations (in parentheses) were calculated by propagating the errors originating from the fitting, the measurement of the thickness of pellets (±0.1 mm) and diameter of the electrodes (±0.2 mm).

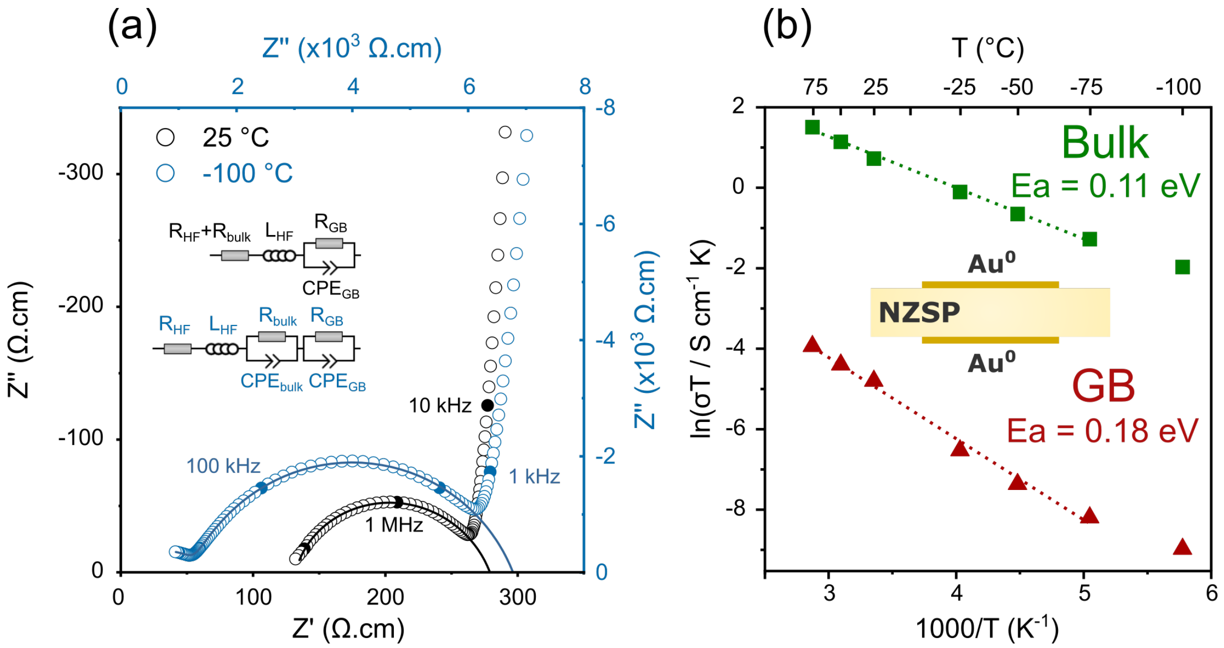

Figure 5.6: Ionic conductivity of NZSP samples. (a) Nyquist plots of a Au|NZSP|Au symmetrical cell measured at two temperatures. The axes for the measurement at -100 °C are the top and right ones. The equivalent circuits used for fitting are included in inset (the top circuit was used for the 25 °C data and the bottom circuit for the -100 °C data). Pellet type: $NZSP_{AS}$, Pellet thickness: $t = 1.7(0.1)$ mm, Electrode diameter: $\varnothing$=5.9(0.2) mm, frequency marker every decade; (b) Arrhenius plot of the same symmetrical cell.

both temperatures and is due to the ion blocking nature of Au blocking electrodes. This tail was not fitted in our models.

Because a semi-circle corresponding to bulk diffusion can be detected in the -100 ° C Nyquist plot and not in the 25 ° C one, two different equivalent circuits were used to model the data. The circuit used to model the -100 ° C data is composed of two R-CPE elements (R_{bulk}//CPE_{bulk} and R_{GB}//CPE_{GB}), a resistor (R_{HF}), and an inductor (L_{HF}). In this model, the resistor R_{HF} accounts for the resistance of the measurement setup (referred to as "high frequency" resistance). An inductor is included to improve the quality of the fit at high frequencies where inductive effects can distort the data.

In contrast, the model used for the 25 ° C Nyquist plot consists of only a single R-CPE element (R_{GB}//CPE_{GB}). As suggested by its name, the resistor R_{bulk}+R_{HF} combines both the bulk resistance of the NZSP pellet and the resistance of the measurement setup.

The Brug formula was employed to convert the calculated CPE values into "true" ca-

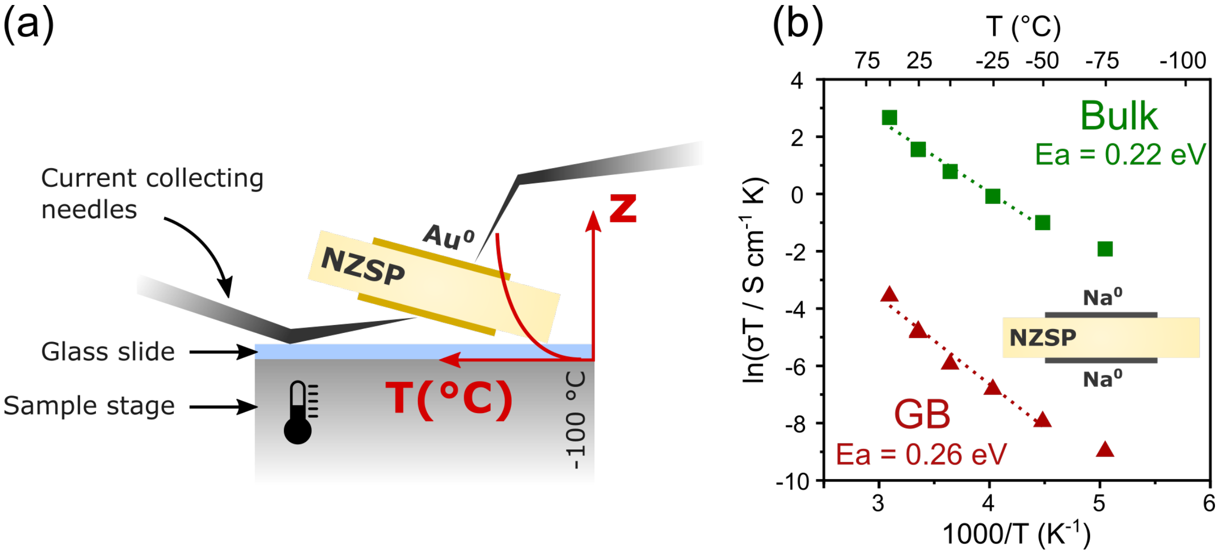

Figure 5.7: (a) Instrumental issue when measuring Au|NZSP|Au symmetrical cells with the Linkam temperature control stage. (b) Arrhenius plot of NZSP ionic conductivities measured in a Na|NZSP|Na symmetrical cell configuration.

pacitances and the values are presented in Table 5.2. The grain capacitance at 25 °C and -100 °C is in the order of $C_{GB}\approx1.4\text{x}10^{-9}$ F. The bulk capacitance could only be calculated for the data collected at -100 °C and a value of $C_{bulk}=6(2)\text{x}10^{-12}$ F was found. The error on the bulk capacitance is large because only a small part of the semi-circle is detected. The bulk and GB capacitances are in good agreement with the values conventionally attributed to bulk and grain boundary diffusion.[170]

The acquisition of impedance spectra across a range of temperatures allowed to construct the Arrhenius plot presented in Figure 5.6(b). From this Arrhenius plot, the activation energies of bulk and grain boundary diffusion could be extracted and values of $Ea_{bulk}=0.11(\pm0.01)$ eV and $Ea_{GB}=0.18(\pm0.01)$ eV were found [1]. These activation energies deviate from previous studies for which higher values were found (Ma *et al.* found that the diffusion of Na^+ ions in bulk NZSP had an activation energy of 0.28 eV for instance).[16] An instrumental error could potentially explain this large difference in activation energy: as schematically represented in Figure 5.7(a), it is suspected that the cell is actually at a higher temperature (*i.e.* faster conductivity) than the stage temperature because of geometrical constraints in the measurement setup; more specifically, the current collectors in the Linkam stage are needles and the bottom electrode of the Au|NZSP|Au cell was con-

---

[1] Standard deviations (in parentheses) were calculated by propagating the error obtained from the linear fit of the Arrhenius plot.

tacted by introducing a small angle with the sample stage (which is a thermally insulating layer of air between the sample and the cooling/heating stage). In Figure 5.7(b), an Arrhenius plot obtained with a symmetrical cell with Na metal electrodes is presented. This time, the cell (enclosed in a thermally conducting stainless steel coin cell casing) was put in direct contact with the sample stage. A better match with previously reported activation energies was obtained with this cell (Ea_{bulk}=0.22(±0.02) eV and Ea_{GB}=0.26(±0.02) eV).

Electronic conductivity

The electronic conductivity of NZSP samples was estimated from a time resolved polarization experiment using an asymmetric Au|NZSP|Na^0 cell (Wagner-Hebb setup).[171] In Figure 5.8, a voltage of 3.5 V was applied across the (-) Au|NZSP|Na^0 (+) cell. The polarity of the electrodes is important as Na^+ ions need to be driven away from the blocking electrode. After a quick initial drop (in the first minute of polarization), the residual current which can be measured by the potentiostat can be assigned to electronic leakage through the electrolyte. The electronic conductivity of NZSP was estimated from the average current measured between 8 and 10 minutes after the beginning of polarization. An electronic conductivity of $\sigma_e = 2.0(0.2)x10^{-9}$ S cm^{-1} was found. This low value confirms that the transference number of NZSP will be close to unity. Electrochemical reactions at

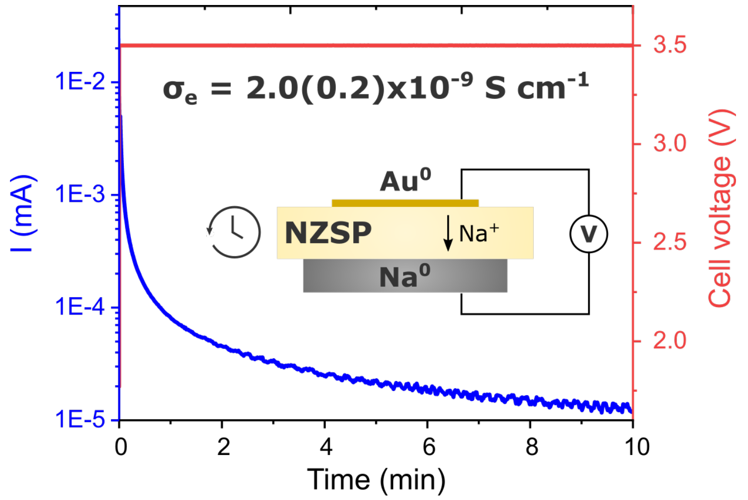

Figure 5.8: Electronic conductivity of NZSP pellets. Measurement of the leakage current of a Au^0|NZSP|Na^0 cell in a Wagner-Hebb configuration (pellet type: $NZSP_{AS}$, pellet thickness: 1.4(±0.1) mm, Au electrode diameter: ∅=5.9(±0.2) mm)

the Na|NZSP interface (decomposition of NZSP and formation of an interphase) could also contribute to the measured electronic current.[120] If this is the case, then the electronic conductivity of NZSP could be even lower than the one measured with this experiment. The electrochemical stability of the Na|NZSP interface will be investigated in more details in Chapters 7 and 8.

5.3 Important aspects of the NZSP synthesis

The next subsections shine light on three important aspects of the NZSP synthesis to obtain dense and pure pellets.

Optimal Na and P excess for the synthesis

The first attempts at reproducing the Jülich synthesis protocol in our laboratory at Imperial College were disappointing (in terms of density, phase purity and electrochemical performance of pellets). It was later identified that the success of the synthesis relied on the controlled addition of an excess of Na and P during the synthesis. This controlled addition, in the proportions $Na_{3.4}Zr_2Si_{2.4}P_{0.6}O_{12}.xNa_3PO_4$, improves the purity of pellets, their densification, and thereby increases their ionic conductivity. To find the optimum amount of Na and P excess for the synthesis, three batches of $NZSP.xNa_3PO_4$ powder were produced with different Na and P excesses (x = 0 at.%, 1.5 at.%, and 5 at.%).

X-ray diffractograms of sintered NZSP pellets from the three batches are presented in Figure 5.9. The diffractrograms show that a composite NZSP phase consisting of both the rhombohedral $R\overline{3}cH$ and monoclinic $C2/c$ NaSICON phases is obtained whichever Na and P excess is employed. More importantly, the fraction of impurities is larger for the 0 % and 5 % excess syntheses. In comparison, the 1.5 % synthesis barely contains any other crystalline phases than the $R\overline{3}cH$ and $C2/c$ ones. A reflection at 10.5 ° 2θ is observed for the 0 % and 5 % but its phase of origin has not yet been found.

A microstructural analysis by SEM of the surface and cross-section of a 0 % and 1.5 % pellet is presented in Figure 5.10. The contrast observed on the surface micrographs has the same origin has the one described in subsection 5.1: the dark regions on the surface of the pellets consist of a sodium phosphate phase (an EDX analysis not included here confirmed the composition of the islands for the 0 % sample). Counter-intuitively, the surface micrographs reveal that the 0 % pellet has a larger fraction of its surface covered by these sodium phosphate islands than the 1.5 % pellet. The cross-sectional images

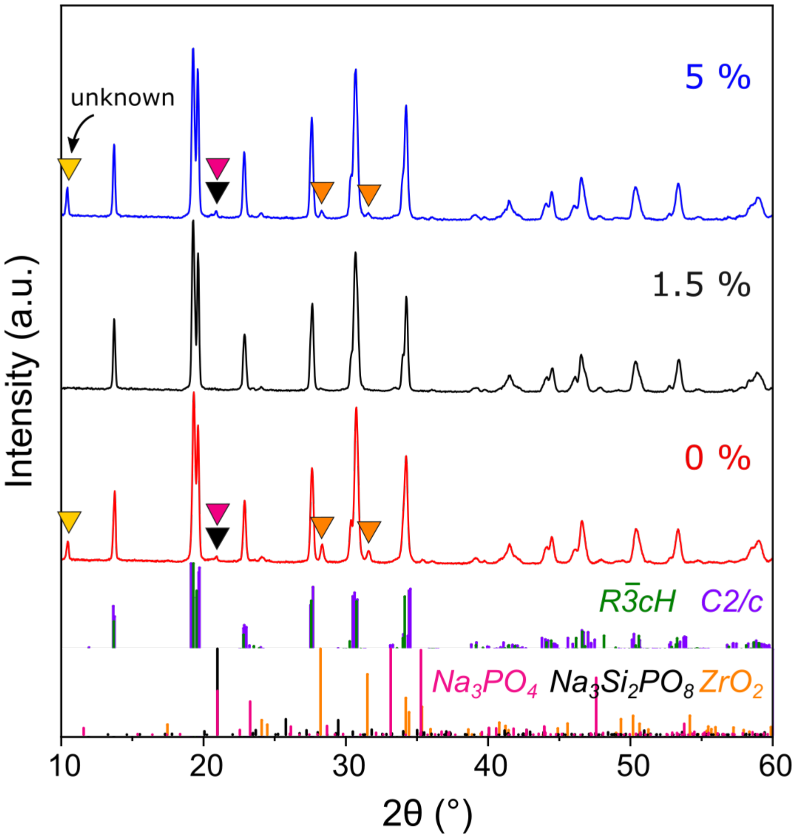

Figure 5.9: Impact of Na$_3$PO$_4$ excess on the crystal structure of NZSP pellets. X-Ray diffractograms of pellets with different amounts of Na$_3$PO$_4$ excess. Reflections caused by impurity phases are marked with a coloured triangle (only the most intense reflections are indicated). The reflection at 10.5 ° 2*θ* is unidentified yet. The reflection at 20.9 ° 2*θ* could be caused by two different phases.

reveal that the 1.5 % pellet is denser than the 0 % pellet: for the 0 % pellet, large pores can be observed in the middle of the pellet. Unfortunately, a microstructural analysis of the 5 % excess pellet was not conducted.

The XRD and SEM results indicate that the addition of a 1.5 % excess Na$_3$PO$_4$ prevents the decomposition of the NZSP phase into secondary phases during sintering. A possible hypothesis is that the addition of Na$_3$PO$_4$ during the synthesis may shift the equilibrium of the decomposition reaction (equation 5.1) and thus prevent the decomposition of NZSP into other phases, such as ZrO$_2$ and Na$_3$PO$_4$. For the 1.5 % excess samples, the presence of Na$_3$PO$_4$ between NZSP grains during sintering is believed to activate the coalescence of grains possibly through a liquid phase sintering mechanism.

Finally, the ionic conductivities of the three NZSP compositions were measured in a

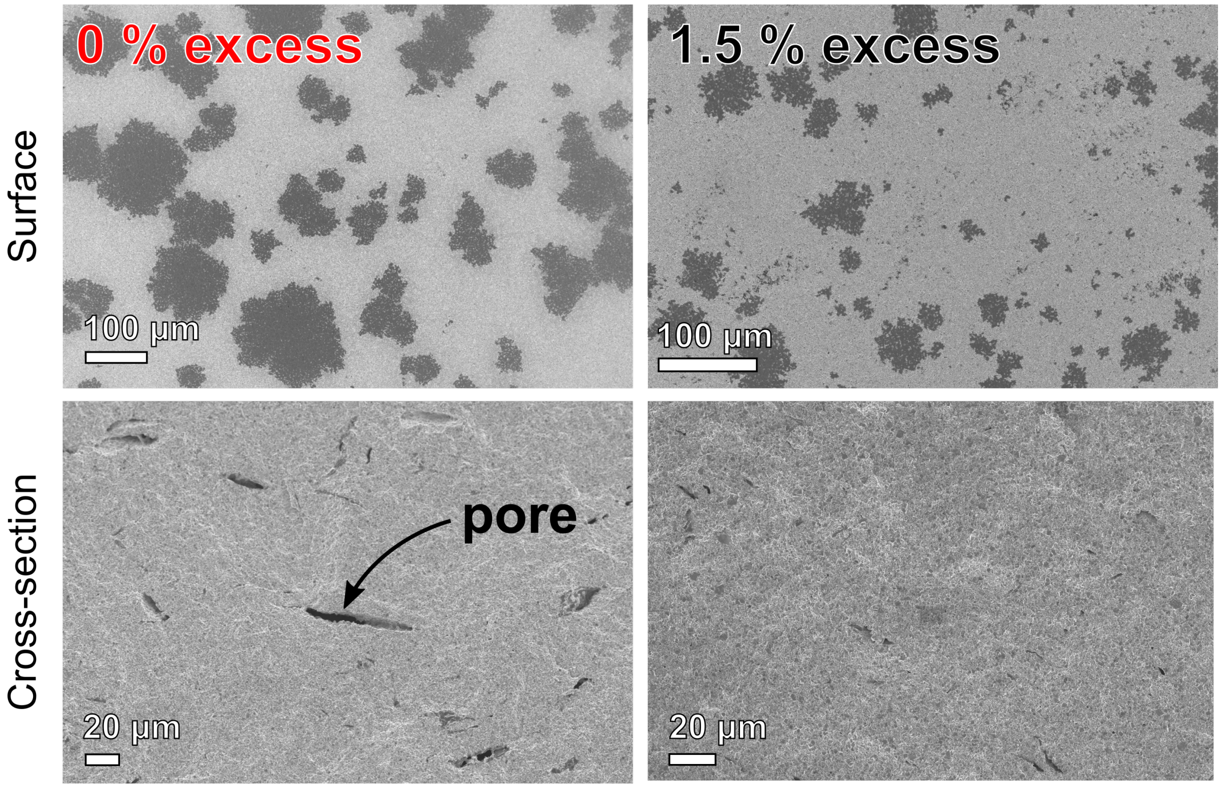

Figure 5.10: Impact of Na_3PO_4 excess on the microstructure of NZSP pellets. Micrographs from the surface of pellets and from their cross-section (snapped pellet).

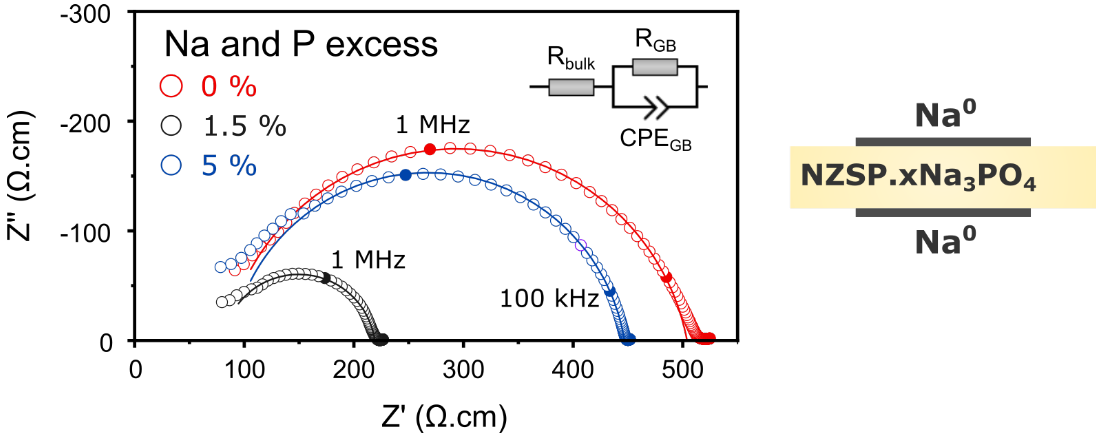

Figure 5.11: Impact of Na_3PO_4 excess on the ionic conductivity of NZSP pellets. Data collected at 25 °C. Frequency range (7 MHz to 5 Hz), markers every decade. Normalization parameters (pellet thickness=t, electrode diameter=∅): 0 % (t=1.3(±0.1) mm, ∅=8.2(±0.2) mm), 1.5 % (t=1.3(±0.1) mm, ∅=8.8(±0.2) mm), 5 % (t=1.4(±0.1) mm, ∅=8.1(±0.2) mm).

	$\sigma_{\mathbf{bulk}}$ (mS cm^{-1})	$\sigma_{\mathbf{GB}}$ (mS cm^{-1})	$\sigma_{\mathbf{total}}$ (mS cm^{-1})	$C_{\mathbf{GB}}$ (F)
NZSP0%	12(±1)	8.8(±0.8) 10^{-3}	2.0(±0.2)	1.65(±0.06) 10^{-9}
NZSP1.5%	12(±1)	1.4(±0.1) 10^{-2}	4.5(±0.4)	3.0(±0.2) 10^{-9}
NZSP5%	11(±1)	9.7(±0.8) 10^{-3}	2.2(±0.2)	1.71(±0.04) 10^{-9}

Table 5.3: Ionic conductivities and grain boundary capacitances of NZSP pellets as a function of Na_3PO_4 excess. Standard deviations (in parentheses) were calculated by propagating the errors originating from the fitting, the measurement of the thickness of pellets (±0.1 mm) and diameter of the electrodes (±0.2 mm).

Na|NZSP|Na symmetrical cell configuration. The corresponding Nyquist plots are presented in Figure 5.11. The sets of impedance data were all fitted to the equivalent circuit included in inset[2] and the parameters extracted from the fit are listed in Table 5.3. To calculate grain boundary conductivities, the bulk capacitance value $C_{\text{NZSP-bulk}}$=6 10^{-12} F calculated in section 5.2 was employed. An optimum ionic conductivity was found for the 1.5 % excess Na_3PO_4 synthesis: at 25 °C, the bulk ionic conductivity of pellets reaches an impressive σ_{bulk}=12(±1) mS cm^{-1}; the total ionic conductivity of pellets is lower (σ_{total}=4.5(±0.4) mS cm^{-1}) because the samples are polycrystalline with resistive grain boundaries (σ_{GB}=1.4(±0.1) 10^{-2} mS cm^{-1}).

Ball milling

Ball milling was also identified as a crucial step to achieve a good densification of pellets. The impact of the ball milling step is illustrated by comparing the microstructure of two pellets, sintered from the same batch of powder: one pellet was sintered with the powder before it was ball milled, and the other after it was ball-milled (see Figure 5.12).

The difference in the microstructure of sintered pellets is clear in Figure 5.12(a): the pellet sintered with the non-ball-milled powder has a large fraction of pores on its surface which is not the case for the pellet employing the ball-milled powder. The photograph of the pellets in Figure 5.12(b) also shows that the diameter of pellet sintered with the non-ball-milled powder has not shrunk as much as the ball-milled sample. The exact impact of the ball-milling step on the precursor NZSP powder remains to be identified. It does not seem from the SEM images that the ball milling step particularly reduces the particle size which is already nanometric for the non-ball-milled powder (and remains nanometric

---

[2] here, only the part of the spectra corresponding to the NZSP response was fitted. More details on how to model the contribution of the Na|NZSP interface will be included in Chapter 6

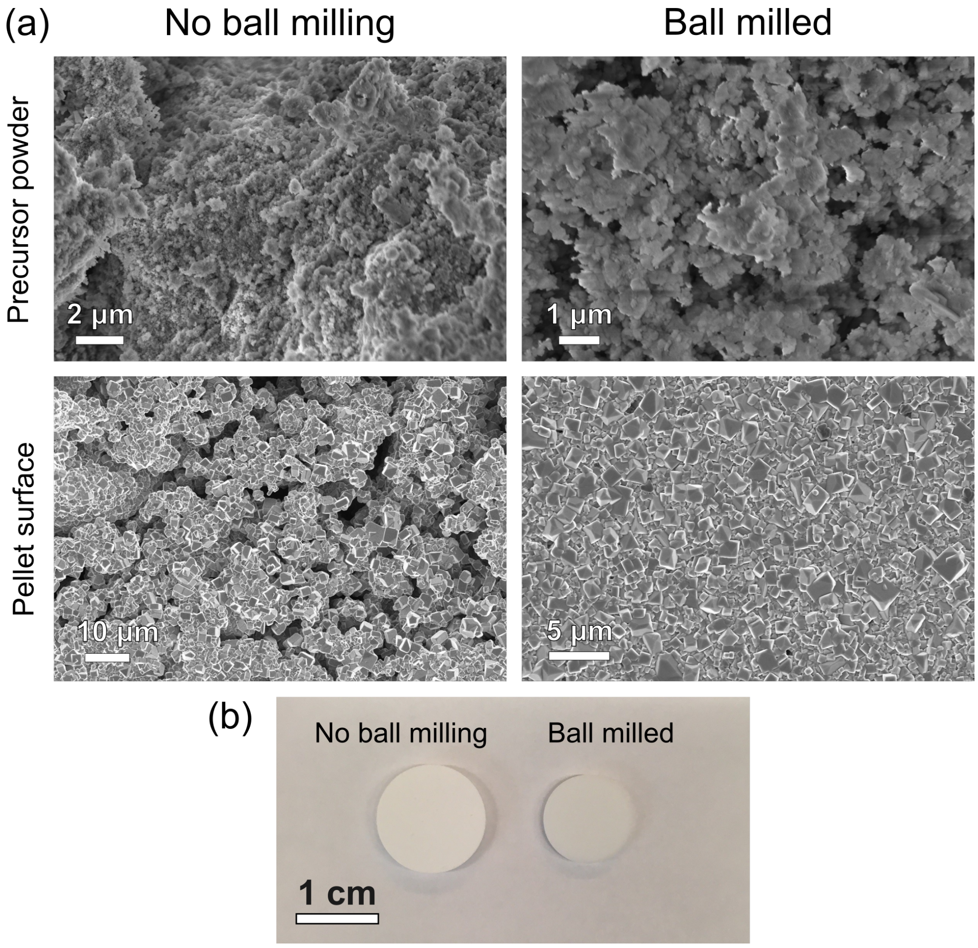

Figure 5.12: Impact of ball-milling on the sinterability of NZSP pellets. (a) Surface SEM images of the precursor powder before and after ball-milling. The resulting microstructure of sintered pellets is also presented. (b) Photograph of the two pellets showing the better densification of the pellet whose precursor powder was ball-milled.

after ball-milling). The low energy ball-milling step in ethanol may have contributed to homogenize the composition of the NZSP powder.

Impact of air exposure

After sintering, NZSP pellets should be quickly transferred to a glovebox and stored there until further use.[172] The reason for this is briefly discussed in this section. Storing NZSP pellets in air results in a significant degradation of their surface microstructure after one week of exposure as illustrated in Figure 5.13: this figure contains SEM micrographs of the surface of a freshly sintered NZSP pellet and of the same pellet after one week of aging in air.

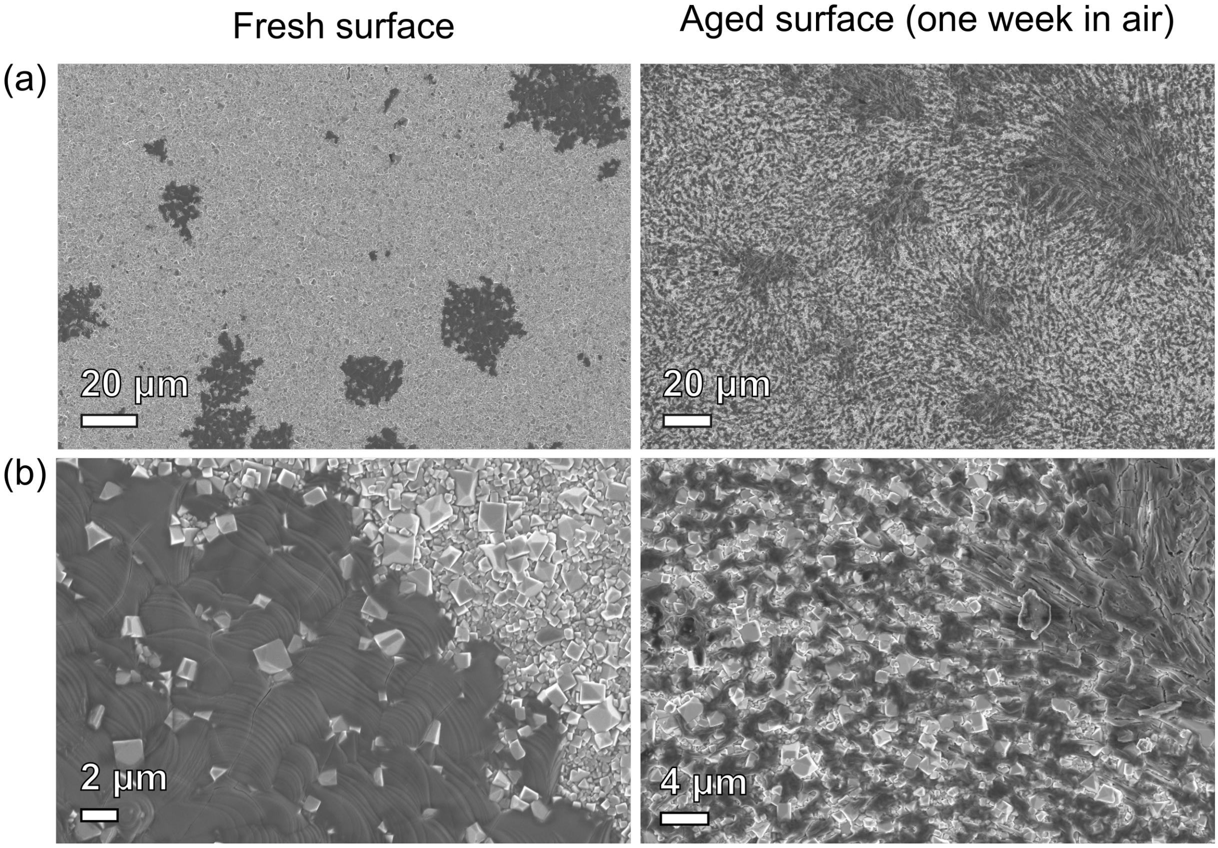

Figure 5.13: Impact of air exposure on the surface microstructure of NZSP pellets. (a) Low magnification images. (b) Higher magnification images.

The sodium phosphate phase which forms islands on the surface of freshly sintered samples is observed over the entire surface after one week of aging in air. In addition, aged NZSP pellets were found to be much more brittle and often break during cell assembly.

The exact cause for this peculiar aging behaviour remains to be identified. We suggest that the highly hygroscopic nature of Na_3PO_4 could play a role in the degradation. Notwithstanding, a brief exposure of NZSP samples to air was not found to have any significant impact on the surface of NZSP samples. Unlike other more reactive ISEs (such as LLZO[71]), NZSP samples can therefore be sintered in air and transferred to characterization instruments without necessarily employing a vacuum suitcase, but should be kept in a protective atmosphere for longer storage periods.

5.4 Summary

This chapter provided a structural, microstructural, and electrochemical characterization of the NZSP samples employed in this work. The results presented here indicate that $Na_{3.4}Zr_2Si_{2.4}P_{0.6}O_{12}$.1.5% Na_3PO_4 is a good candidate solid electrolyte which meets the criteria listed in Chapter 2: sintered pellets have a high ionic conductivity (with a σ_{bulk} in the order of 12-15 mS cm^{-1} and a σ_{total} in the order of 3-5 mS cm^{-1}) and a low electronic conductivity (σ_{e} = 2.0x10^{-9} S cm^{-1}), they are dense and have good mechanical properties if the pellets are stored in a glovebox after sintering.

The structural study confirmed that NZSP samples are multiphasic but that only a low amount of inert secondary phases (*e.g.* ZrO_2) can be detected. NaSICON phases have been the subject of numerous structural studies since their discovery but most of the efforts have focused on the $Na_3Zr_2Si_2PO_{12}$ which, until recently,[16] was thought to be the composition with the highest ionic conductivity. The composite structure that $Na_{3.4}Zr_2Si_{2.4}P_{0.6}O_{12}$ adopts is largely unexplored and would require further structural characterization efforts. In particular, mapping the distribution of the different phases across pellets as a function of the sintering conditions (atmosphere, temperature) could be an important research study from both an experimental point of view and a computational one (for instance using large scale molecular dynamics simulations).

The SEM-EDX microstructural study revealed the presence of a Na and P rich phase forming islands on the surface of as sintered NZSP pellets. Interestingly, these islands are observed on sintered pellets regardless of the excess Na and P used during the synthesis and are actually less present on 1.5 % excess pellets than 0 % ones.

The computational study from Dr. Ieuan Seymour presented in section 5.1 is also the first to calculate the surface energies of NaSICON facets and his Wulff construction provides a fundamental explanation for the cuboidal shape that NZSP grains adopt.

In the following chapters, NZSP pellets produced via this optimized synthesis are assembled into symmetrical cells with Na^0 electrodes.

Chapter 6

Minimizing the initial Na|NZSP interface resistance

Electrode|electrolyte interfaces can be the source of large overpotentials in electrochemical devices. The alkali metal|ISE interface in SSBs is no exception. Taking the Na|NZSP interface as an example, Table 3.1 shows that large interface resistances in excess of 100 Ω cm^{-2} are still commonly reported. Yet, to achieve high charge/discharge rate performance, all internal sources of overpotential need to be minimized.

Over the past five years, the question of minimizing the metal|ISE interface resistance has interested many research groups and resulted in numerous publications. A general consensus is that a good adhesion between the metal and the ISE is a prerequisite to obtaining a low interface resistance. Surface contaminants on ISE surfaces (such as carbonates or hydroxides) are typically poorly wetted by alkali metals. By removing these surface contaminants, it was demonstrated that the metal|ISE interface resistance can be considerably reduced, often to value below 10 Ω cm^{-2} (see section 3.1). Some other strategies to improve wetting at metal|ISE interfaces involve the deposition of thin alkaliphilic interlayers. The practicality and long-term stability of interlayer strategies is however debated (see section 3.1).

The initial objective of this chapter was to investigate whether the Na|NZSP interface resistance could be optimized by controlling surface contamination. Our results reveal that, unlike other metal|ISE interfaces, the mechanism by which the Na|NZSP interface resistance can be minimized does not affiliate to a surface cleaning mechanism but rather to a specific sodium phosphate surface termination that NZSP pellets adopt after thermal treatments.

In Section 6.1, NZSP surface treatments yielding low Na|NZSP interface resistances are identified by EIS. In Sections 6.2 and 6.3, XPS and LEIS are employed to reveal surface composition differences between NZSP samples as a function of their surface treatments. Finally, in Section 6.4, first principles calculations are used to identify what causes thermally treated NZSP samples to adopt a specific surface termination.

N.B.: the results presented in this chapter are largely reproduced from a recent publication written in collaboration with my colleagues Ieuan Seymour and Andrea Cavallaro and our collaborators in Jülich, Qianli Ma and Frank Tietz.[57]

6.1 Impact of NZSP surface treatments on the Na|NZSP interface resistance

Polishing and thermal annealing

To evaluate how the NZSP surface processing influences the electrochemical performances of Na^0|NZSP interfaces, impedance spectra of three types of Na^0|NZSP|Na^0 symmetrical cells are compared. The surface of NZSP pellets used for these cells are either unaltered after sintering ($NZSP_{AS}$), roughly polished with ethanol as solvent ($NZSP_{EtOH500}$), or polished and annealed ($NZSP_{EtOH500\text{-}anneal}$). For more information about the samples nomenclature, the reader is referred to Section 4.1. The impedance spectra of the three symmetrical cells are presented in Figure 6.1 in the form of Nyquist plots. The models used for equivalent circuit fitting are included in inset and consist of a resistor R_{HF} (high frequency resistance), an inductor L, and either one or two R-CPE elements depending on the number of observed semi-circles. The calculated fitting parameters for all the Nyquist plots presented in this section are collated in Table 6.1.

As previously discussed in section 5.2, detecting the diffusion of Na^+ ions through the bulk of NSZP grains is not possible at room temperature in the frequency range covered by the frequency response analyzers used in this study. In the equivalent circuits, R_{HF} therefore combines the resistances corresponding to the measurement setup and the resistance corresponding to bulk diffusion (see Figure 4.13 in section 4.6)[1]. For all three samples, the semi-circle observed at high frequency (with an apex at a frequency of around 1 MHz and capacitance of $C_{GB} \approx$ 3-5 10^{-9} F) can be attributed to grain boundary diffusion, as was already demonstrated in section 5.2.

---

[1] In the calculations of the bulk ionic conductivity in table 6.1, the contribution from the measurement setup resistance was neglected

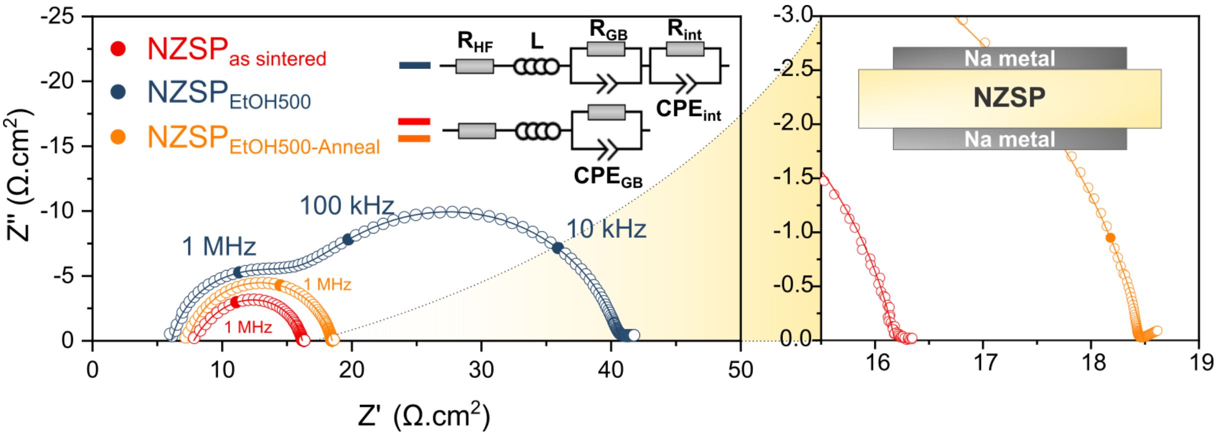

Figure 6.1: Impact of thermal treatments on the Na|NZSP interface resistance. Nyquist plots of Na|NZSP|Na symmetrical cells ($NZSP_{AS}$, $NZSP_{EtOH500}$ and $NZSP_{EtOH500\text{-}anneal}$). Data points are shown as open circles, frequency markers are shown as filled circles, and the respective fits (obtained with the equivalent circuits shown in inset) are represented as a solid line. The data presented are normalized (multiplied by the electrodes area, divided by two).

A second semi-circle attributed to the transfer of Na^+ ions across the Na|NZSP interface (modelled by R_{int}//CPE_{int}, equivalent capacitance $C_{int} = 8.3(\pm 0.3)\ 10^{-8}$ F) can be clearly observed for the $NZSP_{EtOH500}$ sample. The calculated interface resistance of 24.2(±0.9) Ω cm^2 is quite low in comparison to other studies reported in Table 3.1. As an interface semi-circle is not distinguishable for the $NZSP_{AS}$ sintered and $NZSP_{EtOH500\text{-}anneal}$ samples, an upper limit for their interface resistances was estimated using the procedure described by Krauskopf et al.[173] by calculating the difference between Z'_{data} (fmin) and Z'_{fit} ($f \rightarrow 0$ Hz). This results in interfacial resistances as low as 0.2 and 0.1 Ω cm^2 for the $NZSP_{AS}$ and $NZSP_{EtOH500\text{-}anneal}$ samples, respectively [2].

NZSP surface roughness

A significant impact on the Na|NZSP interface resistance is observed when NZSP samples are finely polished ($NZSP_{EtOH4000}$) as illustrated in Figure 6.2 and reported in Table 6.1. An interface resistance of 3700(±200) Ω cm^2 was obtained for the Na|$NZSP_{EtOH4000}$|Na symmetrical cell. Yet, even if NZSP samples are finely polished, thermal annealing can restore a negligible Na|NZSP interface resistance as demonstrated by the low R_{int} (0.4 Ω cm^2) of the cell employing a $NZSP_{EtOH4000\text{-}anneal}$ pellet.

---

[2] Given these calculated R_{int} are extremely small, the error associated with them is relatively large (a 0.1 Ω cm^2 error resulting in a 100 % relative error)

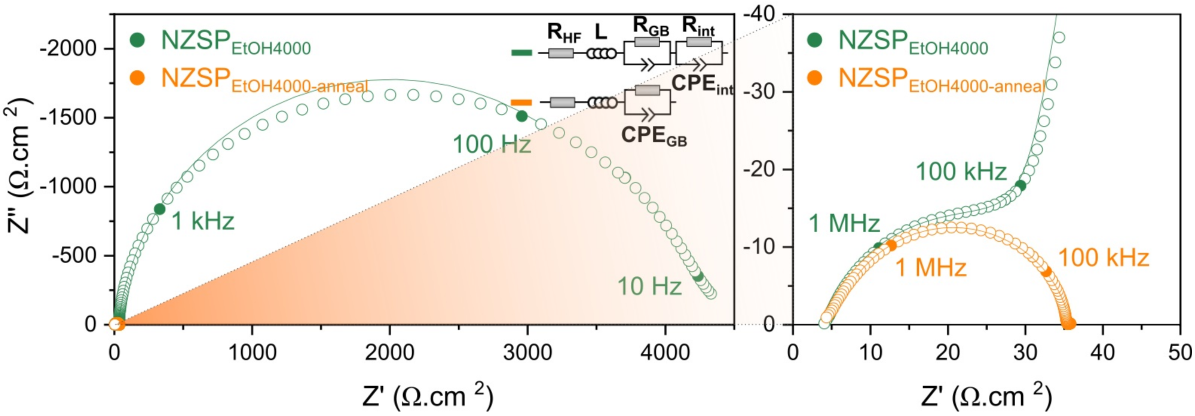

Figure 6.2: Impact of NZSP surface roughness on the Na|NZSP interface resistance. Nyquist plots of Na|NZSP|Na symmetrical cells (NZSP$_{\text{EtOH4000}}$, NZSP$_{\text{EtOH4000-anneal}}$). Left: overall view, right: magnified view.

Polishing solvent

To rule out a possible influence of the solvent in the larger interface resistance of polished NZSP samples, another set of symmetrical cells were assembled from dry polished samples (NZSP$_{\text{dry500}}$ and NZSP$_{\text{dry4000}}$). The interface resistances calculated for the two cells in Figure 6.3 is equivalent to the cells with ethanol polished NZSP pellets: the NZSP$_{\text{dry500}}$ cell has an interface resistance of 21.9(±0.9) Ω cm^2 (in comparison to 24.2 Ω cm^2 for NZSP$_{\text{EtOH500}}$); and the finely polished NZSP$_{\text{dry4000}}$ cell has a much larger interface resistance of 9000(±300) Ω cm^2 which is of the same order of magnitude as the NZSP$_{\text{EtOH4000}}$ cell (3700 Ω cm^2). The results obtained with another set of samples (not presented here) which were polished with a non-polar solvent (n-hexane) are also in agreement: roughly polished NZSP samples resulted in cells with interface resistances of a few tens of Ω cm^2 whilst cells with finely polished pellets had much higher interface resistances (thousands of Ω cm^2). These results suggests that the polishing solvent is not a parameter directly influencing R$_{\text{int}}$.

Summary of the EIS experiments

The results presented in this section demonstrate that NZSP surface treatments have a direct impact on the Na|NZSP interface resistance. The grain boundary conductivity of samples was calculated using Equation 4.18 with the bulk capacitance value calculated

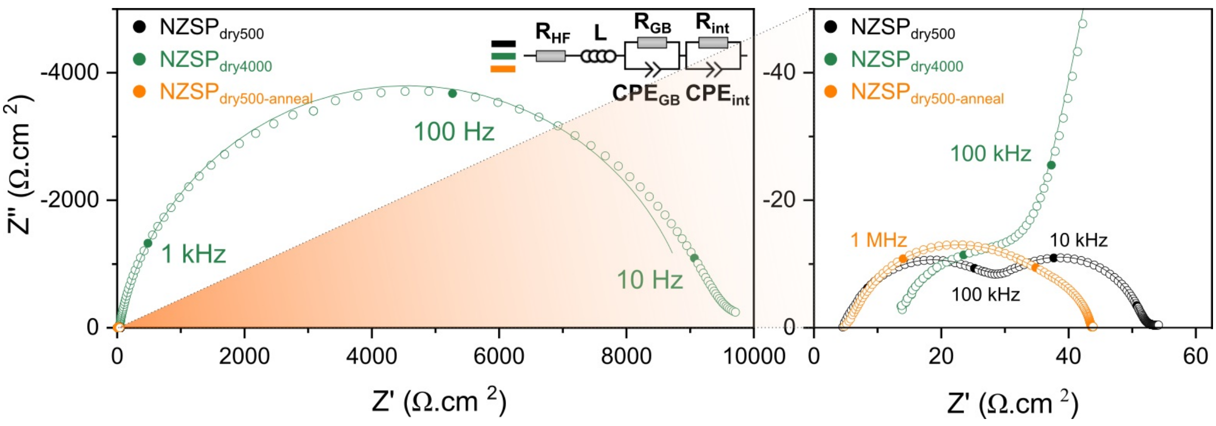

Figure 6.3: Impact of polishing solvent on the Na|NZSP interface resistance. Nyquist plots of Na|NZSP|Na symmetrical cells polished without a solvent (NZSP$_{\text{dry500}}$, NZSP$_{\text{dry4000}}$, and NZSP$_{\text{dry500-anneal}}$). Left: overall view, right: magnified view.

	t (mm)	∅ (mm)	σ_{bulk} (10^{-3} S cm^{-1})	σ_{GB} (10^{-6} S cm^{-1})	σ_{total} (10^{-3} S cm^{-1})	C_{GB} (10^{-9} F)	C_{int} (10^{-7} F)	R_{int} (Ω cm^2)
Thermally activated								
NZSP$_{\text{AS}}$	1.5	10.3	15(±1)	8.1(±0.6)	4.6(±0.4)	4.9(±0.1)	-	0.2
NZSP$_{\text{EtOH500-anneal}}$	1.5	10.2	4.1(±0.3)*	12.1(±0.9)	2.5(±0.2)	3.04(±0.09)	-	0.1
NZSP$_{\text{EtOH4000-anneal}}$	1.5	8.5	4.1(±0.3)*	4.6(±0.4)	1.5(±0.1)	3.2(±0.1)	-	0.4
NZSP$_{\text{dry500-anneal}}$	1.5	8.5	2.2(±0.2)*	4.8(±0.4)	1.2(±0.1)	3.4(±0.1)	1.9(±0.2)	4.7(±0.3)
Rough polish								
NZSP$_{\text{EtOH500}}$	1.2	10.3	11.9(±0.1)	6.8(±0.6)	4.0(±0.4)	5.3(±0.5)	0.83(±0.03)	24.2(±0.9)
NZSP$_{\text{dry500}}$	1.4	9.8	1.6(±0.1)*	4.2(±0.3)	1.0(±0.8)	4.0(±0.3)	1.51(±0.08)	21.9(±0.9)
Fine polish								
NZSP$_{\text{EtOH4000}}$	1.3	8.5	3.8(±0.3)*	4.0(±0.4)	1.5(±0.1)	3.7(±0.7)	0.51(±0.01)	3700(±200)
NZSP$_{\text{dry4000}}$	1.8	10.3	7.4(±0.5)	9.0(±0.6)	2.7(±0.2)	2.8(±0.5)	0.56(±0.1)	9000(±300)

Table 6.1: Electrochemical parameters extracted from impedance data fitting. Bulk conductivities with a star * indicate that R_{HF} was corrected on the Nyquist plots (more details in section 4.6). For the Nyquist plots where an interface semi-circle could not be resolved, a C_{int} value cannot be calculated. Standard deviations (in parentheses) were calculated by propagating the errors originating from the fitting, the measurement of the thickness of pellets (t, ±0.1 mm) and diameter of the electrodes (∅, ±0.2 mm).

in Section 5.2 (C_{bulk} = 6x10^{-12} F). Thermally activated NZSP pellets produce Na|NZSP interfaces with the lowest interface resistance. Polishing NZSP pellets has a detrimental impact on the Na|NZSP interface resistance but this effect can be cancelled by annealing pellets after they have been polished.

6.2 XPS analysis of the composition of NZSP surfaces

XPS was employed to reveal surface composition differences between NZSP samples as a function of their surface treatments. Figure 6.4 compares the signals of six NZSP core levels (Na1s, Si2p, O1s, P2p, Zr3d and C1s) for three samples (NZSP$_{\mathrm{AS}}$, NZSP$_{\mathrm{EtOH500}}$ and NZSP$_{\mathrm{EtOH500\text{-}anneal}}$). To ease the comparison of relative elemental intensities between samples, it is convenient to consider the concentration of one element in the NZSP phase to be fixed. Here, the Zr concentration in the NZSP phase was chosen as the normalization constant. More precisely, the signals were normalized so that the Zr3d$_{5/2}$ peak area of all samples are equal. The survey spectra of the three samples can be found in Figure C.1 in Appendix C.

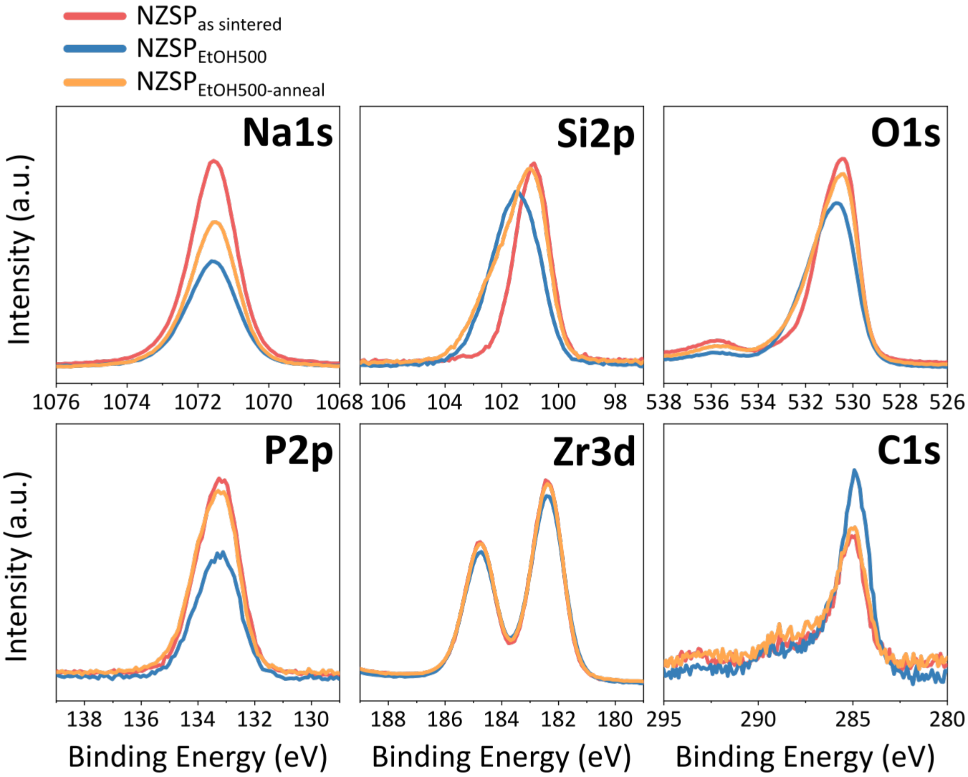

Figure 6.4: Comparison of the surface chemistry of NZSP samples by XPS. Core level XPS spectra of samples NZSP$_{\mathrm{AS}}$, NZSP$_{\mathrm{EtOH500}}$ and NZSP$_{\mathrm{EtOH500\text{-}anneal}}$. (charge correction: Zr3d$_{5/2}$ at 182.4 eV; intensity normalization between samples: Zr3d$_{5/2}$ peak area).

Contamination of NZSP surfaces

C1s spectra were collected for each sample to monitor the impact of polishing and thermal treatments on surface carbon contamination. Adventitious carbon species are present on essentially all surfaces exposed to ambient air and are a common feature observed in XPS spectra.[137] In addition to ambient air contamination, polishing samples can also impact their surface composition. In recent studies, polished surfaces of various SEs were demonstrated to be composed of carbonate or hydroxide species.[71, 25] Poor ionic transport across metal|SE interfaces is often observed when SE surfaces are covered with adventitious species.[71, 25, 72, 73]

Figure 6.4 reveals that NZSP samples, whichever surface treatment they have received, have a similarly low level of surface carbon contamination (quantitatively, around 4 at.% of the total surface signal). The only exception is for the finely polished NZSP samples ($NZSP_{EtOH4000}$ and $NZSP_{dry4000}$) for which a higher level of C contamination was detected as can be seen in Figures C.2 and C.3 in Appendix C.

Some differences between samples can be observed in their O1s region. It is possible that surface contaminating hydroxide species contribute to the O1s signal. Yet, the coexistence of several phases on the surface of NZSP samples (possibly including $R\overline{3}cH$ and $C2/c$ NaSICON phases, ZrO_2, segregated sodium phosphate islands, see Chapter 5) multiplies the number of possible O environments, thereby complicating the fitting model for O1s signals. For this reason, and to avoid making too many speculations, the O1s signal was not fitted in this work.

Si2p signal

Noticeable differences in the position and width of the Si2p signal depending on the surface treatment of NZSP samples can be observed in Figure 6.4. The Si2p signal of $NZSP_{EtOH500}$ is broader than the $NZSP_{AS}$ one and shifted towards higher binding energies by about 0.8 eV (from 100.7 eV to 101.5 eV). The Si2p signal of $NZSP_{EtOH500\text{-}anneal}$ shares features from $NZSP_{EtOH500}$ and $NZSP_{AS}$: it is broad but its highest intensity is around around 100.7 eV. These observations suggest that there are two chemical environments for Si depending on the NZSP surface treatment. This is confirmed by the fitting presented in Figure C.4 in Appendix C where two doublets are required to obtain a physically meaningful fit for the Si2p signals. The rest of this section describes our attempts to attribute these fitted peaks to specific phases, which unfortunately have been unsuccessful. All the additional data is presented in Appendix C.

The following experiments were conducted to identify the composition of the two Si environments:

- XPS spectra of NZSP pellets polished with Al_2O_3 polishing pads instead of SiC ones is presented in Figure C.5. The chemical shift and broadening of the Si2p signal for NZSP polished with Al_2O_3 pads is similar to the NZSP polished with SiC. This experiment (in addition to an absence of a signal corresponding to SiC in the C1s spectra) confirmed that residual SiC particles are not responsible for the second Si environment observed on polished samples.
- XPS spectra of a NZSP pellet which was dry polished inside a glovebox and transferred under vacuum to the XPS instrument is presented in Figure C.6. This experiment was conducted to characterize the surface composition of a polished NZSP sample which was not exposed to air nor a solvent. After the surface composition of the unexposed surface was analyzed, the NZSP sample was briefly exposed to air for a few minutes (the same exposure that a sample would receive during polishing outside the glovebox), and its surface composition was analyzed again. A comparison of the results shows that the short exposure to air does not impact the surface composition of the sample. These dry polished NZSP samples also have a high binding energy Si environment.
- XPS spectra of the cross-section of a NZSP pellet (measured in the middle of the pellet) and that of NZSP powder from a crushed pellet are presented in Figure C.7. The objective of this experiment was to identify in which environment Si is found in the centre of a NZSP pellet. For the cross-section sample, its Si2p signal overlaps almost perfectly with that of a $\mathrm{NZSP_{AS}}$ surface which suggests that the doublet centered at 100.7 eV could correspond to the fourfold O coordinated environment that Si theoretically adopts in NaSICON structures. Yet, the Si2p signal of the crushed powder, which should also reveal the environment that Si adopts in the bulk of pellets, looks like the signal obtained for polished NZSP samples... Unfortunately this conundrum could not be resolved. Interestingly, the Na1s and P2p signals of the $\mathrm{NZSP_{cross\text{-}section}}$ sample are less intense than that of the $\mathrm{NZSP_{AS}}$ surface, which is another indication that the Na and P enrichment of thermally treated NZSP sample occurs on the surface exposed to air and not in the bulk of pellets.

Overall, the XPS analysis presented in this chapter clearly shows that two Si environments can be formed on NZSP surfaces, but the experiments which were designed to identify these phases did not converge yet to a convincing conclusion.

Na1s and P2p signals

As can be seen from Figure 6.4, the Na1s and P2p signals of the thermally activated samples (NZSP$_{\text{AS}}$ and NZSP$_{\text{EtOH500-anneal}}$) are more intense than the polished sample (NZSP$_{\text{EtOH500}}$). This difference in peak intensity reflects changes in the surface atomic concentrations between samples. More precisely, since the peak intensities were normalized to the Zr3d$_{5/2}$ peak area, a higher intensity of the Na1s and P2p signals means that the Na:Zr and P:Zr surface atomic ratios of the thermally activated samples are larger than that of the polished sample. These results either suggest that:

1. the concentration of Na and P in surface NZSP grains are simultaneously increasing
2. a secondary phase rich in Na and P segregates on the surface of thermally activated samples

For hypothesis (1), an increase of the P concentration could possibly be explained by a redistribution of Si and P atoms between the surface and bulk of grains during thermal treatments (with P atoms migrating towards the sample surface and Si towards the bulk). This redistribution can, in theory, respect the NaSICON general stoichiometry $Na_{1+x}Zr_2Si_xP_{3-x}O_{12}$. But a substitution of Si by P atoms should also be compensated by a lower Na concentration to respect charge balance. The fact that an increase in the Na concentration is observed either suggests that hypothesis (1) is incorrect, or that another charge compensation mechanism is involved (for instance with O vacancies, $v_{\ddot{O}}$). The experimental results presented in the following sections suggest that hypothesis (2) is correct and explain the XPS results better.

For finely polished samples as well, annealing increases the surface concentration of Na and P (see Figure C.2 in Appendix C): the annealed sample (NZSP$_{\text{EtOH4000-anneal}}$), which was characterized by a low interface resistance, has more intense Na1s and P2p signals than the polished sample (NZSP$_{\text{EtOH4000}}$).

6.3 LEIS analysis of the outer atomic layer of NZSP surfaces

The XPS analysis presented in the previous section revealed that thermally treated NZSP samples have higher surface concentration of Na and P. One of the hypothesis which could explain this higher concentration is that their surface is covered by a thin sodium phosphate layer. In this section, LEIS is employed to test this hypothesis and determine the composition and the coverage of the layer. The acquisition and treatment of the data presented in this section is the work of my colleague Dr. Andrea Cavallaro. The results are part of the same publication which was previously mentioned.[57]

For all the LEIS analyses, the He^+ ion primary beam was scanned on a large area of 500 x 500 µm. The SEM images presented in Figure 5.3 (section 5.1) show that the LEIS analysis area will contain crystalline NZSP regions and the islands whose composition is presumed to be Na and P rich. The composition determined by LEIS is an average over this entire surface.

Figure 6.5(a) compares the surface (in red) and bulk (in blue) LEIS signals of a $NZSP_{AS}$ sample. The surface spectrum was collected with a He^+ ion dose of $8x10^{14}$ ions cm^{-2}. After having collected this surface spectrum, an Ar^+ ion sputtering beam was used to reveal deeper layers of the sample. At regular intervals, the Ar^+ sputtering beam was alternated with the He^+ ion analysis beam to obtain a depth profile. The average signal of all the spectra collected during this depth profile is the bulk spectrum in Figure 6.5(a). The LEIS energy spectrum of the $NZSP_{AS}$ first atomic layer indicates that it is only constituted of Na, P and O atoms. Zr and Si do not appear on the surface of $NZSP_{AS}$. In contrast, the bulk energy spectrum (in blue) shows that O, Na, Si, P and Zr are present underneath a thin surface layer. Regarding the Na peak, the bulk of $NZSP_{AS}$ samples seems to be almost completely depleted of sodium in comparison to their surface. In reality, the low intensity of the Na peak in the bulk spectrum is associated to a challenging issue of preferential sputtering (see section 4.5 for more details). Overall, the LEIS spectra in Figure 6.5(a) suggest that the entire surface of $NZSP_{AS}$ is terminated by Na, P and O atoms. The presence of a Zr in-depth signal around 2500 eV in the surface energy spectrum indicates that the sodium phosphate surface layer must be extremely thin.

In Figure 6.5(b), the surface composition of $NZSP_{AS}$ is compared with the composition of a polished ($NZSP_{EtOH4000}$) and a polished and annealed ($NZSP_{EtOH4000\text{-}anneal}$) sample. A freshly cleaved NZSP sample ($NZSP_{Xsection}$) was also analyzed. This measurement provides extra information about the bulk composition of NZSP samples. For each sample, LEIS spectra were collected on three different areas. On each area, four consecutive measurements with the He^+ ion beam were collected. Figure 6.5(c) schematically illustrates the positions of the twelve regions analysed per sample. In Figure 6.5(b), the averaged Na, Zr, Si, P and O peak relative intensities are plotted as a function of the He^+ primary ion dose. As an example, the relative fraction of Zr %(Zr) was obtained by calculating:

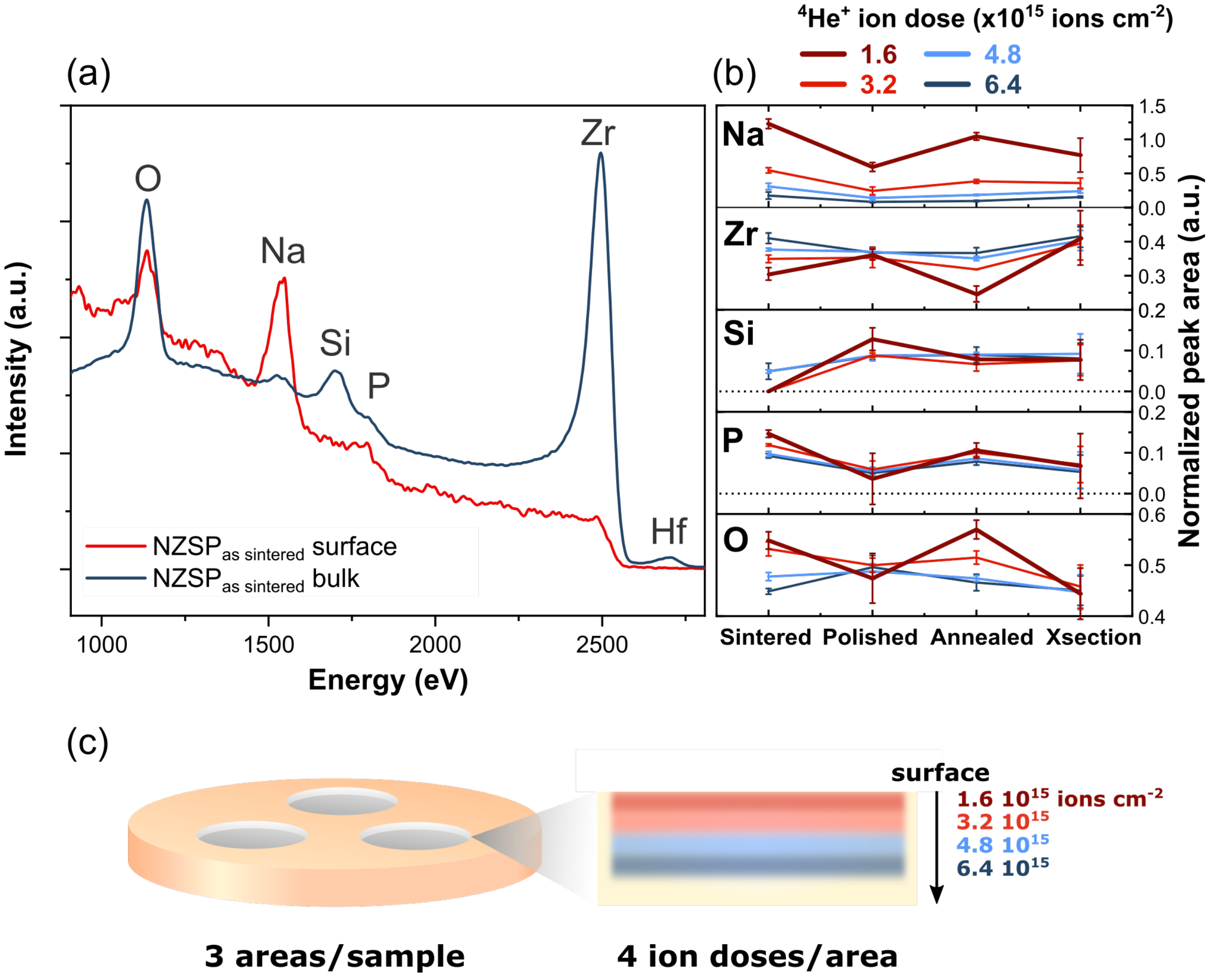

Figure 6.5: LEIS reveals the composition of the outer surface layer of samples. (a) $^4He^+$ ion LEIS energy spectra of a $NZSP_{AS}$ sample comparing the signal of its first atomic layer (for a 8x10^{14} ions cm^{-2} dose, in red) to its average bulk signal (in blue). (b) Comparison of the normalized LEIS peak areas of four NZSP samples with increasing ion doses (“Sintered”=$NZSP_{AS}$, “Polished”=$NZSP_{EtOH4000}$, “Annealed”=$NZSP_{EtOH4000\text{-anneal}}$, “Xsection”=$NZSP_{AS\text{-cross-section}}$). Each point is the average of three peak areas measured on three different points on the surface of each sample. Error bars correspond to standard deviations. (c) Schematic illustrating where the 12 LEIS spectra were measured on each sample.

$$\%(Zr) = \frac{A(Zr)}{A(Zr) + A(Si) + A(P) + A(O)} \tag{6.1}$$

where A(X) is the integrated peak area associated to an interaction of He^+ ions with atoms X on the surface. The intensity of the Na peak is not included in the denominator because of the previously mentioned issue of preferential sputtering.

Figure 6.5(b) can be used to compare, the surface composition of the different NZSP samples at a given ion dose. The largest differences can be found for the lowest He^+ ion dose (1.6×10^{15} ions cm^{-2}, shown in dark red). As expected, thermally activated NZSP samples have more Na and P on their surface than polished samples. The Na and P normalized peak areas of $NZSP_{AS}$ are more than twice as large as the $NZSP_{EtOH4000}$ sample. More importantly, the signal corresponding to Si cannot be initially detected on the surface of $NZSP_{AS}$ samples and only appears after an accumulated ion dose of 4.8×10^{15} ions cm^{-2}.

Figure 6.5(b) also shows that the surface composition of thermally activated samples changes more rapidly with the received ion dose than the polished sample. As the $^4He^+$ ion dose increases from 1.6 to 6.4×10^{15} ions cm^{-2} and deeper atomic layers are slowly revealed, differences in the surface chemical composition of samples attenuate. Taking $NZSP_{AS}$ as an example, the intensity of the P peak diminishes with an increasing ion dose, while simultaneously the intensity of the Zr and Si peaks increases. Since $^4He^+$ ions only slowly sputter the surface, this suggest that the sodium phosphate layer on the surface of thermally activated NZSP samples must be very thin (few atomic planes). By removing this surface layer with a low ion dose, a surface composition close to that of a polished sample is obtained. In comparison to $NZSP_{AS}$, the composition of $NZSP_{EtOH4000}$ does not significantly change with an increasing ion dose and stays within its error bars. Variations in the intensity of the Na peak are not related to changes in composition but rather to the previously mentioned problem of preferential sputtering; this explains why the intensity of the Na peak decreases for all samples with higher ion doses.

Our SEM/EDX analysis of NZSP surfaces presented in Section 5.1 already revealed the existence of micrometric sodium phosphate islands on the surface of $NZSP_{AS}$ samples. Because the analysis area is large, the LEIS results presented in this section indicate that the entire $NZSP_{AS}$ surface is covered by a thin sodium phosphate layer (not just the islands which were observed by SEM). Combining the SEM/EDX, XPS, and LEIS results, a clearer picture about the surface composition of thermally treated NZSP samples starts to emerge: the entire surface is covered by an atomically thin sodium phosphate layer (which could be a complexion layer[52, 53]), which locally forms larger micrometric islands on NZSP_{AS} samples. In the following section, first principles calculations are employed to look for a fundamental explanation for the segregation of the sodium phosphate layer.

6.4 Searching the driving force for the surface layer formation from first principles calculations

The experimental results presented in the previous sections converge to the conclusion that a thin sodium phosphate layer covers the surface of thermally activated NZSP samples. Here, first principles calculations relying on DFT and ab-initio molecular dynamics were employed to obtain the surface energies of Na_3PO_4 terminated NaSICON surfaces and compare them with the energies of bare NaSICON surfaces (which were previously calculated in Section 5.1). The calculations presented here were conducted by my colleague Dr. Ieuan Seymour.[57] As in section 5.1, the calculations were performed using the two end-member compositions $NaZr_2P_3O_{12}$ (NZP) and $Na_4Zr_2Si_3O_{12}$ (NZS) which are easier to model by DFT than $Na_{3.4}Zr_2Si_{2.4}P_{0.6}O_{12}$.

It was established in section 5.1 that the facet with the lowest energy for both the NZS and NZP phases is the $(1\bar{1}02)$ one. Thus, for the calculations, a single layer of Na_3PO_4 was added on top of a $(1\bar{1}02)$ oriented NZP/NZS surface. Among the other sodium phosphate phases which could form (e.g. $Na_4P_2O_7$ or $Na_5P_3O_{10}$), the specific composition Na_3PO_4 was selected because it is one of the phases that $Na_{3.4}Zr_2Si_{2.4}P_{0.6}O_{12}$ is predicted to decompose to in Equation 5.1 (Section 5.1).

After constructing the Na_3PO_4|NaSICON models, a short (4 ps) ab initio molecular

Soich.	**Termination**	**Slab formula**	**Zr surface coord.**	**Surface energy (J m^{-2})**
$NaZr_2P_3O_{12}$	Bare	$Na_6Zr_{12}P_{18}O_{72}$	5	0.69
	Na_3PO_4	$Na_{16}Zr_8P_{16}O_{64}$	6	0.44
$Na_4Zr_2Si_3O_{12}$	Bare	$Na_{24}Zr_{12}Si_{18}O_7$	5	0.67
	Na_3PO_4	$Na_{28}Zr_8Si_{12}P_4O_{96}$	6	0.58

Table 6.2: DFT computed surface energies of bare and Na_3PO_4 terminated $(1\bar{1}02)$ surfaces for NZP and NZS.

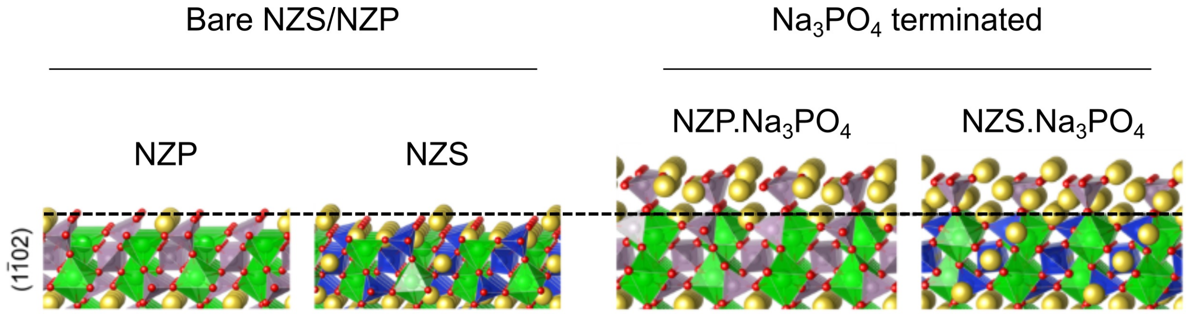

Figure 6.6: Surface energy DFT calculations of Na_3PO_4 terminated NZS/NZP. DFT optimized $NaZr_2P_3O_{12}$ and $Na_4Zr_2Si_3O_{12}$ $(1\bar{1}02)$ surfaces capped with a monolayer of Na_3PO_4. The termination plane of the original stoichiometric (uncapped) surface is indicated with a black dashed line.

dynamics run at 500 K was used to equilibrate the surface atomic positions, followed by structural optimization. The resulting surfaces are shown in Figure 6.6. For both materials, the PO_4 groups in the Na_3PO_4 layer are bound to the fivefold coordinated Zr sites on the surfaces, resulting in a stable ZrO_6 octahedron. From Table 6.2, it can be seen that the surface energy of the Na_3PO_4 capped NZP and NZS $(1\bar{1}02)$) surfaces is lower than the corresponding bare surfaces. As $Na_{3.4}Zr_2Si_{2.4}P_{0.6}O_{12}$ is an intermediate composition between NZS and NZP, it is expected that its surface energy will also be lowered by a Na_3PO_4 termination. The lower energy of the Na_3PO_4 capped surfaces provides a fundamental explanation for the presence of Na_3PO_4 on the surface of $Na_{3.4}Zr_2Si_{2.4}P_{0.6}O_{12}$.

Although the current analysis of Na_3PO_4 surface layers was limited to the $(1\bar{1}02)$ surface, it is likely that the presence of Na_3PO_4 will also have an impact on higher energy surfaces, particularly ones with low Zr coordination. A single monolayer of Na_3PO_4 was adopted in the current study to limit the computational cost. The impact of the thickness of the Na_3PO_4 layer will be the subject of future work. It also remains to be demonstrated where the Na and P atoms forming the surface layer originate from. The source of Na and P for the formation of the layer still needs to be identified. The Na and P excess added during the synthesis could explain the formation of the layer on as-sintered samples. For polished and annealed samples, it is suggested that Na and P could segregate from surface emerging grain boundaries.

6.5 Discussion

Charge transfer and interface resistances

In the first studies looking at integrating metal electrodes with ISEs, the metal|ISE interface resistances were often extremely large, which led to the speculation that the charge transfer resistance across metal|ISE interfaces was intrinsically large. However, interface and charge transfer resistances should not be confused: the interface resistance corresponds to the apparent sum of all resistive diffusion processes across an interface [3]; the charge transfer resistance only accounts for the resistance associated with the $Na^0{}_{anode} \leftrightarrow Na^+{}_{SE} + e^-{}_{anode}$ conversion across a perfect interface. Hence, charge transfer is only one contribution to the interface resistance. In a recent study, Krauskopf *et al.* were able to carefully produce a pristine Li|LLZO interface, virtually free from any contamination: an extremely low interface resistance of 0.1 Ω cm^2 at room temperature was measured and attributed to charge transfer across the Li|LLZO interface.[173] With this study, they proved, at least for the Li|LLZO interface, that charge transfer is a marginal contribution to the interface resistance and that all resistive contributions above 0.1 Ω cm^2 should be attributed to other ionically blocking processes.

Pragmatically, contaminant-free and perfectly wetting interfaces are difficult to obtain and manipulate. Therefore, under more conventional experimental conditions, the alkali metal|SE interface resistance is predominantly affected by:

1. pores between the metal anode and SE resulting in improper contact[69]
2. adventitious contaminants sandwiched between the anode and the SE (layers formed on the surface of the SE or metal anode by reaction with a gas environment prior to cell assembly)[71, 25, 72, 73, 74]
3. a resistive SEI forming at the interface[78, 76, 77]

With the aim to isolate the contribution of charge transfer from other resistive contributions to the interface resistance, in this study, a uniaxial load of 500 N was systematically applied during cell assembly (not during electrochemical testing) to guarantee an intimate contact between NZSP and Na metal and thus minimize constriction resistance effects. Regarding adventitious contamination, our XPS results suggest that NZSP surfaces,

---

[3] on a Nyquist plot, the interface semi-circle arises from all diffusion processes across the interface with similar time constants

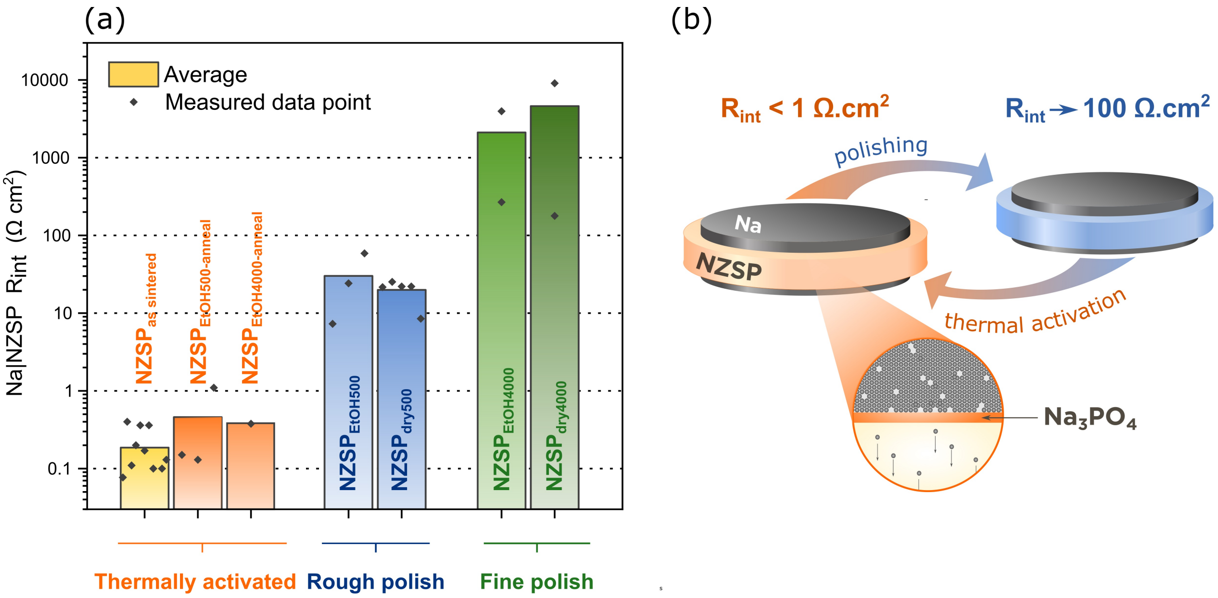

Figure 6.7: Interface resistances of Na|NZSP|Na symmetrical cells. (a) Mean interface resistance values obtained with Na|NZSP|Na symmetrical cells. (b) Schematic illustrating the role of thermal activation on NZSP surfaces.

whichever surface treatment they received, are stable even if handled briefly in ambient air (the C signal in Figure 6.4 only accounts for 4 at.% of the total surface signal). This is not the case for some other oxide ISEs such as LLZO or Na-β/β”-alumina.[71, 25] The contribution of a SEI to the measured interfacial resistance was mitigated by measuring the cells quickly after cell assembly (typically less than 30 minutes after cell assembly). The electrochemical stability of the Na|NZSP interface will be investigated in more detail in Chapters 7 and 8.

Minimizing the Na|NZSP interface resistance

The normalized interfacial resistances from all symmetrical cells tested in this study are presented in Figure 6.7. This figure illustrates the range of interfacial resistances which can be obtained for the same alkali metal | ISE system when the processing of the ISE surface is changed. In particular, these results explain why the reported Na|NaSICON R_{int} values in the literature are so widely spread (see Table 3.1 in Section 3.1). An important outcome of this study is that a negligibly low interface resistance can be consistently obtained when thermally activated NZSP samples are used in symmetrical cells. Regardless of the processing history of the NZSP sample (polished or not, rough or smooth surface), if the last step of the surface processing is a thermal treatment, a low Na|NZSP interface resistance is obtained.

Combining two surface sensitive techniques (XPS and LEIS), a sodium phosphate surface termination (possibly Na_3PO_4) was identified on the surface of thermally activated NZSP samples. The fact that this sodium phosphate layer can be sputtered even with a low dose of low energy ions indicates that its thickness must be only of a few atomic planes. Although more experiments would be required to confirm this hypothesis, the Na_3PO_4 layer could be a form of complexion on the NZSP surface.[52, 53, 131] The formation of this surface termination is demonstrated to be thermodynamically favorable by DFT calculations. Whilst polishing NZSP samples removes this Na_3PO_4 surface termination, a thermal annealing will promote the reconstruction of a Na_3PO_4 surface to minimize surface energy. The LEIS results indicate that the Na_3PO_4 layer covers the entire NZSP surface uniformly. The presence of larger micrometric sodium phosphate islands on the surface of $NZSP_{AS}$ is attributed to the excess of Na and P used to promote densification during synthesis. These local inhomogeneities in the thickness of the Na_3PO_4 layer do not seem to affect the electrochemical performance of cells.

The improvement in the Na|NZSP interface resistance when the sodium phosphate layer is present are believed to be associated to an improvement in interfacial adhesion. Further computational and experimental studies will be required to confirm this hypothesis. In the following chapters, the impact of this surface layer on the electrochemical stability of the Na|NZSP interface will be investigated

Impact of NZSP roughness on interface resistance

Figure 6.7 also illustrates the large impact that the surface roughness of NZSP pellets has on the Na|NZSP interface resistance. Up to two orders of magnitude separate the interface resistance of cells employing finely polished NZSP pellets in comparison to cells employing roughly polished ones (see Figure 6.7). Several hypotheses, which will need to be confirmed in future experiments, could explain this large difference:

- **A native Na^0 passivation layer:** This chapter focused mostly on analysing the chemistry of NZSP surfaces to explain differences in Na|NZSP interface resistances. The surface chemistry of the Na^0 electrode prior to cell assembly may however also have an impact on R_{int}. As will be discussed in more detail in the following chapter (Section 8.2), as-prepared Na^0 films form a passivation layer on their surface even if prepared in clean gloveboxes. During the assembly of the cell, the load which is applied to press the Na^0 electrodes against the NZSP pellets make them plastically deform. If the NZSP pellet is roughly polished, protrusions on its surface will indent the Na^0 electrodes in multiple locations, thereby breaking the passivation layer and creating unobstructed diffusion pathways for Na^+ ions across the interface. Instead, for finely polished NZSP pellets, the passivation layer present on the Na^0 foil may not be penetrated to a great extent, and will constitute a blocking layer. In a recent publication, Otto *et al.* also found that the Li|LLZO interface resistance was impacted by the roughness of the LLZO pellet and attributed the difference to the passivation layer present on their Li^0 electrodes.[174]

- **Rough and fine polishing induce different modes of abrasion:** DFT calculations presented in Section 5.1 revealed that the surface energies of NaSICON grains were highly impacted by the facet exposed to the surface. The calculations demonstrated that the cuboidal shape of NZSP grains could be predicted from a Wulff construction and was probably associated to the $(1\bar{1}02)$ planes being the lowest in energy. If the SiC grit size is smaller than the NZSP grain size, then the NZSP grains will be cleaved during polishing (see Figure 6.8). If the samples are roughly polished, there is a higher chance that grains will be ripped off the surface instead of cleaved. The composition of grain boundaries in NZSP samples remains to be identified, but supposing that sodium phosphate complexions forms at grain boundaries, these layers may be exposed to the surface via rough polishing whilst they would be polished off by fine polishing. Besides, fine polishing possibly reveals higher energy NZSP facets which could be more reactive towards adventitious contaminants (if the formation of a passivation layer minimizes their surface energy). The XPS analysis of finely polished NZSP surfaces revealed a larger concentration of contaminants on their surface than on roughly polished ones (see C1s signal of $NZSP_{dry4000}$ and $NZSP_{EtOH4000}$ in Figures C.2 and C.3). This higher concentration of ionically blocking species on the surface of NZSP could explain the higher R_{int} of cells employing finely polished pellets.[71, 25, 73, 175]

6.6 Summary and future work

Enabling fast-charging SSBs requires to optimize the interface between alkali metal anodes and ISEs. The initial objective of this chapter was to identify the experimental conditions under which the Na|NZSP interface resistance could be minimized. This chapter described the steps which have led to the discovery that an atomically thin sodium

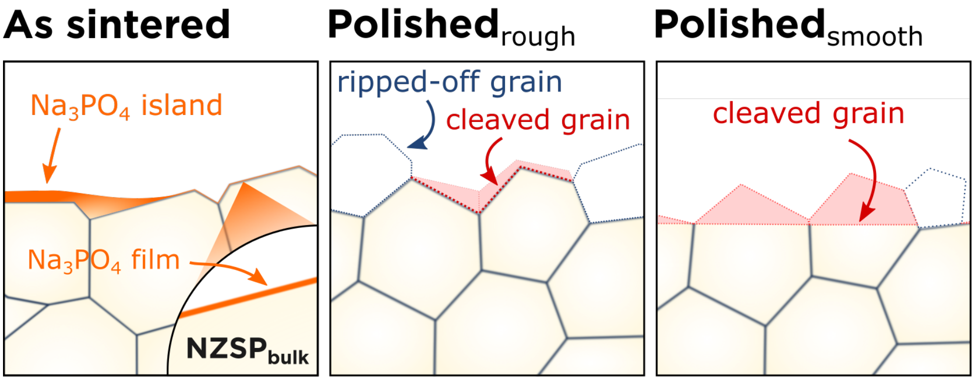

Figure 6.8: Suggested difference in the mode of abrasion between rough and fine polishing.

phosphate terminates the surface of thermally treated NZSP samples. The study demonstrates that this sodium phosphate layer forms *in-situ* by thermally activating NZSP samples (either by sintering or annealing pellets after polishing). The Na|NZSP interface resistance of cells employing thermally activated NZSP pellets is consistently below 1 Ω cm^2 which suggests that the presence of this sodium phosphate layer improves the adhesion of Na metal towards NZSP. The mechanism by which the Na|NZSP interface resistance can be minimized sets NZSP apart from other ISEs for which a minimization of the interface resistance is often related to the removal of surface contaminants from their surface (for instance at the Li|LLZO[71] or Na|Na-β/β"-alumina interfaces[25]). The negligible interface resistance obtained with as-sintered NZSP samples is very promising for industrial prospects because no additional processing steps are required to optimize the interface electrochemistry.

This study is the first to suggest that NZSP grains form a sodium phosphate termination on their surface upon thermal treatments. Further characterization of this surface layer using cryogenic transmission electron microscopy (TEM) or atom probe tomography (APT) would be very valuable to determine its exact composition and thickness. Identifying the experimental conditions (annealing temperature and atmosphere for instance) promoting the segregation of the layer during thermal treatments will also be an important next-step. For instance, it would be important to know if the annealing temperature and atmosphere play a role in the formation of the layer. This could provide an explanation as to why the segregation of the sodium phosphate layer was not observed in an experiment conducted at Harwell (in collaboration with Dr. Shaoliang Guan and Pr. Robert Weatherup) where polished NZSP pellets were annealed *under vacuum* inside a XPS instrument (see Figure C.8 in Appendix C).

Chapter 7

Interfacial degradation by Ca poisoning

In the previous chapter, a method to minimize the $Na^0|NZSP$ interface resistance in the few hours after cell assembly was presented. To ensure that this performance can be maintained over the lifetime of cells, it is essential to study the stability of the $Na^0|NZSP$ interface over longer periods of time. With the exception of section 7.5, in this chapter, the electrochemical stability of the the $Na^0|NZSP$ interface is studied at rest (*i.e.* not under cycling conditions) over aging periods of several days. This study reveals that the Na|NZSP interface can be poisoned by contaminants (and more specifically Ca) contained in Na metal electrodes.

In section 7.1, time resolved EIS shows that the interface is affected by a degradation which eventually prevents efficient Na^+ ion diffusion across the interface. The unexpected presence of Ca at the interface is revealed by XPS in section 7.2. Using time resolved EIS, section 7.3 demonstrates that the poisoning of the interface can be prevented by employing high purity Na metal electrodes. Finally, section 7.5 looks at the behaviour of a poisoned cell in cycling conditions.

7.1 Time resolved EIS analysis of cells during aging

Figure 7.1(a) shows the impedance of a $Na|NZSP_{AS}|Na$ resolved over 17 h with a set of data measured every half-hour (an additional spectrum was acquired after 53 hours). The symmetrical cell was assembled with 99 % pure Na metal electrodes (Alfa Aesar). A semicircle corresponding to interfacial diffusion (apex frequency of 823 Hz) is observed quickly after cell assembly. For the impedance spectrum measured after 53 h of cell assembly, an inward tail is observed at low frequencies (below 65 Hz, in panel (a)). Such distortions of impedance spectra at low frequencies are often observed in cells whose temperature is changing over the course of the measurement.[176] But here, as the temperature is maintained constant by a climate chamber, the inward tail would rather suggest that the mechanism causing the increase in the interface resistance can be partially reversed. This hypothesis will be discussed in more detail in Section 7.5.

The equivalent circuit which was used to fit the impedance data is presented in inset of panel (a). Figure 7.1(b) shows the evolution of the fitting model parameters ($R_{\text{NZSP-bulk}}$, $R_{\text{NZSP-GB}}$, $R_{\text{Na|NZSP}}$, C_{GB} and $C_{\text{Na|NZSP}}$). The parameters relative to the NZSP electrolyte are stable over the course of the experiment. But the normalized interface resistance grows linearly from 0.13(±0.01) Ω cm^2 to 7.7(±0.3) Ω cm^2 in the first 17 hours after cell assembly. After 53 hours of aging, the interface resistance reached 20.4(±0.9) Ω cm^2. This value was obtained by setting the low frequency limit for the fit of the interface semi-circle well before the tail distortion (328 Hz). The errors associated to the resistance values are smaller than the symbols used on the figure (they are hidden by the dots).

Figure 7.1 shows that the interface capacitance reduces by an order of magnitude from $C_{\text{Na|NZSP}}$=2(1)x10^{-4} F to $C_{\text{Na|NZSP}}$=1.34(0.05)x10^{-5} F during the first 5 hours of aging and stabilizes after that. It is unclear if this large drop is due to an electrochemical process or a fitting artefact. In the first hours of aging, the calculated interface capacitances have large error because the interface semi-circle was not well defined which resulted in larger fitting errors.

The time-resolved impedance analysis clearly indicate that a degradation is affecting the Na|NZSP interface. This degradation occurs at rest (*i.e.* under no applied load) and can be noticed within a few hours of cell assembly. The degradation was consistently observed over a large number of assembled cells. To identify what causes the degradation of the interface, XPS is used in the following section to characterize the composition of the interface of aged cells.

7.2 *Ex-situ* XPS characterization of the Na|NZSP interface

In this section, XPS is employed to analyse the chemical composition of the interface of an aged cell. For this, a three steps protocol was followed (see Figure 7.2): (1) the

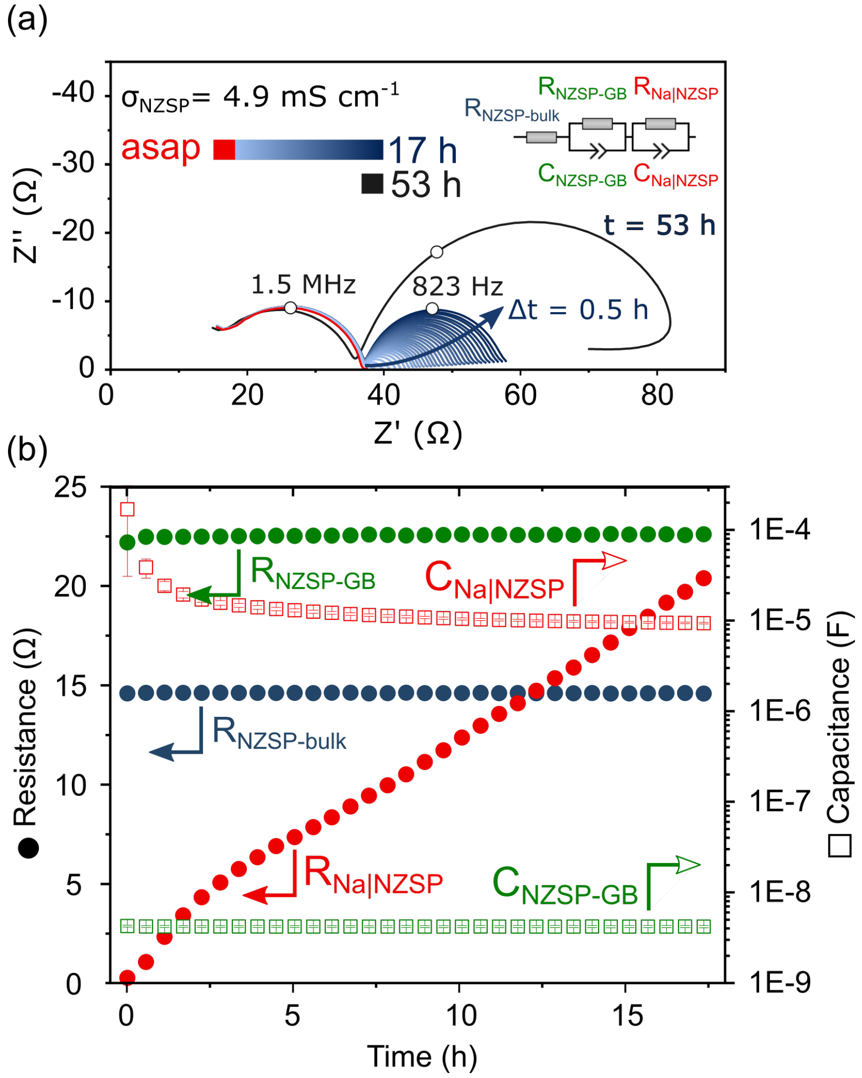

Figure 7.1: Aging of a Na|NZSP$_{\mathbf{AS}}$|Na cell at rest. (a) Time resolved impedance measurements. Only the apex frequencies of the observed semi-circles are indicated to minimize the amount of information on the graph. (b) Parameters extracted from impedance fitting. (pellet thickness : 1.3(±0.1) mm, diameter Na electrodes : 9.8(±0.2) mm)

impedance of a Na|NZSP|Na symmetrical cell was monitored over several days; (2) one of its Na^0 electrode was electrochemically stripped to reveal the buried Na|NZSP interface; (3) the chemical composition of the stripped NZSP surface was analysed by XPS; to the avoid altering the composition of the interface by exposing it to ambient air, the samples were transferred to the XPS instrument via a vacuum suitcase. The degradation of cells assembled with an as-sintered NZSP pellet is presented in section 7.2. The degradation of a cell assembled with a polished NZSP pellet is studied in section 7.2. One of the question which this section tries to answer is whether the degradation is associated to a decomposition of NZSP in contact with Na metal.

XPS analysis of $NZSP_{\text{AS-stripped}}$ surfaces

The symmetrical employed in this section is the same as the one whose aging dynamics was presented in the first section of this chapter (section 7.1). Figure 7.2(c) shows the voltage profile of the symmetrical cell during the stripping of one of its Na^0 electrode. A sharp overpotential appeared after 5 h indicating the coalescence of pores at the $Na^0|NZSP_{AS}$ interface (see Section 9.1). The voltage cutoff limit of 5 V was reached after 6.5 h and corresponded to a stripped Na^0 capacity of 4.87 mAh (corresponding to a Na^0 thickness of 57 µm). The electrode has been stripped from 37 % of its initial capacity (13.05 mAh, which was estimated during cell assembly by measuring the weight of the electrode $m_{Na} = 0.0112$ g, and knowing the capacity of Na metal $q_{Na} = 1165$ mAh g^{-1}). An optical image of the stripped NZSP surface after cell disassembly (taken by a camera inside the XPS instrument, Figure 7.3) shows that, apart from some isolated dark spots, the stripped surface is free from Na metal. The Na metal found on the other side of the pellet (the plated electrode) was partly removed with the blade of a scalpel but a thin layer of Na metal was still present on the bottom side of the pellet when it was loaded via a vacuum transfer vessel inside the XPS chamber.

Figure 7.3 compares XPS signals of a bare $NZSP_{AS}$ surface (in orange) with that of degraded $NZSP_{AS}$ surface (in blue, further referred to as $NZSP_{\text{AS-stripped}}$). The measurements were acquired with the flood gun off because activating the flood gun may have driven Na metal plating from the thin Na metal counter electrode which could not be removed (see chapter 8 for more explanation). To ensure a valid comparison, the XPS signals of the reference sample were also acquired with the flood gun off. The BE scales were corrected to align the $Zr3d_{5/2}$ peaks of the two datasets.

A large C1s signal associated to hydrocarbon species (∼288 eV) and carbonates (∼291.9

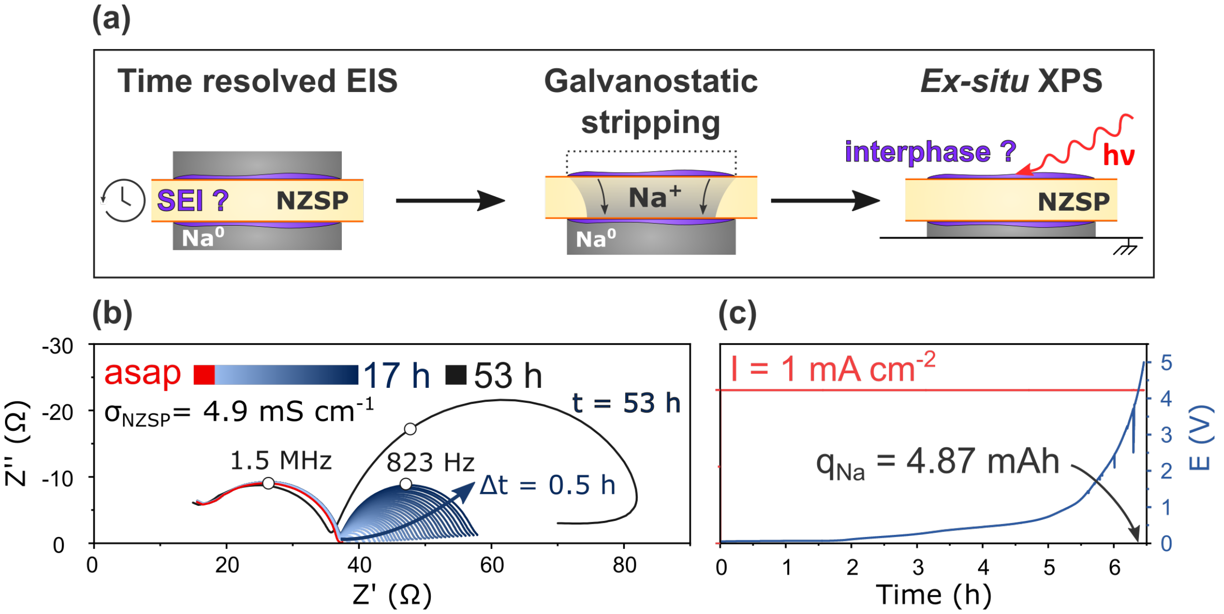

Figure 7.2: (a) Schematic description of the three steps of the experiment. (b) Time resolved impedance measurements of the Na|NZSP$_{\text{AS}}$|Na cell in the 53 hours after cell assembly. (c) Evolution of the Na|NZSP$_{\text{AS}}$|Na cell potential during the electrodissolution of one of the electrode at a current density of 1 mA cm^{-2}.

eV) was observed on the NZSP$_{\text{AS-stripped}}$ surface. Unfortunately, it is not possible to know if these carbon species where present in the cell during aging and segregated to the Na|NZSP interface from an unidentified source (which could explain the increase in the interface resistance), or if the C species were formed *ex-situ* when the surface was exposed to an atmosphere during disassembly (which is more likely, although extra caution was taken to protect the surface during the transfer of the sample from the glovebox to the XPS). The presence of contaminants on the NZSP$_{\text{AS-stripped}}$ prevents a direct comparison of relative peak intensities with NZSP$_{\text{AS}}$. In Figure 7.3, the intensity of each individual core level signal was normalized on a [0-1] scale (min-max normalization). Thus, the C1s signal of the two samples appear to have the same intensity in Figure 7.3 (it will however appear clearly that the concentration of C on the NZSP$_{\text{AS}}$ surface is lower as its C1s signal is much closer to the background noise level). Whilst information about relative intensities is lost with this normalization, chemical shifts can still be detected.

No chemical shifts are observed between the two samples for the Zr3d, Si2p and P2p signals which almost perfectly overlap. The hypothesis that a resistive interphase formed by decomposition of NZSP in contact with Na metal is therefore not supported by these XPS results. The Zr3d signal is fitted in Figure D.1 (Appendix D) and a second bonding

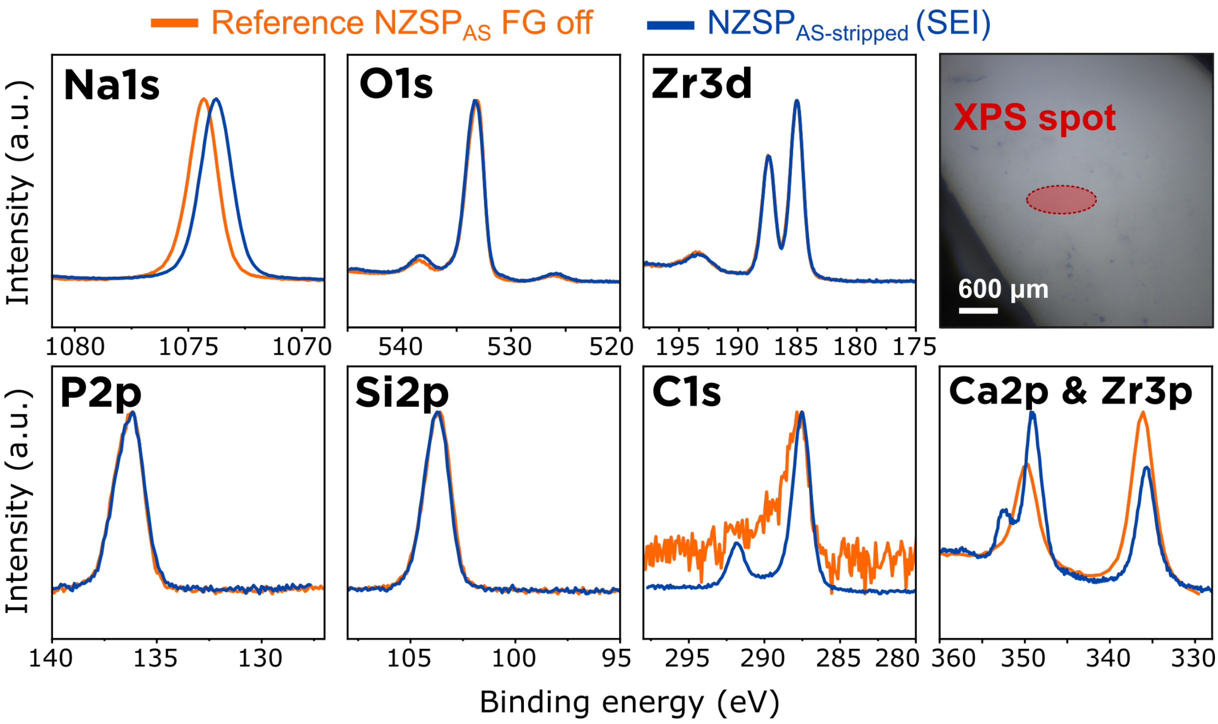

Figure 7.3: *Ex-situ* XPS characterization of the Na|NZSP$_{AS}$ interface post-aging. Core level spectra from a NZSP$_{AS\text{-stripped}}$ sample (in blue) and a reference NZSP$_{AS}$ sample (in orange). The intensity of each individual core level signal was normalized on a [0-1] scale (min-max normalization). A correction was applied to the BE scale to align the Zr3d$_{5/2}$ peaks of the the two samples. For the Zr3p signal of the reference NZSP$_{AS}$ sample, the data from the survey spectrum was taken. The photograph shows the surface of the NZSP$_{AS\text{-stripped}}$ sample.

environment (in addition to NZSP) is present but only in trace amounts. A chemical shift to lower binding energies is observed for the Na1s signal. Possible reasons which could explain this shift are still investigated (*N.B.*: the shift is not observed when the NZSP is polished, see Figure 7.6).

More surprisingly, photoelectrons corresponding to Ca were detected in the surveys collected on the NZSP$_{AS\text{-stripped}}$ surface. The Ca2p doublet is observed around 350 eV region in Figure 7.3. The Ca2p signal overlaps with the signal from Zr3p photoelectrons which can also be observed in the XPS data of NZSP$_{AS}$ (the Zr3p doublet has a large spin orbit splitting of 13.7 eV whereas the Ca2p has a 3.5 eV one). Figure 7.4 presents a fitting model of the 325-260 eV region with a separation of the Zr3p and Ca2p contributions. Future studies will have to identify the composition of the Ca containing species at the interface.

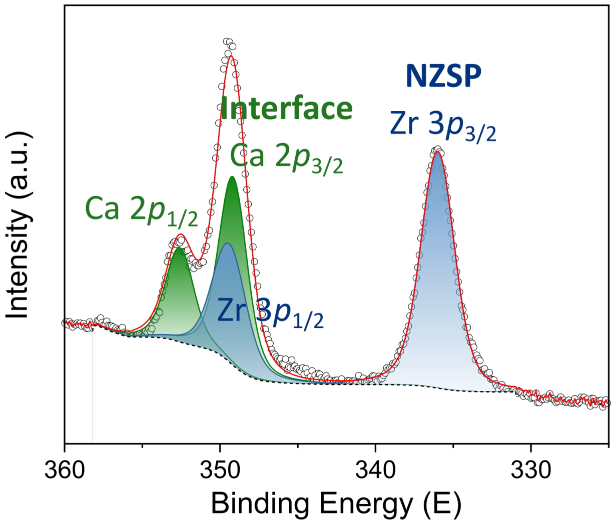

Figure 7.4: Fitting model of the Ca2p and Zr3p region of $\text{NZSP}_{\text{AS-stripped}}$

So far, the XPS analysis of the $\text{NZSP}_{\text{AS-stripped}}$ surface presented in this section indicates that NZSP did not decompose in contact with Na metal during the aging of the cell. Several options could explain the increase in the Na|NZSP interface resistance observed in Figure 7.1: (1) the decomposition layer (resistive interphase) detached from the NZSP surface and remained attached to the current collector during disassembly; (2) a poisoning layer formed of Ca containing species forms at the Na|NZSP interface during aging; (3) or, a blocking layer composed of C species forms during aging. Hypotheses (1) and (2) are investigated in the following sections of this chapter. Hypothesis (3) is harder to test without an *in-situ* experiment. Besides, it is likely that the C species observed on the $\text{NZSP}_{\text{AS-stripped}}$ surface formed during the disassembly of the cell.

XPS analysis of the current collector

Following the galvanostatic stripping step and the disassembly of the coin cell inside a glovebox, the stainless steel current collector was easily separated from the NZSP pellet. Figure 7.5(a) is a photograph taken just after cell disassembly (inside a glovebox) which shows that some Na metal is still attached to the current collector. In this section, the surface composition of the Na metal stuck on the current collector is analysed by XPS.

The two digital images included in Figure 7.5(b) were taken by the camera located inside the XPS chamber. The surface appears to consist of two regions which were both analysed: some tarnished areas (Point 1) and some shiny areas (Point 2). The current

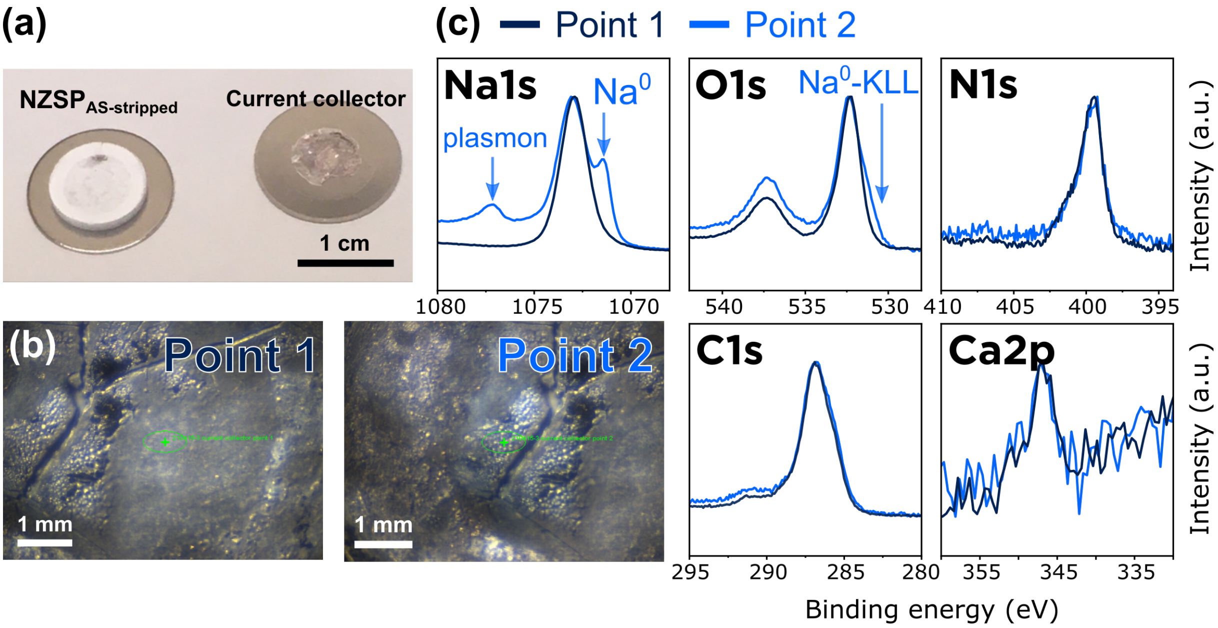

Figure 7.5: Chemical composition of the Na metal electrode. (a) Photograph of the symmetrical cell after disassembly showing that some Na metal is still attached on the current collector; (b) Digital images locating the two area of analysis; (c) XPS signals of selected core levels from Points 1 and 2. A correction was applied to the BE scale to align the Na1s oxide peaks of the the two samples. The intensity of each core level signal was normalized on a [0-1] scale (min-max normalization).

collector surface was initially analysed to look for possible decomposition products from the Na^0|NZSP interface. However, no signals corresponding to Si, P, or Zr could be found in the survey spectrum (see Figure D.2 in Appendix D). Instead, only Na, O, N, C, and a small fraction of Ca could be detected on the surface. Narrow-region spectra were acquired for all these elements and are presented in Figure 7.5(c).

The tarnished and shiny regions on the current collector surface have slightly distinct chemical composition. The Na1s signal of the tarnished region (Point 1) has a main peak corresponding to Na oxides (1072.9 eV) and a tail at low BE from metallic Na. The Na1s signal of the shiny region (Point 2) features a distinctive Na^0 peak (at 1071.4 eV) and a plasmon peak (at 5.9 eV higher binding energy). The O1s signal of Point 2 has a shoulder around 530.7 eV (corresponding to a Na^0-KLL transition) which is not observed for Point 1. Overall, the analysis suggests that some regions of the Na metal have formed a thicker passivation layer than others. It is unclear if the layer formed during the aging of the cell or after its disassembly. The presence of N on the surface is so far unexplained.

The aim of this section was to test the validity of hypothesis (1) established at the end of the previous section: new phases resulting from the decomposition of NZSP in contact with Na^0 could not be found on the surface of the electrode. The validity of hypothesis (2) will be tested in Section 7.3. Before that, the next section investigates whether polished NZSP surfaces react similarly to as sintered ones in contact with Na metal.

XPS analysis of $NZSP_{polished}$ surfaces

The three steps protocol described in Sections 7.2 was repeated with a polished $NZSP_{4000EtOH}$ pellet. The results are described here more succinctly than in Section 7.2 because they share a lot of similarities. The time-resolved impedance of the cell presented in Figure 7.6(a) shows that a similar degradation affects the Na|NZSP interface resistance: from 17.6 Ω cm^2 immediately after cell assembly, the interface resistance increased to 26.3 Ω cm^2 in the first 22 hours of aging. The impedance of the cell was also measured 100 hours after cell assembly ($R_{Na|NZSP}$ = 55 Ω cm^2). Figure 7.6(b) shows the evolution of the cell potential as one of its electrode is galvanostatically stripped at a current density of 1 mA cm^{-2}. From the 10.49 mAh initial capacity of the electrode, 4.59 mAh (43.8 %) could be stripped from it before the 5 V voltage cutoff was reached.

In Figure 7.6(c), the $NZSP_{polished-stripped}$ XPS data is compared with a reference dataset ($NZSP_{polished}$). As in Section 7.2, the ex-situ XPS data presented in Figure 7.6(c) does not indicate that NZSP decomposed in contact with Na^0. A contamination at the surface by adventitious C species is again observed. An intense Ca signal is also observed on the surface.

Overall, the experiment indicates that the $NZSP_{polished}$ surface behaves similarly to the $NZSP_{AS}$ surface. This suggest that, under the experimental conditions employed in this study, NZSP does not react in contact with Na^0. The unexpected presence of a large Ca signal is a common denominator in both Sections 7.2 and 7.2. In the following section, Na metal electrodes with higher purity are employed to test if the Ca impurities are responsible for the increase in the interface resistance.

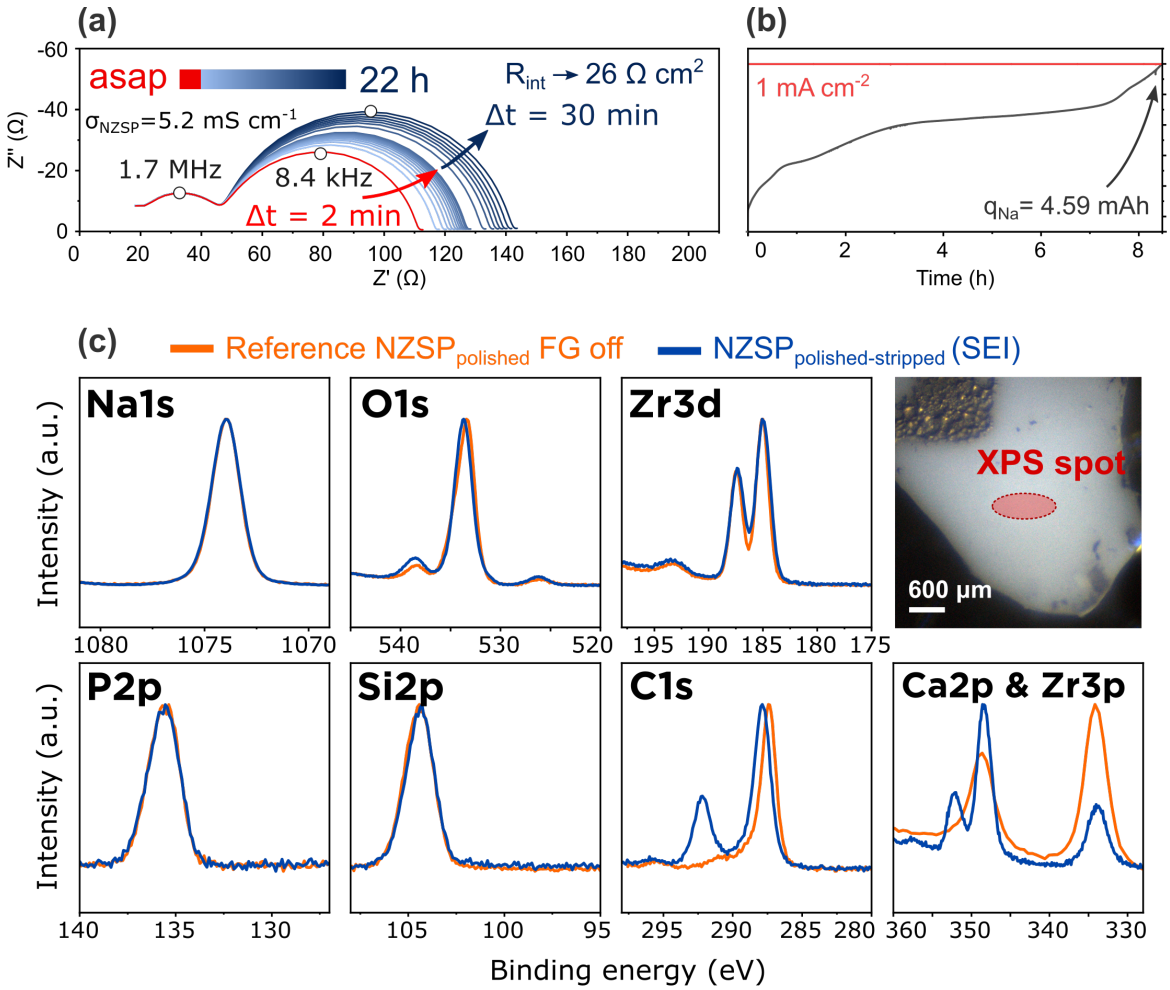

Figure 7.6: Aging dynamics of Na|NZSP$_{\text{polished}}$ interfaces. (a) Time resolved Nyquist plots of the symmetrical Na|NZSP$_{\text{polished}}$|Na cell. Only the apex frequencies of the observed semi-circles are indicated to minimize the amount of information on the graph (pellet thickness : 1.31 mm, diameter Na electrodes : 8.3 mm). (b) Evolution of the cell potential during the electrodissolution of one of the electrode at a current density of 1 mA cm^{-2} (mass of the stripped anode m_{Na}= 0.009 g, corresponding capacity $q_{Na\text{-}tot}$ = 10.49 mAh, capacity extracted q_{Na} = 4.59 mAh). (c) Selected core level spectra from NZSP$_{\text{polished-stripped}}$ (in blue) compared with the signals of a reference NZSP$_{\text{polished}}$ sample (in orange). The intensity of each core level signal was individually normalized on a [0-1] scale. Binding energy scale shift: alignment of the Zr3d$_{5/2}$ signals.

7.3 Impact of Na metal purity on the interface degradation

The impurities with highest concentrations in Na metal rods/cubes are Calcium and Potassium (see Table D.1 in Appendix D). Because it was only discovered in the later stages of this PhD that impurities in Na metal electrodes could affect the Na|NZSP interface, the majority of the cells assembled during this thesis employed Na metal electrodes produced from a 99 % pure Na metal rod (Alfa Aeasar). In this section, the impact of the purity of the Na metal precursor on the aging of the Na^0|NZSP interface is investigated. For this, the time-resolved impedance data of 5 cells assembled with high purity Na metal electrodes (Sigma Aldrich, Na metal cubes, 99.9%) is compared with 6 cells assembled with lower purity Na metal electrodes (Alfa Aesar, Na metal rod, 99%) in Figure 7.7. The impedance of each cell was typically measured every hour for 24 hours (sometimes for longer) and additional measurements were acquired after a few days of aging.

Among the cells assembled with the 99 % pure Na metal (in red), none seem to have the exact same aging behaviour: although all cells eventually experience a large increase in interface resistance, the onset of the increase and the growth rate of $R_{Na|NZSP}$ is sample

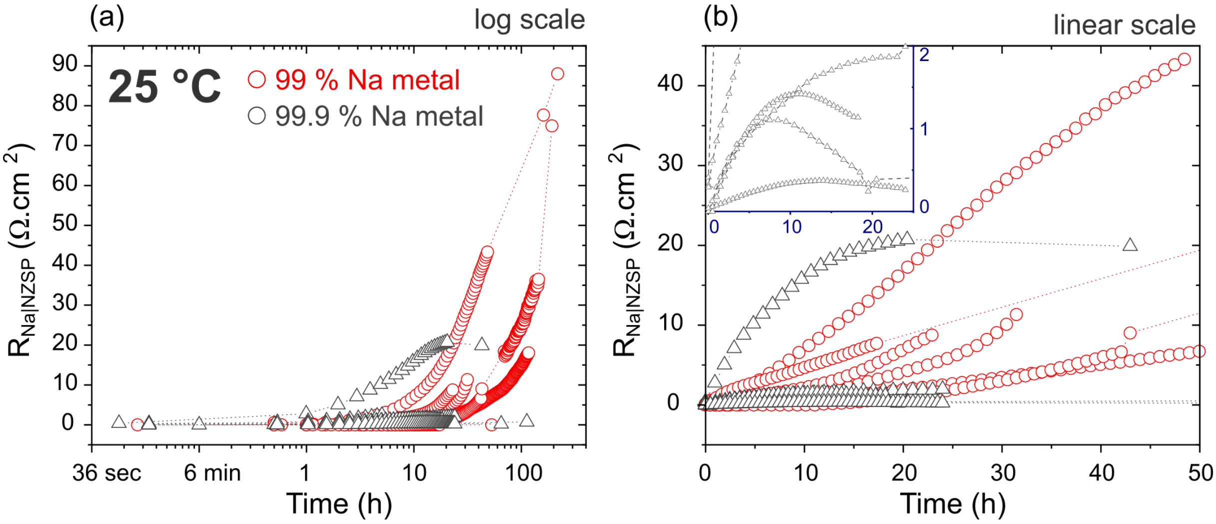

Figure 7.7: Impact of Na metal purity on the degradation of Na|NZSP interfaces. (a) Evolution of the interface resistance of cells employing 99 % pure (in red) and 99.9 % pure (in grey) Na^0 electrodes. Aging time represented in log scale. (b) The same data but with the aging time represented in linear scale. A zoomed-in view of the 0 to 2 Ω cm^2 region is included in inset.

dependent. For some samples, the onset of interface degradation is immediate, whilst for others, it is only 10 hours after cell assembly that an interface degradation starts to be noticed. Once initiated, the interface degradation is continuous and does not reach an asymptote within the studied aging period of the cells.

In contrast, the five cells assembled with the 99.9 % pure Na metal electrodes (in grey) show greater stability and do not experience a continuous degradation of their interface. For four of these cells, the interface resistance never exceeds 2 Ω cm^2 over their aging period. The fifth cell has an interface resistance which grows more significantly (up to 20.7 Ω cm^2). But even for this singular cell, its interface resistance reaches an asymptote after around 15 hours of aging unlike the cells assembled with the lower purity Na metal. It is not clear why the interface resistance of two of the 99.9 % cells initially increases and then drops after 8 hours of cell aging (the evolution of their interface resistance is clearly observed in the inset of Figure 7.7(b)).

This study demonstrates that the purity of the Na^0 electrodes influences the mode of degradation of the Na^0|NZSP interface:

- When high purity Na^0 electrodes are used (99.9 %), the increase in $R_{Na|NZSP}$ is limited and could be assigned to the formation of a self-limiting SEI
- When Na^0 electrodes with a higher concentration of impurities are used, the Na^0|NZSP interface resistance grows linearly during the ($\sim$100 h) period of analysis

The existence of two outlier samples is also acknowledged in Figures D.3 and D.4 in Appendix D. The first of these outlier samples is a symmetrical cell assembled with 99 % Na metal electrodes and whose interface resistance only grew up to 5 Ω cm^2 after 4 months of cell assembly. The second of these outlier samples is a cell assembled with 99.9 % Na metal electrodes and whose interface resistance increased by 44.5 Ω cm^2 within 24 hours of cell assembly. The degradation which affected this cell was not studied in further detail.

7.4 Mechanism of interface poisoning

The results of the previous sections established that the Na|NZSP interface is affected by the presence of contaminants (especially Ca) in the Na metal electrodes. In this section, the mechanism by which the interface gets poisoned is sought. In a first part, the Gibbs free energies of several reactions involving Ca and species expected to be found at the NZSP surface are calculated. The second part of the section suggests hypotheses regarding the kinetics of interface poisoning.

Thermodynamics

To find the driving force for interface poisoning, reaction energies between Ca and $Na_3Zr_2Si_2PO_{12}$, Na_3PO_4, Na_2ZrO_3, Na_2O, NaOH, Na_2CO_3 were calculated using energetics from the Materials Project.[164] These species were selected because:

- $Na_{3.4}Zr_2Si_{2.4}P_{0.6}O_{12}$ is not included on the Materials Project database and $Na_3Zr_2Si_2PO_{12}$ is the closest composition available
- a sodium phosphate surface termination of thermally activated NZSP pellets was identified in Chapter 6; Na_3PO_4 models this sodium phosphate phase
- Na_2O, NaOH, and Na_2CO_3 are surface contaminants which could be present on NZSP surfaces

The predicted reactions and their energies are indicated below (ranked from highest to lowest reaction energies):

$$0.75\ Ca + 0.25\ Na_2CO_3 \rightarrow 0.5\ Na + 0.75\ CaO + 0.25\ C\ (-0.818\ eV/atom)$$

$$0.069\ Na_3Zr_2Si_2PO_{12} + 0.931\ Ca \rightarrow 0.034\ Ca_4P_2O + 0.793\ CaO + 0.138\ ZrSi + 0.207\ Na\ (-0.682\ eV/atom)$$

$$0.154\ Na_3PO_4 + 0.846\ Ca \rightarrow 0.077\ Ca_4P_2O + 0.538\ CaO + 0.462\ Na\ (-0.677\ eV/atom)$$

$$0.6\ Ca + 0.4\ NaOH \rightarrow 0.2\ CaH_2 + 0.4\ Na + 0.4\ CaO\ (-0.659\ eV/atom)$$

$$0.5\ Na_2O + 0.5\ Ca \rightarrow Na + 0.5\ CaO\ (-0.574\ eV/atom)$$

The predicted reaction energies are all negative and provide an explanation as to why Ca would react at the interface. In other words, Ca can be considered as an "Oxygen getter" and will react with all the candidate species which could be present at the interface. Ca

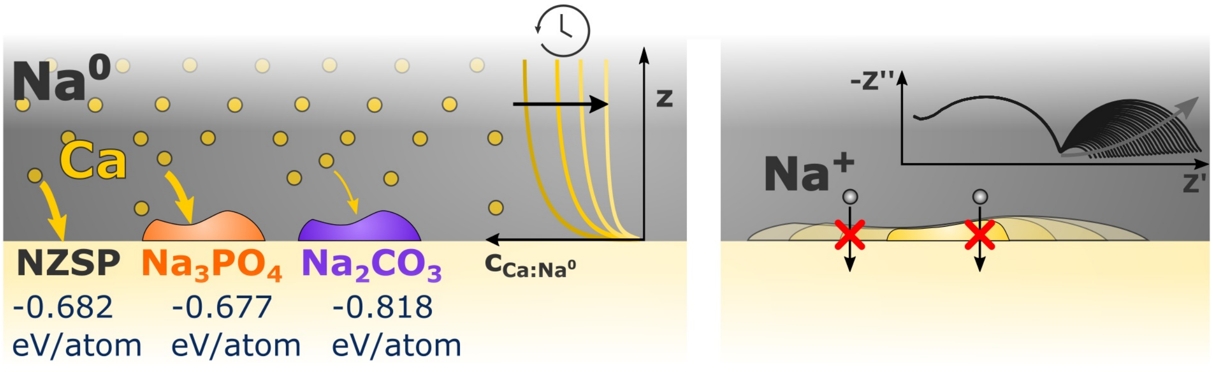

Figure 7.8: Schematic representation of the poisoning of the Na^0|NZSP interface by Ca impurities. The reaction energies of three possible interface reactions are indicated.

atoms close enough to the interface have high chances of reacting to form the predicted species.

Kinetics

This section suggests some hypotheses to explain the linear increase in the interface resistance with aging time in cells employing low purity Na metal. Experiments or models allowing to confirm these hypotheses will be required in future studies.

The poisoning of the interface likely initiates with Ca atoms located near the interface just after cell assembly. Once these Ca atoms are consumed, a gradient in the concentration of Ca atoms in the Na metal electrodes is created. It is speculated that this concentration gradient creates a flux of Ca towards the interface (Fick's first law of diffusion) which perpetuates the poisoning reaction. In other words, the interface can be considered as a Ca sink with a boundary condition: $\forall t > 0, c_{\mathrm{Ca}}(z = 0, t) = 0$ (see Figure 7.8).

Another question is whether 1 % Ca contamination is enough to fully block an interface and prevent Na^+ ion diffusion. A quick calculation whose details are summarized in Appendix D reveals that if all the Ca atoms contained in a 99 % pure electrode of a typical capacity of 13 mAh react to form a monolayer of CaO at the interface, it will be possible to cover an area of 971 cm^2 which is three orders of magnitude larger than the typical area of electrodes used in this work (around 0.5 cm^2). Thus, a 1 % contamination could completely poison the interface if all the Ca contained in the Na metal concentrated at it. The poison phases forming at the interface are unlikely to be good Na^+ conductors which would explain why an increase in the interface resistance is observed during cell aging.

7.5 Cycling behaviour of poisoned interfaces

In this last section of the chapter, a closer look is taken at the inward tail which was observed in the Nyquist plots of aged symmetrical cells employing 99 % pure Na metal electrodes (section 7.1). This study comes in the last section of this chapter as the hypotheses developed here require prior knowledge that the Na|NZSP interface can be poisoned by impurities.

The inward tail in the Nyquist plots suggests that, at low frequencies, the interface resistance of poisoned cells can be reduced. The hypothesis which is investigated in this section is that the interface resistance can be reduced if fresh Na metal is replenished at the interface. This replenishment of Na metal at the interface at low AC frequencies could possibly explain the inward tail observed at low AC frequencies: for an excitation voltage of 50 mV[1] and a cell with a total resistance of 100 Ω, a maximum current of around 0.5 mA can be expected across the cell at low frequencies; at a 5 Hz frequency, this corresponds to a maximum plated capacity of 1.39 10^{-5} mAh per “half-cycle”[2]; considering that this Na metal plates evenly across the entire Na|NZSP interface, this corresponds to a thickness of plated Na^0 of 2.27 Å, *i.e.* a replenishment of around one monolayer of Na metal per "half-cycle" (for an electrode diameter of 8.3 mm).

The experiment described in this section seeks to validate the idea that the resistance of a poisoned interface can be reduced by plating fresh Na^0 at the interface (see Figure 7.9). To test this hypothesis, a two steps experiment was designed: (1) a Na|$NZSP_{AS}$|Na symmetrical cell was assembled, and its impedance was monitored over 312 hours during which an increase of its interface resistance was observed; (2) the cell was then galvanostatically cycled ten times at a current density of 0.5 mA cm^{-2} with impedance measurements at the end of each half-cycle (5 minutes). The plating of fresh Na^0 at the interface during step (2) should result in a drop of the interface resistance according to our initial hypothesis.

The Nyquist plots corresponding to the initial aging (step 1) and the cell voltage during the galvanostatic cycles (step 2) are presented in Figures 7.10(a) and (b) respectively. The aging behaviour of the cell and growth of an interface semi-circle follows the same trend as

---

[1] the amplitude of the excitation voltage could have been minimized to see if the effect could be minimized

[2] here, the sinusoidal excitation signal is simplified to a square one

Figure 7.9: Schematic description of the experiment and hypothesis tested

previously described in Figure 7.1. The evolution of the electrochemical parameters of the cell, calculated by equivalent circuit modelling, can be found in Figures 7.10(c) (for the parameters relative to the interface) and (d) (for the parameters relative to NZSP). The electrochemical parameters relative to the NZSP electrolyte (*i.e.* $R_{\text{NZSP-bulk}}$, $R_{\text{NZSP-GB}}$ and $C_{\text{NZSP-GB}}$) remain stable during the initial aging of the cell. The semi-circle corresponding to interfacial diffusion could not be separated from the grain boundary semi-circle in the first 10 hours after cell assembly (*i.e.* $R_{\text{Na|NZSP}}$ approaches 0 Ω cm^2). After 10 hours of cell assembly, the interface semi-circle can be distinguished. The interface resistance continues to grow over the 312 hours of initial cell aging and the same inward tail can clearly be observed in the last datasets in Figure 7.10(a). After 312 hours of cell assembly, $R_{\text{Na|NZSP}}$ is approximated to around 16.3(±0.8) Ω cm^2.

After this initial aging, the symmetrical cell is galvanostatically cycled at a current density of ± 0.5 mA cm^{-2} for periods of 5 minutes. At the end of each half-cycle, the electrochemical impedance of the cell is measured. During each half-cycle, Na^0 is stripped/plated from one electrode and plated/stripped on the counter electrode. Considering the cell is symmetric, one could legitimately expect the voltage response of the cell during the positive and negative current half-cycles to also be symmetric. Figure 7.10(b) shows that the voltage response of the cell is in fact asymmetric: during the negative current half-cycles, a small drop in the cell potential is measured in the first 30 seconds of each cycle (from -22 mV to -20 mV for the first cycle for instance) before the cell potential reaches a plateau at around -20 mV; in contrast, during the positive current half-cycles, the cell potential initially starts from around 20 mV but it increases rapidly to 40 mV (or even higher in the last cycles). The origin of the overpotential observed on the positive current half-cycle cannot be inferred just from this DC measurement. But EIS can be used to identify the electrochemical process responsible for this overpotential. The analysis of the impedance spectra collected at the end of each galvanostatic half-cycle leads to three conclusions:

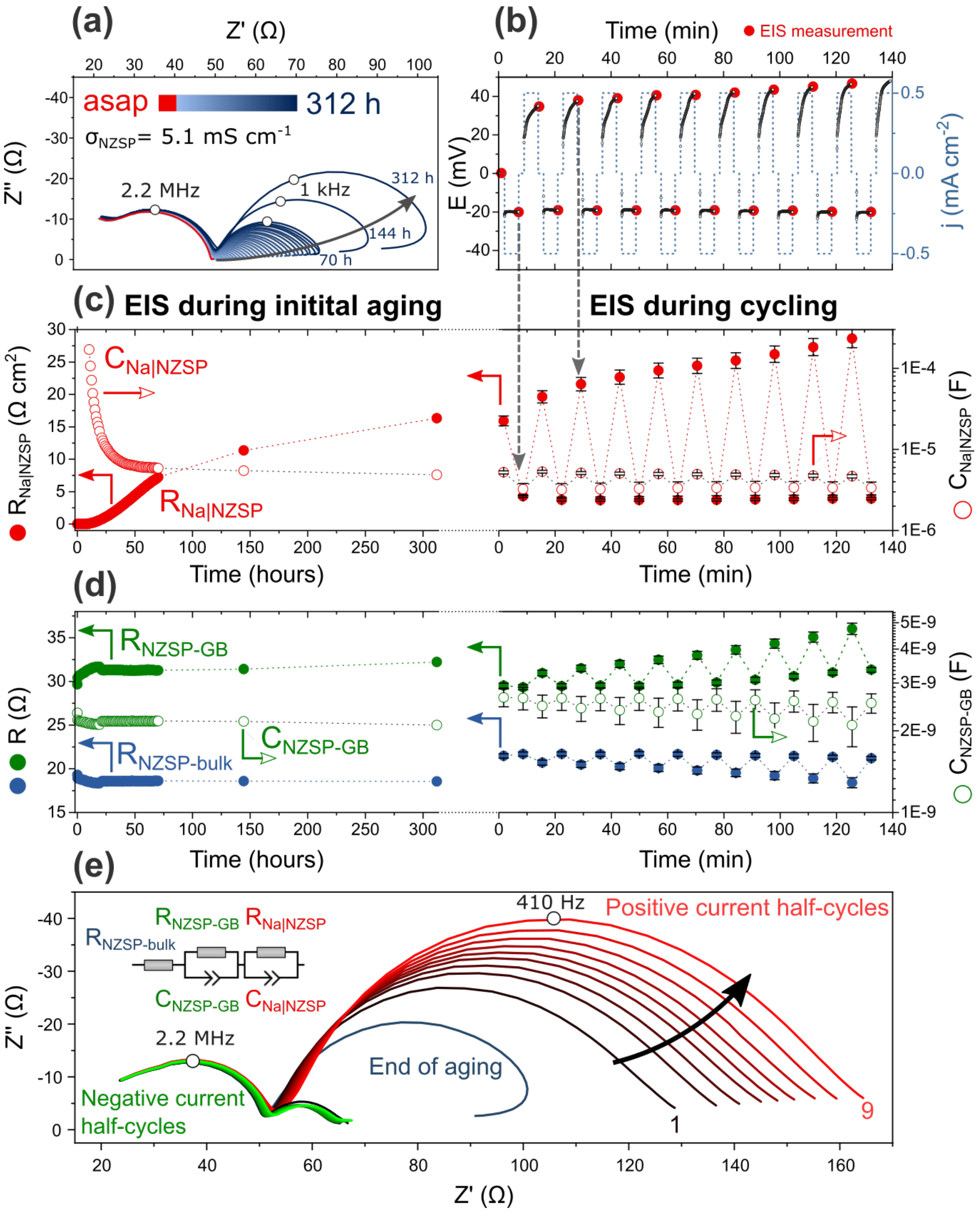

Figure 7.10: Cycling behaviour of poisoned interfaces. (a) Nyquist plots of the symmetrical cell during the initial 312 h of aging at rest (no cycling). (b) Evolution of the cell potential during the galvanostatic cycling of the cell (post-aging). The red dots indicate when the cell impedance was measured. (c) Evolution of the Na|NZSP interface resistance and capacitance over the full lifetime of the cell: during its aging period at rest (on the left) and during cycling (on the right). (d) Evolution of the NZSP ceramic electrochemical parameters over the full lifetime of the cell: during the aging period (left) and during cycling (right) (e) Nyquist plots of the cell during cycling. Pellet thickness: 1.4(±0.1) mm, electrodes diameter: 8.3(±0.2) mm.

- it is possible to minimize the Na^0|NZSP interface resistance of an aged cell by cycling it: in Figure 7.10(c), $R_{Na|NZSP}$ is lowered from 16.3(±0.8) Ω cm^2 to 4.0(±0.2) Ω cm^2 after the first galvanostatic half-cycle. When measured after a negative current half-cycle, $R_{Na|NZSP}$ is always below 4 Ω cm^2.
- the large overpotentials measured during the positive current half-cycles is caused by an increase in the interface resistance. In fact, the interface becomes even more resistive than after the aging step: over the course of the 10 cycles, $R_{Na|NZSP}$ increases from 16.3(±0.8) Ω cm^2 to 29(±1) Ω cm^2 during the positive current half-cycles. The rapid increase in overpotential at the beginning of each positive half-cycle resembles the phenomenon of "occluded" pores described by Kasemchainan *et al.*[103]: during the first half-cycle, among the two interfaces, the "plating" one should form a thin layer of fresh Na^0 which pushes the poisoning Ca species away from the interface into the bulk Na metal; on the next half-cycle, as soon as this thin layer of Na^0 is stripped, the Ca species are brought back in contact with the interface, resulting in an overpotential increase.

Some fluctuations of the bulk and grain boundary electrochemical parameters of NZSP ($R_{\text{NZSP-bulk}}$, $R_{\text{NZSP-GB}}$ and $C_{\text{NZSP-GB}}$) are also observed during the galvanostatic cycling step (right panel of Figure 7.10(d)). These fluctuations are small and cannot be clearly detected in the Nyquist plots in Figure 7.10(e). The fluctuations of the grain boundary capacitance are not significant (they stay within the error bars of the measurement). The variations of the bulk and GB resistances are more significant which suggests that they are not only a fitting artefact. The behaviour is so far unexplained and will require further analysis.

Overall, the experiment shows that the poisoning of the Na^0|NZSP interface is a partially reversible process: the interface resistance can be reduced by plating fresh Na metal at the interface during cycling.

7.6 Summary

This chapter described the steps which led to the unexpected discovery that impurities contained in Na metal electrodes can poison the Na|NZSP interface.

In section 7.1, the electrochemical response of cells undergoing a poisoning of their interfaces was monitored by time-resolved EIS. The presence of Ca at the interface was indicated by an *ex-situ* XPS analysis in section 7.2. Apart from the Ca signal, no new phases which could have suggested that NZSP decomposed in contact with Na metal could be found at the interface. This experiment therefore suggests that NZSP might be kinetically stable against Na metal. The detection of Ca at the interface was studied in more details in the following sections and it was established in section 7.3 that cells employing higher purity Na metal electrodes were more stable.

The implications of this discovery are important for industrial prospects. The reaction energies of Ca with Na-β/β"-alumina or with closo-borate electrolytes (such as $Na_2B_{10}H_{10}$) are also high and indicate that these interfaces will suffer equally from Ca poisoning than the Na|NaSICON one. Two options are available for the manufacturing of Na^0-ASSBs: either to employ high purity Na metal foils during cell assembly; or to implement "anode-free" cell architectures (since the metal anode is then 100 % pure as it is plated during the first charge cycle).

The discovery that contaminants can poison the Na|NZSP interface occured in the later stages of this PhD work. As this thesis is not written in a chronological order, in the following chapters, experiments which were conducted prior to this discovery (*i.e.* with cells employing 99 % pure Na metal electrodes) have also been included. The purity of Na metal electrodes used to make cells will be indicated clearly at the beginning of each chapter.

Chapter 8

Electrochemical stability of NZSP against pure Na metal

An important conclusion of the previous chapter is that employing high purity Na metal electrodes can prevent a fast degradation of the Na|NZSP interface. Yet, even when high purity electrodes are employed, the interface resistance of symmetrical cells increases slightly in the first hours after cell assembly before reaching plateau (see Figure 7.7). This electrochemical behaviour could be the sign that a SEI type interphase forms at the Na|NZSP interface (see section 3.2). The aim of this chapter is therefore to determine if NZSP decomposes in contact with pure Na metal to form a SEI. At several occasions in the previous chapter, it was mentioned that exposing the interface which needs to be analysed to an atmosphere during the disassembly of a cell can lead to multiple interpretations of the XPS data. Thus, in this chapter, the stability of NZSP in contact with pure Na metal is studied without exposing the interface to an atmosphere. To achieve this, a protocol which allows Na metal to be plated on the surface of a NZSP pellet whilst analysing the composition of the interface by XPS *operando* was employed.

Section 8.1 describes the *operando* XPS protocol employed to evaluate the stability of the Na|NZSP interface. In section 8.2, the model developed to fit the XPS spectra of a pristine Na^0 foil are discussed. The fitting models established for the Na|NZSP interface are presented in section 8.3. The chapter is concluded by a discussion where the conclusions of the *ex-situ* XPS characterization of the interface (Chapter 7) are compared with the conclusions of the *operando* XPS characterization (this chapter).

8.1 Plating Na^0 on NZSP using the XPS flood gun

The plating of a thin layer of Na^0 on the NZSP surface inside the XPS chamber is achieved by diverting the XPS charge compensating flood gun from its traditional use and using it as a "virtual electrode" (see Figure 8.1(a)).[96] The source of Na for this thin plated layer comes from a Na^0 counter electrode (99 % pure) pressed against the other side of the NZSP pellet. Even if the counter electrode is not 100 % pure, the Na^0 plated on the surface analysed by XPS will be free of any impurities because such impurities will have been blocked by the NZSP separator. Thus, the experiment allows to study the stability of NZSP in contact with pure Na metal. The plating reaction occurring inside the XPS chamber is similar to the plating reaction occurring at the negative electrode during charge:

$$v_{Na}(int) + Na^+(NZSP) + e'(FG) \rightarrow Na^0(int) + v_{Na^+}(NZSP) \tag{8.1}$$

with $v_{Na}(int)$ a vacant site which can be occupied by a Na^0 atom at the interface, $Na^+(NZSP)$ a Na^+ ion in a Na site of NZSP, e'(FG) an electron provided by the FG, $Na^0(int)$ a Na^0 atom plated at the interface, and $v_{Na^+}(NZSP)$ a vacancy in a Na site of NZSP close to the interface.

Figure 8.1(b) demonstrates that the FG can efficiently be used to drive Na^0 plating on an as-sintered $NZSP_{AS}$ pellet. The Na^0 plating rate was controlled by optimizing the FG parameters: the output voltage was set to 3 V, and the current was set to 30 µA (yielding an actual measured electronic current of 4.8 µA from a Faraday cup). The adequate FG current was found empirically by testing different currents; it should be high enough for the plating reaction to occur (X-rays generate holes and shift the equilibrium of the reaction 8.1). The base pressure of the instrument (FG off) is typically around $5x10^{-9}$ mbar and raises to around $1x10^{-7}$ mbar when the FG is activated. The change in pressure is related to the introduction of a residual volume of Ar gas in the analysis chamber associated with the design of the dual mode flood source (see section 4.4 for details). To minimize the Ar^+ ion current from the flood source, the extractor voltage of the instrument was reduced to 30 V following the advice of a previous study.[141]

The analysis sequence starts with the FG initially turned off. A first set of survey and core level spectra is measured and constitutes a reference for the bare NZSP surface prior to any plating (data in red in Figure 8.1(b)). The FG is then turned on and core level spectra are measured in an iterative loop with each acquisition cycle (*i.e.* one set of Na1s,

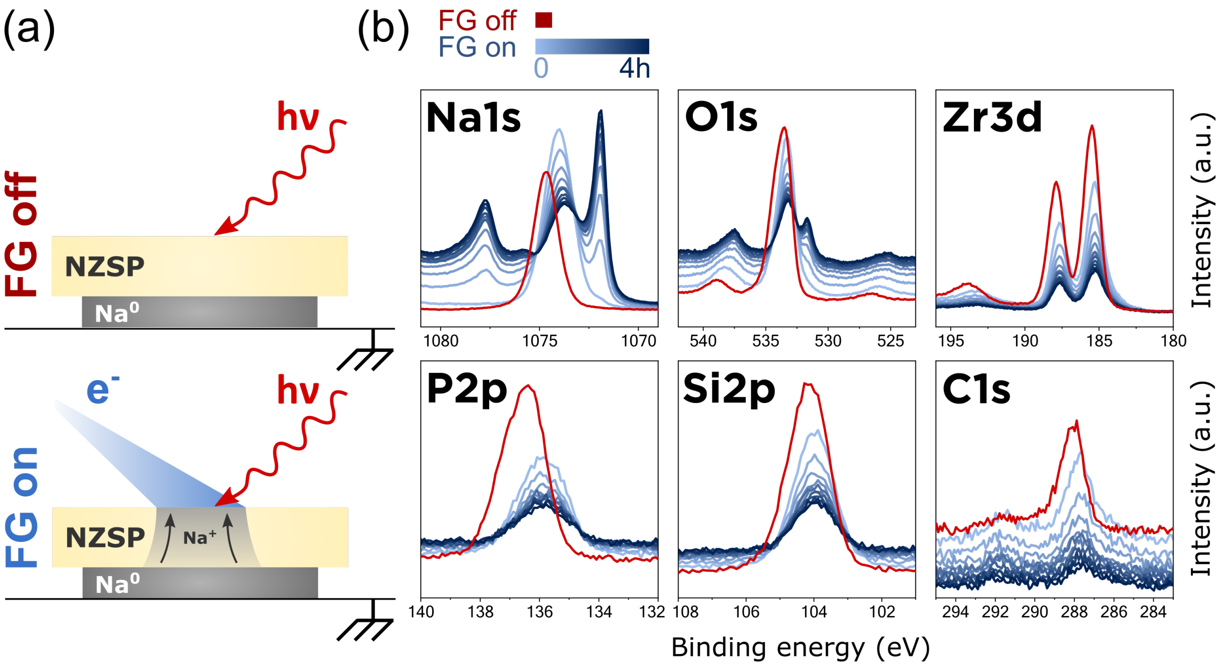

Figure 8.1: Demonstration of the working principle of the *operando* plating of Na^0 inside the XPS (a) Schematic representation of the two XPS analysis configurations: when the FG is off, the chemical composition of the bare NZSP surface is analyzed; when the FG is on, Na^0 can plate on the top surface of NZSP and the changes in chemical composition are monitored *in-operando*; (b) Evolution of selected core level regions with increasing Na^0 plating time. An initial set of data (in red) was measured with the FG off (reference signal from NZSP$_{\mathrm{AS}}$).

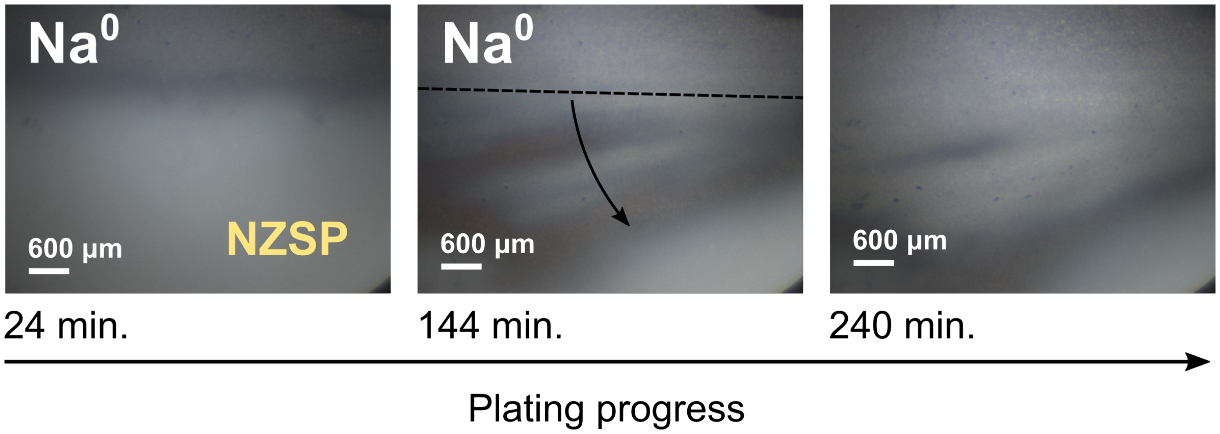

Figure 8.2: Optical photos (top view, XPS camera) of the XPS analysis area whilst Na^0 is plating on the surface of the NZSP pellet.

Zr3d, P2p, Si2p, O1s and C1s measurement) lasting 24 minutes. A compromise between the speed of acquisition and the quality of the data had to be determined: short iterations are required because the continuous plating of Na^0 leads to a rapid attenuation of the interface signals; but iterations should be long enough to detect chemical shifts in low intensity signals. The successive sets of XPS spectra are presented in Figure 8.1(b) in shades of blue, from light blue for the first cycle (0 h of plating) to dark blue for the last cycle (around 4 h of plating).

A qualitative description of the XPS data reveals that:

1. Na^0 is successfully plated on the surface of NZSP using the FG; this is indicated by the growth of an intense XPS peak at 1071.8 eV in the Na1s region (whose attribution to Na^0 will be detailed later) and by optical micrographs taken from the instrument camera which show a progressing Na^0 front (see Figure 8.2)

2. several new peaks appear in the Na1s and O1s core level regions as plating progresses

3. the intensity of the Zr3d/P2p/Si2p/C1s signals decreases as plating progresses which confirms that an overlayer is growing on top of NZSP

4. a change in the shape of the Zr3d signal with a tail to lower binding energies in comparison to the reference sample is observed as plating progresses

5. the rate at which the Na metal peak grows is rapid in the first iterations and slows down subsequently

6. all core level spectra experience a shift to lower binding energy between the flood gun off and flood gun on condition

7. a continuous shift to lower BE of the peak referenced as Na NZSP and Na Auger is observed in the Na1s and O1s core level regions

These observations are discussed in the following sections. **Points 1 and 2** will be discussed in Section 8.2: a pristine Na^0 foil is analyzed as a reference to identify which spectral features in the Na1s and O1s regions can be attributed to Na metal. **Points 1 to 4** are discussed in Section 8.3 with the establishment of a fitting model for the XPS data. **Points 5 to 7** are discussed in Section 8.4 and will also constitute an area for future work.

The same experiment was also conducted with a polished NZSP pellet instead of an as-sintered one (see Figure E.1 in Appendix E). The same qualitative observations can be made about the data. In Section 8.3, the fitting models for the $Na^0|NZSP_{AS}$ and $Na^0|NZSP_{polished}$ interfaces will be compared.

8.2 XPS signature of Na^0

Na metal preparation

To isolate the contribution of photoelectrons produced by the Na^0 overlayer in the XPS data presented in Figure 8.1(b), the surface composition of a bare Na^0 foil is analyzed in this section. For this, a piece of Na metal was freshly cut inside a glovebox and transferred to the XPS chamber via a vacuum transfer module. Despite this careful preparation and transfer, the surface of the as-prepared Na metal foil (t = 0min) is passivated as indicated by the presence of C and O on the surface in the survey spectra in Figure 8.3. Because Na-KLL Auger photoelectrons are found in the same region as O1s photoelectrons, the O-KLL region (∼1000 eV) is better to monitor the level of O contamination of the surface from the surveys.

To remove the passivation layer, the Na metal foil was sputter cleaned using a 2 keV Ar^+ ion gun. A total sputtering time of 3 hours was necessary to remove all residual contaminants from the surface. This was confirmed by the disappearance of the signals in the O-KLL and C1s regions and by the metallic Fermi edge in the valence band spectrum (see Figure 8.3). To demonstrate the high reactivity of Na metal towards residual gases, the sample was then left for 6 hours in the XPS chamber under ultra-high vacuum ($5x10^{-9}$ mbar). Its surface chemical composition was analysed *a posteriori* and the detection of a signal in the O-KLL region confirms that residual gases in the XPS chamber reacted with Na metal during the 6 hours of pause. A clear signal corresponding to Ca and Ti (at around 347 eV for Ca2p and 458 eV for Ti2p) is also observed. The presence of Ti might be the result of the activation of the Ti sublimation pump overnight during the 6 hours of pause. For the Ca signal, the Na metal foil was 99 % pure which could explain the presence of this contaminant in the sample. Yet, the Ca signal is much more intense in the survey spectrum after the pause (in green) than after the 3 hours of sputtering (in blue). This suggests that Ca has segregated to the surface during the 6 hours of pause inside the chamber. Like in the previous chapter, we suspect that Ca acts as "O getters" and react with oxide species from the passivation layer. To confirm this hypothesis, the reaction

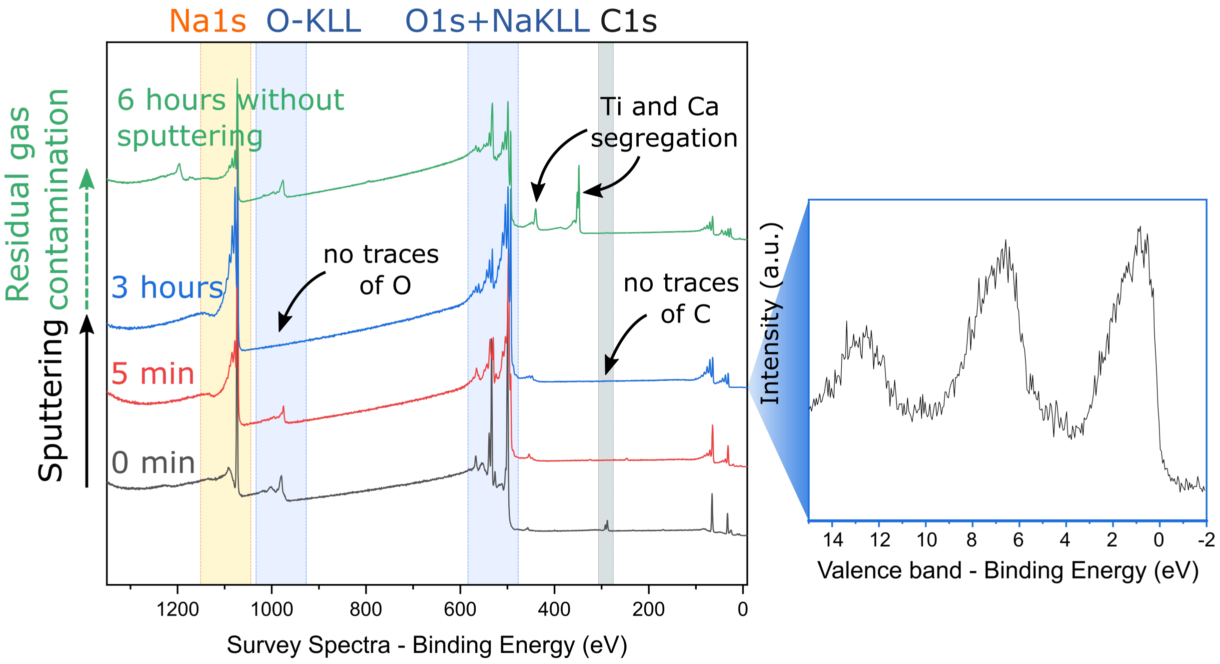

Figure 8.3: Survey spectra of a pristine Na metal foil as a function of sputtering time

energies of Ca with Na_2O (and also of Ti with Na_2O) was calculated using the Materials Project database (Equations 8.2 and 8.3).[164] Ca and Ti have both large reaction energies with Na_2O.

$$Na_2O + Ca \rightarrow CaO + 2Na(-0.574eV/atom) \tag{8.2}$$

$$Na_2O + Ti \rightarrow TiO + 2Na(-0.375eV/atom) \tag{8.3}$$

Na^0 spectral signature

Figure 8.4 shows XPS signals of the Na1s and “O1s” regions of the Na^0 sample acquired when the surface was free of surface contaminants (*i.e.* after the 3 hours of sputtering). The two regions were scanned over wide BE ranges to ensure the detection of multiple plasmon resonance losses. Although the region between 520 and 545 eV is referred here as the “O1s” region, it should be noted that the signals measured in this region are primarily caused by Na metal Auger photoelectrons and their plasmon losses. This nomenclature (the “O1s region”) was only chosen in relation to Figure 8.1.

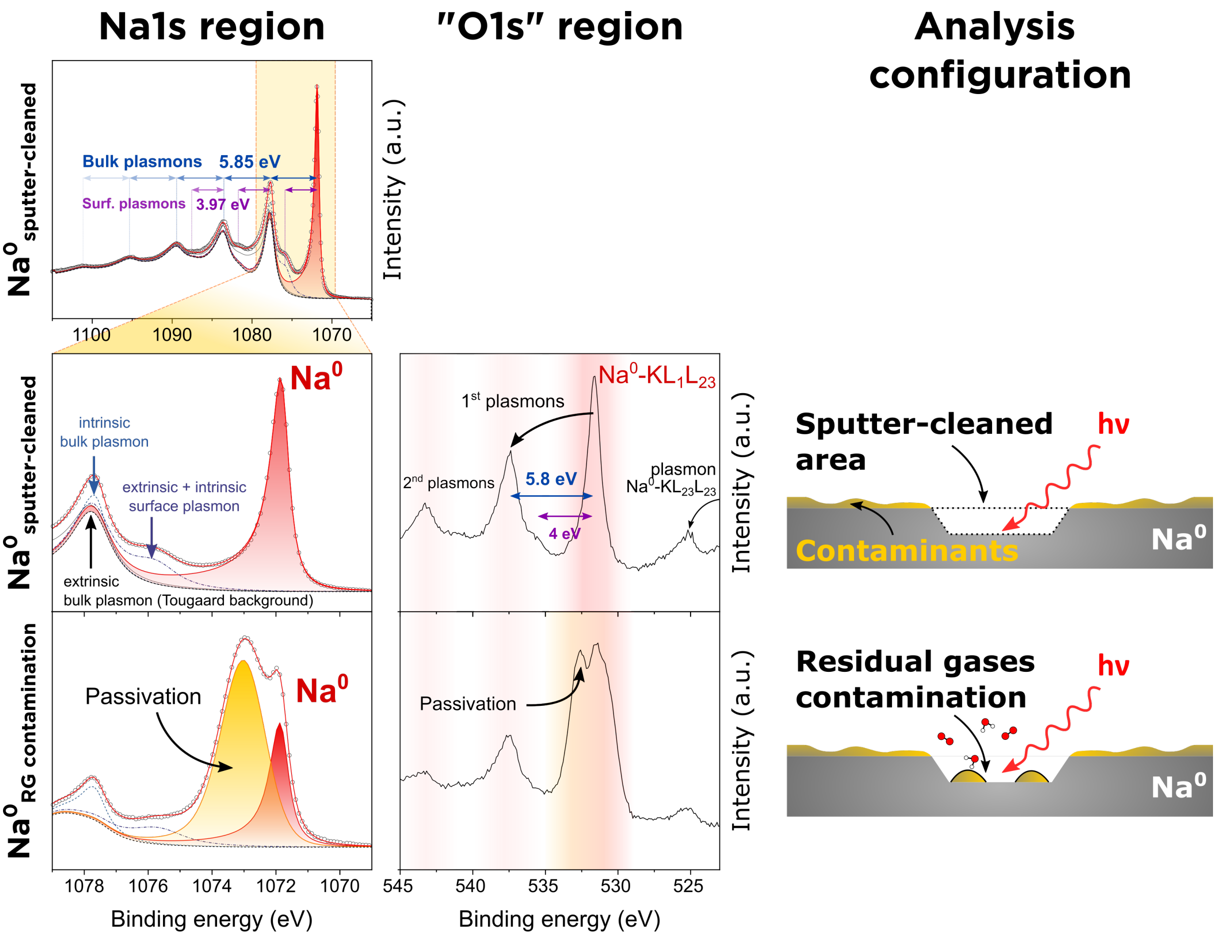

Figure 8.4: Na1s and O1s region scans of a sputter cleaned Na metal sample (top and middle panels, $Na^0_{sputter-cleaned}$) and of the same Na metal sample after 6 hours of exposition to residual gases of the XPS chamber (bottom panel, $Na^0_{RG-contamination}$). The top panel shows the fitting of the Na1s signal of $Na^0_{sputter-cleaned}$ over a wide BE range. In the middle and lower panels, a narrower range for the Na1s and O1s signals was adopted to show the fitting model more precisely. Intrinsic plasmon losses are represented with dashed lines in blue and purple. Fitting parameters and constraints are listed in Table E.1.

Focusing first on the Na1s region, the Na^0 signal is constituted of a main peak at 1071.83 eV followed by a series of periodic plasmon resonance losses. A detailed description of these plasmon losses was provided in the experimental methods chapter (section 4.4). A Tougaard background was required as explained in section 4.4. The main Na^0 peak was fitted with an asymmetric LF type function (to see the shape of this function, see Section 4.4). A LF function was preferred over a Doniach Sunjic one to limit the extent of the peak tail at high binding energies and ensure the peak area can be integrated without introducing an arbitrary cutoff.[154] A list of all fitting parameters yielding the best fits can be found in Table E.1 in Appendix E. The peak centered around 1081.6 eV corresponds to a BP+SP resonance. The 1077 to 1080 eV region was found to be more complex to model, but fortunately, the information of interest for our study is located at lower binding energies (1070 to 1075 eV) and an accurate fitting of the contributions occurring in the 1077-1080 eV region is therefore not absolutely required.

Turning to the “O1s” region, several peaks are observed. The most intense peak at 531.6 eV is a Na-$KL_1L_{2,3}$ Auger peak from metallic Na^0. In comparison, the Na-$KL_1L_{2,3}$ Auger from NZSP is found at 7.3 eV higher binding energies (around 538.9 eV in Figure 8.1). The difference in Auger peak positions matches well with previous results from Barrie.[153] These Auger photoelectrons can also excite bulk and surface plasmon resonances. These losses are observed with the same periodicity as in the Na1s region at multiples of 5.8 eV and 4 eV from the main peak for bulk and surface plasmon resonances respectively.

XPS signals of the surface of Na^0 after the 6 hours pause are also included in Figure 8.4. The Na1s and O1s signals clearly indicate the formation of new species on the Na^0 surface. Establishing the exact composition of the passivating species which formed on the Na^0 surface was not required for this study. The Na1s photoelectron signal emitted by these passivation species was therefore modelled by a single peak with a wide FWHM. The presence of new species at the Na^0 surface is also indicated by a new peak at 532.6 eV in the O1s region. An important conclusion of this paragraph is that the passivation layer forms quickly in just a few hours. Given that the *operando* experiment lasts around 4 hours (Section 8.1), it can therefore be expected that the plated Na^0 surface may also form a passivation layer.

In the next section, the fitting model of pristine Na^0 will be reused as an input for the fitting model of the Na^0|NZSP interface (where the signals emitted by Na^0, NZSP and the interphase overlap).

8.3 Fitting models for the Na^0|NZSP interface

In this section, fitting models for the Na^0|NZSP$_{\text{AS}}$ and Na^0|NZSP$_{\text{polished}}$ interfaces are developed. The objective of quantitative XPS analysis is to find the simplest model which can fit a XPS dataset whilst being physically meaningful (regardless of the quality of the fit). The creation of a fitting model is an iterative process where each iteration gains in complexity. The steps usually consist in: (1) making a hypothesis about the species present at a surface (here at the interface); (2) employing fitting algorithms to reproduce the shape of the XPS data using this synthetic surface model; (3) verifying if the parameters extracted from the fit (such as the position of peaks, their FWHM, or their areas) are physically meaningful.

Describing chronologically the fitting strategy that was applied to model the Na^0|NZSP interfaces would be a fairly long and indigestible read. Instead, in the two following subsections, two sets of XPS data were selected for the Na^0|NZSP$_{\text{AS}}$ and the Na^0|NZSP$_{\text{polished}}$ interfaces respectively, and our final most physically meaningful fitting models are described for each interface. The challenges faced in establishing these fitting models are discussed after, in section 8.5.

The Na^0|NZSP$_{\text{AS}}$ interface

It was found in section 8.1 that the most significant changes in the XPS signals of the interface during Na^0 plating concern the Na1s, O1s, and Zr3d regions. These regions are therefore modelled with a special interest in Figure 8.5 where the XPS signals of three samples are compared: the Na^0|NZSP$_{\text{AS}}$ interface after 240 minutes of plating (Na^0|NZSP$_{\text{AS}}$), a reference NZSP surface (NZSP$_{\text{AS}}$), and a reference sputtered Na metal surface (Na^0, same sample as in Section 8.2).

Na1s The Na1s region of Na^0|NZSP$_{\text{AS}}$ (t=240 min) is constituted of four peaks. Three of these peaks correspond to the Na1s signature of Na^0 (as observed in Figure 8.4) and are produced by the freshly plated Na^0: the most intense peak is the asymmetric Na^0 peak at 1071.9 eV (in red in Figure 8.5); it is followed by the first surface and bulk plasmon losses respectively at 3.96 eV and 5.86 eV from the main peak towards higher BE (in dashed lines). As a reminder, these plasmon features are part of the Na^0 peak background and are not produced by a separate phase.

Besides these three Na^0 peaks, another sharp feature is observed between 1073 and 1074 eV. This feature is fitted with one peak (in orange) associated to photoelectrons

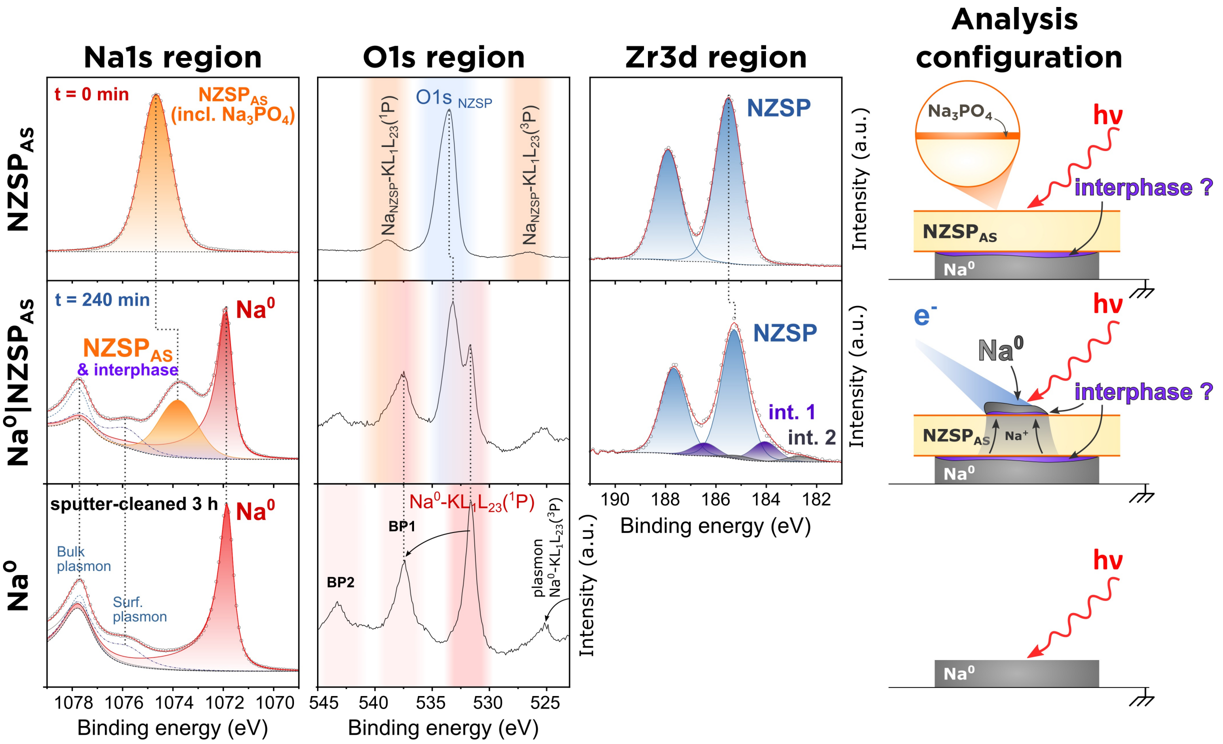

Figure 8.5: Fitting model for the Na^0|NZSP$_{\text{AS}}$ interface. The Na1s, O1s, and Zr3d XPS signals are modelled using the signals of two reference samples (NSZP$_{\text{AS}}$ and Na^0) as starting points. The fitting model is represented for the dataset collected after 240 minutes of Na^0 plating. Fitting parameters and constraints are listed in Tables E.2 and E.3.

emitted by the NZSP phase. This peak was assigned to NZSP photoelectrons after studying the rate of attenuation of the peak area as a function of Na^0 plating time (see Figure 8.9 in Section 8.4). It is also possible that a small fraction of the signal comes from an interphase (see section 8.4).

O1s The O1s region of Na^0|NZSP$_{\text{AS}}$ was only qualitatively compared with that of NZSP$_{\text{AS}}$ and Na^0 in Figure 8.5 because of the large number of overlapping peaks in this region. For the reference NZSP$_{\text{AS}}$ sample, the main contribution corresponds to O1s photoelectrons from NZSP (around 533 eV) but Na-KLL Auger photoelectrons are also observed at 538.5 and 526 eV. For the sputtered Na^0 reference, the peaks in its O1s region have been identified in the previous section. The peaks observed in the O1s region of Na^0|NZSP$_{\text{AS}}$ will be a combination of all these contributions with the addition of photoelectrons produced by a hypothetical interphase.

Zr3d A tail at low BE is observed in the Zr3d region of Na^0|NZSP$_{\text{AS}}$. This tail was

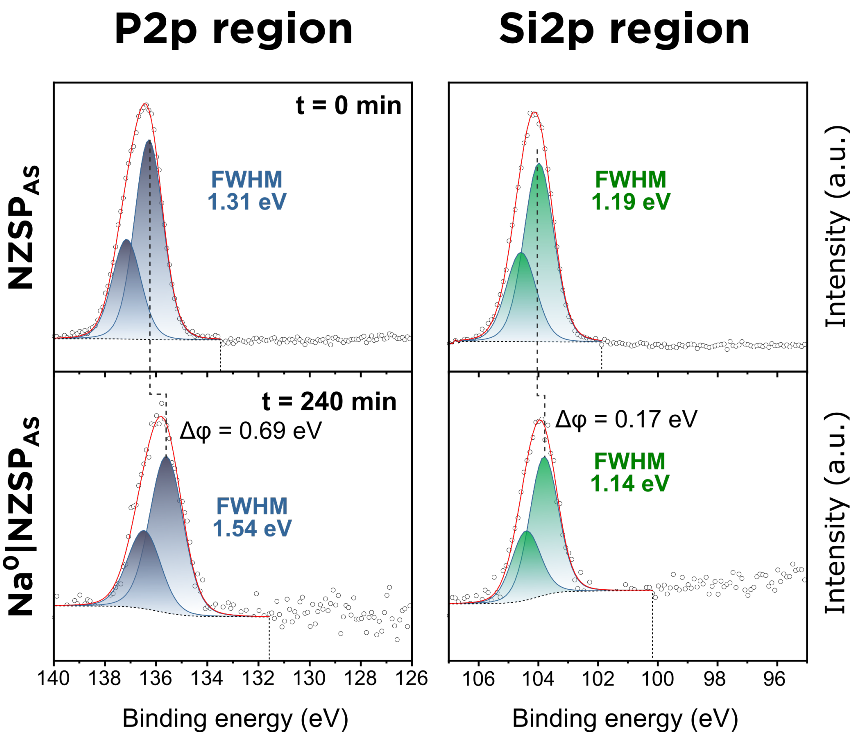

Figure 8.6: The P2p and Si2p core level regions of the Na^0|NZSP$_{AS}$ interface compared with those of a reference NZSP$_{AS}$ sample. The plated Na^0 layer causes the intensity of the Si2p and P2p signals in the Na^0|NZSP$_{AS}$ dataset to be attenuated which is why the data looks more noisy.

attributed to two new bonding environments (fitted with two extra doublets named “int. 1” and “int. 2” in Figure 8.5). The FWHM of these doublets was constrained to be the same as that of the NZSP doublet. The appearance of these doublets indicate that NZSP decomposes when Na^0 starts plating. Chemical shifts of Zr to lower BE were previously reported at Na|$Na_3Zr_2Si_2PO_{12}$ interfaces but also at the Li|LLZO interface.[177, 91] The extent of decomposition is however limited and the relative fraction of the interphase signal to the NZSP signal remains low (see Figure 8.9 in Section 8.4 for more details).

Si2p/P2p No significant changes in the shape of the Si2p and P2p were observed for Na^0|NZSP$_{AS}$ in comparison to NZSP$_{AS}$ (Figure 8.6). Importantly, the formation of Na_3P, ZrSi and ZrP could not be detected. First principles calculations predicted that these three phases should form at the interface between $Na_3Zr_2Si_2PO_{12}$ and Na metal.[177] If these decomposition products were present, the oxidation state of P in Na_3P or ZrP (-III) and of Si in ZrSi (-IV) would result in peaks at lower BE in comparison to the NZSP peaks (where P is in a (+V) state and Si is in a (+IV) state).

The Si2p and P2p signals were fitted with a model which assumes that the photoelectrons are emitted by the NZSP_{AS} phase only[1]. As qualitatively described in Section 8.1, a solid shift of all core levels towards lower BE is observed between the FG off measurement (reference) and when the FG is turned on. For the P2p signal, this shift is even more pronounced ($\Delta\phi = 0.69$ eV versus $\Delta\phi = 0.17$ eV for Si2p). This larger shift and the broadening of the P2p peaks (larger FWHM) could be associated to a potential gradient across the Na_3PO_4 islands which are present at the surface of as sintered NZSP samples.

In summary, the appearance of new species in the Zr3d signal after the initiation of plating indicates a reactivity of NZSP_{AS} towards Na^0. In the next section, the experiment is reproduced with a polished NZSP pellet instead of a NZSP_{AS} one. This experiment will give us insights on how the NZSP surface chemistry impacts its stability versus Na^0.

The $\text{Na}^0|\text{NZSP}_{\text{EtOH500}}$ interface

The *operando* XPS experiment is here repeated with a polished NZSP pellet. In Chapter 6, it was demonstrated that polishing NZSP pellets removes the sodium phosphate layer found on the surface of as-sintered NZSP samples. The results of this section will indicate whether the Na_3PO_4 layer has an influence on the stability of NZSP versus Na^0.

Like previously, we compare the Na1s, O1s, and Zr3d core levels of the $\text{Na}^0|\text{NZSP}_{\text{polished}}$ interface (after 91 minutes of plating) with two reference samples ($\text{NZSP}_{\text{polished}}$ and Na^0). Our most physically meaningful fitting models are presented in Figure 8.7.

Na1s the Na1s region of $\text{Na}^0|\text{NZSP}_{\text{polished}}$ has an additional peak in comparison to $\text{Na}^0|\text{NZSP}_{\text{AS}}$ (in a purple-yellow gradient in Figure 8.7). In a first attempt, the same model as the one which was used to fit the $\text{Na}^0|\text{NZSP}_{\text{AS}}$ XPS data was employed. As will be explained further in Section 8.5, this model resulted in unphysical conclusions and therefore had to be modified to include an extra contribution. The phase of origin of the photoelectrons resulting in that peak is still not exactly determined. Two possible origins for the photoelectrons are suggested: (1) the signal could come

---

[1] for simplicity, here, photoelectrons from the sodium phosphate surface layer and NZSP phases are combined into a single NZSP_{AS} phase. The existence of a sodium phosphate layer on the surface of NZSP_{AS} pellets was demonstrated in Chapter 6.

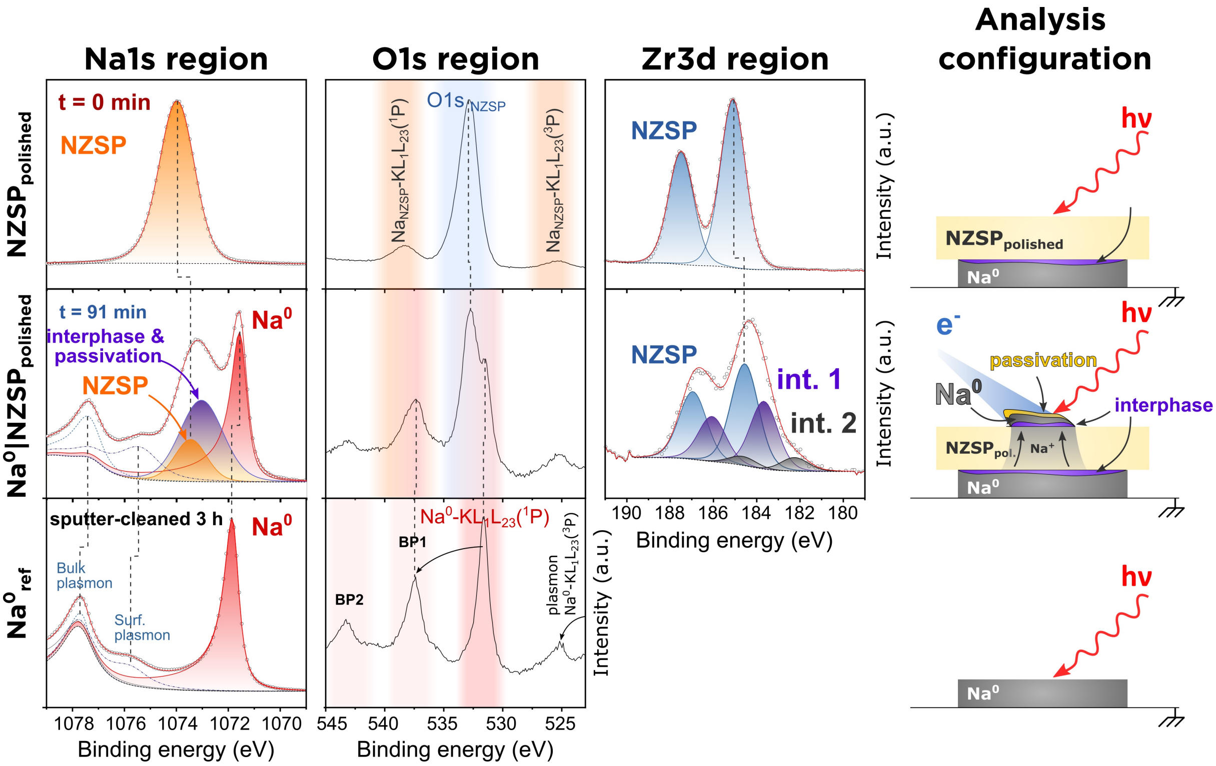

Figure 8.7: Fitting model for the Na^0|NZSP$_{\mathrm{EtOH500}}$ interface. Fitting parameters and constraints are listed in Tables E.4 and E.5.

from Na atoms from a decomposition layer and/or (2) from Na atoms from a passivation layer on top of the plated Na^0. The formation of a passivation layer on the Na^0 surface is suspected because the area of the purple-yellow peak stays constant with increasing plating time (see Figure 8.9 in Section 8.4). This suggests that these photoelectrons are not entirely emitted by a buried interphase, otherwise an attenuation of the peak intensity should be observed with increasing Na^0 thickness (like the attenuation which is observed for the NZSP photoelectrons). The specific contributions of the interphase and passivation layer could not be separated into individual peaks without making too many assumptions. It was therefore preferred to keep these contributions merged into a single peak with limited constraints.

The fitting model of the Na1s core level still includes three features from the plated Na^0 layer (a main peak at 1071.6 eV and two plasmon losses) and one peak from the NZSP phase. Regarding the NZSP peak, new constraints on its area, FWHM, and position had to be introduced to obtain a physically meaningful fit. The details of the fitting procedure are included in Section 8.5.

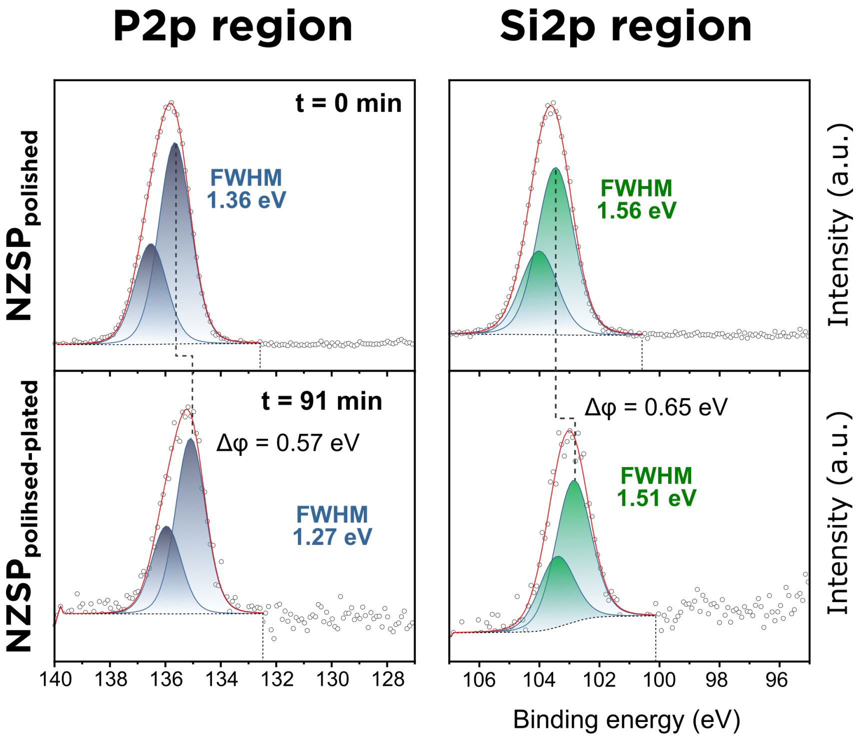

Figure 8.8: The P2p and Si2p core level regions of the $Na^0|NZSP_{polished}$ interface compared with those of a reference $NZSP_{polished}$ sample

Zr3d The Zr3d doublet of $NZSP_{polished}$ experiences a noticeable change in shape as soon as Na^0 plating started (see Figure E.1 in Appendix E). This change in shape is attributed to the growth of the same two phases which were already observed at the $Na^0|NZSP_{AS}$ interface (“int. 1” and “int. 2”). In comparison to $Na^0|NZSP_{AS}$, the relative fraction of Zr3d photoelectrons emitted by these new phases is much larger. Again, the presence of these new phases suggests that, under these experimental conditions, $NZSP_{polished}$ decomposes in contact with Na^0.

Si2p/P2p No significant changes are observed in the Si2p and P2p regions (see Figure 8.8). Unlike the $Na^0|NZSP_{AS}$ interface, similar shifts of the Si2p ($\Delta\phi = 0.65$ eV) and P2p ($\Delta\phi = 0.57$ eV) peaks are observed when the FG was turned on (in comparison to the FG off measurement).

Overall, the results of this section indicate that $NZSP_{polished}$ also reacts with Na^0 and that the interphase could be thicker than with $NZSP_{AS}$. This point will be discussed in more detail in the following section.

8.4 Evolution of the interphase chemical composition and electrical properties

Two Na^0|NZSP interface models have been established in the previous sections. These models condense a lot of information into a few parameters for each peak (position, area and FWHM). Trends in the evolution of these parameters as Na^0 plating progresses are analysed in this section.

Evolution of the peak areas as a function of plating time

Figure 8.9(a) and (b) plot the relative evolution of peak areas as Na^0 plating progresses. The peaks were individually normalized relative to their maximum area over the course of the experiment. The moment when this maximum is reached differs depending on the peak: for instance, the Na^0 peak reaches its maximum at the end of the experiment (*i.e.* when the plated Na^0 layer is the thickest), whereas the peaks corresponding to NZSP are most intense at the beginning of the experiment (before NZSP gets covered by an overlayer).

For both the $Na^0|NZSP_{AS}$ and $Na^0|NZSP_{polished}$ interfaces, the growth of the Na^0 peak follows the same trend and can be separated into two regions: a fast initial growth (in the first 100 minutes of plating) followed by a more linear increase. In contrary, the peaks assigned to the NZSP phase attenuate. The rate of attenuation follows the rate of Na^0 plating, with the intensity of the NZSP signals dropping rapidly in the first 100 minutes of plating followed by a more linear decrease. The attenuation of the intensity of the NZSP signals as a function of plating time ($I(t, KE)$) can be explained in a first approximation through Beer-Lambert law:

$$I(t, KE) = I_0 exp\left(\frac{-d(t)}{\lambda_x(KE)}\right) \tag{8.4}$$

where $d(t)$ is the thickness of the Na^0 layer which varies with time, and $\lambda_x(KE)$ is the IMFP of photoelectrons (with a kinetic energy KE) travelling through a material x (here Na^0).

What equation 8.4 tells is that, as the Na^0 layer gets thicker, the probability for photoelectrons emitted by the buried NZSP phase to reach the surface without being inelastically scattered is exponentially reduced. P2p, Si2p and Zr3d photoelectrons have similar

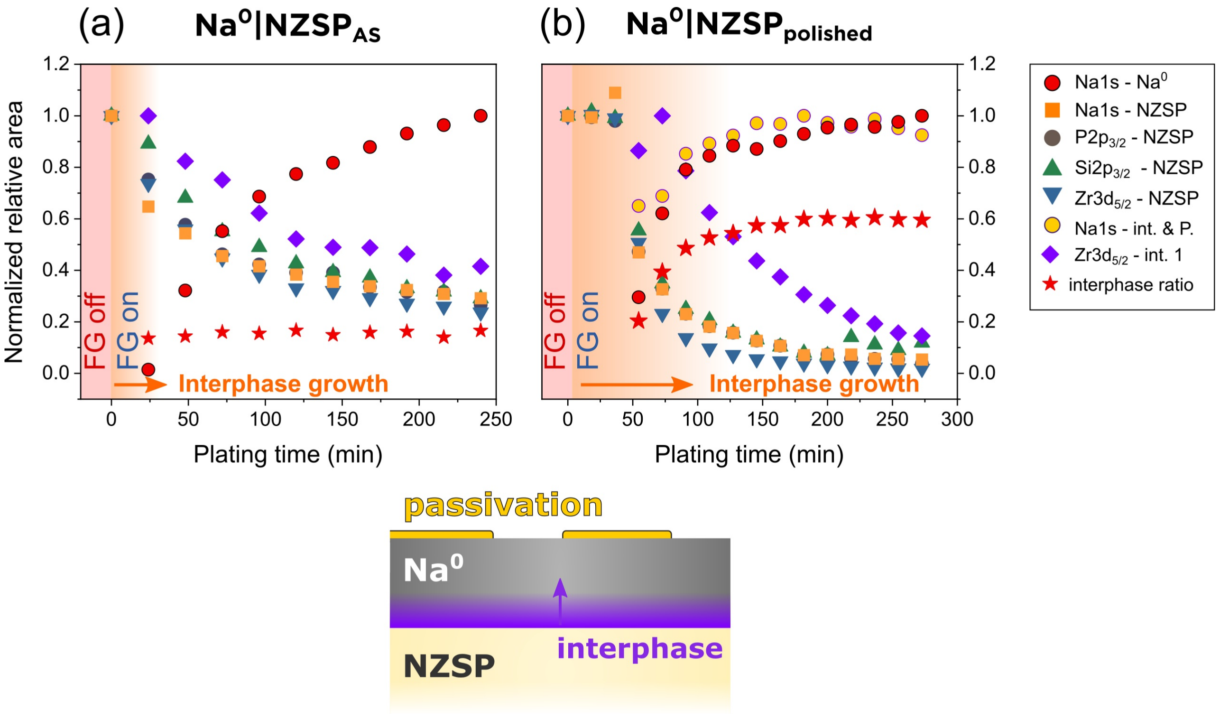

Figure 8.9: Evolution of the peak areas as a function of plating time. (a) Fitted peak areas (normalized to their relative maximum) as a function of plating time for the Na^0|NZSP$_{\mathrm{AS}}$, and (b) for the Na^0|NZSP$_{\mathrm{polished}}$ interface. A schematic cross-section of the proposed interface model is included below the graphs.

kinetic energies (1351 eV, 1382 eV and 1302 eV respectively) and therefore similar IMPFs[2] (5.12 nm, 5.22 nm and 4.97 nm respectively). As their IMFPs are similar, the attenuation of the P2p, Si2p and Zr3d signals from the NZSP phase occurs at the same rate in Figure 8.9(a) and (b). In contrast, Na1s photoelectrons have much lower kinetic energies (413 eV) and IMPF (2.00 nm). The Na1s signal originating from the NZSP phase should therefore attenuate faster than the P2p, Si2p and Zr3d signals. Yet, in Figure 8.9(a), the Na1s-NZSP peak attenuates at the same rate as the other NZSP signals. This suggests that the Na1s-NZSP peak is more intense than it should be and that part of the intensity of the peak may not be emitted by NZSP but by another phase (for instance from the interphase or from a passivation layer on the surface of the plated Na^0). This explains why the peak is called "NZSP & interphase" in the model presented in in Figure 8.5.

The formation of an interphase at both the Na^0|NZSP$_{\mathrm{AS}}$ and Na^0|NZSP$_{\mathrm{polished}}$ interfaces was detected by the appearance of new species in the Zr3d signals in Figures 8.5 and 8.7.

---

[2] IMFP values were obtained from the NIST database (see section 4.4 for details on the TPP-2M equation used to calculate IMFPs).[178]

The evolution of the normalized relative area of one of these peaks (“int. 1”) is included in Figure 8.9(a) and (b) (in purple). Figure 8.9(a) shows that the normalized area of the "int. 1" peak attenuates as plating progresses (at similarly the same rate as the NZSP signals) which indicates that Na^0 grows on top of the "int. 1" phase. The normalized relative area of the "int. 1" peak is larger than the NZSP peaks (*e.g.* Zr3d) which also suggests that the new phase lays on top of the NZSP phase (the "int. 1" signal is less attenuated by the Na^0 layer so the phase is closer to the surface than NZSP).

In contrast, for the $Na^0|NZSP_{\mathrm{polished}}$ interface, the intensity of the "int. 1" peak initially increases in the first minutes of Na^0 plating before attenuating. The rate at which the "int. 1" peak attenuates is also slower than that of the NZSP peaks. This suggests that the decomposition of NZSP and the formation of an interphase occurs over a longer time with a polished pellet than with an as sintered one.

The ratio of the Zr3d signal emitted by the interphase products to the total Zr3d signal (%interphase) was also plotted in Figure 8.9 (red stars) with :

$$\%interphase = \frac{A_{int.1}^{Zr3d_{5/2}} + A_{int.2}^{Zr3d_{5/2}}}{A_{NZSP}^{Zr3d_{5/2}} + A_{int.1}^{Zr3d_{5/2}} + A_{int.2}^{Zr3d_{5/2}}} \tag{8.5}$$

where $A_{int.1}^{Zr3d_{5/2}}$, $A_{int.2}^{Zr3d_{5/2}}$ and $A_{NZSP}^{Zr3d_{5/2}}$ correspond to the area of the $Zr3d_{5/2}$ peaks of the interphase 1, interphase 2 and NZSP phases in the peak fitting models used in Figures 8.5 and 8.7.

This ratio informs about the progression of the decomposition reaction occurring at the interface. The decomposition reaction takes around 2 hours to stabilize for the $Na^0|NZSP_{\mathrm{polished}}$ interface whereas it is almost immediate for the $Na^0|NZSP_{\mathrm{AS}}$ interface. The fraction of the Zr3d signal emitted by the interphase is around 15 % for the $Na^0|NZSP_{\mathrm{AS}}$ interface and up to 60 % for the $Na^0|NZSP_{\mathrm{polished}}$ interface. $NZSP_{\mathrm{polished}}$ surfaces therefore decompose to a much greater extent than $NZSP_{\mathrm{AS}}$ surfaces in contact with Na^0.

The main conclusion of this sub-section is that the NZSP surface chemistry influences its stability versus Na^0. $NZSP_{\mathrm{AS}}$ is more stable in contact with Na^0 than $NZSP_{\mathrm{polished}}$ which could be due to its Na and P rich surface termination (whose existence was demonstrated in Chapter 6). The predicted stability of Na_3PO_4 in contact with Na metal could explain why $NZSP_{\mathrm{AS}}$ is more stable in contact with Na^0.[82] Another important conclusion is that for both $Na^0|NZSP_{\mathrm{AS}}$ and $Na^0|NZSP_{\mathrm{polished}}$, the decomposition reaction eventually stabilizes which suggests that the reaction products are electronically insulating and form a self-limiting SEI-type interphase (see the interphase types in Chapter 3). As a reminder, the formation of a self-limiting interphase is crucial to ensure the long-term viability of Na^0|NZSP based batteries.

Relative shifts of the peak positions as a function of plating time

Figure 8.10(a) and (b) show the relative shifts in the positions of peaks as plating progresses (for the $Na^0|NZSP_{AS}$ and $Na^0|NZSP_{polished}$ interfaces). The reference for each peak is the position measured when the FG was still off. This reference position is then used to calculate the relative shifts.

The original *operando* XPS study from Wood et al. devoted a special attention to extract information from relative shifts in peak positions.[96] In their study, a shift of the peaks to lower BE was always observed when the FG was turned on in comparison to a measurement taken with the FG off. The peaks position is in part affected by the surface potential that the photoelectrons experience as they escape to the surface. In other words, if a surface potential accelerates photoelectrons when they leave the surface, the resulting peak will appear in the spectrum at a lower BE than it would normally appear without the surface potential. The surface potential is continuously changing in the *operando* experiment from the combined effect of Na^0 plating and the formation of an interphase. Thus, it is not surprising to observe a shift in the position of peaks in Figure 8.10.

For the $Na^0|NZSP_{AS}$ interface (Figure 8.10(a)), an initial shift of all of the peaks happens in the first few minutes of plating but the peaks then stop shifting for the rest of the experiment. The relative shifts of the Na1s and P2p peaks are more pronounced (-0.6 to -0.8 eV) than the Si2p or Zr3d peaks (around -0.2 eV). The proposed explanation for the difference in relative shifts is that the sodium phosphate islands present on $NZSP_{AS}$ samples (see 5.1) create a larger surface potential leading to a larger average shift of the Na1s and P2p peaks (and also to peaks with larger FWHM) in comparison to the Si2p and Zr3d signals.

For the $Na^0|NZSP_{polished}$ interface (Figure 8.10(b)), the position of the peaks is seen to continuously shift in the first 90 minutes of plating before reaching more stable values. The Si2p and P2p peak positions begin to scatter after 150 minutes of plating (sometimes by more than 0.2 eV between two consecutive iterations). This scatter is a fitting artefact which is caused by the difficulty to extract a precise position for the peaks when their

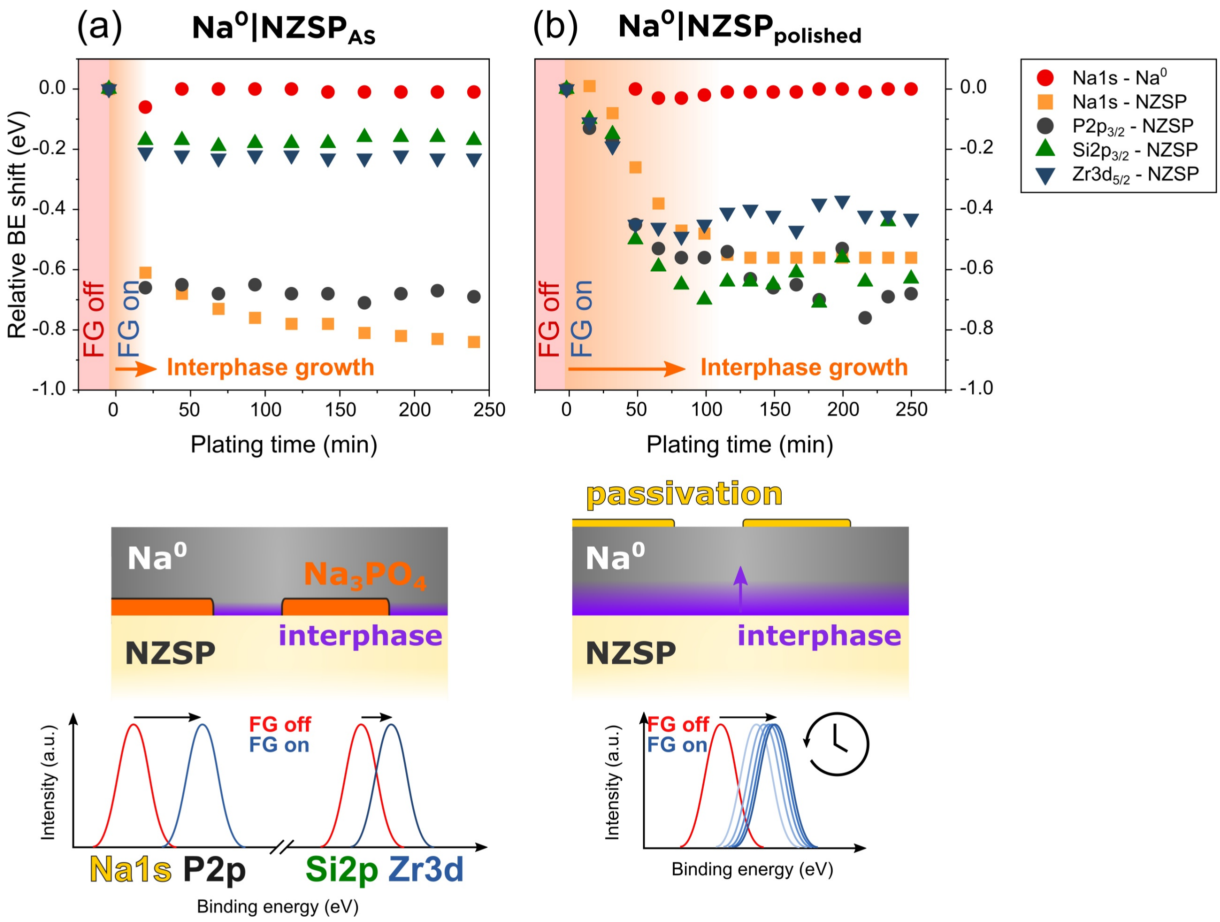

Figure 8.10: Relative shifts in peak positions as a function of plating time for the $Na^0|NZSP_{AS}$ interface (a) and the $Na^0|NZSP_{polished}$ interface (b).

intensity is too low (which is the case for these signals after 150 minutes of plating because the Na^0 overlayer is thick). The continuous shift of the peaks in the first 90 minutes of plating indicates that a surface potential is building up. This growing surface potential can be attributed to the growing thickness of the interphase. In other words, the evolution of the peak positions confirms that the interphase forms over a longer period for the $Na^0|NZSP_{polished}$ interface in comparison to the $Na^0|NZSP_{AS}$ interface.

8.5 Challenges of establishing a physically meaningful fitting model

As described previously, establishing a model to fit XPS data requires to make hypotheses, test them, and verify that the results are physically meaningful. This section

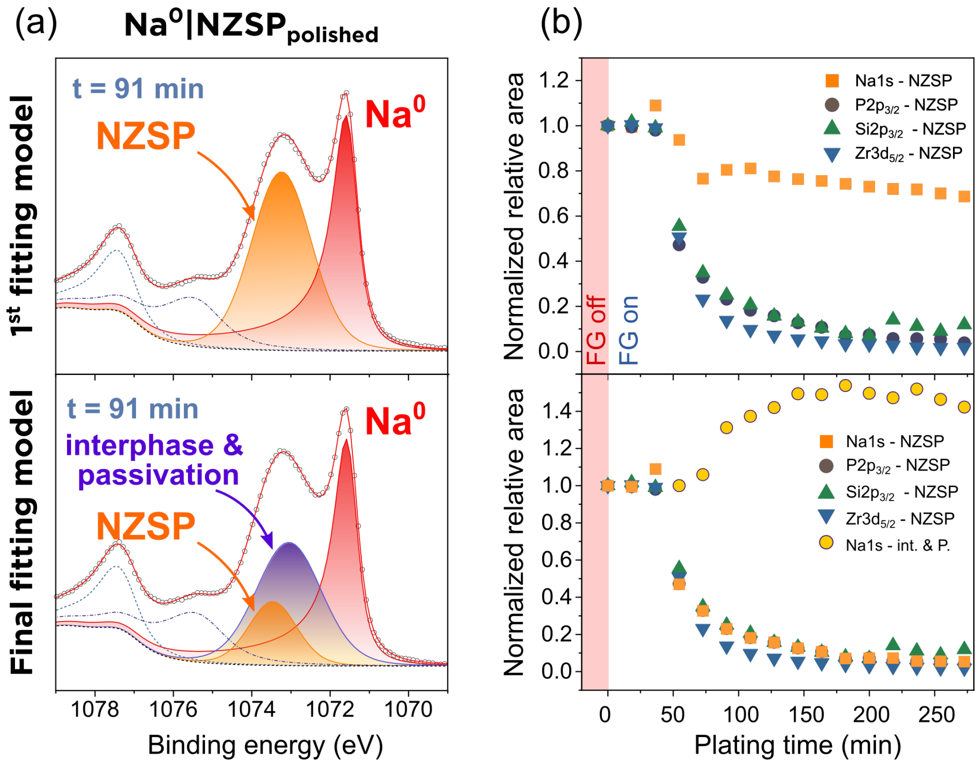

Figure 8.11: Challenges of establishing a physically meaningful fitting model. (a) Two fitting models for the Na1s region of Na^0|NZSP$_{\text{polished}}$. (b) Comparison of the normalized relative areas of a selection of peaks for the two models: for the first fitting model the attenuation of the Na1s-NZSP peak area dissociates from that of the other NZSP peaks; for the second fitting model, the attenuation of the Na1s-NZSP peak area is constrained to match the attenuation of the P2p-NZSP peak area. An additional peak ("interphase & passivation") is required for the second fitting model

provides an example of how this logic had to be followed to establish the fitting model of the Na1s core level of Na^0|NZSP$_{\text{polished}}$ (Section 8.3). As a reminder, the fitting model of the Na^0|NZSP$_{\text{polished}}$ interface differs from the Na^0|NZSP$_{\text{AS}}$ interface by the addition of an extra peak assigned to "interphase & passivation" layers.

Figure 8.11 compares two fitting models for the Na^0|NZSP$_{\text{polished}}$ interface. The first model only features one peak attributed to the NZSP phase in the 1073-1074 eV region (in orange in Figure 8.11(a)). The evolution of the normalized peak areas as a function of plating time is presented in Figure 8.11(b).

Figure 8.11(b) shows that, with this first fitting model, the Na1s-NZSP signal attenuates at a much slower rate than the other NZSP core levels (Si2p, P2p, and Zr3d). However, as explained in Section 8.3, the Na1s signal should attenuate faster that the other NZSP core levels because of the lower kinetic energy of Na1s photoelectrons. Thus, although a fit with low residuals could be obtained, this model had to be abandoned because it lacked physical grounds.

To remediate to this problem, the evolution of the Na1s (NZSP) peak area was constrained to match the rate of attenuation of P2p (NZSP) photoelectrons. The FWHM of the Na1s (NZSP) peak was also constrained to stay within 0.15 eV of the FWHM which had been obtained for the Na1s signal of the reference sample ($NZSP_{polished}$). The position of the peak was also constrained so that the peak could only shift towards lower binding energies (the full list of constraints which was employed in the second fitting model is included in Appendix E). With these new constraints added for the NZSP phase, it was necessary to include another peak in the model to fit the remaining part of the measured intensity. This peak is named “interphase & passivation” in Figure 8.11(a). Figure 8.11(b) shows that, unlike the other peaks whose intensity attenuate with plating progression, the intensity of the “interphase & passivation” peak stabilizes after around 150 minutes of plating. This suggests that the phase from which the photoelectrons are emitted lays above the Na^0 layer. Na1s photoelectrons from the interphase and from the surface passivation layer could not be separated with this study, hence they were combined into a single peak in Figure 8.11(a).

8.6 Comparing the conclusions of the *ex-situ* and *operando* experiments

Depending on the XPS protocol employed to test the electrochemical stability of the Na|NZSP interface (*ex-situ* in chapter 7 and *in-operando* in this chapter), different conclusions are reached:

- the ***operando*** experiment concludes that NZSP decomposes in contact with Na^0 to form a stable SEI whose thickness depends on the surface treatment that the NZSP surface has received (*i.e.* if the pellet is used as-sintered or if it polished)
- the ***ex-situ*** experiment suggests that NZSP forms a kinetically stabilized interface with Na^0(new Zr species which could be part of a SEI were only detected at trace levels).

The difference between the two experiments appears clearly in Figure 8.12(a). Here, the Zr3d regions of four NZSP surfaces (as-sintered or polished, and characterized *ex-situ*

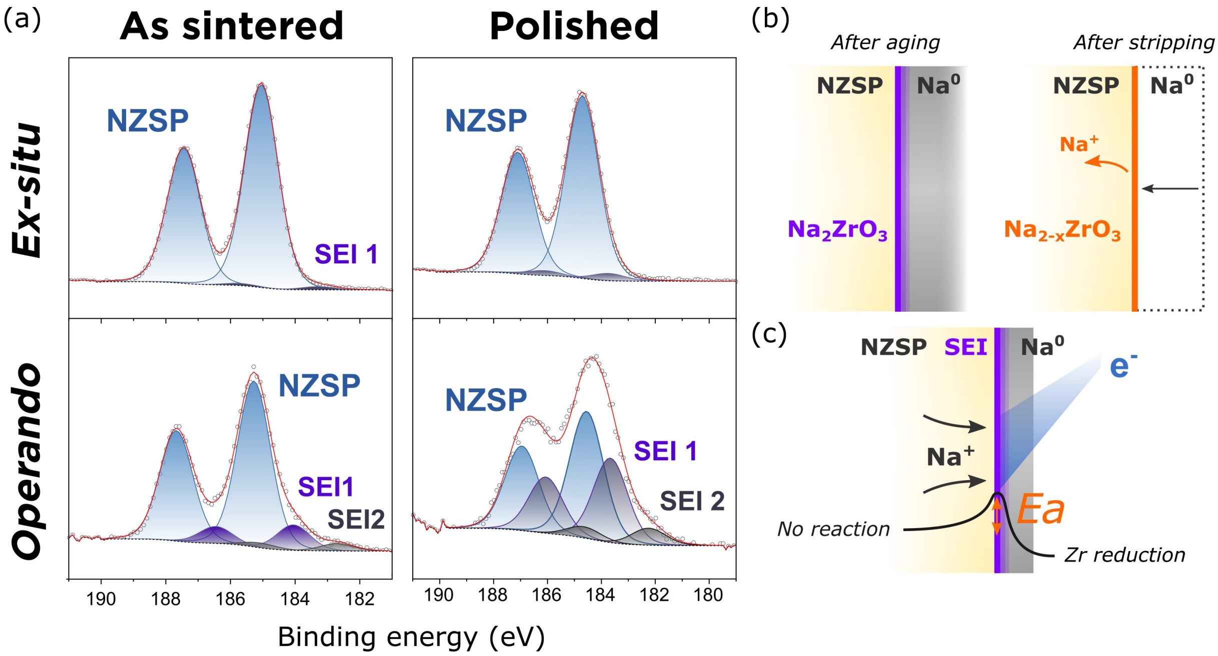

Figure 8.12: (a) Comparison of the Zr3d signals and fitting models obtained via two XPS characterization protocols. (b) Schematic description of hypothesis 1. Na_2ZrO_3 is used as an example of a SEI phase which could be redox active. (c) Schematic description of hypothesis 2. The nucleation of the SEI requires a certain activation energy which could be provided by the accelerated flood gun electrons.

or *operando*) are presented. The intensity of the SEI phases is much more pronounced when the interface composition is probed *in-operando* than *ex-situ*.

The aim of this section is to provide two hypotheses which could explain this paradox (see Figures 8.12(b) and (c)). The main difference between the two hypotheses is that the first one assumes that NZSP is unstable against Na^0 and that a SEI forms regardless of the characterization protocol; for the second one, it is speculated that NZSP is kinetically stable against Na^0 but that the energy provided by the flood gun electrons in the *operando* experiment exceeds the activation energy for NZSP decomposition. The fact that the Na metal purity varies between the two chapters (the interface is formed with 99 % pure Na metal in Chapter 7 versus essentially 100 % pure Na metal in this chapter) is an added complexity which is not included in our discussion.

Hypothesis 1 - a redox active SEI

In this first scenario, it is speculated that a SEI forms every time when NZSP is in contact with Na^0. For the *ex-situ* protocol, the Na^0 electrode needs to be galvanostatically stripped before the NZSP surface can be analysed. Assuming that the SEI phases are redox active, then it is possible that some Na^+ ions could be extracted from their structures during the stripping of the electrode. The extraction of cations from the structure should theoretically result in a chemical shift of the Zr3d signals towards higher binding energies possibly making them merge with the NZSP peaks (thereby making them hardly distinguishable).

Hypothesis 2 - the FG electrons activate the decomposition

The second hypothesis (see Figure 8.12(c)) proposes that the Na|NZSP interface is kinetically stable but that the kinetic energy of the flood gun electrons in the *operando* experiment exceeds the activation energy for NZSP decomposition. This hypothesis was recently formulated in a side-by-side study comparing the stability of Li^0|LLZO interfaces depending on which characterization protocol was employed.[91] In this study, Connell and Fuchs observed that the stability of the Li^0|LLZO interface depended on the technique chosen to deposit Li^0 on the LLZO surface. If Li^0 was deposited by e-beam vapor deposition, the Li^0|LLZO interface was stable; in contrast, when Li^0 was plated on LLZO using the same *operando* technique as the one described in this chapter, the formation of a SEI (new Zr phases were detected). The authors proposed the idea that the SEI nucleation could be activated by the flood gun electrons. More recently, Gibson *et al.* suggested that the flood gun electrons may not be responsible for the decomposition but rather the Ar^+ ions reaching the surface in dual mode flood sources (like the one employed in this study).[179]

8.7 Summary and future work

Characterizing the decomposition reaction of a buried interface with a technique whose depth resolution is limited to a few nanometres is a challenging task. The *operando* experiment described in this chapter provides a lot of information in a single experiment and is therefore a very valuable tool in the characterization of alkali metal|SE interfaces. More precisely, the information which can be extracted from it includes: the detection of new phases from the decomposition reaction at the interface; the equilibration time for the decomposition reaction; the rate of Na^0 plating on the NZSP surface; surface potentials associated with the growth of the interphase. One limitation to the technique, which was highlighted in the last section of this chapter, is that it might be activating the reaction of decomposition at an interface which would normally (*i.e.* inside a cell) be kinetically stabilized. Thus, analysing the stability of the interface with the *operando* protocol might provide a worse case scenario but not a representative picture of what happens inside a cell.

The data analysis in this chapter focused on establishing physically meaningful fitting models for the $Na^0|NZSP_{AS}$ and $Na^0|NZSP_{polished}$ interfaces. For the Na1s core level in particular, the models had to separate the signal emitted by the Na^0 overlayer from the signals emitted by NZSP and the SEI. In future work, the XPS signals coming from the SEI will have to be assigned to specific phases. A starting point for the identification of new phases is the list of decomposition products predicted by first principles calculations, including for instance Na_2ZrO_3 or Na_4SiO_4.[82, 177] One important conclusion of the study is the superior stability of $NZSP_{AS}$ surfaces in contact with Na^0 in comparison to $NZSP_{polished}$ ones.

Future work will also focus on describing the impact of surface potentials on the peak positions more quantitatively. These modelling efforts are run in collaboration with Nicholas Williams, a PhD colleague at Imperial College London.

As a last point of conclusion to close the last two chapters which looked at the electrochemical stability of the $Na^0|NZSP$ interface, it was demonstrated that the interface is either kinetically stabilized or forms a self-limiting SEI. In either case, this confirms that the $Na^0|NZSP$ interface (especially if as-sintered NZSP samples are used) is viable on a technical point of view for long-term SSB operation.

Chapter 9

The Na^0|NZSP interface under cycling conditions

In this chapter, the ability of the Na^0|NZSP interface to maintain its electrochemical performance under an applied current is investigated. The questions of interfacial pores/voids coalescence during stripping and of short-circuits by metal filaments during plating will receive a special attention. The first section of this chapter (9.1) focuses on identifying the overpotential signature associated with the formation of pores at the Na^0|NZSP interface. Having established how interfacial pores can be detected electrochemically, the following sections (9.2 and 9.3) investigate the cycling behaviour of symmetrical cells with an emphasis on the impact of the current density and cycled capacity as experimental parameters. These sections will highlight a correlation between short-circuits on plating cycles which follow stripping cycles with large overpotential increases.

N.B.: the cells used in this chapter were all assembled with 99 % pure Na metal electrodes. Ca poisoning will introduce an extra source of interface overpotential (especially for cells tested over long periods) which cannot be separated from the overpotential related to the formation of pores.

9.1 Formation of interfacial voids during stripping

The issue of pore coalescence at alkali metal|ISE interfaces under stripping is now well reported in the literature (see section 3.3) and is often considered to be one of the root causes for ISE failures. This section aims to identify the electrochemical response of a symmetrical Na^0|NZSP|Na^0 cell when one of its electrodes is forming pores. More

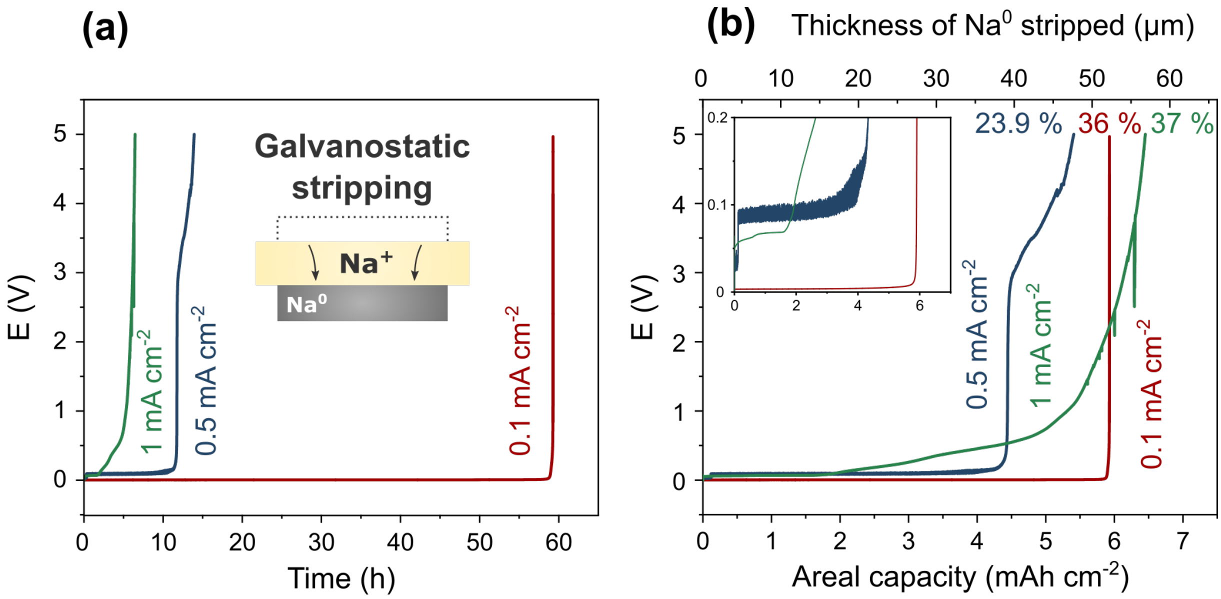

Figure 9.1: Electrochemical characterization of void formation at the Na^0|NZSP interface. (a) Cell potential versus time for three cells stripped at different current densities. (b) Cell potential versus areal capacity (or the equivalent Na^0 thickness) for the same three cells. The inset figure is a zoom of the 0-0.2V region. Percentages indicate the relative fraction of the initial electrode capacity which has been stripped.

specifically, Figure 9.1 shows the evolution of the voltage of three symmetrical cells as one of their Na^0 electrodes is galvanostatically stripped. The impact of the stripping rate on the formation of pores was tested by stripping the electrodes at three different rates (0.1 mA cm^{-2}, 0.5 mA cm^{-2}, and 1 mA cm^{-2}). All experiments were conducted at room temperature and with no externally applied pressure on the cells. The three symmetrical cells were assembled with an as sintered NZSP pellet. The experiment was stopped when the cell voltage reached 5 V.

Figure 9.1(a) shows the evolution of the cell voltage as a function of stripping time. For the three cells, the cell voltage shoots up after a critical time t_0 which varies depending on the stripping current density: 58 h (at 0.1 mA cm^{-2}), 11 h (at 0.5 mA cm^{-2}), and 5.5 h (at 1 mA cm^{-2}). Unsurprisingly, the lower the stripping current density, the longer it takes for pores to be formed at the interface.

In Figure 9.1(b) the data was normalized to show the evolution of the cell voltages as a function of the stripped areal capacity (bottom x-axis). The areal capacity is directly proportional to a stripped thickness of Na^0 (which is shown as the top x-axis). Figure 9.1(b) shows that the amount of Na^0 which can be extracted from an electrode is not related to the current density at which the electrode was stripped. Similar results have been previously reported for the Li|LLZO interface by Krauskopf.[68] In Figure 9.1(b), the critical stripped thickness of Na^0 varies from 47.6 μm (for the 0.5 mA cm^{-2} cell) to 56.8 μm (for the 1 mA cm^{-2} cell). The percentages indicated next to each line correspond to the relative fraction of Na^0 which was extracted from the initial electrode capacity (which was estimated by weighing the electrodes before cell assembly). A large fraction of the electrodes (up to 76 % for the cell stripped at 0.5 mA cm^{-2}) remains attached to the current collector.

By repeating the experiment on other cells (data not presented here), it was observed that the relative fraction of Na^0 which can be extracted from an electrode (at equal stripping current density) varies greatly from cell to cell. For instance, for two other cells stripped at 1 mA cm^{-2}, the relative fractions of Na^0 which could be extracted from the total electrode capacity were 52 % (90 µm) for one and 10 % (16 µm) for the other (in comparison to 37 % for the data presented in Figure 9.1). These large variations from sample to sample could possibly be due to interface defects (micropores for instance) which are unique to each cell as they are manually assembled. These preexisting defects can act as nucleation points for the rapid coalescence of pores, a problem which will be amplified at high current densities. The oscillations in the potential of the cell stripped at 0.5 mA cm^{-2} which can be observed in the inset of Figure 9.1(b) have not been studied in detail but could be related to a defect relaxation mechanism at the interface.[180]

A gradual increase in the cell overpotential is observed more clearly at high stripping current densities. For instance, the voltage of the cell stripped at the lowest current density (0.1 mA cm^{-2}) remains constant at a value of around 3.5 mV for the entire experiment until its critical time is reached. In contrast, the cell stripped at 1 mA cm^{-2} displays a continuous increase in cell voltage. This increase in the cell voltage can be attributed to the coalescence of pores at the interface which cannot be annihilated if the electrode is stripped at fast current densities (see section 3.3 and Appendix B).

Overall, the experiment indicates that the coalescence of pores at the Na^0|NZSP interface can be detected by an increase in the cell overpotential.

9.2 Critical current density/overpotential for NZSP failure

The tolerance of a SE to failure by filament penetration is typically tested by measuring its CCD (see sections 4.6 and 3.4). The impact of interfacial pores (formed during stripping cycles) and of the initial interface resistance on the CCD will be investigated in sections 9.2 and 9.2 respectively.

Dependence of the CCD on the cycled capacity

Previous studies have established that the formation of pores at the interface during stripping cycles can lead to short-circuits on following plating cycles.[103] To study how interfacial voids impact the CCD, an electrochemical testing protocol which enables to control the extent of pores accumulation at the Na^0|NZSP interface whilst simultaneously cycling the cell at increasing current densities needs to be adopted. Here, these constraints are met by changing the areal capacity which is stripped/plated at each half-cycle (different thicknesses of Na^0 will be cycled depending on the cell). The larger the capacity of Na^0 stripped, the likelier voids form at the interface (see section 9.1).

The results of the CCD test of three symmetrical cells are presented in Figure 9.2. The cells were cycled with a respective Na^0 capacity of 0.25 mAh cm^{-2} (cell **a**), 1 mAh cm^{-2} (cell **b**), and 5 mAh cm^{-2} (cell **c**). The thickness of Na^0 stripped/plated at each half-cycle corresponds for cell (a) to 2.2 μm (around 2 % of the electrode thickness), for cell (b) 8.8 μm (around 8 % of the electrode thickness), and for cell (c) to 44 μm (around 46 % of the electrode thickness). The three cells studied in this subsection were all assembled with an as sintered NZSP pellet. Their impedance was measured after cell assembly to ensure that their initial interface resistances were all similar (all were $< 1\ \Omega$ cm^{-2}). For each cell, the CCD testing was preceded by a 6 h OCV period.

For cell (a), the cell potential follows an ohmic behaviour as the current density is increased. The first large overpotential increase is observed at a stripping current density[1] of 9 mA cm^{-2}, and the cell potential increases to 2.1 V. Another large overpotential is measured at the 10 mA cm^{-2} stripping half-cycle and the cell shorts at the following plating half-cycle. The CCD of cell (a) is therefore quite high at 10 mA cm^{-2}. Despite this impressive performance, it is important to remember that a cycled capacity of 0.25

---

[1] as the two electrodes in symmetrical cells are identical, the "stripping" half-cycles were arbitrarily attributed to positive current densities in Figure 9.2

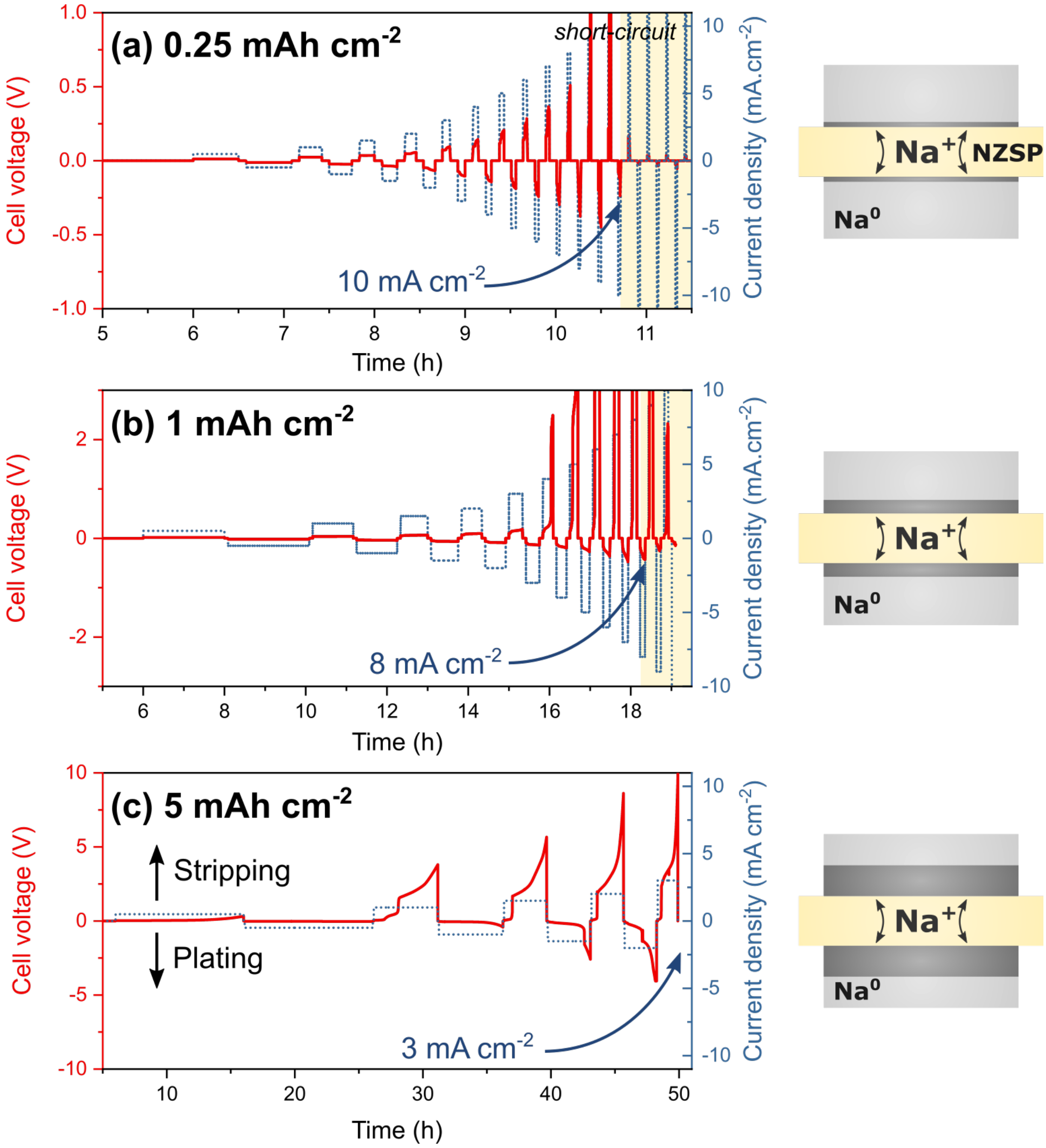

Figure 9.2: CCD of symmetrical cells as a function of cycled capacity. Schematics representing the symmetrical cells are shown on the right: the total Na^0 electrode thickness is represented in light grey and the thickness stripped/plated at each cycle is represented in dark grey (not to scale).

mAh cm^{-2} is not sufficient for commercial applications (the target is closer to 5 mAh cm^{-2} for a cell with a sufficiently high energy density).

For cells (b) and (c), the onset for the overpotential increase occurs at much lower current densities: a large increase is observed at 4 mA cm^{-2} for cell (b) and at 1 mA cm^{-2} for cell (c) (the left ordinate axes in Figure 9.2 have different scales). For cell (b), its potential increases to 6.1 V at the end of the 8 mA cm^{-2} stripping cycle. The cell soft-shorts at the following plating half-cycle establishing the CCD of that cell at 8 mA cm^{-2}. For cell (c), the CCD of the cell was not determined because the experiment stopped when the voltage safety limit of the experiment (10 V) was reached. The maximum current density at which the cell was cycled was 3 mA cm^{-2}.

Following the results from section 9.1, the large overpotentials observed in Figure 9.2 can legitimately be attributed to the coalescence of pores at one of the cells' interfaces. Interestingly, large overpotentials are always predominantly observed on odd half-cycles (the "stripping" ones). This is particularly clear for cell (b) for which a large asymmetry in the cell potential between stripping (top part of the graph) and plating (bottom part) cycles is observed. This asymmetry between the plating and stripping half-cycles suggests that the pores forming on the first half-cycle are the most detrimental and that cells could have a "memory" of which of their interfaces accumulated pores first. This asymmetry could suggest that the voids formed at the stripped interface during the first stripping half-cycle are not completely filled during the following plating half-cycle and instead form "occluded" voids, a concept mentioned in the work from Kasemchainan.[103] In particular, occluded voids could explain why the overpotential shoots up so rapidly on the stripping cycles: according to Kasemchainan *et al.*, the pores formed during the stripping cycles are not filled during the plating half-cycles but are be pushed away from the interface into the bulk of the Na^0 electrode (see Figure 9.3); on the next stripping half-cycle, the occluded voids are pulled back to the interface and, as soon as the thin layer of Na^0 which had been plated at the interface in the preceding half-cycle is stripped, a sudden increase in overpotential is observed.

This section demonstrates that cells always short-circuit after large overpotentials on stripping cycles (void accumulation). It is suggested that metal filaments nucleate at the Na|NZSP interface because of intense current constriction on a limited interface active area. The current densities which can readily be withstood by NZSP at room temperature and without any interface engineering are however extremely promising in comparison to other ISEs (for instance LLZO).

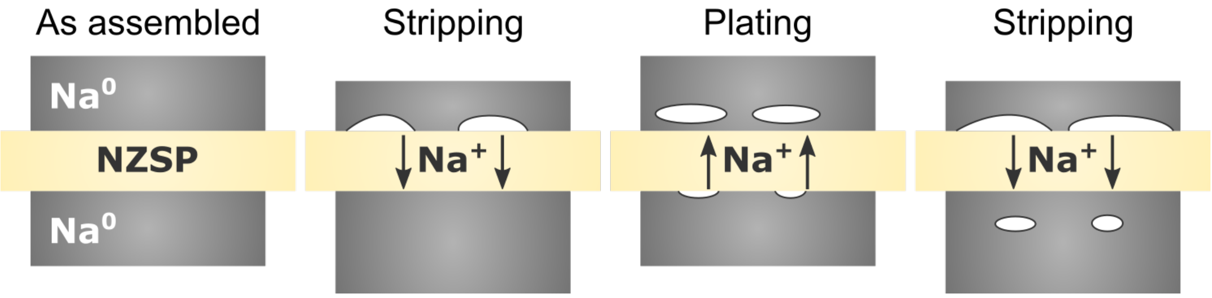

Figure 9.3: The "memory" effect affecting symmetrical cells. Voids formed on the first stripping half-cycle are not fully filled on the following plating half-cycle and become occluded. On the following stripping half-cycle, the cell potential will shoot up once the layer of Na^0 separating the interface from the occluded voids is stripped.

Impact of initial interface resistance

Chapter 6 demonstrated that the Na^0|NZSP interface resistance can be controlled by the surface treatments that NZSP pellets receive after sintering (for instance by polishing pellets). The impact of this source of interface overpotential on the CCD of cells is studied in this section. The data presented here were collected by our collaborators at Forschungzentrum Jülich (Dr. Qianli Ma, Dr. Frank Tietz) for a joint publication.[57]

For this experiment, three symmetrical cells were assembled with either an unpolished $NZSP_{\text{as sintered}}$ pellet (cell **a**), a roughly polished $NZSP_{\text{EtOH400}}$ pellet ((cell **b**), or a finely polished $NZSP_{\text{EtOH4000}}$ pellet (cell **c**). The results of the CCD experiment are presented in Figure 9.4. To facilitate the discussion of the CCD results, the cells impedance data is presented alongside. For their CCD measurements, our collaborators kept the dwell time at each galvanostatic half-cycles constant (5 minutes).

As already discussed in chapter 6, the cell with the lowest interface resistance (< 1 Ω cm^{-2}) is the one assembled with the $NZSP_{\text{as sintered}}$ pellet (cell (a)). From Figure 9.4(a), we see that cell (a) is also the one with the highest CCD (8 mA cm^{-2}). The CCD of cell (b) is slightly lower at 4 mA cm^{-2}. Finally, the CCD of cell (c) is one order of magnitude lower at 0.3 mA cm^{-2}. Cell (c) is also the one with the largest $R_{Na^0|NZSP}$ with a value exceeding 4000 Ω cm^{-2}. In comparison to the previous sub-section, large overpotentials are not observed in the results presented in Figure 9.4. This is in part because 5 min half-cycles at each current density are not long enough to induce significant void coalescence. For instance, at 8 mA cm^{-2}, only 0.67 mAh of Na^0 are transferred from one electrode to the other in 5 minutes.

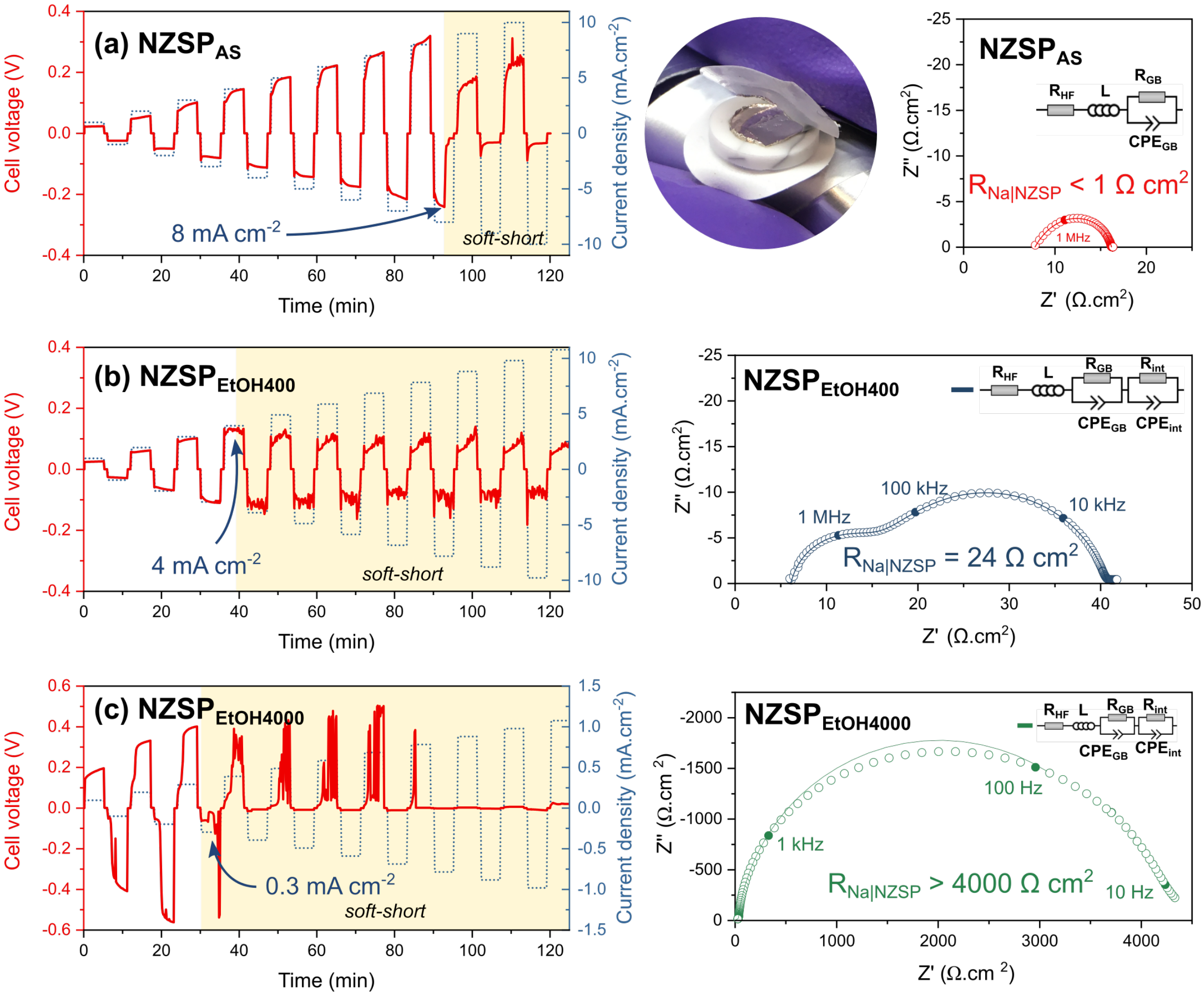

Figure 9.4: Impact of R$_{Na|NZSP}$ on the CCD of symmetrical cells. Evolution of the cell voltage of three cells during a CCD measurement as a function of their NZSP surface treatment. The Nyquist plots included alongside the CCD graphs show the Na^0|NZSP interface resistance of the cells after assembly. A photograph of cell (a) after it short-circuited shows that Na^0 filaments propagated through the NZSP pellet.

The influence of the alkali metal|SE interface resistance on the CCD of cells has been discussed in previous studies: typically, the lower the interface resistance, the higher the CCD.[25, 71] Our results confirm the correlation between a low interface resistance and high CCD. We can also observe that the cell potential does not immediately drop to 0 V once the cell is shorted but is quite erratic. This phenomenon is commonly observed when SEs fail and is attributed to "soft" short-circuits from extremely thin penetrating filaments. Because they are extremely thin, it is suggested that Joule heating can melt these filaments which momentarily breaks the filament and causes the cell potential to fluctuate.[118]

This section demonstrated that interface overpotentials, whether they originate from the accumulation of voids at the interface or from how the NZSP surface was treated, are correlated to cell failure by short-circuits. To minimize the risks of short-circuits, the adhesion of metal anodes towards ISE surfaces should therefore be improved. The thin sodium phosphate layer present on the surface of thermally treated NZSP pellets (Chapter 6) is suspected to serve that purpose, by acting as a contact mediator between Na^0 and NZSP (although more experiments would be required to confirm this hypothesis).

9.3 Delaying interfacial pore coalescence with formation cycles

The detrimental impact that interfacial voids have on the performance of the Na^0|NZSP interface during cycling has been established in the previous section. In particular, it was noticed in section 9.2 that, although the two Na^0|NZSP interfaces in a symmetrical cell should be similar, the largest overpotentials are always observed on odd half-cycles which suggest that the pores forming on the first half-cycle are the most detrimental to a cell. It was hypothesized that this phenomenon could be caused by preexisting interface defects which act as nucleating point for pore coalescence. Indeed, the procedure which is used to assemble cells consists in pressing the Na^0 electrodes against NZSP pellets with a moderate force. This method is unlikely to produce a perfect contact at the nano (even micro) scale and numerous defect site are probably present at the interface. This section explores whether the interface contact can be electrochemically improved by introducing formation cycles during which cells are cycled at low current densities and capacities.

For this, three symmetrical cells (assembled with $NZSP_{AS}$ pellets and 99 % pure Na^0

electrodes[2]) have been tested under harsh cycling regimes with the objective to reach a cycling current density of 10 mA cm^{-2} with half-cycle dwell times of 30 min (which would correspond to commercially relevant areal capacities of 5 mAh cm^{-2} equivalent to cycled thicknesses of Na^0 of 44 μm).[19]

For the first program (cell **i**), no formation cycles were employed and the cell was cycled directly at ± 10 mA cm^{-2} for 30 minutes half-cycles. This cell is a reference sample against which the performance of the other two cells can be compared. Unfortunately, an inadequate sampling rate was chosen when setting up the cycling program which explains why the data appears terraced. The evolution of the cell voltage for the first two half-cycles is presented in Figure 9.5(a). The cell voltage is initially stable for the first 2.5 minutes of stripping after which the cell voltage shoots up and continuously increases up to a value of 9.4 V at the end of the first half-cycle. During the following plating half-cycle, the cell potential remains at 0 V indicating that the cell has shorted. Cell (i), which was cycled with no formation cycles, was therefore able to withstand a current density of 10 mA cm^{-2} for 2.5 minutes before voids coalesced at the stripped interface (eventually leading to the cell shorting on the next half-cycle).

For the second program (cell **ii**), the symmetrical cell was also directly cycled at 10 mA cm^{-2} but, this time, the duration of the half-cycles was progressively increased from 30 seconds to 30 minutes. A large increase in the cell potential is only first noticed after the sixth stripping cycle corresponding to a dwell time of 5.5 minutes. Despite the clear formation of voids on stripping cycles, the cell survived until the thirteenth cycle when it shorted. With these formation cycles, the cell could withstand a 10 mA cm^{-2} current density for 12 minutes. Again, large overpotentials were not observed on even half-cycles (plating) which we attribute to the "memory" effect previously described in section 9.2.

For the third program (cell **iii**), both the current density and the duration of each half-cycle were progressively increased. The current density was increased from 1 mA cm^{-2} to 10 mA cm^{-2} in steps of 1 mA cm^{-2} and the duration of each half-cycle was increased from 30 seconds to 30 minutes. Figure 9.5(c) shows that by gradually increasing the galvanostatic dwell duration at the same time as the current density, the stripping and plating of Na^0 can be greatly stabilized. A large overpotential is only first noticed in the eleventh stripping cycle (15 minutes at 10 mA cm^{-2}). The overpotential is much larger when the dwell time is increased from 15 minutes to 30 minutes (the cell resistance increases to 798 Ω). Cell (iii) shorted on the following plating half-cycle, again following a

---

[2] the study was conducted prior to knowing about the impact of Ca poisoning

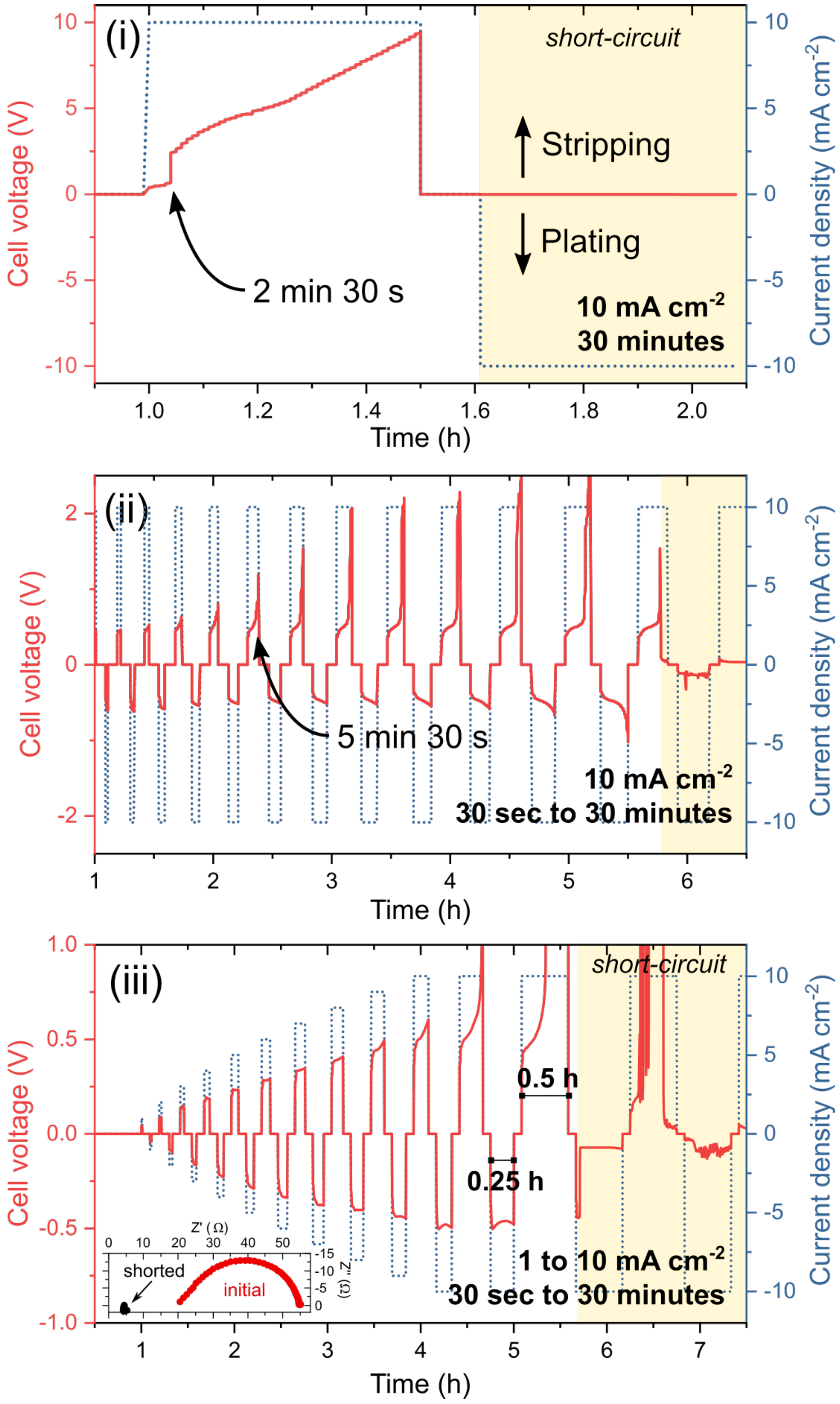

Figure 9.5: Delaying pore coalescence with formation cycles. The evolution of the cell voltage of three symmetrical cells differs depending on their cycling program: cell (i) has no formation cycles; for cell (ii), the current density is constant but the dwell time of each half-cycle is progressively increased; for cell (iii), both the dwell time and current density of each half-cycle are increased.

large increase in overpotential during a stripping half-cycle. With these formation cycles, the asymmetry in the plating and stripping half-cycles is also greatly reduced.

In summary, this experiment demonstrates that the onset for interfacial pore coalescence can be delayed by introducing formation cycles. These formation cycles were introduced to improve the contact at the Na^0|NZSP interface and mitigate the impact of cell assembly defects during the initial stripping cycles. The results presented here suggest that formation cycles can serve that purpose and are able to delay the apparition of an overpotential at a current density of 10 mA cm^{-2} from 2.5 minutes (when no formation cycles are employed) to 15 minutes (when they are). This is an impressive performance considering the large current density that the cells were cycled at and the absence of any pressure applied on the cells during cycling. Following these findings, formation cycles were routinely included at the beginning of each new electrochemical test (the formation cycle program consists in 1 minute half-cycles at ± 0.2 mA cm^{-2} for 2 hours).

9.4 Summary and future work

The promise that ASSBs could have virtually unlimited charging rates comes from the fact that, unlike conventional batteries, Na^0 or Li^0 plating in ASSBs is not a safety hazard requiring to slow down the charging rate. This promise has however proven to be hard to meet experimentally and the fast charging of ASSBs has so far been plagued by challenges at alkali metal|ISE interfaces. Two of theses challenges are the formation of voids at the interface during fast discharge and the propagation of metal filaments across the ISE during fast charge.

The experiments presented in this chapter demonstrates the great potential of NZSP electrolytes for high power batteries. The results presented in section 9.2 demonstrated that Na^0|NZSP|Na^0 symmetrical cells are readily able to withstand cycling at current densities of up to 10 mA cm^{-2} without sophisticated interface engineering. By way of comparison, a common objective for commercial ASSBs is to hold cycling at 10 mA cm^{-2} for 30 min half-cycles.[19]

Despite the tolerance that NZSP electrolytes display at withstanding large current densities, the results presented in this chapter also reveal that they are not readily able to withstand several cycles at such large current densities. The most important aspect to increase the longevity of cells seems to be maintaining the contact at the Na^0|NZSP interface. More specifically, the coalescence of pores at the Na^0|NZSP interface during stripping cycles should be prevented as a reduction of the interface area active for charge transfer considerably increases the risks of metal filament propagation on subsequent plating cycles.

Chapter 10

Future interface designs for high power SSBs

The coalescence of pores at metal|ISE interfaces under fast cycling conditions was identified in Chapter 9 as a major challenge limiting the power performance of SSBs. In this final chapter, two interface engineering strategies designed to prevent void formation are briefly explored. The first strategy (section 10.1) relies on maximizing the interface contact area by extending the interface in 3D (instead of a planar one). For the second strategy (section 10.2), a sodium-potassium alloy, liquid at room temperature, is employed instead of pure Na metal electrodes.

N.B. 1: These two strategies were initially designed as MSc research projects. Covid restrictions unfortunately prevented students from being allowed in laboratories to conduct experiments. The data for these two projects were collected as a side project and the results are therefore only preliminary.

N.B. 2: the 3D interface study was conducted prior to knowing that impurities could poison the Na/NZSP interface, 99 % pure Na metal electrodes were employed. The NaK alloy study employed 99.9 % pure Na metal to make the alloy and for the counter electrode.

10.1 3D interfaces

Taking inspiration from previous work from Hitz and Wachsman, a 3D interface architecture is investigated in this section as a solution to prevent void formation at the Na^0|NZSP interface.[20] In this cell architecture, the separator still consists of a dense NZSP pellet, but the anode consists of a NZSP scaffold in the pockets of which Na^0 can

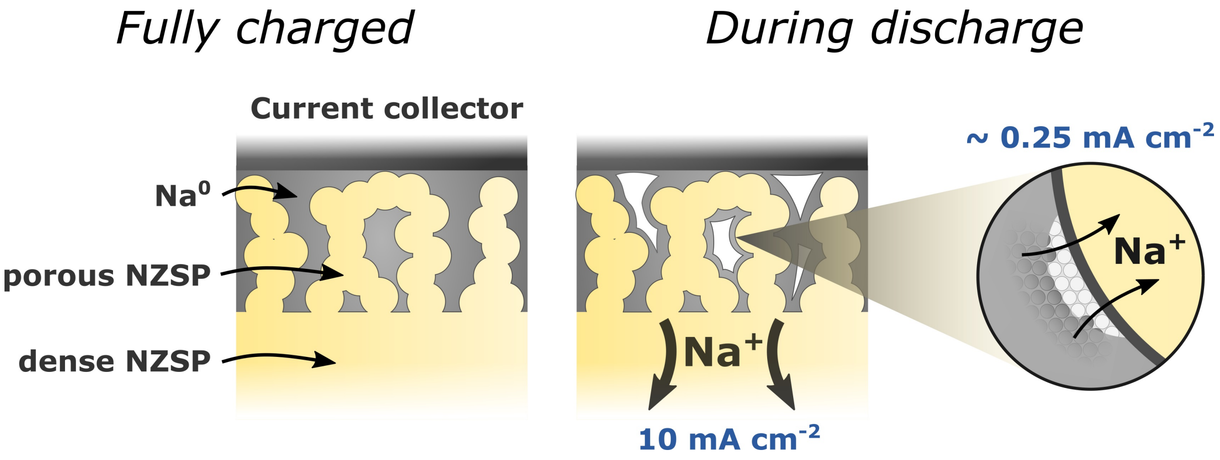

Figure 10.1: How 3D interfaces mitigate pore formation.

be plated/stripped (see Figure 10.1). Because the area of contact between NZSP and Na^0 is increased, the local current densities at each infinitesimal portion of interface in a 3D architecture can be reduced whilst maintaining a high apparent current density (at the cell level). In the previously cited study from Hitz *et al.*, the 3D interface architecture was estimated to increase the contact area by a factor of 40, thus reducing an apparent current density of 10 mA cm^{-2} to 0.25 mA cm^{-2} locally.[20] The porous ISE layer is typically obtained by using a sacrificial pore former and needs to be cosintered together with the dense ISE separator to ensure good ionic percolation. The steps of sample preparation and Na^0 infiltration are discussed in the following subsections.

Sample preparation and characterization

For this proof-of-concept experiment, the porous NZSP layer was created using rice starch (Sigma Aldrich) as a sacrifical pore former, following a previous study which had produced a porous NaSICON this way.[112] The scaffold (NZSP) to pore ratio is an important parameter to optimize in the porous layer. To maximize the cell's energy density, the fraction of NZSP needs to be minimized because this phase is not redox active. Yet, the fraction of NZSP also needs to be large enough for the scaffold not to be too fragile and for the electrochemical benefits of the 3D architecture to be obtained. Finding the optimum NZSP:pore ratio for the best performance was not the main objective of this study and only two compositions were tested here for the porous layer. The two porous layer compositions were obtained by mixing NZSP and starch powders in a 50:50 weight ratio (composition 1) and in a 25:75 ratio (composition 2). The NZSP and starch were

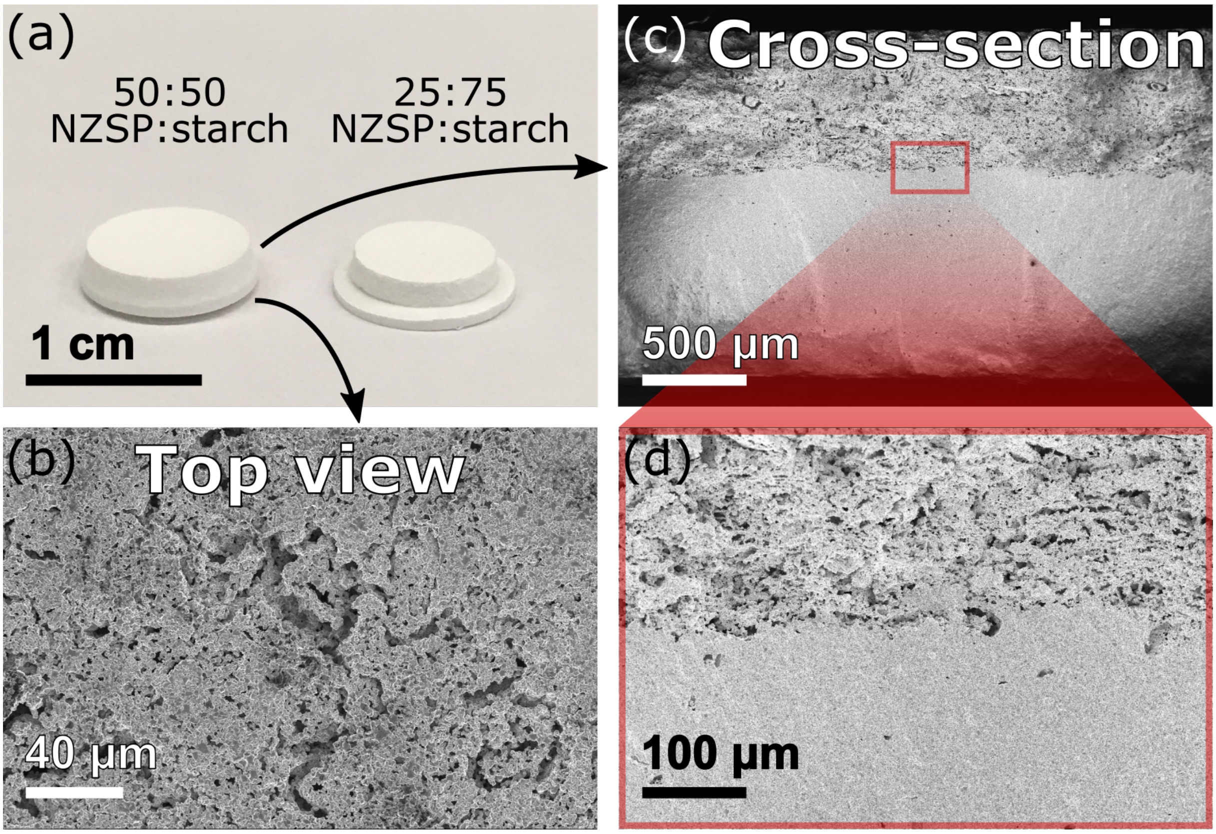

Figure 10.2: Cosintering of $\mathrm{NZSP_{dense}|NZSP_{porous}}$ bilayer samples. (a) Photograph of two bilayer pellets with different compositions (50:50 or 25:75) of the porous layer. (b) Top view SEM image of the porous layer obtained with a 50:50 (NZSP:starch) composite. (c) Cross-section SEM image showing good bonding of the $\mathrm{NZSP_{dense}|NZSP_{porous}}$ interface across the entire pellet. (d) Magnified view of a cross-section of the $\mathrm{NZSP_{dense}|NZSP_{porous}}$ interface.

thoroughly mixed using a vibrational mixer mill (Retsch MM 200). The bilayer pellets (a porous NZSP layer on top of a dense one) were produced by depositing a layer of the composite NZSP:starch powder on top of a bed layer of pure NZSP and then pressing the stack in a die with a load of 1.5 T for 1 min. The pellets were then sintered following the same sintering program as normal NZSP pellets.

Figure 10.2(a) is a photograph of the resulting two pellets after sintering. The porous layer (which is on top for both pellets) considerably shrank for the composition 2 which had the largest mass fraction of starch. The shrinkage is so large that the porous layer delaminated from the dense layer making this composition unusable. Some shrinkage of the porous layer is also noticeable in the 50:50 composition (the pellet is slightly warped)

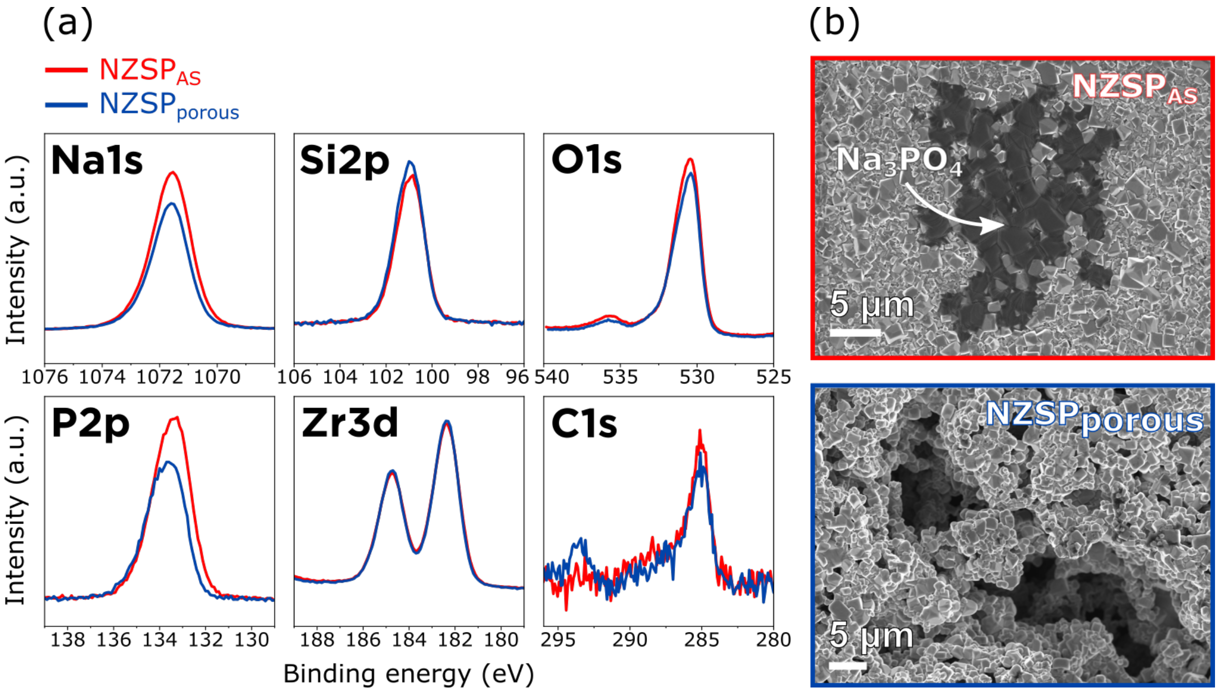

Figure 10.3: XPS analysis of the porous NZSP layer surface. (a) XPS comparison of the surface chemistry of $\mathrm{NZSP_{porous}}$ and $\mathrm{NZSP_{AS}}$ samples by XPS (charge correction: Zr3d5/2 at 182.4 eV; intensity normalization between samples: same Zr3d5/2 peak area). (b) Top view SEM images showing the presence of Na_3PO_4 islands on the surface of $\mathrm{NZSP_{AS}}$ pellets. Large Na_3PO_4 islands could not be found on $\mathrm{NZSP_{porous}}$ surfaces.

but the dense and porous layers are still joined. A microstructural characterization of the interface between the dense and porous layer by SEM (Figure 10.2(c) and (d)) reveals that the two layers are indeed well bonded together over the entire length of the interface. The SEM images also confirm that pockets are available for $\mathrm{Na^0}$ to plate in.

The surface chemical composition of the porous layer was analysed by XPS to assess whether residues from the decomposition of the rice starch during the cosintering step could be found on the surface of the NZSP phase. As discussed in Chapter 6, the presence of surface contaminants can negatively impact $\mathrm{R_{Na^0|NZSP}}$ which would make the benefits of this 3D architecture vanish. In Figure 10.3(a), the surface XPS signals from the surface of the porous NZSP layer and the XPS signal of a reference $\mathrm{NZSP_{AS}}$ pellet are compared. The results were normalized so that the area of the $\mathrm{Zr3d_{5/2}}$ peaks are the same and the BE scale was shifted so that the positions of $\mathrm{Zr3d_{5/2}}$ peaks align. The most important result is that the intensity of the C1s signal is similar on the surface of the porous layer and on the reference NZSP sample which suggests that the decomposition of the starch is complete and leaves no secondary phases. The other noticeable difference between the porous NZSP surface and the reference $NZSP_{AS}$ is that the surface concentration of Na and P is higher on the dense pellet. The higher concentration of Na and P is likely due to the presence of micrometric Na_3PO_4 islands on the surface of $NZSP_{AS}$ which could not be found on the surface of the porous NZSP (see Figure 10.3(b)). The XPS analysis confirmed that the porous NZSP surface composition has not been affected by mixing it with starch powder. Without the added complexity of new phases at the interface, it can be expected that charge transfer at the $Na^0|NZSP_{porous}$ interface will behave similarly than at the $Na^0|NZSP_{AS}$ interface. In particular, an intrinsically low $R_{Na^0|NZSP}$ can be expected. In the next section, the Na^0 infiltration technique in the pockets of the porous layer is presented.

Na^0 plating in the pores and electrochemical performance of the cell

The scaffold electrode structure produced in the previous section needs to be filled with Na^0 to become redox active. The first attempt consisted in melting Na^0 on top of a pellet and letting it sink by gravity into the porous layer. For this the NZSP sample was placed on a hot plate heated to 150 °C inside a glovebox with its porous layer facing upwards and a piece of fresh Na^0 was pressed against it (the melting point of Na^0 is 98 °C). Unfortunately this attempt was unsuccessful and did not result in any infiltration of Na^0 in the NZSP porous layer even when the temperature was increased to 200 °C. The formation of a passivation layer at the Na^0 surface might have prevented it from liquefying and infiltrating the electrode. Following this unfruitful attempt, Na^0 was plated in the pores electrochemically from a Na^0 counter electrode.

The electrochemical behaviour of a $Na^0|NZSP_{dense}:NZSP_{porous}|Na^0$ symmetrical cell in its first cycles is described in the following paragraphs. Na^0 is used as the *current collector* on the porous NZSP side because it is a ductile metal which gives a good contact area when it is pressed against the porous NZSP layer (unlike stainless steel which would only offer a few points of contact with NZSP). The decision to use Na^0 as the current collector can seem surprising at first, but the aim of the experiment was never to produce a cell with a commercially relevant architecture, but rather to produce a functioning composite electrode whose power performance could be tested against a conventional planar interface symmetrical cell.

The full cycling history of the cell is described in the four panels of Figure 10.4. Na^0

was plated/stripped in the NZSP porous layer during four cycles: the first two cycles were conducted at a moderate apparent current density of 0.35 mA cm^{-2}; the performance of the cell at higher current densities was tested in the following two cycles at 1 mA cm^{-2} and 5 mA cm^{-2} respectively (the cell shorted in the last cycle). Over the course of the experiment, potentiostatic impedance spectra were collected every hour to identify the processes responsible for overpotential increases (the galvanostatic cycling was stopped during the collection of these impedance measurements). The capacity of Na^0 required to fill the pores fully was calculated from an estimation of the pore volume obtained geometrically[1]: to achieve a full filling of the pores, a capacity of 6.96 mAh would need to be plated/stripped at each half-cycle. However, the counter electrode was too thin and could not provide this large capacity. So for each half-cycle, a capacity of 2.125 mAh was plated/stripped (*i.e.* the pores were filled to 30 % of their volume at the maximum).

The evolution of the cell potential during the first cycle is presented in Figure 10.4(a). The cycling of the cell started by a pore stripping half-cycle (I) instead of a plating one because of an error in setting up the potentiostat. Discontinuities in the cell potential can be noticed in cycle (II) and are due to the intermittent pauses imposed by the impedance measurements (they are not related to a erratic Na^0 plating/stripping behaviour). The cell voltage was smoothed with a 10 points adjacent average algorithm (this smoothing however did not remove all the discontinuities).

The coloured markers in panel (a) indicate the moments when the five impedance spectra presented in panel (b) were acquired (out of the forty spectra acquired during this first cycle, only five are represented). The impedance spectrum of the as-assembled cell (in light blue) consists of a single semi-circle with an apex frequency at 613 kHz. This semi-circle is attributed to grain boundary diffusion from the characteristic time constant extracted for the process ($\tau_{\text{NZSP-GB}}$ = 2.4x10^{-7} s). The two other impedance spectra from the stripping half-cycle (in darker shades of blue) are similar to the as-assembled impedance spectrum with the exception that the grain boundary semi-circle grows slightly and that a small semi-circle appears at low frequencies. This second semi-circle is likely related to an interface process (either the formation of voids, a SEI, or potentially Ca poisoning).

Two impedance spectra acquired during the pore plating half-cycle (II) are presented in green and red in panel (b). The grain boundary semi-circle considerably shrank during the pore plating cycles which could be a sign that the interface contact area increased and

---

[1] the pockets represent 50 % of the volume fraction in the porous layer from our geometrical calculations

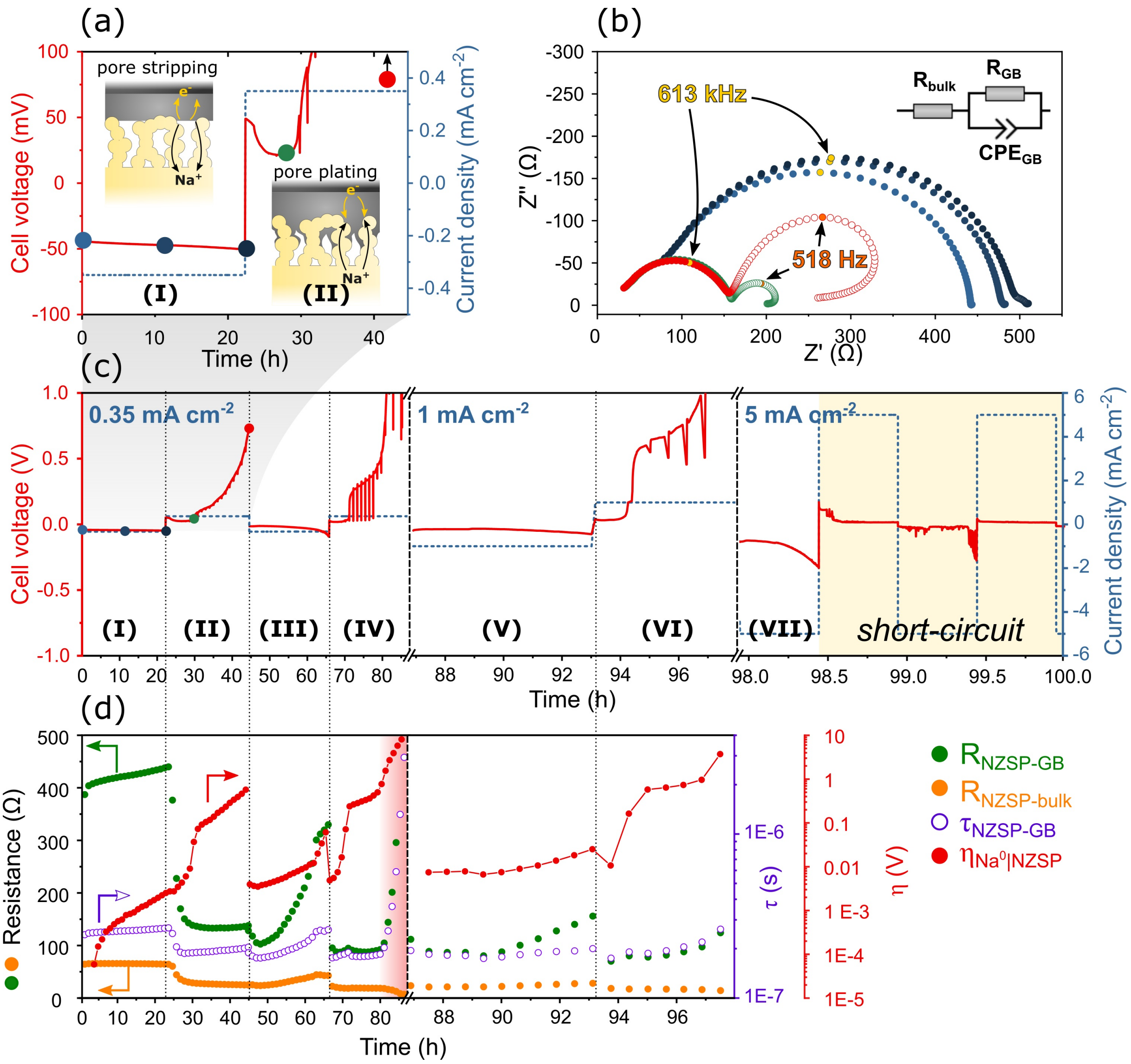

Figure 10.4: First cycles of a $Na^0|NZSP_{dense}:NZSP_{porous}|Na^0$ symmetrical cell (a) Evolution of the cell voltage during the first cycle at 0.35 mA cm^{-2}. The first half-cycle (negative current densities) is a pore stripping cycle followed by a pore plating cycle. The coloured dots are markers for the impedance spectra presented alongside in panel (b). (b) Selected impedance spectra acquired during the first cycle. Frequency markers for the semi-circles are presented as yellow/orange dots. Only the semi-circle corresponding to grain-boundary diffusion was fitted. The non-fitted part of the spectra is presented as open dots. The equivalent circuit used for the fit is presented in inset. (c) Evolution of the cell potential over its full cycling history: two cycles at 0.35 mA cm^{-2}, one cycle at 1 mA cm^{-2} and one cycle at 5 mA cm^{-2}. The reader will notice the variations in the scale of the time axis depending on the cycling current density. (d) Evolution of the cell electrochemical parameters extracted from its impedance spectra (no impedance spectra were acquired during the last cycle at 5 mA cm^{-2}).

that pores were filled with Na^0. A second semi-circle with an apex frequency of 518 Hz is now also clearly distinguishable. This second semi-circle is attributed to the diffusion of Na^+ ions across the interface. The inward tail at low frequencies suggests that the process has not reached equilibrium. It is surprising that the interface resistance increased during the pore plating cycles. Two hypotheses are proposed to explain the phenomenon: (1) the formation of pores on the counter Na^0 electrode; (2) or Ca poisoning as the Na^0 electrodes used in this experiment were only 99 % pure (see 7.2).

All the collected impedance spectra were fitted and the parameters extracted from the models are presented in panel (d). Because the interface contact area varies during the experiment, instead of reporting the grain boundary capacitance ($C_{\text{NZSP-GB}}$), the characteristic time constant of grain boundary diffusion is reported in panel (d): $\tau_{\text{NZSP-GB}} = R_{\text{NZSP-GB}}.C_{\text{NZSP-GB}}$. Because the interface semi-circles are distorted at low frequencies (inward tails), these parts of the spectra were not fitted. Instead, the evolution of the interface resistance is monitored in panel (d) by plotting the interface overpotential ($\eta_{\text{Na}^0|\text{NZSP}}$). The interface overpotential is calculated by subtracting the ohmic overpotential associated to the NZSP electrolyte from the cell potential measured just before the acquisition of a new impedance spectrum. More specifically, for an impedance measurement whose acquisition started at a time t_0 following a galvanostatic cycling step whose last datapoint was acquired at a time $t_0 - dt$, the interface overpotential is obtained by:

$$\eta_{\text{Na}^0|\text{NZSP}}(t_0) = E(t_0 - dt) - I(t_0 - dt).(R_{\text{NZSP-bulk}}(t_0) + R_{\text{NZSP-GB}}(t_0)) \tag{10.1}$$

with $E(t_0 - dt)$ and $I(t_0 - dt)$, the measured cell voltage and imposed current before the impedance measurement, and $R_{\text{NZSP-bulk}}(t_0)$ and $R_{\text{NZSP-GB}}(t_0)$ the bulk and grain boundary resistances extracted from fitting the impedance at time t_0. Having introduced the various elements of Figure 10.4, the following paragraphs discuss about the results. The half-cycles numbers in panel (c) will be used when referring to a specific half-cycle.

In half-cycle (I), Na^0 is stripped from the porous layer side and plated on the counter electrode. The NZSP electrochemical parameters do not vary much during this half-cycle: $R_{\text{NZSP-bulk}}$ is stable (around 64 Ω), $R_{\text{NZSP-GB}}$ increases from 386 Ω to 440 Ω, and $\tau_{\text{NZSP-GB}}$ is constant at around 2.5×10^{-7} s. The increase in the cell potential which was observed in panel (a) is mostly caused by the increase in $R_{\text{NZSP-GB}}$ but also partly by the increase in $\eta_{\text{Na}^0|\text{NZSP}}$: at the end of half-cycle (I), the interface overpotential is 2.5 mV.

In half-cycle (II), Na^0 is plated in the pockets of the porous layer side and stripped from the counter electrode. Plating Na^0 in the porous layer results in a rapid drop of

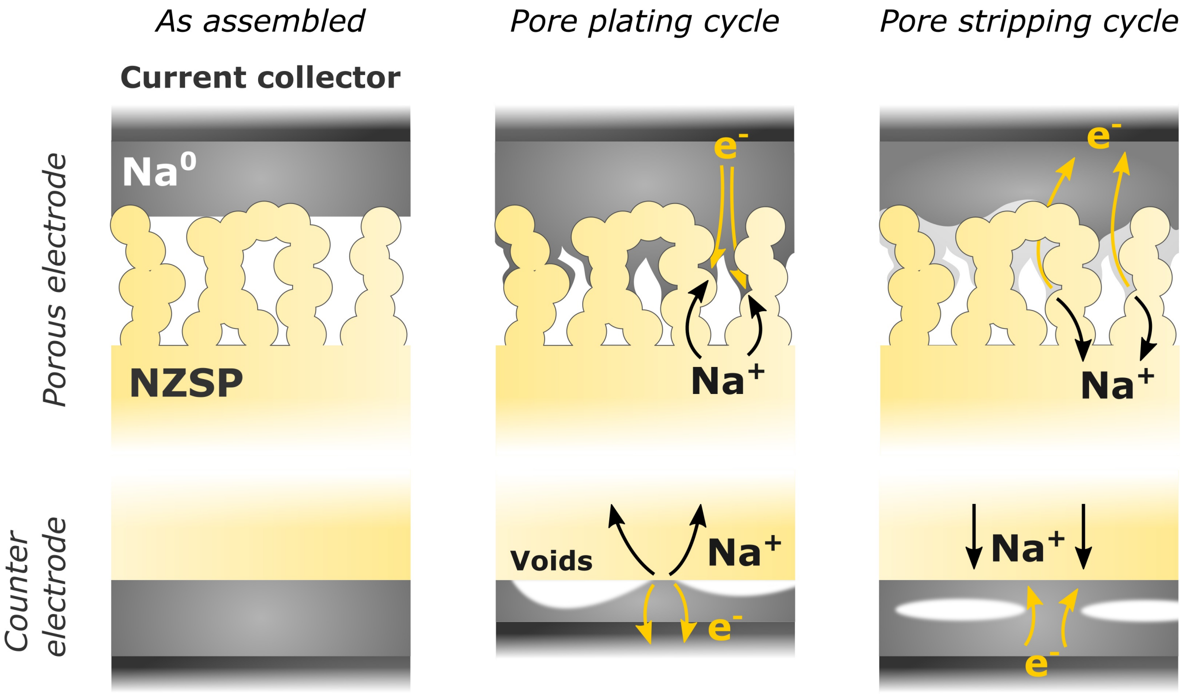

Figure 10.5: Plating and stripping cycles on the $Na^0|NZSP_{dense}:NZSP_{porous}|Na^0$ cell. The suggested impact of stripping/plating on both the porous and the counter electrodes are presented.

$R_{NZSP\text{-}bulk}$ (from 64 Ω to 24 Ω) and $R_{NZSP\text{-}GB}$ (from 440 Ω to 132 Ω). This drop in the NZSP resistance is likely due to an increase in the interface contact area once Na^0 plated in the porous layer. After this initial drop, $R_{NZSP\text{-}bulk}$ and $R_{NZSP\text{-}GB}$ then remain stable for the rest of half-cycle (II). The large increase in the cell potential in the second part of half-cycle (II) is caused by an interface overpotential which increases from 9 mV (at 28.7 h) to 570 mV (at 43.6 h). Unfortunately, in the absence of a reference electrode, it is not possible to determine whether this interface overpotential comes from the porous electrode or from the counter electrode. Considering that 2.125 mAh of Na^0 is plated/stripped at each half-cycle, it is very likely that interfacial voids form on the counter electrode as schematically represented in Figure 10.5.

The stripping of Na^0 from the porous layer in half-cycle (III) results initially in a further reduction of $R_{NZSP\text{-}GB}$ and $R_{NZSP\text{-}bulk}$ followed by a large increase (from 102 to 330 Ω for $R_{NZSP\text{-}GB}$ and from 23 to 42 Ω for $R_{NZSP\text{-}bulk}$). The large increase in the NZSP resistances can be attributed to the progressive loss of interface contact area as Na^0 is stripped from the porous layer. Future experiments will have to identify why $R_{NZSP\text{-}GB}$ increases faster than $R_{NZSP\text{-}bulk}$. It is suggested that ionic conduction in the porous NZSP layer deviates from the ideal isotropic conditions of the brick layer model and could partly explain the resuts.

Similar trends are observed for the half-cycles (IV) to (VI). To only mention two important events which occurred during these half-cycles:

- $\eta_{\mathrm{Na^0|NZSP}}$ increases a lot during half-cycle (IV) and reaches 8 V at the end of the half-cycle. Towards the end of this half-cycle, the grain boundary semi-circle was highly distorted by the interface semi-circle in the Nyquist plots which resulted in large errors in the data fitting. This region is indicated in panel (d) by a red box and the large increase in $\mathrm{R_{NZSP\text{-}GB}}$ is considered to be a fitting artefact (especially considering that $\mathrm{R_{NZSP\text{-}bulk}}$ drops simultaneously and that $\tau_{\mathrm{NZSP\text{-}GB}}$ changes by an order of magnitude)
- at the end of half-cycle (VI), $\eta_{\mathrm{Na^0|NZSP}}$ again reaches a large value of 3.7 V

The cell withstood the stripping half-cycle (VII) at 5 mA $\mathrm{cm^{-2}}$ well but ultimately shorted on the following plating half-cycle (VIII).

Summary

The experiment described in this section was designed as a proof-of-concept to study whether 3D electrodes could prevent the formation of voids at the $\mathrm{Na^0}$|NZSP interface during stripping at high apparent current densities. Some challenges unfortunately prevented us from answering this initial research objective in the short amount of time we had to conduct this experiment. In particular, employing a planar $\mathrm{Na^0}$ counter electrode where voids can form during cycling made it impossible to know where the large interface overpotentials originated from. Integrating a reference electrode in the cell design would be an important next step to help answer that question.

Although the study did not meet our initial research objective, very promising preliminary preliminary results were obtained. These positive results include:

- the possibility to create an interconnected NZSP scaffold by simply cosintering a NZSP:starch composite powder
- a confirmation by XPS that the cosintering of the NZSP:starch composite does not affect the surface chemistry of NZSP in the porous layer

- and a proof that Na^0 can be readily plated in the porous layer without necessarily employing interlayers

Regarding this last bullet point, an interlayer might nonetheless be required in future cell designs to help with the initial plating of Na^0 in the porous layer. Such interlayers are conventionally used in the cell architectures developed by the group of Eric Wachsman. Among the interlayers they have reported to promote wetting of Li^0 on LLZO, they have used: lithiophilic interlayers (for instance Al_2O_3, which, through a reactive wetting mechanism promotes the spreading of Li^0 along the interface),[20] and electron conducting interlayers (for instance an amorphous carbon coating which provides electronic pathways at the surface of the entire porous layer and enables plating to initiate not only close to the current collector in the first cycles but at every infinitesimal portion of interface).[181]

Last, completing the study will also require to include a microscopic characterization of sample cross-sections at different points during cycling to confirm that Na^0 plated in the porous layer.

10.2 NaK alloy anode

In this last section, preliminary results of another experiment attempting to minimize void formation at the Na^0|NZSP interface are briefly summarized. The strategy explored here relies on using a liquid NaK alloy anode to improve wetting at the NaK|NZSP interface and minimize void formation. This study was inspired by the recently reported outstanding power performances of alkali metal|ISE interfaces operated above the melting point of the alkali metal (for instance at the Na^0|Na-β/β"-alumina or the Li^0|LLZO interfaces).[24, 113] Instead of increasing the cell temperature, an alloy which is liquid at room temperature is employed in this section. An asymmetric Na|NZSP|NaK cell was assembled with the objective of testing the maximum current density at which the NaK electrode could be stripped before a large overpotential would be observed.

Cell assembly

Conventionally employed cell formats (coin, pouch, Swagelok cells) are unsuitable for containing liquid anodes. A different cell setup therefore had to be employed for the experiment. This cell setup is schematically represented in Figure 10.6(a). In this cell, the NaK alloy electrode is deposited as a droplet on top of a $NZSP_{AS}$ pellet with Na^0 as counter electrode. The top part of the cell holder has a hole which allows to see the droplet

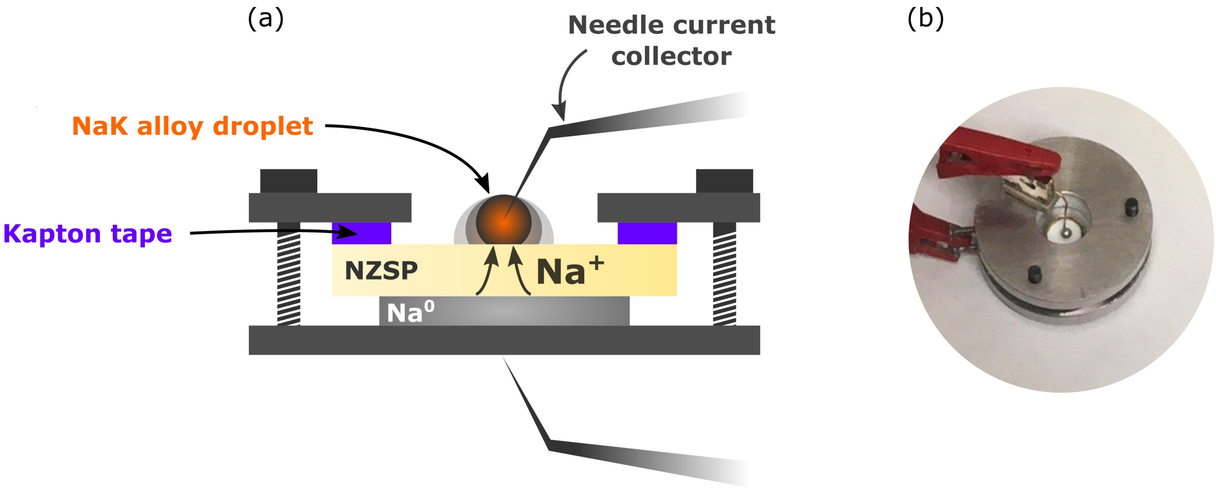

Figure 10.6: Cell setup employed to test the NaK alloy cells.(a) Schematic view of a cross-section, and (b) Photograph.

in Figure 10.6(b). A needle in contact with the droplet was used as current collector. The outside edge of the NZSP pellet was electronically insulated from the metallic holder using Kapton tape.

The NaK alloy was produced inside an Ar filled glovebox by putting two pieces of Na^0 and K^0 in contact in a clean glass vial. The produced alloy was a 50:50 wt % Na-K alloy which, as can be seen from the Na-K phase diagram in Figure 10.7, is liquid above 2 °C.[182] At 25 °C, the Na-K alloy is liquid for compositions ranging from 42 wt. % to 90 wt. % of K. The objective is to stay in that compositional range during Na^0 stripping/plating for the NaK alloy to remain liquid.

All the steps of cell assembly and electrochemical testing were performed inside an Ar filled glovebox. The Na^0 counter electrode was first pressed against the NZSP pellet before a droplet of the NaK alloy was deposited on the other interface using a syringe. A poor wetting (large contact angle) of the NaK droplet on the NZSP surface can be observed in Figure 10.6(b). The results of the first plating cycle are presented in the following subsection.

Electrochemical results

The evolution of the Na^0|NZSP|NaK cell potential in its first galvanostatic plating cycle (Na^0 is plated at the NaK interface) is presented in Figure 10.8(a). During the 7 h 40 min of plating, the composition of the alloy can be considered to have remained

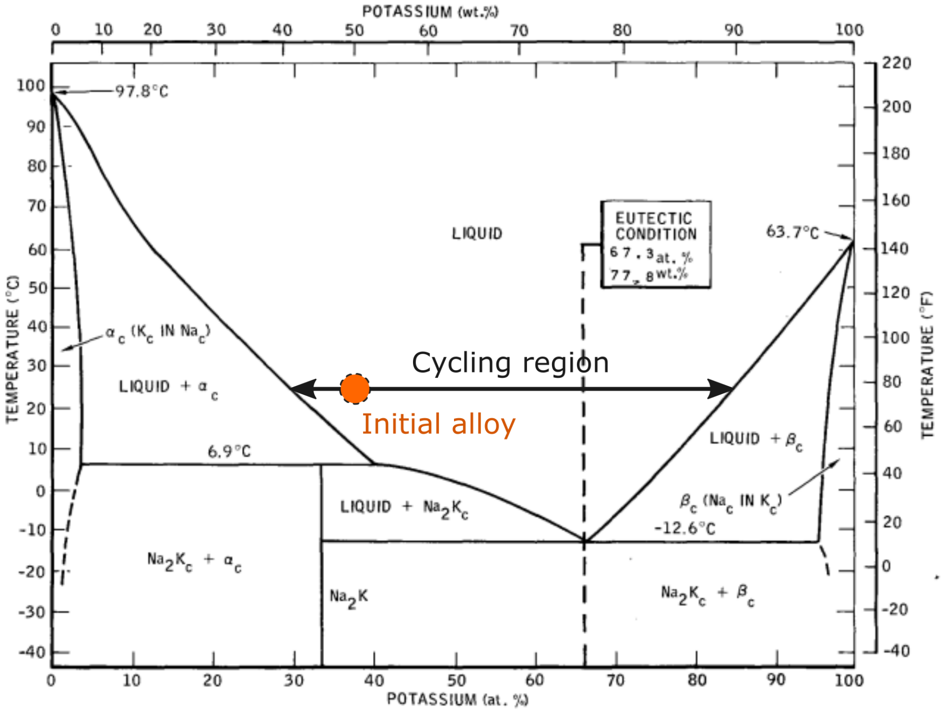

Figure 10.7: Na-K phase diagram. Reproduced from [182]

constant. Indeed, only a small Na^0 capacity of 6.94 10^{-2} mAh was transferred from the counter electrode to the NaK electrode which corresponds to a mass of 5.96 µg of Na^0. In comparison to the mass of the NaK droplet which was estimated to be 3.8 mg, this Na^0 addition is therefore negligible and the composition of the NaK alloy did not change significantly.

The coloured dots in Figure 10.8(a) indicate the moments when the plating was stopped to acquire impedance spectra which are presented in the form of Nyquist plots in Figure 10.8(b). The Nyquist plots show two well-resolved semi-circle attributed to grain boundary diffusion (semi-circle with an apex frequency of 774 kHz) and interface diffusion (semi-circle with an apex frequency of 260 Hz).

The initial impedance of the cell (before plating started) is largely dominated by its interface semi-circle. The data was fitted to the equivalent circuit included above panel (b) and the resistance of the NZSP|NaK interface was $9.2\text{x}10^4$ Ω. The values of $R_{\text{NZSP-bulk}}$ and $R_{\text{NZSP-GB}}$ which were extracted from the fit can be used to estimate the contact area at the NZSP|NaK interface. Assuming a circular interface contact area and an ionic conductivity of $\sigma_i = 5$ mS cm^{-1} for the NZSP pellet, the diameter of the contact area is

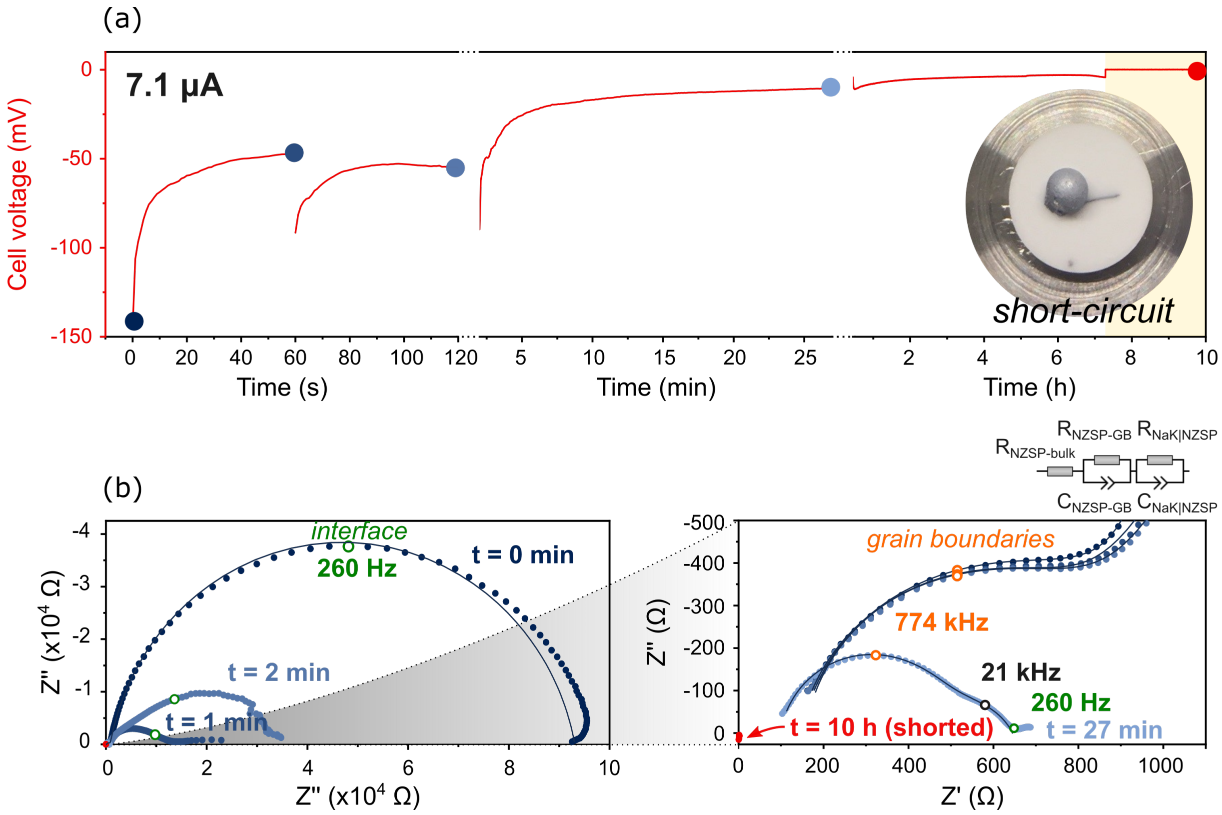

Figure 10.8: Electrochemical behaviour of a Na^0|NZSP|$NaK_{50:50}$ cell during a plating cycle of the alloy electrode. (a) Evolution of the cell voltage during four galvanostatic cycles at an imposed current of 7.1 µA. A photograph of the cell after it short-circuited is included in inset. (b) Impedance spectra of the cell at regular intervals represented as Nyquist plots.

estimated to be 2 mm. The small plating current of 7.1 µA therefore corresponds to a 0.225 mA cm^{-2} current density at the NZSP|NaK interface.

The first three impedance spectra showed in panel (b) (up to t = 2 min) indicate that the NZSP|NaK interface resistance is greatly reduced in the first minutes of Na^0 plating. The grain boundary semi-circles of these first three impedance spectra overlap which suggests that the area of the NaK droplet has not changed. The interface semi-circle of the impedance spectra collected at t = 1 min and t = 2 min have an outward extending tail at low frequencies which indicates that the probed interface process has not reached equilibrium. During the ~5 minutes that the measurement of an EIS spectrum takes, the composition of the NaK droplet will progressively homogenize (it is likely that a concentration gradient exists at the end of a plating step, with an enrichment of Na near the interface). An explanation for the presence of the outward extending tails could be that the NaK|NZSP interface resistance is larger than the Na|NZSP one.

The impedance spectra collected at t = 27 min has a much smaller interface semi-circle (170 Ω) and also a smaller grain boundary semi-circle. The reduction of the NZSP bulk and grain boundary resistance could be due to a change in the NZSP|NaK interface contact area. If so, using previous assumptions, the droplet diameter would have increased to 2.7 mm. The cell potential after 27 minutes of plating has dropped to 10.5 mV in panel (a).

From 27 min to 7 h of plating, the cell potential continues to decrease down to 3 mV. The cell shorted after 7 h and 40 min of plating. A crack filled by metal can clearly be seen in the middle of the NZSP pellet in Figure 10.8(a). The failure of the cell by fracture of the NZSP pellet was observed in four other cells tested in the same conditions. It therefore seems to be a generic failure mechanism.

Future experiments will have to identify what causes NZSP to crack at such low plating rates. The cracking could be due to a reaction of the NaK alloy with the NZSP pellet (an interfacial reaction energy of -0.177 eV/atom between NaK and $Na_3Zr_2Si_2PO_{12}$ was calculated from the Materials Project database). The design of the cell is also not ideal since the NaK droplet is exposed to the glovebox atmosphere: this resulted in the formation of a passivation layer on the droplet surface (as can be noticed on the photograph in inset of Figure 10.8). It may also be that the interface contact area (estimated from the grain boundary resistance extracted from EIS fitting) was in reality much lower. As a consequence, the current densities may have been much larger locally which could have resulted in the nucleation of metal filaments 9.

10.3 Summary

Preventing pore coalescence at metal|ISE interfaces will be crucial for the longevity of SSBs. This chapter provided an example of two interface engineering strategies designed at preventing pore coalescence at the Na|NZSP interface. The results presented in this chapter are only preliminary and future studies will have to confirm the efficacy and viability of the 3D interface and NaK anode concepts.

Chapter 11

Conclusion and Future work

Using the Na|NASICON interface as a model system, this thesis investigated the viability of employing alkali metal negative electrodes in room temperature SSBs with oxide solid electrolytes. This study more specifically focused on how the reactions occurring at Na|NZSP interface can affect the power performance and longevity of SSBs.

The basis of all the experiments developed in this work rests on the synthesis of technologically relevant NaSICON separators. Crucial steps of the synthesis enabling to obtain dense (> 96 % of the theoretical density) and phase pure NaSICON pellets with a high room temperature ionic conductivity ($\sigma_{\text{i-bulk}}$ = 12-15 mS cm^{-1} and $\sigma_{\text{i-total}}$ = 3-5 mS cm^{-1}) and a low electronic conductivity (σ_{e} = 1.9 10^{-9} S cm^{-1}) were discussed in **Chapter 5**. An important discovery established in this Chapter is that the addition of an off-stoichiometric excess of Na and P during the synthesis (in the ratio $Na_{3.4}Zr_2Si_{2.4}P_{0.6}O_{12}$.1.5% Na_3PO_4) improves the quality (phase purity, density) and performance (ionic conductivity) of pellets. As a first report of this empirical observation, this work could provide a seed for future experiments to explain the dynamics of phase separation and grain boundary formation during the sintering of NaSICON phases.

The study on the optimization of the Na|NZSP interface resistance described in **Chapter 6** was motivated by the observation that the values reported in the literature varied by orders of magnitude and that cell-assembly protocols had not been systematically studied. In an attempt to assess whether contaminants on NZSP surfaces could explain large Na|NZSP interface resistances (a mechanism which had previously been identified at other metal|ISE interfaces), our study demonstrated that the surface composition of NZSP pellets changes under the action of a thermal treatment. More specifically, the characterization of NZSP surfaces by XPS and LEIS revealed that a thin sodium phosphate layer terminates the surface of thermally treated samples. DFT calculations suggested that a minimization of the NZSP surface energy could be the driving force for the formation of the surface layer. The Na|NZSP interface resistance of cells having sodium phosphate terminated NZSP pellets is consistently below 1 Ω cm^2 which would suggest that the presence the layer improves the adhesion of Na metal towards NZSP. The excellent performance of as-sintered NZSP separators is very promising for industrial prospects because very few processing steps are required to produce half-cells with low ohmic losses.

The stability of the Na|NZSP interface was first assessed in **Chapter 7**. A degradation process leading the Na|NZSP interface resistance to increase uninterrupted in the first few days following cell assembly was detected by time-resolved EIS. Whilst it was initially believed that this increase in resistance could be related to the formation of a resistive interphase from the decomposition of NZSP in contact with Na^0, the analysis of both NZSP and Na^0 surface compositions of disassembled aged cells by XPS paradoxically refuted this hypothesis. Instead, the results presented in Chapter 7 revealed that contaminants present in metal electrodes can poison the Na|NZSP interface. By increasing the purity of the Na metal electrodes from 99 % to 99.9 %, the degradation observed in the first days after cell assembly was efficiently suppressed. To the best of our knowledge, this mode of interface degradation has not yet been described in the literature for room temperature SSBs. It is expected to be not only limited to Na|NZSP interfaces but also affect other Na-SSBs. An important consequence for the manufacturing of Na-SSBs is that high purity Na metal electrodes or "anode-free" cell architectures should be employed.

The electrochemical stability of NZSP in contact with a pure Na metal electrode was investigated in **Chapter 8**. To achieve this, a newly developed XPS protocol was employed, whereby the metal electrode is plated on the ISE surface whilst the composition of the metal|SE interface is simultaneously analysed. The study demonstrated the formation of reduced Zr species when Na^0 is plated on the surface of NZSP samples. The extent of reduction was shown to depend on preceding NZSP surface treatments, and in particular, polished NZSP pellets produced a thicker interphase in contact with Na^0 in comparison to as sintered NZSP pellets. The study also demonstrated that, in both cases, the interphase eventually stopped growing. Although the species contained in the decomposition layer were not uniquely identified in this study, the fact that the interphase growth is self-limiting indicates that the decomposition species are certainly electronically insulating and that a stabilizing SEI forms. Paradoxically, this chapter clearly suggested that NZSP forms a SEI in contact with Na^0 whereas a decomposition was barely detectable by XPS in Chapter 7. It remains to be demonstrated if the formation of a SEI at the

Na|NZSP interface is a kinetically limited process which might have been activated by the bombardment of the interface with electrons in the *operando* experiment.

The two final chapters of this thesis (**Chapters 9** and **10**) explores the ability of the Na|NZSP interface to support high plating and stripping rates. It was demonstrated that Na^0|NZSP|Na^0 symmetrical cells are readily able to withstand cycling at current densities of up to 10 mA cm^{-2} (generally considered as a target current density for fast-charging SSBs) without sophisticated interface engineering. This highlights the great potential of NZSP electrolytes for high power batteries. The challenge is to maintain this performance over multiple cycles with large plated/stripped capacities. In particular, the coalescence of pores at the Na^0|NZSP interface during stripping cycles was identified as the main issue to solve. Chapter 10 concludes this study with two interface engineering attempts aimed at preventing void formation: the first relies on the maximization of the interface active area by employing a 3D interface; the second relies on employing a room temperature liquid alloy to improve wetting.

In recent years, research in the field of solid-state batteries (SSBs) has reached a sufficient maturity to affirm with ever more confidence that SSBs will eventually be able to replace conventional liquid electrolyte batteries in applications where energy density or safety are important. Several startups have announced that they were starting to take their prototype cells out of their laboratories to make them enter the next stages towards commercialization (*e.g.* QuantumScape, Solid Power). These announcements are inspiring but should not hide that a lot of research will still be required to improve the performance and longevity of this first generation of cells.

Suggested future work

Ending a PhD is a frustrating experience. It is at a time when ambitious experiments can be more easily conceptualized that, unfortunately, a finish line must be drawn. Summarized below are some of the experiments I think would be worth investigating in the future regarding interfaces in SSBs and the Na|NaSICON system.

At several points towards the end of this work, I realized that a lot of characterization work was still required to understand the structure of $Na_{3.4}Zr_2Si_{2.4}P_{0.6}O_{12}$ separators better. As evidenced by previous structural studies from our colleagues at Forschungszentrum Jülich (and also by our XRD results in Chapter 5), the $Na_{3.4}Zr_2Si_{2.4}P_{0.6}O_{12}$ stoichiometry is metastable and produces multiphasic samples after sintering consisting of two NaSICON phases (monoclinic and rhombohedral) and intergranular "complexions".[16] This metastability was also predicted in recent computational work.[165] The dynamics of phase separation during sintering need to be better understood. Some answers to these questions could possibly be provided experimentally by sintering NZSP pellets *in operando* in a high-temperature XRD, or computationally by employing large scale ab-initio molecular dynamics simulations. Having access to the exact composition of grain boundaries would be extremely informative to understand the electrochemical properties of NZSP pellets. Measuring the composition of grain boundaries requires instruments with an atomic scale precision. Thus, it is suggested that Atom Probe Tomography (APT) or Transmission Electron Microscopy (TEM) could be used for that purpose. A TEM study of NZSP samples was attempted in this study in collaboration with Dr. Rowena Brugge, however NZSP samples were extremely beam sensitive and experienced radiolysis damage (amorphization). It is therefore suggested to perform the study under cryogenic temperatures (cryo-TEM) to minimize sample damage.

Depending on the XPS protocol employed to characterize the Na|NZSP interface, it was established in this thesis that NZSP either forms a kinetically stabilized interface or a self-limiting SEI with Na^0. Additional experiments will be required to validate one of the scenarios and to identify the composition of the SEI phases. Other XPS protocols could for instance be employed, such as the one designed by Wenzel *et al.* where a thin layer of metal is sputtered *in-situ* on the SE pellet (see Figure 3.4).[95] The unique capabilities of the newly commissioned Hi5 instrument at Imperial College London (a focused ion beam secondary ion mass spectrometer, FIB-SIMS) could also certainly help to answer some of these questions: with its high energy Xe^+ primary ion beam, the interface would be accessed by sputtering one of the Na metal electrodes of an aged cell; and, without ever exposing it to air, the simultaneous collection of negative and positive ions from the interface would inform about the formation of a SEI, its thickness, and its compositional homogeneity.

Guaranteeing the long-term performance of SSBs operated at high current densities will require to solve the problem of pore coalescence at the interface. Recent computational models indicate that the crux of the problem is to increase the adhesion between the metal electrode and SE surface.[183] Thus, sodiophilic interlayers could well provide a solution to prevent void formation, provided that a solution is found to improve their long-term morphological stability (see section 3.2). In parallel, the strategies already briefly explored in Chapter 10 in this thesis could be perfected. For instance, the morphology of the 3D interface could be greatly improved by introducing more advanced techniques to form a porous scaffold such as freeze drying. This would allow to obtain a porous electrode with a low volume fraction of SE which would be ideal not to impact the energy density of cells too much. Promising results with freeze-dried NZSP scaffolds were obtained from an experiment in collaboration with Dr. Maria Crespo. As a next step, this porous scaffold will have to be produced and sintered on top of a dense NZSP separator.

Regarding the fabrication of SE separators, one of the engineering challenge ahead will be to develop manufacturing techniques able to produce thin, dense separators (10-100 μm) at a large scale and a fast pace.

For NZSP to be qualified as a SE for industrial applications, electrochemical tests under cycling conditions over more extended time periods would be required to identify any possible long-term degradation. The integration of cathodes into full cells will also bring its own challenges.

Appendix A

Deriving an Arrhenius type relationship for the ionic conductivity

The aim of this Appendix is to establish from fundamental equations why the conductivity can be described by an Arrhenius type relationship (and thus find the missing link between equations 2.3 and 2.4). The following derivation assumes that the individual ion jumps are non-correlated.

At resting state (no potential applied across the electrolyte) a mobile cation will attempt to jump to a neighboring vacant site at a frequency ν_0 called the attempt frequency. All jump attempts will not be successful. Assuming that the migration is 1D along the x axis (as schematically represented in Figure 2.3), the jumps can either happen in the forward (ν_+) or reverse (ν_-) direction. Successful jumps will happen a jump frequency ν in either direction according to:

$$\nu_\pm = \nu_0.exp\left(\frac{-\Delta G_m}{k_B T}\right) = \nu_0.exp\left(\frac{\Delta S_m}{k_B}\right).exp\left(\frac{-\Delta H_m}{k_B T}\right) \tag{A.1}$$

where ΔG_m, ΔS_m, and ΔH_m are the free energy, entropy, and enthalpy of migration (with $\Delta G_m = \Delta H_m - T\Delta S_m$), ν_0 is the attempt frequency, k_B is the Boltzmann constant, and T is the temperature. The attempt frequency ν_0 is often approximated to the Debye frequency of the solid. Another approximation for ν_0 which reveals its parameters of influence was given by Rice and Roth[184]: $\nu_0 = 1/\alpha_0.\sqrt{2.\Delta H_m/M}$, where α_0 is the jump distance for the mobile cation and M is its mass. This expression indicates that mobile cations will vibrate faster (consequently increasing their jump frequencies) if the distance between sites is smaller (smaller α_0), the walls of the energy well are steeper (larger ΔH_m), or if the moving particles are lighter (lower M).

What equations A.1 tells us, is that at 0 K no jumps will occur, but that the jump frequency increases exponentially with temperature. The velocity of mobile particles in direction x (v_x) is related to ν_+ and ν_- by:

$$v_x = \frac{1}{2}\alpha_0.(1-c).(\nu_+ - \nu_-) \tag{A.2}$$

where $\frac{1}{2}\alpha_0$ is half the distance between two stable sites, $(1-c)$ is the fraction of nearest neighbor sites that are empty, with c the concentration of energetically equivalent sites which are occupied. At rest, the probability for a mobile cation to jump forward or reverse is equal ($\nu_+ = \nu_-$). The velocity v_x therefore averages to zero which is what is observed in practice: there is no net current flux in the absence of an applied potential. This does not mean that the mobile cations remain in the same position (in fact, at room temperature, cations in superconducting ISEs will travel considerable distances) but just that the random migration of cations does not result in a net flux.

To find the missing link between equations 2.3 and 2.4, one needs to consider what happens when an electric field E is applied.

The application of an electric field E across a solid electrolyte changes its energy landscape (as represented by the dashed line in Figure 2.3): in the forward direction, the energy barrier is lowered by $-\frac{1}{2}\alpha_0 qE$ whilst in the reverse direction, the energy barrier is increased by $+\frac{1}{2}\alpha_0 qE$. One can quickly find that this expression is homogeneous to an energy by remembering that an electric field is the spatial derivative of an electrical potential ϕ ($E = \frac{d\phi}{dx}$, if the electric field is applied along the x-axis); multiplying E by a distance $\frac{1}{2}\alpha_0$ (which corresponds to half the distance between mobile cation sites, i.e. the distance between an energy minimum and an energy maximum on an ion migration pathway) yields a potential difference $\Delta\phi$. And the multiplication of a potential difference by a charge q is homogeneous to an energy. This change in activation energy results in an increased jump frequency in the positive direction. More precisely:

$$\nu_+ = \nu_0.exp\frac{\Delta Sm}{k_B}.exp\frac{-(\Delta Hm - \frac{1}{2}\alpha_0.q.E)}{k_B T} = \nu_0.exp\frac{-\Delta Gm}{k_B T}.exp\frac{\frac{1}{2}\alpha_0.q.E}{k_B T} \tag{A.3}$$

$$\nu_{-} = \nu_0 .exp\frac{\Delta Sm}{k_B}.exp\frac{-(\Delta Hm + \frac{1}{2}\alpha_0.q.E)}{k_B T} = \nu_0.exp\frac{-\Delta Gm}{k_B T}.exp\frac{-\frac{1}{2}\alpha_0.q.E}{k_B T} \quad \text{(A.4)}$$

Combining equations A.2, A.3, and A.4, the velocity of charge carriers (v_x) then becomes:

$$v_x = \frac{1}{2}\alpha_0.(1-c).\nu_0.exp\frac{-\Delta Gm}{k_B T}\left(exp\left(\frac{\frac{1}{2}\alpha_0.q.E}{k_B T}\right) - exp\left(\frac{-\frac{1}{2}\alpha_0.q.E}{k_B T}\right)\right) \quad \text{(A.5)}$$

For $\alpha_0 qE << 2k_B T$ the difference in exponential terms can be simplified to $(\frac{\alpha_0.q.E}{k_B.T})$ since the first order Taylor series approximation of $exp(x)$ is $1 + x$.

Rewriting Equation A.5 yields:

$$v_x = \frac{1}{2}{\alpha_0}^2.(1-c).\nu_0.\frac{q.E}{k_B.T}.exp\frac{-\Delta G_m}{k_B T} \quad \text{(A.6)}$$

This expression describes the velocity of particles in one dimension. To obtain the velocity of particles in three dimensions, if the system is isotropic with the same jump distance in all directions, then $\frac{1}{2}{\alpha_0}^2$ should be replaced by $\frac{1}{6}{\alpha_0}^2$.[33]

At this point, by combining the relationship between the mobility and velocity ($\mu_i = v/E$) and equation 2.3 ($\sigma_i = c_i.q_i.\mu_i$), an Arrhenius-type relationship can be obtained for the ionic conductivity σ_i:

$$\sigma_i = \left(\frac{1}{6}{\alpha_0}^2.c.(1-c).\nu_0.\frac{q^2}{k_B}.exp\frac{\Delta S_m}{k_B}\right).\frac{1}{T}.exp\frac{-\Delta H_m}{k_B T} = \frac{\sigma_0}{T}.exp\frac{-\Delta H_m}{k_B T} \quad \text{(A.7)}$$

The pre-exponential factor σ_0 is, in a first approximation, independent of the temperature (in reality, the formation of intrinsic vacancies is temperature dependent and the term c is therefore not entirely temperature independent). The reader might notice a difference between equations 2.4 and A.7 in the activation energy term. The measurable activation energy E_a in equation 2.4 combines the energy barrier for migration (E_m or ΔH_m) and the energy required to form a mobile defect (E_f or ΔH_f): $E_a = \Delta H_m + \frac{1}{2}\Delta H_f$. However, in superionic conductors, the enthalpy of defect formation is often negligible, and the measured activation energy is a good approximation of the enthalpy of migration ($E_a \approx \Delta H_m$).

Most efforts to increase the ionic conductivity or design superionic ISEs have focused on increasing the defect concentration (*i.e.* maximizing the product $c.(1-c)$ in equation A.7) or reduce the energy barrier for migration ΔH_m. Specific solutions to achieve a higher concentration of defects or a lower ΔH_m in an ISE are described in section 2.3.

Appendix B

Models of stripping induced contact loss

Self-diffusion of vacancies

One of the first models used to describe the morphological stability of metal|ISE interfaces draws on the theory of diffusion. As described by Krauskopf *et al.*, the stability of a metal|ISE interface depends on the rate at which vacancies are created (injected) at the interface and the rate at which they can be annihilated.[69] If the vacancy annihilation rate is lower than the injection one, voids will form. The vacancy injection rate is determined by the applied current. On the other hand, the vacancy annihilation rate is controlled by two mechanisms: (1) vacancy diffusion and (2) pressure induced mechanical deformations.[68] In the following equations, vacancy annihilation by mechanical deformation of the metal anode is not taken into account. In a stationary state, Fick's first law indicates that particles will diffuse in a medium as to minimize any concentration gradients. In our problem, the concentration of metal vacancies is not constant throughout the metal anode: the concentration of metal vacancies is high at the interface where they are injected and reaches a plateau away from the interface (in the bulk of the metal anode). Thus, assuming a flux of metal vacancies j_v along the x direction:

$$j_v = -D_v \cdot \frac{\partial c_v}{\partial x} \tag{B.1}$$

In this expression D_v is the diffusion coefficient of metal vacancies and c_V is metal vacancy concentration at a distance x from the interface. Assuming that a stationary regime is reached, the gradient will be constant and defined by the vacancy concentration at the interface $c_v(\xi = 0)$ and the bulk vacancy concentration c_v^0 which is reached at a relaxation distance δ from the interface (ξ_R in Figure B.1). A common approximation to δ in the theory of diffusion is $\delta = \sqrt{(D_v.\tau_v)}$ with τ_v the relaxation time to reach the equilibrium vacancy concentration. Equation B.1 can thus be modified to:

$$j_v = -D_v.\frac{c_v(\xi = 0) - c_v^0}{\delta} = \frac{-D_v}{\sqrt{D_v \tau_v}}.c_v^0.\left(1 - \frac{c_v(\xi = 0)}{c_v^0}\right) = \sqrt{\frac{D_v}{\tau_v}}.c_v^0.\left(1 - \frac{c_v(\xi = 0)}{c_v^0}\right) \tag{B.2}$$

The critical current density is then obtained by multiplying j_v by the charge of the mobile cation z (z=1 for Na^+ ions) and the Faraday constant F:

$$i_v = z.F.j_v \tag{B.3}$$

This model provides a simple tool to predict the critical current above which vacancies accumulate at an alkali metal surface if the only mechanism of vacancy annihilation is self-diffusion. A source of error is that the diffusion coefficient D_V is difficult to measured accurately and can spread over a large range of values depending on the microstructure of the metal anode (the annihilation of metal vacancies is faster in metals with a large concentration of linear defects such as dislocations or grain boundaries).

Estimating D_V from electrochemical measurements requires a model which is valid beyond the stationary regime (based on Fick's second law). For a one-dimensional diffusion of vacancies, D_V can be estimated using Sand's equation:

$$\frac{1}{\sqrt{t_0}} = \frac{2}{\sqrt{D_{SD}.\pi.c_0.F}}.i \tag{B.4}$$

In this equation, t_0 is the time required to deplete the interface from active sites (for instance t_0 would be 11 h in Figure 3.5), i is the current density, c_o is the initial concentration of metal atoms (not vacancies) and D_{SD} is the self-diffusion coefficient of Na in Na metal. D_v is obtained from D_{SD} by $D_v = D_{SD}.{\chi_v}^{-1}$ (where $\chi_v = c_v^0.{c_0}^{-1}$ is the molar fraction of vacancies in the metal anode). By measuring t_0 over a range of current densities and linearly fitting the function $1/sqrt(t_0) = f(i)$, a value for D_SD can be extracted. A deviation from the linear behavior predicted by Sand's equation has been observed at high current densities by Krauskopf *et al.*.[173] Surface diffusion (which is typically faster than bulk diffusion) was suggested to participate to vacancy annihilation and explain the observed deviation.

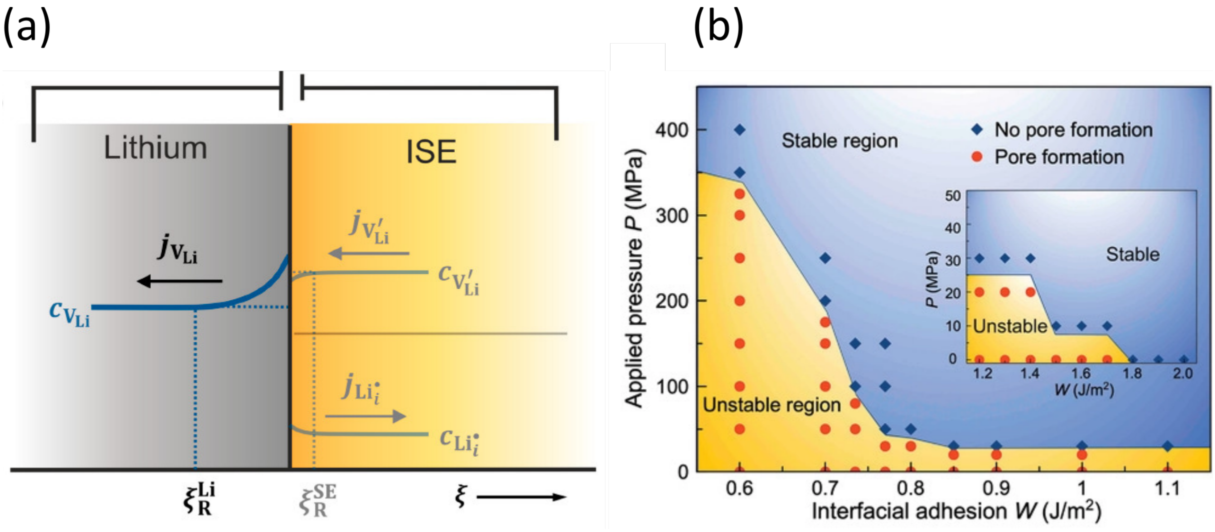

Figure B.1: Predicting conditions of morphological stability under stripping. (a) A vacancy diffusion model has been proposed to explain the formation of pores at a Li|Li-ISE interface. The blue curve indicates the concentration of vacancies ($c_{V_{L}i}$) from bulk to surface. In classical diffusion, this concentration gradient creates a driving force for vacancy diffusion; (b) Predicted stability regions for a Li|Li-ISE interface under stripping conditions calculated by molecular dynamics. This model includes parameters such as the mechanical properties of Li metal, the interfacial adhesion, and externally applied pressure to establish conditions of morphological stability. The stability region for a Na|Na-ISE interface would be different because of the different mechanical properties of Na in comparison to Li. Reproduced with permissions from [68] and [185]

Overall, these 1D diffusion models generally underestimate the critical current density for vacancy coalescence in comparison to experimental values. Other modes of diffusive vacancy annihilation (surface diffusion, effect of microstructure) could partially explain the higher current densities observed experimentally. In addition, the role of the ISE in these models is strictly limited to being a generator of interface metal vacancies. The properties of the ISE and of the metal|ISE interface (such as its work of adhesion) are not captured although energetic effects associated with vacancy injection and segregation can play an important role.

Interface adhesion approach

Different models based on the interfacial vacancy formation and vacancy migration energies have recently been developed. These models also yield conditions under which the metal|ISE interface could be morphologically stable. The advantage of the energetic models in comparison to the diffusion models is that the properties of the metal|ISE interface are also included.

A simple bond breaking model was applied by Seymour et al. to know under which conditions the injection of metal vacancies at a metal|ISE interface is energetically unfavourable.[183] A simple relation between the metal|ISE work of adhesion (W_{ad}) and the metal surface energy (σ_m) was found to be conditioning the suppression of metal vacancies: $W_{ad} \geq 2\sigma_m$. Interestingly, this condition is consistent with the Young-Dupré equation which is classically used in solid|liquid wetting science: $W_{ad} = sigma_m(1 + cos(\theta))$. Introducing the condition $W_{ad} = 2\sigma_m$ leads to a contact angle of $\theta = 0°$ (i.e. perfect wetting). The validity of this condition was studied using first-principles calculations based on density functional theory methods. For several metal|ISE coherent interfaces, the energy difference between a bulk and interface vacancy ($\Delta E_{Vm}^{bulk-int}$) was indeed demonstrated to be negative when $W_{ad} \geq 2\sigma_m$ indicating that the vacancies injected at the interface are incited to migrate to the bulk of the metal. For semi-coherent and incoherent interfaces, this simple model only provides a lower limit. To guarantee the annihilation of interfacial vacancies, one must calculate $\Delta E_{Vm}^{bulk-int}$ at the weakest binding site at the interface (*i.e.* the centre of a misfit dislocation core). Due to the computational cost of atomistic scale DFT simulations, this model is only limited to the fundamental understanding of explicit interfaces with a small number of atoms. For larger scale simulations, a molecular dynamics method was used by Yang *et al.* to study how the work of adhesion and applied pressure impacted the morphological stability of the interface.[185] Their results are summarized in Figure B.1 which can be used as a guide for materials selection. Interestingly, their simulation and the bond breaking model from Seymour *et al.* find that the stability of a Li|ISE interface is greatly increased above a work of adhesion of ≈ 0.7 J m^{-2} (which corresponds to about twice the surface energy of Li metal $\sigma_m = 0.368$ J m^{-2}).[183] The stability of the Na|ISE requires more investigation but the lower surface energy of Na metal (0.230 J m^{-2} for relaxed BCC Na (100) slabs) indicates that, on an energetics point of view, it might be easier to find Na|ISE pairs with morphologically stable interfaces in comparison to Li|ISE interfaces.

Appendix C

Supplementary data to Chapter 6

The Figures included in this Appendix are complementary experiments related to Chapter 6 and more specifically Section 6.2. Figures C.5 to C.7 present the results of three experiments which were conducted to explain the chemical shift of the Si2p peak in Figure 6.4 between polished and thermally treated NZSP samples.

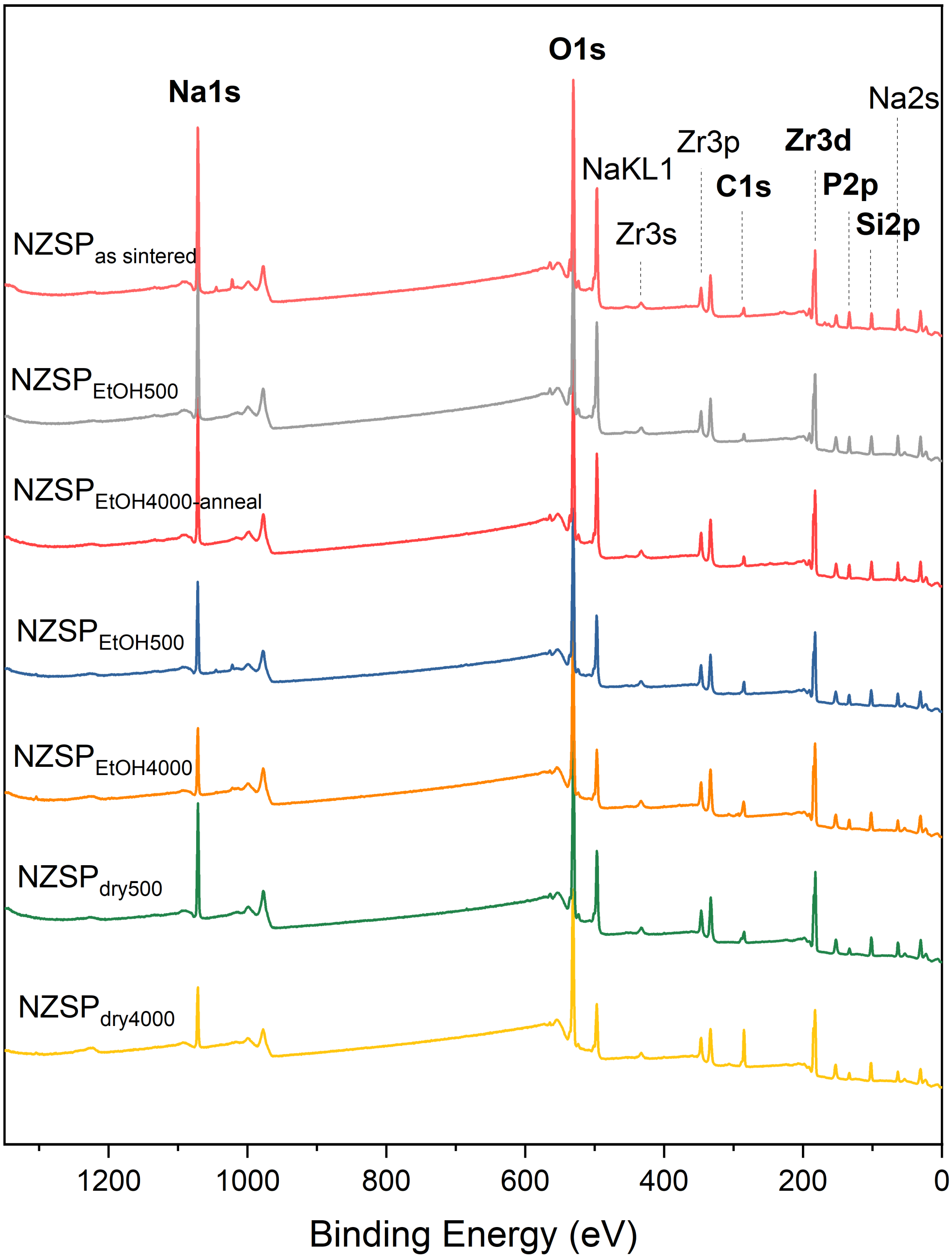

Figure C.1: XPS survey spectra of NZSP samples presented in Section 6.2. The core levels identified in bold were selected for the study.

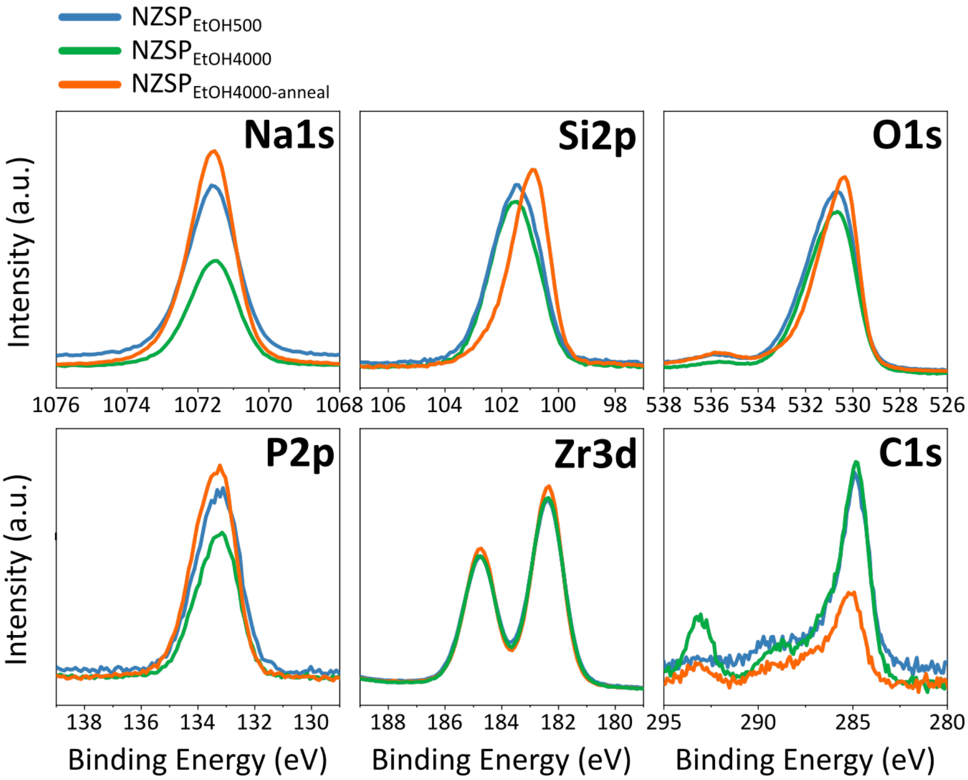

Figure C.2: Core level XPS spectra of NZSP$_{\mathrm{EtOH4000}}$ and NZSP$_{\mathrm{EtOH4000\text{-}anneal}}$ (charge correction: Zr3d$_{5/2}$ at 182.4 eV; intensity normalization: Zr3d$_{5/2}$ peak area).

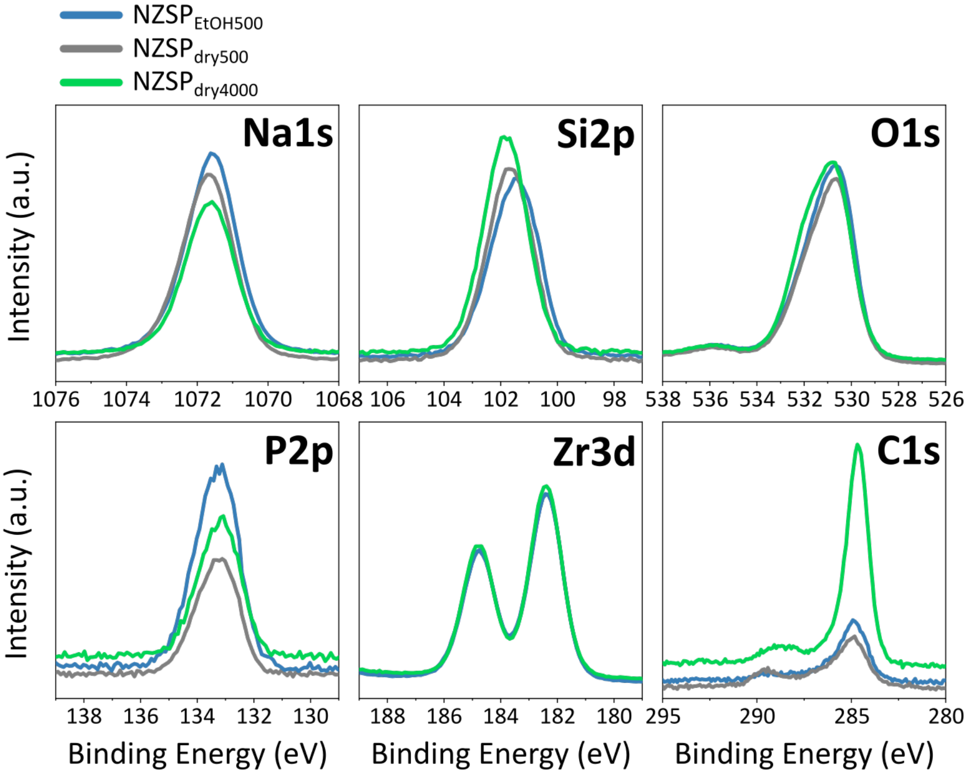

Figure C.3: XPS spectra of NZSP samples polished with ethanol as solvent (NZSP$_{\text{EtOH500}}$) or without a solvent (NZSP$_{\text{dry500}}$ and NZSP$_{\text{dry4000}}$). The higher amount of C contaminants on the surface of NZSP$_{\text{dry4000}}$ induces an alignment mismatch in the background level of this sample compared to NZSP$_{\text{EtOH500}}$ and NZSP$_{\text{dry500}}$ (the background is shifted up): the assumption that the Zr surface concentration is identical for all samples is not valid here because of the higher concentration of contaminants on NZSP$_{\text{dry4000}}$. (charge correction: Zr3d$_{5/2}$ at 182.4 eV; intensity normalization: Zr3d$_{5/2}$ peak area).

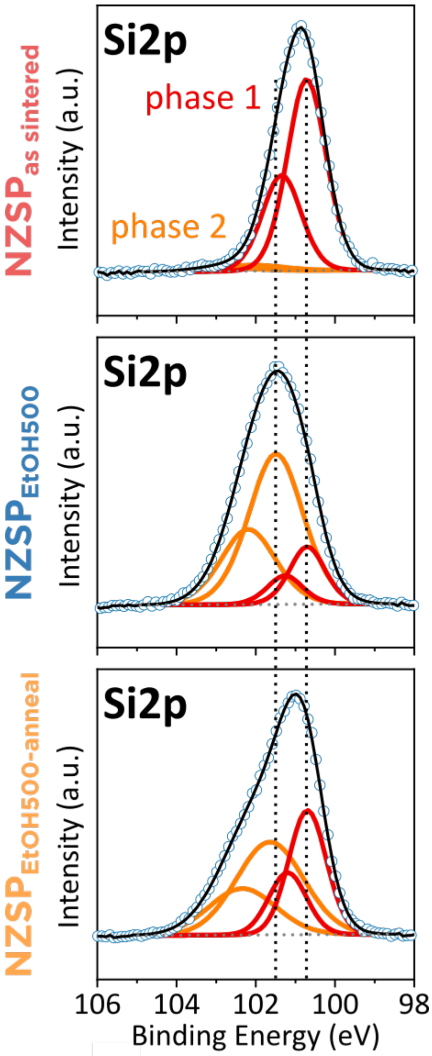

Figure C.4: Fitting of Si2p XPS signals (same raw data as Figure 6.4). The NZSP$_{AS}$ signal was fitted first using only one doublet ("phase 1", in red) with a narrow FWHM. The position and FWHM of this doublet were used as fitting constraints for the fitting of the NZSP$_{EtOH500}$ and NZSP$_{500EtOH\text{-}anneal}$ signals. An additional doublet ("phase 2", in orange) was required to fit these two sets of data.

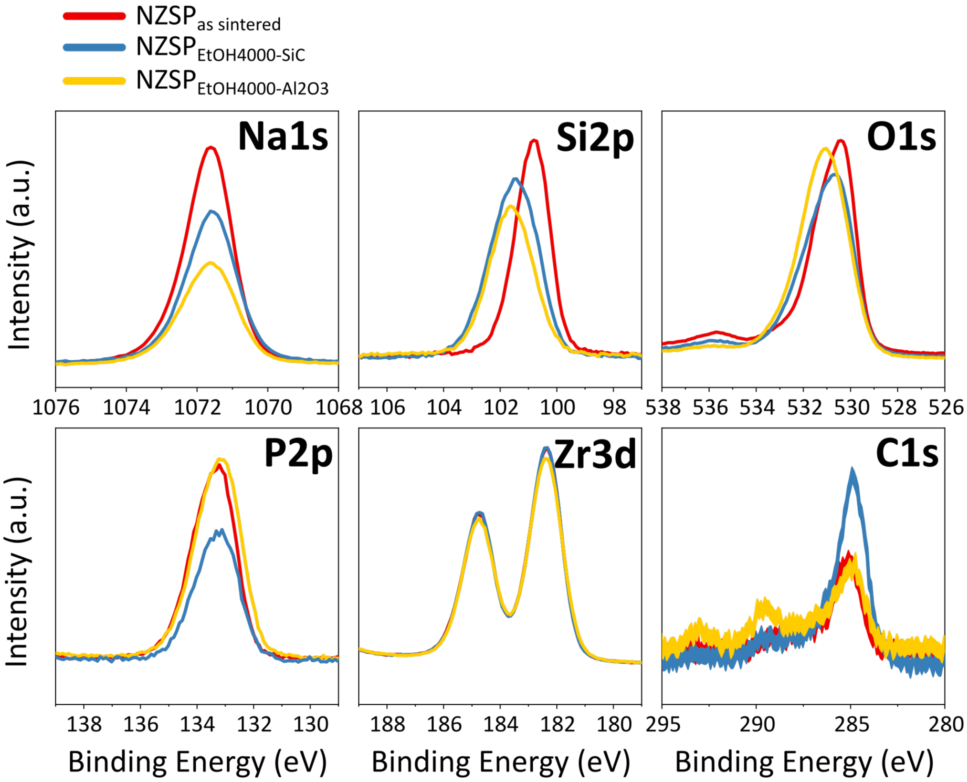

Figure C.5: Demonstrating that the Si2p chemical shift is not due to SiC residues. Comparison of the XPS signals of NZSP pellets polished either with SiC or Al_2O_3 polishing pads (and ethanol as solvent). The XPS signals of a $NZSP_{AS}$ are included for comparison.

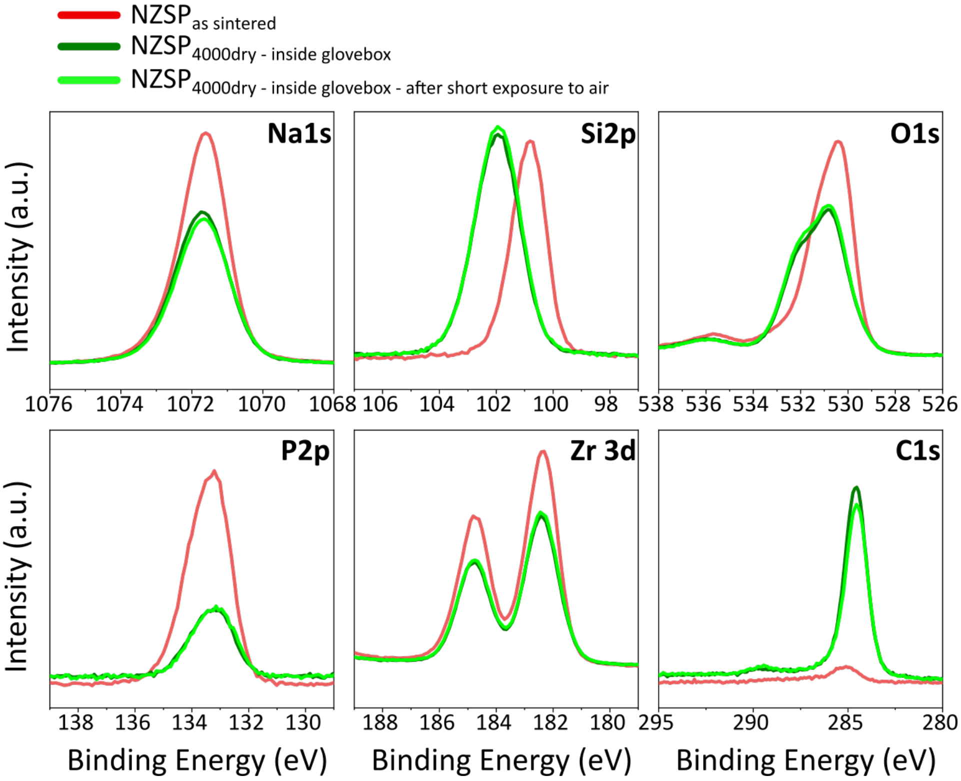

Figure C.6: Impact of air exposure on the chemical composition of polished NZSP samples. The XPS signals in dark green correspond to the surface of a NZSP pellet which was dry polished inside a glovebox and transferred to the XPS via a vacuum suitcase. The signals in light green correspond to the same dry-polished NZSP pellet after it was exposed to ambient air for five minutes.

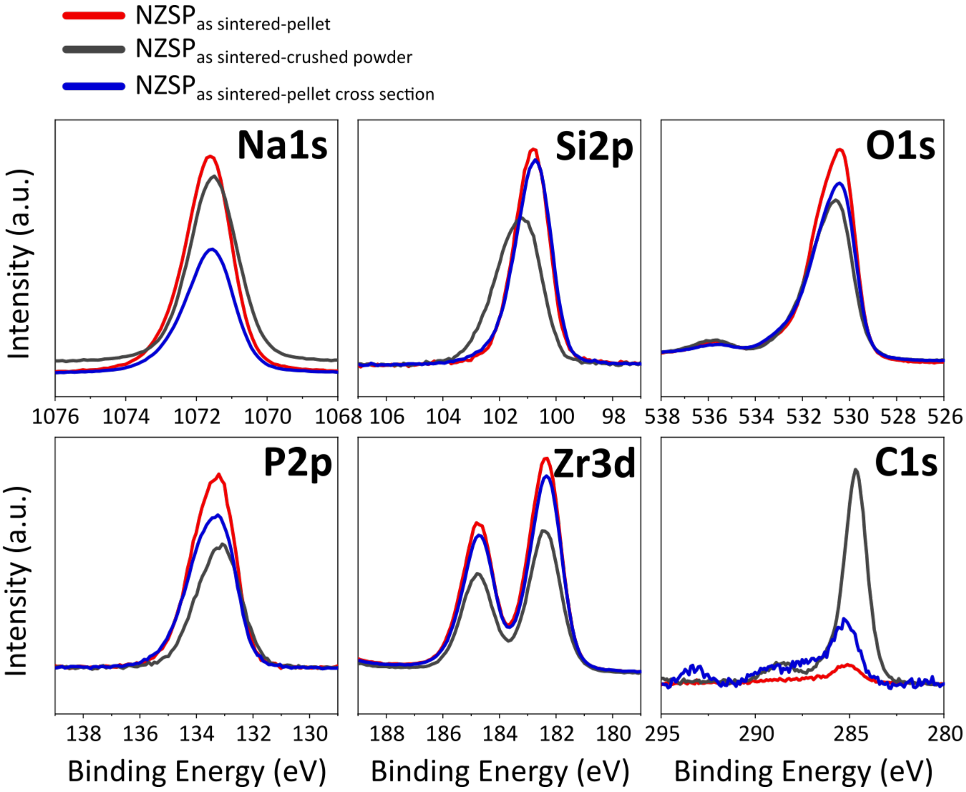

Figure C.7: Determining the chemical composition of the bulk of NZSP pellets. Comparison of the XPS signals of the cross-section of a NZSP pellet (in blue) with that of the powder obtained from a crushed pellet (in grey) and with the surface of an as-sintered pellet (in red, reference).

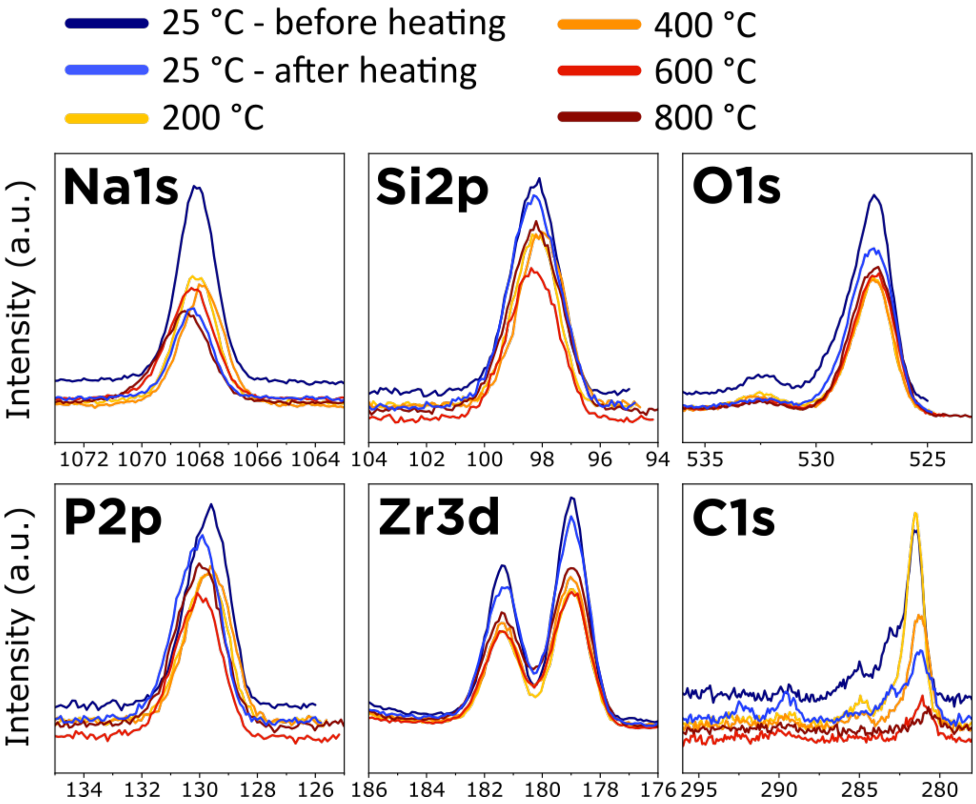

Figure C.8: Evolution of the chemical composition of a polished NZSP sample analysed by temperature-dependent XPS. For this experiment, a polished NZSP pellet was heated under ultra high vacuum inside the XPS instrument and its surface composition was measured every 200 °C from 25 °C to 800 °C. The position of the peaks are corrected for the Zr3d$_{5/2}$ to be aligned. The intensity of the signals are not normalized. A increase in the Na and P concentration is not observed with this experiment. The other thermally treated NZSP pellets employed in Chapter 6 were heated in ambient air.

Appendix D

Supplementary data to Chapter 7

The Figures and calculation included in this Appendix are complementary experiments related to Chapter 7.

Residual impurities in 99.9 % Na metal cubes

The following table is reproduced from the certificate of analysis provided by Sigma Aldrich for the product with CAS number 7440-23-5 (99.9 % Na metal cubes). The certificate of analysis for the 99 % Na metal rods also used in this thesis could not be found from Alfa Aesar.

Element	**Concentration**
Calcium (Ca)	368.1 ppm
Potassium (K)	101.3 ppm
Rubidium (Rb)	11.0 ppm
Cesium (Cs)	10.3 ppm
Magnesium (Mg)	3.1 ppm
Boron (B)	2.8 ppn
Strontium (Sr)	2.3 ppm
Lithium (Li)	2.0 ppm

Table D.1: Residual impurities (>2.0 ppm) in 99.9 % Na metal cubes, Sigma Aldrich

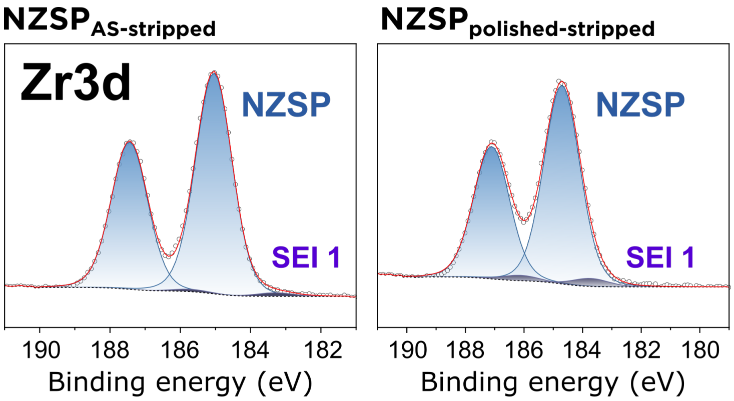

Figure D.1: Fitting models of the Zr3d region of NZSP$_{\text{AS-stripped}}$ and NZSP$_{\text{polished-stripped}}$ showing the presence of a secondary phase in a minor concentration. Related to sections 7.2 and 7.2

Calculation of the surface covered by a monolayer of CaO

The following calculations assume that the 1 % impurity contained in a 99 % pure Na metal electrode consists entirely of Ca (which is not exactly true, but Ca is the main impurity). The calculation also assumes that Ca reacts to form CaO for simplicity.

Assuming a Na metal electrode weighs 11.2 mg (such as in section 7.2), we estimate that the fraction corresponding to Ca is 1 % of this (0.112 mg). From the atomic mass of Ca (M_{Ca}=40.08 g mol^{-1}), we can calculate that this corresponds to about 2.79 10^{-6} mol of Ca. Assuming the reaction proceeds until all Ca is consumed, 2.79 10^{-6} mol of CaO will be formed. Using the molar mass of CaO (M_{CaO}=56.08 g mol^{-1}), we can calculate that this corresponds to 0.156 mg of CaO. With the density of cubic CaO at room temperature (3.35 g cm^{-3}[186]), we can calculate that this corresponds to a volume of CaO of 4.66 10^{-5} cm^3. And finally, with the CaO unit cell parameter (a=4.8 Å), we can calculate that if the CaO forms a monolayer, it will cover a surface of 971 cm^2.

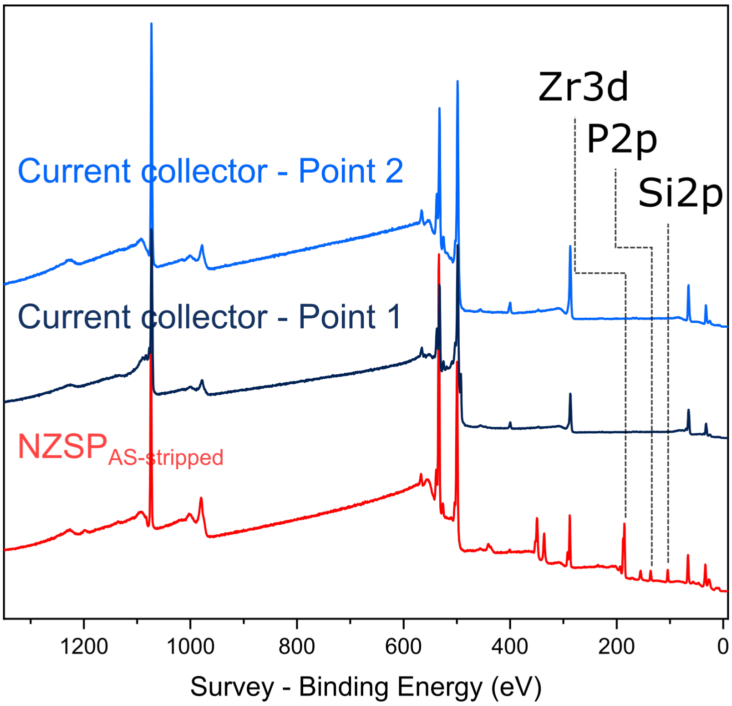

Figure D.2: Comparison of three XPS surveys corresponding to the NZSP$_{\text{AS-stripped}}$ surface and the current collector (two points were analysed on the surface). Related to section 7.2

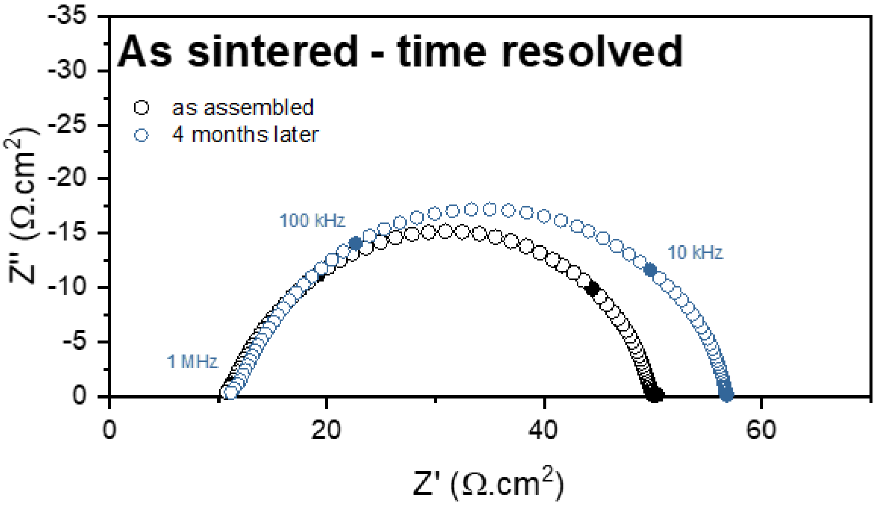

Figure D.3: Outlier sample 1. Two Nyquist plots of a Na|NZSP$_{AS}$|Na symmetrical cell assembled with 99% pure Na^0 electrodes measured at 4 months of interval. Unlike other cells, this one did not display a large increase in interface resistance. Related to section 7.3

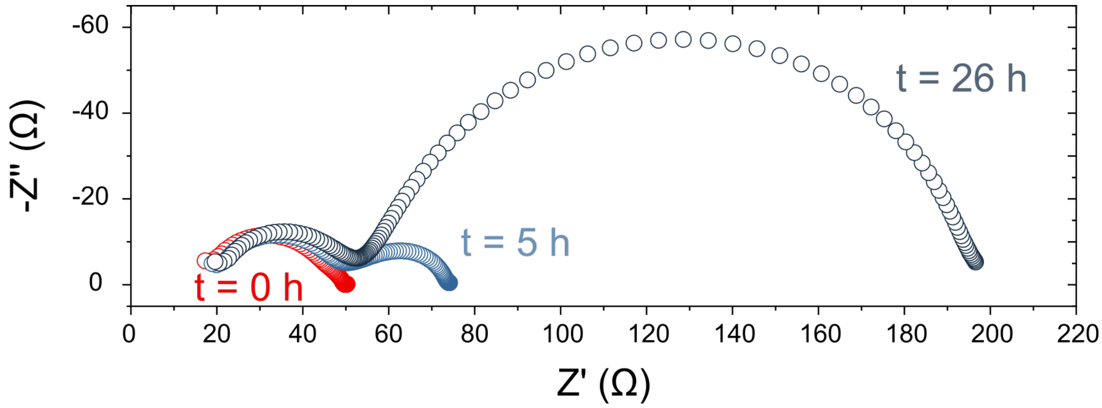

Figure D.4: Outlier sample 2. Three Nyquist plots of a Na|NZSP$_{AS}$|Na symmetrical cell assembled with 99.9% pure Na^0 electrodes measured over 26 h. A large increase in the interface resistance was observed. The degradation that this interface suffered was not identified. Related to section 7.3

Appendix E

Supplementary data to Chapter 8

		Fitting			Constraints			
Region	Peak	BE (eV)	FWHM (eV)	Area	Line shape	BE (eV)	FWHM (eV)	Area
Na1s	Na0	1071.83	0.61	277172	LF(0.58,1.15,200,50)	1071.8 - 1071.9	<0.65	-
	Na SP1	1075.8	1.77	93174	//	1075.8-1075.85	-	-
	Na BP1	1077.61	0.59	23667	//	1077.61-1077.65	-	-
	extra peak	1079.8	2.92	100000	//	1079.8-1079.85	-	<100000
	Na BP1+SP1	1081	3.93	18973	//	1081-1082	-	-

Table E.1: Fitting parameters Na metal. SP = surface plasmon, BP = bulk plasmon. Related to Figure 8.4.

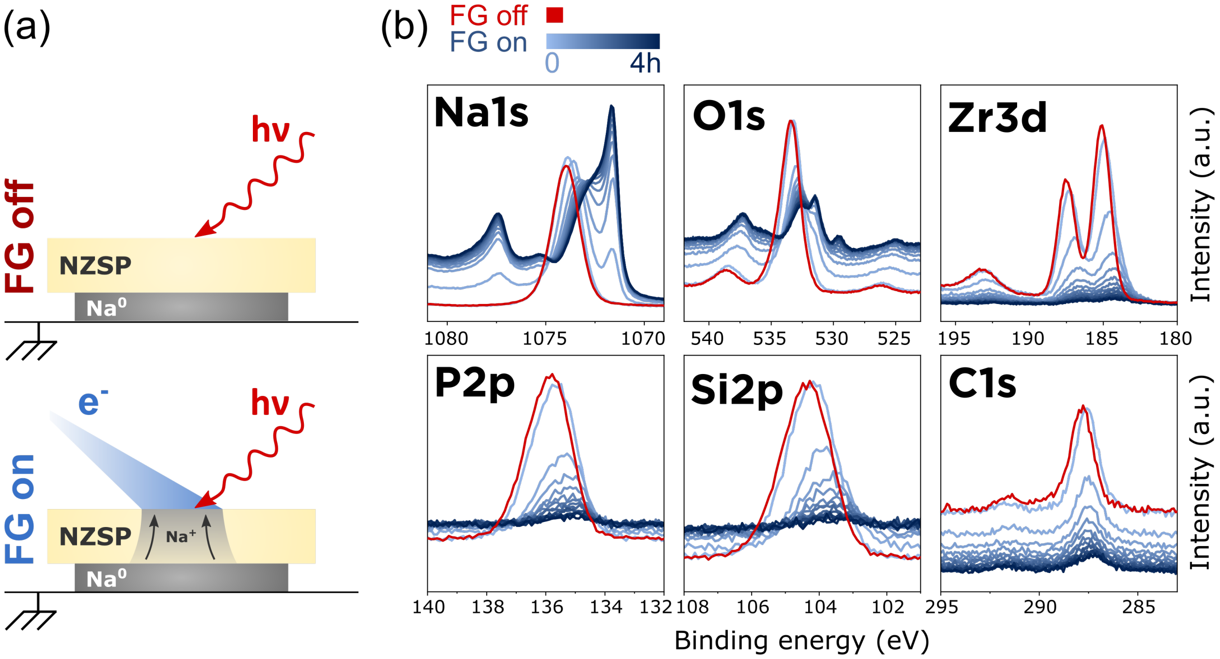

Figure E.1: *Operando* XPS experiment with a NZSP$_{\text{polished}}$ sample. (a) Schematic representation of the two XPS analysis configurations; (b) Evolution of selected core level regions with increasing Na^0 plating time. An initial set of data (in red) was measured with the FG off (reference signal from NZSP$_{\text{polished}}$). The following spectra (in shades of blue) were measured in iterative loop (4 h in total) with each acquisition cycle lasting 18 minutes and 11 seconds.

		Fitting			**Constraints**			
Region	Peak	BE (eV)	FWHM (eV)	Area	Line shape	BE (eV)	FWHM (eV)	Area
Na1s	NZSP	1074.63	1.4	166765	LA(1.15,1.4,243)	-	-	-
P2p	3/2 NZSP	136.29	1.31	3830	LA(1.53,243)	-	-	-
	1/2 NZSP	135.96	1.31	1915	//	P2p3/2 + 0.87	P2p3/2 *1	P2p3/2*0.5
Si2p	3/2 NZSP	103.55	1.19	3659	LA(1.53,243)	-	-	-
	1/2 NZSP	104.15	1.19	1829	//	Si2p3/2 +0.6	Si2p3/2*1	Si2p3/2*0.5
Zr3d	5/2 NZSP	184.55	1.24	25307	LA(1.53,243)	-	-	-
	3/2 NZSP	186.95	1.24	16872	//	Zr3d5/2 (NZSP) + 2.4	Zr3d5/2 (NZSP)*1	Zr3d5/2 (NZSP)*0.667

Table E.2: Fitting parameters NZSP$_{\text{AS}}$ - ref 0 min. Related to Figure E.2.

		Fitting			**Constraints**			
Region	Peak	BE (eV)	FWHM (eV)	Area	Line shape	BE (eV)	FWHM (eV)	Area
Na1s	Na0	1071.88	0.65	91684	LF(0.58,1.17,200,80)	-	0.65	-
	SP1	1075.84	1.79	46081	//	-	-	-
	BP1	1077.4	1.03	28606	//	1077-1080	-	-
	NZSP	1073.8	1.8	50932	LA(1.53,243)	-	-	-
P2p	3/2 NZSP	135.6	1.54	1020	LA(1.53,243)	-	-	-
	1/2 NZSP	136.47	1.54	510	//	P2p3/2 + 0.87	P2p3/2 *1	P2p3/2*0.5
Si2p	3/2 NZSP	103.81	1.14	1063	LA(1.53,243)	-	-	-
	1/2 NZSP	104.41	1.14	531.5	//	Si2p3/2 +0.6	Si2p3/2*1	Si2p3/2*0.5
Zr3d	5/2 NZSP	185.27	1.21	6001	LA(1.53,243)	-	-	-
	3/2 NZSP	187.67	1.21	4000.6	//	Zr3d5/2 (NZSP) + 2.4	Zr3d5/2 (NZSP)*1	Zr3d5/2 (NZSP)*0.667
	5/2 SEI 1	184.05	1.21	923	//	-	Zr3d5/2 (NZSP)*1	-
	3/2 SEI 1	186.45	1.21	615.6	//	Zr3d5/2 (SEI1) + 2.4	Zr3d5/2 (NZSP)*1	Zr3d5/2 (SEI1)*0.667
	5/2 SEI 2	182.7	1.21	270.3	//	-	Zr3d5/2 (NZSP)*1	-
	3/2 SEI 2	185.1	1.21	180.21	//	Zr3d5/2 (SEI2) + 2.4	Zr3d5/2 (NZSP)*1	Zr3d5/2 (SEI2)*0.667
Background: - the Na1s region was fitted with a Tougaard background (U 4 Tougaard: 1.45, 33, 0.8, 0). The first cross-section term (which modulates the intensity of the background) was optimized for each plating cycle to minimize residuals - all other peaks were fitted with a Shirley type background								

Table E.3: Fitting parameters NZSP$_{\text{AS plated}}$ - 240 min. Related to Figure 8.5.

		Fitting			**Constraints**			
Region	Peak	BE (eV)	FWHM (eV)	Area	Line shape	BE (eV)	FWHM (eV)	Area
Na1s	NZSP	1073.94	1.59	227806	LA(1.25,1.53,243)	-	-	-
P2p	3/2 NZSP	135.66	1.36	4448	LA(1.53,243)	-	-	-
	1/2 NZSP	136.53	1.36	2224	//	P2p3/2 + 0.87	P2p3/2 *1	P2p3/2*0.5
Si2p	3/2 NZSP	104.2	1.56	3500	LA(1.53,243)	-	-	-
	1/2 NZSP	104.8	1.56	1750	//	Si2p3/2 +0.6	Si2p3/2*1	Si2p3/2*0.5
Zr3d	5/2 NZSP	185.09	1.37	22059	LA(1.53,243)	-	-	-
	3/2 NZSP	187.49	1.37	14706	//	Zr3d5/2 (NZSP) + 2.4	Zr3d5/2 (NZSP)*1	Zr3d5/2 (NZSP)*0.667

Table E.4: Fitting parameters NZSP$_{\text{polished}}$ - ref 0 min. Related to Figure 8.7.

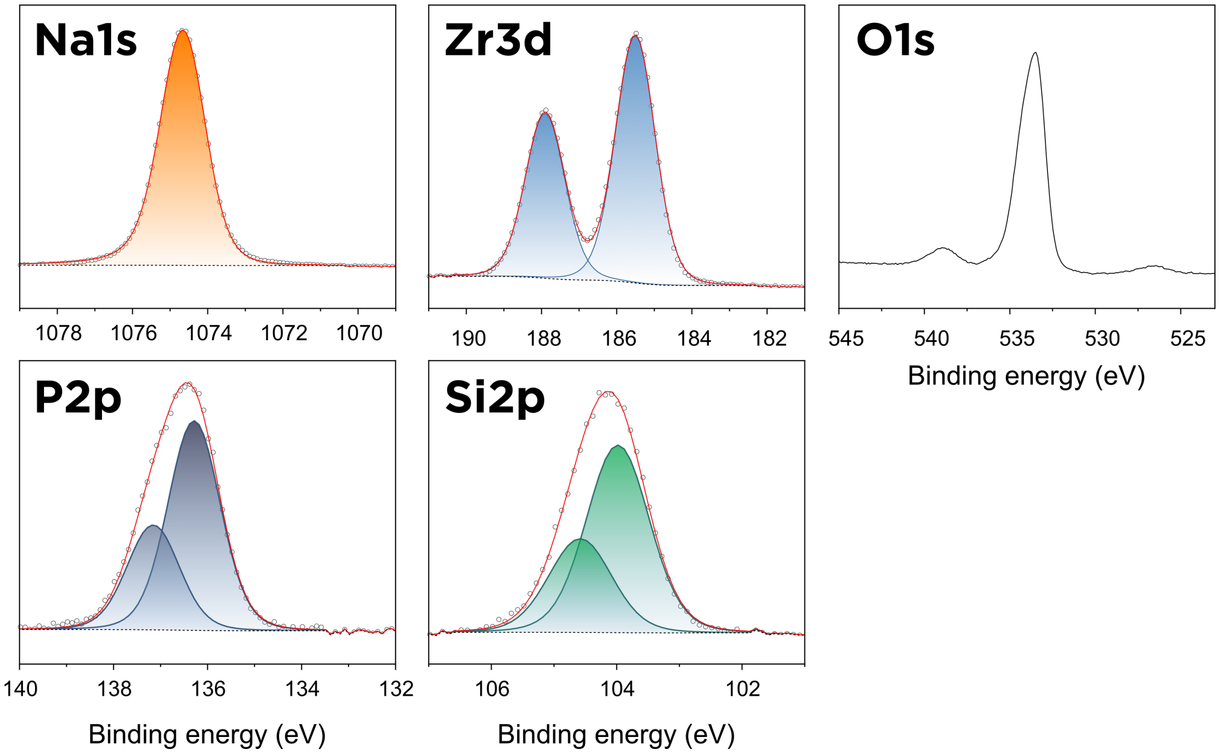

Figure E.2: Fitting of selected core levels from a NZSP$_{AS}$ reference sample. Related to Table E.2.

		Fitting			Constraints			
Region	Peak	BE (eV)	FWHM (eV)	Area	Line shape	BE (eV)	FWHM (eV)	Area
Na1s	Na0	1071.56	0.66	160808	LF(0.58,1.17,200,85)	-	0.6 - 0.75	-
	SP1	1075.39	1.81	95959	//	1075.2 - 1075.6	1 - 1.2	-
	BP1	1077.37	1.13	75696.6	//	1077 - 1079	1 - 1.2	-
	NZSP	1073.47	1.45	51917	LA(1.53,243)	1073.2 - 1073.8	1.45 - 1.65	Constrained to match P2p attenuation rate
	interphase & passivation	1073.05	1.97	136388	LA(1.53,243)	-	-	-
P2p	3/2 NZSP	135.09	1.27	1018	LA(1.53,243)	-	-	-
	1/2 NZSP	135.96	1.27	509	LA(1.53,243)	P2p3/2 + 0.87	P2p3/2 *1	P2p3/2*0.5
Si2p	3/2 NZSP	103.55	1.51	858	LA(1.53,243)	-	-	-
	1/2 NZSP	104.15	1.51	429	LA(1.53,243)	Si2p3/2 +0.6	Si2p3/2*1	Si2p3/2*0.5
Zr3d	5/2 NZSP	184.55	1.50	3246	LA(1.53,243)	184 -184.55	1 - 1.5	-
	3/2 NZSP	186.95	1.50	2164	LA(1.53,243)	Zr3d5/2 (NZSP) + 2.4	Zr3d5/2 (NZSP)*1	Zr3d5/2 (NZSP)*0.667
	5/2 SEI 1	183.66	1.50	2159	LA(1.53,243)	183 -183.7	Zr3d5/2 (NZSP)*1	-
	3/2 SEI 1	186.06	1.50	1439.02	LA(1.53,243)	Zr3d5/2 (SEI1) + 2.4	Zr3d5/2 (NZSP)*1	Zr3d5/2 (SEI1)*0.667
	5/2 SEI 2	182.24	1.50	434.607	LA(1.53,243)	181 - 183	Zr3d5/2 (NZSP)*1	-
	3/2 SEI 2	184.64	1.50	289.738	LA(1.53,243)	Zr3d5/2 (SEI2) + 2.4	Zr3d5/2 (NZSP)*1	Zr3d5/2 (SEI2)*0.667
Background: - the Na1s region was fitted with a Tougaard background (U 4 Tougaard: 0.8, 33, 0.8, 0). The first cross-section term (which modulates the intensity of the background) was optimized for each plating cycle to minimize residuals - all other peaks were fitted with a Shirley type background								

Table E.5: Fitting parameters NZSP$_{\text{polished plated}}$ - 91 min. Related to Figure 8.7.

Bibliography

[1] V. Masson-Delmotte, P. Zhai, A. Pirani, S. Connors, C. Péan, S. Berger, N. Caud, Y. Chen, L. Goldfarb, M. Gomis, M. Huang, K. Leitzell, E. Lonnoy, J. Matthews, T. Maycock, T. Waterfield, O. Yelekçi, R. Yu, and B. Zhou, "Climate Change 2021: The Physical Science Basis. Contribution of Working Group I to the Sixth Assessment Report of the Intergovernmental Panel on Climate Change," tech. rep., 2021.

[2] H. Ritchie and M. Roser, "CO_2 and Greenhouse Gas Emissions." `https://ourworldindata.org/emissions-by-sector`, 2020.

[3] M. Placek, "Projected global battery demand from 2020 to 2030, by application (in GWh)." `https://www.statista.com/statistics/1103218/global-battery-demand-forecast/`, 2021.

[4] B. W. Jaskula, "Lithium, U.S. Geological Survey, Mineral Commodity Summaries," tech. rep., 2018.

[5] E. A. Olivetti, G. Ceder, G. G. Gaustad, and X. Fu, "Lithium-Ion Battery Supply Chain Considerations: Analysis of Potential Bottlenecks in Critical Metals," *Joule*, vol. 1, pp. 229–243, 2017.

[6] T. Frankel, "Cobalt mining for lithium ion batteries has a high human cost." `https://www.washingtonpost.com/graphics/business/batteries/congo-cobalt-mining-for-lithium-ion-battery/?tid=batteriesbottom`, 2016.

[7] P. Whoriskey, "China pollution caused by graphite mining for smartphone battery." `https://www.washingtonpost.com/graphics/business/batteries/graphite-mining-pollution-in-china/?tid=batteriesbottom`, 2016.

[8] P. Pattisson, “"Like slave and master": DRC miners toil for 30p an hour to fuel electric cars.” `https://www.theguardian.com/global-development/2021/nov/08/cobalt-drc-miners-toil-for-30p-an-hour-to-fuel-electric-cars`, 2021.

[9] R. McKie, “Child labour, toxic leaks: the price we could pay for a greener future .” `https://www.theguardian.com/environment/2021/jan/03/child-labour-toxic-leaks-the-price-we-could-pay-for-a-greener-future`, 2021.

[10] C. P. Grey and J. M. Tarascon, “Sustainability and in situ monitoring in battery development,” *Nature Materials*, vol. 16, no. 1, pp. 45–56, 2016.

[11] B. Dunn, H. Kamath, and J.-M. Tarascon, “Electrical energy storage for the grid: a battery of choices.,” *Science (New York, N.Y.)*, vol. 334, pp. 928–35, nov 2011.

[12] Q. Ma and F. Tietz, “Solid-State Electrolyte Materials for Sodium Batteries: Towards Practical Applications,” *ChemElectroChem*, vol. 7, pp. 2693–2713, jul 2020.

[13] J. M. Tarascon, “Na-ion versus Li-ion Batteries: Complementarity Rather than Competitiveness,” *Joule*, vol. 4, pp. 1616–1620, aug 2020.

[14] C. Masquelier and L. Croguennec, “Polyanionic (Phosphates, Silicates, Sulfates) Frameworks as Electrode Materials for Rechargeable Li (or Na) Batteries,” *Chemical Reviews*, vol. 113, pp. 6552–6591, 2013.

[15] J. P. Pender, G. Jha, D. H. Youn, J. M. Ziegler, I. Andoni, E. J. Choi, A. Heller, B. S. Dunn, P. S. Weiss, R. M. Penner, and C. B. Mullins, “Electrode Degradation in Lithium-Ion Batteries,” *ACS Nano*, vol. 14, pp. 1243–1295, feb 2020.

[16] Q. Ma, C.-L. Tsai, X.-K. Wei, M. Heggen, F. Tietz, and J. T. S. Irvine, “Room temperature demonstration of a sodium superionic conductor with grain conductivity in excess of 0.01 S cm -1 and its primary applications in symmetric battery cells,” *Journal of Materials Chemistry A*, vol. 7, pp. 7766–7776, 2019.

[17] K. N. Wood, E. Kazyak, A. F. Chadwick, K. H. Chen, J. G. Zhang, K. Thornton, and N. P. Dasgupta, “Dendrites and pits: Untangling the complex behavior of lithium metal anodes through operando video microscopy,” *ACS Central Science*, vol. 2, pp. 790–801, nov 2016.

[18] C. Monroe and J. Newman, “The Impact of Elastic Deformation on Deposition Kinetics at Lithium/Polymer Interfaces,” *Journal of The Electrochemical Society*, vol. 152, no. 2, p. A396, 2005.

[19] P. Albertus, S. Babinec, S. Litzelman, and A. Newman, “Status and challenges in enabling the lithium metal electrode for high-energy and low-cost rechargeable batteries,” *Nature Energy*, vol. 3, pp. 16–21, jan 2018.

[20] G. T. Hitz, D. W. McOwen, L. Zhang, Z. Ma, Z. Fu, Y. Wen, Y. Gong, J. Dai, T. R. Hamann, L. Hu, and E. D. Wachsman, “High-rate lithium cycling in a scalable trilayer Li-garnet-electrolyte architecture,” *Materials Today*, vol. 22, pp. 50–57, jan 2019.

[21] J. Schnell, T. Günther, T. Knoche, C. Vieider, L. Köhler, A. Just, M. Keller, S. Passerini, and G. Reinhart, “All-solid-state lithium-ion and lithium metal batteries – paving the way to large-scale production,” *Journal of Power Sources*, vol. 382, pp. 160–175, apr 2018.

[22] V. Bocharova and A. P. Sokolov, “Perspectives for Polymer Electrolytes: A View from Fundamentals of Ionic Conductivity,” *Macromolecules*, vol. 53, pp. 4141–4157, jun 2020.

[23] C. Uhlmann, J. Illig, M. Ender, R. Schuster, and E. Ivers-Tiffée, “In situ detection of lithium metal plating on graphite in experimental cells,” *Journal of Power Sources*, vol. 279, pp. 428–438, apr 2015.

[24] D. Landmann, G. Graeber, M. V. Heinz, S. Haussener, and C. Battaglia, “Sodium plating and stripping from Na-β“-alumina ceramics beyond 1000 mA/cm^2,” *Materials Today Energy*, vol. 18, p. 100515, dec 2020.

[25] M. C. Bay, M. Wang, R. Grissa, M. V. Heinz, J. Sakamoto, and C. Battaglia, “Sodium Plating from Na-β"-Alumina Ceramics at Room Temperature, Paving the Way for Fast-Charging All-Solid-State Batteries,” *Advanced Energy Materials*, vol. 10, p. 1902899, dec 2019.

[26] S. Wang, K. Rafiz, J. Liu, Y. Jin, and J. Y. Lin, “Effects of lithium dendrites on thermal runaway and gassing of LiFePO$_4$ batteries,” *Sustainable Energy & Fuels*, vol. 4, pp. 2342–2351, may 2020.

[27] H. Muramatsu, A. Hayashi, T. Ohtomo, S. Hama, and M. Tatsumisago, "Structural change of Li2S–P2S5 sulfide solid electrolytes in the atmosphere," *Solid State Ionics*, vol. 182, pp. 116–119, feb 2011.

[28] J. Li, C. Ma, M. Chi, C. Liang, and N. J. Dudney, "Solid electrolyte: The key for high-voltage lithium batteries," *Advanced Energy Materials*, vol. 5, pp. 1–6, feb 2015.

[29] F. Strauss, J. H. Teo, A. Schiele, T. Bartsch, T. Hatsukade, P. Hartmann, J. Janek, and T. Brezesinski, "Gas Evolution in Lithium-Ion Batteries: Solid versus Liquid Electrolyte," *ACS Applied Materials & Interfaces*, vol. 12, pp. 20462–20468, may 2020.

[30] T. Bartsch, F. Strauss, T. Hatsukade, A. Schiele, A.-Y. Kim, P. Hartmann, J. Janek, and T. Brezesinski, "Gas Evolution in All-Solid-State Battery Cells," *ACS Energy Letters*, vol. 3, pp. 2539–2543, oct 2018.

[31] T. Famprikis, P. Canepa, J. A. Dawson, M. S. Islam, and C. Masquelier, "Fundamentals of inorganic solid-state electrolytes for batteries," *Nature Materials*, vol. 18, no. December, 2019.

[32] C. Kittel, *Introduction to Solid State Physics.* Wiley, 8 ed., 2005.

[33] P. Kofstad and T. Norby, *Defects and Transport in Crystalline Solids.* No. September, 2007.

[34] J. B. Goodenough, "Review Lecture: Fast Ionic Conduction in Solids," *Source: Proceedings of the Royal Society of London. Series A, Mathematical and Physical Sciences*, vol. 393, no. 1805, pp. 215–234, 1984.

[35] S. P. Culver, R. Koerver, T. Krauskopf, and W. G. Zeier, "Designing Ionic Conductors: The Interplay between Structural Phenomena and Interfaces in Thiophosphate-Based Solid-State Batteries," *Chemistry of Materials*, vol. 30, pp. 4179–4192, 2018.

[36] L. Duchêne, A. Remhof, H. Hagemann, and C. Battaglia, "Status and prospects of hydroborate electrolytes for all-solid-state batteries," *Energy Storage Materials*, vol. 25, pp. 782–794, mar 2020.

[37] T. Krauskopf, C. Pompe, M. A. Kraft, and W. G. Zeier, “Influence of Lattice Dynamics on Na^+ Transport in the Solid Electrolyte Na_3PS_4–xSex,” *Chemistry of Materials*, vol. 29, pp. 8859–8869, oct 2017.

[38] X. He, Y. Zhu, and Y. Mo, “Origin of fast ion diffusion in super-ionic conductors,” *Nature Communications*, vol. 8, 2017.

[39] Y. Wang, W. D. Richards, S. P. Ong, L. J. Miara, J. C. Kim, Y. Mo, and G. Ceder, “Design principles for solid-state lithium superionic conductors,” *Nature Materials*, vol. 14, pp. 1026–1032, 2015.

[40] L. Minervini, R. W. Grimes, J. A. Kilner, and K. E. Sickafus, “Oxygen migration in La2NiO4 + δ,” *Journal of Materials Chemistry*, vol. 10, pp. 2349–2354, jan 2000.

[41] Z. Zhang, Z. Zou, K. Kaup, R. Xiao, S. Shi, M. Avdeev, Y. Y.-s. Hu, D. Wang, B. He, H. Li, X. Huang, L. F. Nazar, and L. Chen, “Correlated Migration Invokes Higher Na + -Ion Conductivity in NaSICON-Type Solid Electrolytes,” *Advanced Energy Materials*, vol. 9, p. 1902373, oct 2019.

[42] H.-P. Hong, “Crystal structures and crystal chemistry in the system $Na_{1+x}Zr_2Si_xP_{3-x}O_{12}$,” *Materials Research Bulletin*, vol. 11, no. 2, pp. 173–182, 1976.

[43] J. P. Boilot, G. Collin, and P. Colomban, “Relation Structure-Fast Ion Conduction in the NASICON Solid Solution,” *Journal of Solid State Chemistry*, vol. 73, pp. 160–171, 1988.

[44] M. Guin and F. Tietz, “Survey of the transport properties of sodium superionic conductor materials for use in sodium batteries,” *Journal of Power Sources*, vol. 273, pp. 1056–1064, jan 2015.

[45] Z. Zhu, I.-H. Chu, Z. Deng, and S. P. Ong, “Role of Na^+ Interstitials and Dopants in Enhancing the Na^+ Conductivity of the Cubic Na_3PS_4 Superionic Conductor,” *Chemistry of Materials*, vol. 27, pp. 8318–8325, dec 2015.

[46] Naoto Tanibata, Kousuke Noi, Akitoshi Hayashi, and Masahiro Tatsumisago, “Preparation and characterization of highly sodium ion conducting Na_3PS_4–Na_4SiS_4solid electrolytes,” *RSC Advances*, vol. 4, pp. 17120–17123, apr 2014.

[47] N. J. J. de Klerk and M. Wagemaker, “Diffusion Mechanism of the Sodium-Ion Solid Electrolyte Na_3PS_4 and Potential Improvements of Halogen Doping,” *Chemistry of Materials*, vol. 28, pp. 3122–3130, may 2016.

[48] I.-H. Chu, C. S. Kompella, H. Nguyen, Z. Zhu, S. Hy, Z. Deng, Y. Shirley Meng, and S. Ping Ong, “Room-Temperature All-solid-state Rechargeable Sodium-ion Batteries with a Cl-doped Na_3PS_4 Superionic Conductor,” *Scientific Reports*, vol. 6, p. 33733, 2016.

[49] A. V. Soloninin, R. V. Skoryunov, O. A. Babanova, A. V. Skripov, M. Dimitrievska, and T. J. Udovic, “Comparison of anion and cation dynamics in a carbon-substituted closo-hydroborate salt: ^{1}H and ^{23}Na NMR studies of solid-solution $Na_2(CB_9H_{10})(CB_{11}H_{12})$,” *Journal of Alloys and Compounds*, vol. 800, pp. 247–253, sep 2019.

[50] L. Duchêne, R.-S. Kühnel, D. Rentsch, A. Remhof, H. Hagemann, and C. Battaglia, “A highly stable sodium solid-state electrolyte based on a dodeca/deca-borate equimolar mixture,” *Chemical Communications*, vol. 53, pp. 4195–4198, apr 2017.

[51] J. Luo, “Interfacial engineering of solid electrolytes,” *Journal of Materiomics*, vol. 1, no. 1, pp. 22–32, 2015.

[52] J. Luo, “Let thermodynamics do the interfacial engineering of batteries and solid electrolytes,” *Energy Storage Materials*, vol. 21, pp. 50–60, sep 2019.

[53] P. R. Cantwell, M. Tang, S. J. Dillon, J. Luo, G. S. Rohrer, and M. P. Harmer, “Grain boundary complexions,” *Acta Materialia*, vol. 62, no. 1, pp. 1–48, 2014.

[54] F. Pesci, R. H. Brugge, A. K. O. Hekselman, A. Cavallaro, R. J. Chater, and A. Aguadero, “Elucidating the role of dopants in the critical current density for dendrite formation in garnet electrolytes,” *Journal of Materials Chemistry A*, vol. 6, pp. 19817–19827, oct 2018.

[55] R. H. Brugge, F. M. Pesci, Andrea Cavallaro, Christopher Sole, M. A. Isaacs, Gwilherm Kerherve, R. S. Weatherup, and Ainara Aguadero, “The origin of chemical inhomogeneity in garnet electrolytes and its impact on the electrochemical performance,” *Journal of Materials Chemistry A*, vol. 8, pp. 14265–14276, jul 2020.

[56] M. Samiee, B. Radhakrishnan, Z. Rice, Z. Deng, Y. S. Meng, S. P. Ong, and J. Luo, “Divalent-doped $Na_3Zr_2Si_2PO_{12}$ natrium superionic conductor: Improving the ionic

conductivity via simultaneously optimizing the phase and chemistry of the primary and secondary phases," *Journal of Power Sources*, vol. 347, pp. 229–237, 2017.

[57] E. Querel, I. Seymour, A. Cavallaro, Q. Ma, F. Tietz, and A. Aguadero, "The role of NaSICON surface chemistry in stabilizing fast-charging Na metal solid-state batteries," *Journal of Physics: Energy*, vol. 3, oct 2021.

[58] G. J. May and A. Hooper, "The effect of microstructure and phase composition on the ionic conductivity of magnesium-doped sodium-beta-alumina," *Journal of Materials Science 1978 13:7*, vol. 13, pp. 1480–1486, jul 1978.

[59] G. Gregori, R. Merkle, and J. Maier, "Ion conduction and redistribution at grain boundaries in oxide systems," *Progress in Materials Science*, vol. 89, pp. 252–305, 2017.

[60] A. Atkinson, "Surface and interface mass transport in ionic materials," *Solid State Ionics*, vol. 28-30, pp. 1377–1387, sep 1988.

[61] K. L. Merkle, "Atomic structure of grain boundaries," *Journal of Physics and Chemistry of Solids*, vol. 55, pp. 991–1005, oct 1994.

[62] T. Krauskopf, S. P. Culver, and W. G. Zeier, "Local Tetragonal Structure of the Cubic Superionic Conductor Na_3PS_4," *Inorganic Chemistry*, vol. 57, pp. 4739–4744, apr 2018.

[63] M.-C. Bay, M. V. F. Heinz, R. Figi, C. Schreiner, D. Basso, N. Zanon, U. F. Vogt, and C. Battaglia, "Impact of Liquid Phase Formation on Microstructure and Conductivity of Li-Stabilized Na-β"-alumina Ceramics," *ACS Applied Energy Materials*, vol. 2, pp. 687–693, jan 2018.

[64] S. Naqash, F. Tietz, E. Yazhenskikh, M. Müller, and O. Guillon, "Impact of sodium excess on electrical conductivity of $Na_3Zr_2Si_2PO_{12}$+xNa_2O ceramics," *Solid State Ionics*, vol. 336, pp. 57–66, aug 2019.

[65] M. Balaish, J. C. Gonzalez-Rosillo, K. J. Kim, Y. Zhu, Z. D. Hood, and J. L. M. Rupp, "Processing thin but robust electrolytes for solid-state batteries," *Nature Energy 2021 6:3*, vol. 6, pp. 227–239, feb 2021.

[66] J. Sastre, A. Priebe, M. Döbeli, J. Michler, A. N. Tiwari, and Y. E. Romanyuk, "Lithium Garnet $Li_7La_3Zr_2O_{12}$ Electrolyte for All-Solid-State Batteries: Closing

the Gap between Bulk and Thin Film Li-Ion Conductivities," *Advanced Materials Interfaces*, vol. 7, p. 2000425, sep 2020.

[67] S. Narayanan, S. Reid, S. Butler, and V. Thangadurai, "Sintering temperature, excess sodium, and phosphorous dependencies on morphology and ionic conductivity of NASICON $Na_3Zr_2Si_2PO_{12}$," *Solid State Ionics*, vol. 331, pp. 22–29, mar 2019.

[68] T. Krauskopf, F. H. Richter, W. G. Zeier, and J. Janek, "Physicochemical Concepts of the Lithium Metal Anode in Solid-State Batteries," vol. 120, pp. 7745–7794, aug 2020.

[69] T. Krauskopf, H. Hartmann, W. G. Zeier, and J. Janek, "Toward a Fundamental Understanding of the Lithium Metal Anode in Solid-State Batteries - An Electrochemo-Mechanical Study on the Garnet-Type Solid Electrolyte $Li_{6.25}Al_{0.25}La_3Zr_2O_{12}$," *ACS Appl. Mater. Interfaces*, vol. 11, pp. 14463–14477, apr 2019.

[70] Y. Uchida, G. Hasegawa, K. Shima, M. Inada, N. Enomoto, H. Akamatsu, and K. Hayashi, "Insights into Sodium Ion Transfer at the Na/NASICON Interface Improved by Uniaxial Compression," *ACS Applied Energy Materials*, vol. 2, pp. 2913–2920, 2019.

[71] A. Sharafi, E. Kazyak, A. L. Davis, S. Yu, T. Thompson, D. J. Siegel, N. P. Dasgupta, and J. Sakamoto, "Surface Chemistry Mechanism of Ultra-Low Interfacial Resistance in the Solid-State Electrolyte $Li_7La_3Zr_2O_{12}$," *Chemistry of Materials*, vol. 29, pp. 7961–7968, sep 2017.

[72] H. Huo, J. Luo, V. Thangadurai, X. Guo, C.-W. Nan, and X. Sun, "Li_2CO_3 : A Critical Issue for Developing Solid Garnet Batteries," *ACS Energy Letters*, vol. 5, pp. 252–262, 2020.

[73] J. Meng, Y. Zhang, X. Zhou, M. Lei, and C. Li, "Li_2CO_3-affiliative mechanism for air-accessible interface engineering of garnet electrolyte via facile liquid metal painting," *Nature Communications*, vol. 11, p. 3716, dec 2020.

[74] A. Etxebarria, S. L. Koch, O. Bondarchuk, S. Passerini, G. Teobaldi, and M. Á. Muñoz-Márquez, "Work Function Evolution in Li Anode Processing," *Advanced Energy Materials*, p. 2000520, may 2020.

[75] Y. Noguchi, E. Kobayashi, L. S. Plashnitsa, S. Okada, and J.-i. Yamaki, "Fabrication and performances of all solid-state symmetric sodium battery based on NASICON-related compounds," *Electrochimica Acta*, vol. 101, pp. 59–65, jul 2013.

[76] Z. Gao, J. Yang, H. Yuan, H. Fu, Y. Y. Y. Y. Li, Y. Y. Y. Y. Li, T. Ferber, C. Guhl, H. Sun, W. Jaegermann, R. Hausbrand, and Y. Huang, "Stabilizing $Na_3Zr_2Si_2PO_{12}$/Na Interfacial Performance by Introducing a Clean and Na-Deficient Surface," *Chemistry of Materials*, vol. 32, pp. 3970–3979, may 2020.

[77] S. Wang, H. Xu, W. Li, A. Dolocan, and A. Manthiram, "Interfacial Chemistry in Solid-State Batteries: Formation of Interphase and Its Consequences," *J. Am. Chem. Soc*, vol. 140, pp. 250–257, 2018.

[78] J. Yang, Z. Gao, T. Ferber, H. Zhang, C. Guhl, L. Yang, Y. Li, Z. Deng, P. Liu, C. Cheng, R. Che, W. Jaegermann, R. Hausbrand, and Y. Huang, "Guided-formation of a favorable interface for stabilizing Na metal solid-state batteries," *Journal of Materials Chemistry A*, vol. 8, pp. 7828–7835, 2020.

[79] P. Kehne, C. Guhl, Q. Ma, F. Tietz, L. Alff, R. Hausbrand, and P. Komissinskiy, "Sc-substituted Nasicon solid electrolyte for an all-solid-state Na_xCoO_2/Nasicon/Na sodium model battery with stable electrochemical performance," *Journal of Power Sources*, vol. 409, pp. 86–93, jan 2019.

[80] Q. Ma, M. Guin, S. Naqash, C.-L. Tsai, F. Tietz, and O. Guillon, "Scandium-Substituted $Na_3Zr_2(SiO_4)_2(PO_4)$Prepared by a Solution- Assisted Solid-State Reaction Method as Sodium-Ion Conductors," *Chemistry of Materials*, vol. 28, pp. 4821–4828, 2016.

[81] S. Song, H. M. Duong, A. M. Korsunsky, N. Hu, and L. Lu, "A Na^+ Superionic Conductor for Room-Temperature Sodium Batteries," *Scientific Reports*, vol. 6, p. 32330, oct 2016.

[82] V. Lacivita, Y. Wang, S. H. Bo, and G. Ceder, "Ab initio investigation of the stability of electrolyte/electrode interfaces in all-solid-state Na batteries," *Journal of Materials Chemistry A*, vol. 7, pp. 8144–8155, apr 2019.

[83] Y. Qie, S. Wang, S. Fu, H. Xie, Q. Sun, and P. Jena, "Yttrium–Sodium Halides as Promising Solid-State Electrolytes with High Ionic Conductivity and Stability for Na-Ion Batteries," *The Journal of Physical Chemistry Letters*, vol. 11, pp. 3376–3383, may 2020.

[84] L. Zhang, K. Yang, J. Mi, L. Lu, L. Zhao, L. Wang, Y. Li, and H. Zeng, "Na_3PSe_4: A Novel Chalcogenide Solid Electrolyte with High Ionic Conductivity," *Advanced Energy Materials*, vol. 5, p. 1501294, dec 2015.

[85] A. Hayashi, N. Masuzawa, S. Yubuchi, F. Tsuji, C. Hotehama, A. Sakuda, and M. Tatsumisago, "A sodium-ion sulfide solid electrolyte with unprecedented conductivity at room temperature," *Nature Communications 2019 10:1*, vol. 10, pp. 1–6, nov 2019.

[86] W. D. Richards, T. Tsujimura, L. J. Miara, Y. Wang, J. C. Kim, S. P. Ong, I. Uechi, N. Suzuki, and G. Ceder, "Design and synthesis of the superionic conductor $Na_{10}SnP_2S_{12}$," *Nature Communications 2016 7:1*, vol. 7, pp. 1–8, mar 2016.

[87] A. Hayashi, K. Noi, A. Sakuda, and M. Tatsumisago, "Superionic glass-ceramic electrolytes for room-temperature rechargeable sodium batteries," *Nature Communications*, vol. 3, p. 856, may 2012.

[88] Y. Xiao, Y. Wang, S.-H. Bo, J. C. Kim, L. J. Miara, and G. Ceder, "Understanding interface stability in solid-state batteries," *Nature Reviews*, vol. 5, pp. 105–126, dec 2019.

[89] W. D. Richards, L. J. Miara, Y. Wang, J. C. Kim, and G. Ceder, "Interface Stability in Solid-State Batteries," *Chemistry of Materials*, vol. 28, pp. 266–273, 2016.

[90] H. Hruschka, E. Lissel, and M. Jansen, "Na-Ion conduction in the solid solutions of Na_3PO_4/Na_2SO_4 and Na_3AlF_6/Na_2SO_4," *Solid State Ionics*, vol. 28-30, pp. 159–162, sep 1988.

[91] J. G. Connell, T. Fuchs, H. Hartmann, T. Krauskopf, Y. Zhu, J. Sann, R. Garcia-Mendez, J. Sakamoto, S. Tepavcevic, and J. Janek, "Kinetic versus Thermodynamic Stability of LLZO in Contact with Lithium Metal," *Chemistry of Materials*, vol. 32, pp. 10207–10215, nov 2020.

[92] S. Wenzel, D. A. Weber, T. Leichtweiss, M. R. Busche, J. Sann, and J. Janek, "Interphase formation and degradation of charge transfer kinetics between a lithium metal anode and highly crystalline $Li_7P_3S_{11}$ solid electrolyte," *Solid State Ionics*, vol. 286, pp. 24–33, mar 2016.

[93] Z. D. Hood, X. Chen, R. L. Sacci, X. Liu, G. M. Veith, Y. Mo, J. Niu, N. J. Dudney, and M. Chi, "Elucidating Interfacial Stability between Lithium Metal Anode and Li Phosphorus Oxynitride via *in situ* Electron Microscopy," *Nano Letters*, p. acs.nanolett.0c03438, dec 2020.

[94] C. Ma, Y. Cheng, K. Yin, J. Luo, A. Sharafi, J. Sakamoto, J. Li, K. L. More, N. J. Dudney, and M. Chi, "Interfacial Stability of Li Metal–Solid Electrolyte Elucidated via in Situ Electron Microscopy," *Nano Letters*, vol. 16, pp. 7030–7036, nov 2016.

[95] S. Wenzel, T. Leichtweiss, D. Krüger, J. Sann, and J. Janek, "Interphase formation on lithium solid electrolytes - An in situ approach to study interfacial reactions by photoelectron spectroscopy," *Solid State Ionics*, vol. 278, pp. 98–105, jun 2015.

[96] K. N. Wood, K. X. Steirer, S. E. Hafner, C. Ban, S. Santhanagopalan, S. H. Lee, and G. Teeter, "Operando X-ray photoelectron spectroscopy of solid electrolyte interphase formation and evolution in Li_2S-P_2S_5 solid-state electrolytes," *Nature Communications*, vol. 9, dec 2018.

[97] X. Wu, C. Villevieille, P. Novák, and M. El Kazzi, "Monitoring the chemical and electronic properties of electrolyte-electrode interfaces in all-solid-state batteries using: Operando X-ray photoelectron spectroscopy," *Physical Chemistry Chemical Physics*, vol. 20, no. 16, pp. 11123–11129, 2018.

[98] R. Hausbrand, G. Cherkashinin, H. Ehrenberg, M. Gröting, K. Albe, C. Hess, and W. Jaegermann, "Fundamental degradation mechanisms of layered oxide Li-ion battery cathode materials: Methodology, insights and novel approaches," *Materials Science and Engineering: B*, vol. 192, pp. 3–25, feb 2015.

[99] Y. Zhu, X. He, and Y. Mo, "Strategies Based on Nitride Materials Chemistry to Stabilize Li Metal Anode," *Advanced Science*, vol. 4, aug 2017.

[100] Y. Tian, Y. Sun, D. C. Hannah, Y. Xiao, H. Liu, K. W. Chapman, S. H. Bo, and G. Ceder, "Reactivity-Guided Interface Design in Na Metal Solid-State Batteries," *Joule*, vol. 3, pp. 1037–1050, apr 2019.

[101] V. Chevrier and G. Ceder, "Challenges for Na-ion Negative Electrodes," *J. Electrochem. Soc.*, vol. 158, p. A1011, 2011.

[102] M. J. Wang, R. Choudhury, and J. Sakamoto, "Characterizing the Li-Solid-Electrolyte Interface Dynamics as a Function of Stack Pressure and Current Density," *Joule*, vol. 3, pp. 2165–2178, sep 2019.

[103] J. Kasemchainan, S. Zekoll, D. Spencer Jolly, Z. Ning, G. O. Hartley, J. Marrow, and P. G. Bruce, "Critical stripping current leads to dendrite formation on plating in lithium anode solid electrolyte cells," *Nature Materials*, pp. 1–7, jul 2019.

[104] K. K. Fu, Y. Gong, B. Liu, Y. Zhu, S. Xu, Y. Yao, W. Luo, C. Wang, S. D. Lacey, J. Dai, Y. Chen, Y. Mo, E. Wachsman, and L. Hu, "Toward garnet electrolyte–based Li metal batteries: An ultrathin, highly effective, artificial solid-state electrolyte/metallic Li interface," *Science Advances*, vol. 3, p. e1601659, apr 2017.

[105] W. Feng, X. Dong, Z. Lai, X. Zhang, Y. Wang, C. Wang, J. Luo, and Y. Xia, "Building an Interfacial Framework: Li/Garnet Interface Stabilization through a Cu6Sn5 Layer," *ACS Energy Letters*, vol. 4, no. 7, pp. 1725–1731, 2019.

[106] H. Koshikawa, S. Matsuda, K. Kamiya, M. Miyayama, Y. Kubo, K. Uosaki, K. Hashimoto, and S. Nakanishi, "Electrochemical impedance analysis of the Li/Au-$Li_7La_3Zr_2O_{12}$ interface during Li dissolution/deposition cycles: Effect of pre-coating $Li_7La_3Zr_2O_{12}$ with Au," *Journal of Electroanalytical Chemistry*, vol. 835, no. January, pp. 143–149, 2019.

[107] D. Jin, S. Choi, W. Jang, A. Soon, J. Kim, H. Moon, W. Lee, Y. Lee, S. Son, Y. C. Park, H. Chang, G. Li, K. Jung, and W. Shim, "Bismuth Islands for Low-Temperature Sodium-Beta Alumina Batteries," *ACS Applied Materials and Interfaces*, vol. 11, pp. 2917–2924, jan 2019.

[108] T. Krauskopf, B. Mogwitz, C. Rosenbach, W. G. Zeier, and J. Janek, "Diffusion Limitation of Lithium Metal and Li-Mg Alloy Anodes on LLZO Type Solid Electrolytes as a Function of Temperature and Pressure," *Advanced Energy Materials*, vol. 9, p. 1902568, 2019.

[109] C. D. Fincher, Y. Zhang, G. M. Pharr, and M. Pharr, "Elastic and Plastic Characteristics of Sodium Metal," *ACS Applied Energy Materials*, vol. 3, pp. 1759–1767, feb 2020.

[110] D. W. McOwen, S. Xu, Y. Gong, Y. Wen, G. L. Godbey, J. E. Gritton, T. R. Hamann, J. Dai, G. T. Hitz, L. Hu, and E. D. Wachsman, "3D-Printing Electrolytes for Solid-State Batteries," *Advanced Materials*, vol. 1707132, p. 1707132, 2018.

[111] H. Shen, E. Yi, S. Heywood, D. Y. Parkinson, G. Chen, N. Tamura, S. Sofie, K. Chen, and M. M. Doeff, "Scalable Freeze-Tape-Casting Fabrication and Pore Structure Analysis of 3D LLZO Solid-State Electrolytes," *ACS Applied Materials & Interfaces*, vol. 12, pp. 3494–3501, jan 2019.

[112] T. Lan, C.-L. Tsai, F. Tietz, X.-K. Wei, M. Heggen, R. E. Dunin-Borkowski, R. Wang, Y. Xiao, Q. Ma, and O. Guillon, "Room-temperature all-solid-state

sodium batteries with robust ceramic interface between rigid electrolyte and electrode materials," *Nano Energy*, vol. 65, p. 104040, nov 2019.

[113] B. Kinzer, A. L. Davis, T. Krauskopf, H. Hartmann, W. S. LePage, E. Kazyak, J. Janek, N. P. Dasgupta, and J. Sakamoto, "Operando analysis of the molten Li|LLZO interface: Understanding how the physical properties of Li affect the critical current density," *Matter*, pp. 1–15, 2021.

[114] E. J. Cheng, A. Sharafi, and J. Sakamoto, "Intergranular Li metal propagation through polycrystalline $Li_{6.25}Al_{0.25}La_3Zr_2O_{12}$ ceramic electrolyte," *Electrochimica Acta*, vol. 223, pp. 85–91, jan 2017.

[115] E. Kazyak, R. Garcia-Mendez, W. S. LePage, A. Sharafi, A. L. Davis, A. J. Sanchez, K. H. Chen, C. Haslam, J. Sakamoto, and N. P. Dasgupta, "Li Penetration in Ceramic Solid Electrolytes: Operando Microscopy Analysis of Morphology, Propagation, and Reversibility," *Matter*, vol. 2, no. 4, pp. 1025–1048, 2020.

[116] R. . Ansell, "The chemical and electrochemical stability of beta-alumina," *Journal of Materials Science*, vol. 21, pp. 365–379, feb 1986.

[117] A. Virkar and L. Viswanathan, "Sodium Penetration in Rapid Ion Conductors," *Journal of the American Ceramic Society*, vol. 62, pp. 528–529, sep 1979.

[118] W. Manalastas, J. Rikarte, R. J. Chater, R. Brugge, A. Aguadero, L. Buannic, A. Llordés, F. Aguesse, and J. Kilner, "Mechanical failure of garnet electrolytes during Li electrodeposition observed by in-operando microscopy," *Journal of Power Sources*, vol. 412, pp. 287–293, feb 2019.

[119] L. Porz, T. Swamy, B. W. Sheldon, D. Rettenwander, T. Frömling, H. L. Thaman, S. Berendts, R. Uecker, W. C. Carter, and Y. M. Chiang, "Mechanism of Lithium Metal Penetration through Inorganic Solid Electrolytes," *Advanced Energy Materials*, vol. 1701003, pp. 1–12, 2017.

[120] F. Han, A. S. Westover, J. Yue, X. Fan, F. Wang, M. Chi, D. N. Leonard, N. J. Dudney, H. Wang, and C. Wang, "High electronic conductivity as the origin of lithium dendrite formation within solid electrolytes," *Nature Energy*, p. 1, jan 2019.

[121] Y. Song, L. Yang, W. Zhao, Z. Wang, Y. Zhao, Z. Wang, Q. Zhao, H. Liu, and F. Pan, "Revealing the Short-Circuiting Mechanism of Garnet-Based Solid-State Electrolyte," *Advanced Energy Materials*, vol. 9, jun 2019.

[122] L. E. Marbella, S. Zekoll, J. Kasemchainan, S. P. Emge, P. G. Bruce, and C. P. Grey, “7Li NMR Chemical Shift Imaging To Detect Microstructural Growth of Lithium in All-Solid-State Batteries,” *Chemistry of Materials*, vol. 31, pp. 2762–2769, apr 2019.

[123] D. Spencer Jolly, Z. Ning, J. E. Darnbrough, J. Kasemchainan, G. O. Hartley, P. Adamson, D. E. Armstrong, J. Marrow, and P. G. Bruce, “Sodium/Na β" Alumina Interface: Effect of Pressure on Voids,” *ACS Applied Materials and Interfaces*, vol. 12, pp. 678–685, jan 2020.

[124] R. H. Brugge, J. A. Kilner, and A. Aguadero, “Germanium as a donor dopant in garnet electrolytes,” *Solid State Ionics*, vol. 337, pp. 154–160, sep 2019.

[125] P. Barai, K. Higa, A. T. Ngo, L. A. Curtiss, and V. Srinivasan, “Mechanical Stress Induced Current Focusing and Fracture in Grain Boundaries,” *Journal of The Electrochemical Society*, vol. 166, p. A1752, may 2019.

[126] D. Cao, X. Sun, Q. Li, A. Natan, P. Xiang, and H. Zhu, “Lithium Dendrite in All-Solid-State Batteries: Growth Mechanisms, Suppression Strategies, and Characterizations,” *Matter*, vol. 3, pp. 57–94, jul 2020.

[127] M. Wang, J. B. Wolfenstine, and J. Sakamoto, “Temperature dependent flux balance of the Li/$Li_7La_3Zr_2O_{12}$ interface,” *Electrochimica Acta*, vol. 296, pp. 842–847, feb 2019.

[128] X. Liu, R. Garcia-Mendez, A. R. Lupini, Y. Cheng, Z. D. Hood, F. Han, A. Sharafi, J. Carlos Idrobo, N. J. Dudney, C. Wang, C. Ma, J. Sakamoto, and M. Chi, “Local electronic structure variation resulting in Li ’filament’ formation within solid electrolytes,” *Nature Materials*, 2021.

[129] H.-K. Tian, Z. Liu, Y. Ji, L.-Q. Chen, and Y. Qi, “Interfacial Electronic Properties Dictate Li Dendrite Growth in Solid Electrolytes,” *Chemistry of Materials*, vol. 31, pp. 7351–7359, sep 2019.

[130] Q. Li, T. Yi, X. Wang, H. Pan, B. Quan, T. Liang, X. Guo, X. Yu, H. Wang, X. Huang, L. Chen, and H. Li, “In-situ visualization of lithium plating in all-solid-state lithium-metal battery,” *Nano Energy*, vol. 63, p. 103895, sep 2019.

[131] S. Stegmaier, R. Schierholz, I. Povstugar, J. Barthel, S. P. Rittmeyer, S. Yu, S. Wengert, S. Rostami, H. Kungl, K. Reuter, R. Eichel, and C. Scheurer, “Nano-

Scale Complexions Facilitate Li Dendrite-Free Operation in LATP Solid-State Electrolyte," *Advanced Energy Materials*, p. 2100707, may 2021.

[132] F. M. Pesci, A. Bertei, R. H. Brugge, S. P. Emge, A. K. Hekselman, L. E. Marbella, C. P. Grey, and A. Aguadero, "Establishing Ultralow Activation Energies for Lithium Transport in Garnet Electrolytes," *ACS applied materials & interfaces*, vol. 12, pp. 32806–32816, jul 2020.

[133] A. Le Bail, H. Duroy, and J. L. Fourquet, "Ab-initio structure determination of LiSbWO6 by X-ray powder diffraction," *Materials Research Bulletin*, vol. 23, pp. 447–452, mar 1988.

[134] S. Hofmann, *Auger- and X-Ray Photoelectron Spectroscopy in Materials Science : A User-Oriented Guide.* 1 ed., 2012.

[135] "K-Alpha: Energy Scale Linearity and Calibration," tech. rep., Thermo Fisher Scientific.

[136] D. Briggs and M. Seah, *Practical Surface Analysis, Auger and X-ray Photoelectron Spectroscopy.* Wiley, 2 ed., 1990.

[137] D. R. Baer, K. Artyushkova, H. Cohen, C. D. Easton, M. Engelhard, T. R. Gengenbach, G. Greczynski, P. Mack, D. J. Morgan, and A. Roberts, "XPS guide: Charge neutralization and binding energy referencing for insulating samples," *Journal of Vacuum Science & Technology A*, vol. 38, p. 031204, may 2020.

[138] T. L. Barr, "Studies in differential charging," *Journal of Vacuum Science & Technology A: Vacuum, Surfaces, and Films*, vol. 7, no. 3, pp. 1677–1683, 1989.

[139] K. N. Wood and G. Teeter, "XPS on Li-Battery-Related Compounds: Analysis of Inorganic SEI Phases and a Methodology for Charge Correction," *ACS Applied Energy Materials*, vol. 1, no. 9, pp. 4493–4504, 2018.

[140] G. Greczynski and L. Hultman, "X-ray photoelectron spectroscopy: Towards reliable binding energy referencing," *Progress in Materials Science*, vol. 107, p. 100591, jan 2020.

[141] L. Edwards, P. Mack, and D. J. Morgan, "Recent advances in dual mode charge compensation for XPS analysis," *Surface and Interface Analysis*, vol. 51, pp. 925–933, sep 2019.

[142] J. F. Moulder, W. F. Stickle, P. E. Sobol, and K. D. Bomben, “Handbook of X-ray Photoelectron Spectroscopy,” tech. rep., Physical Electronics Division, Perkin-Elmer Corporation, 1992.

[143] C. J. Powell and A. Jablonski, “Surface sensitivity of X-ray photoelectron spectroscopy,” *Nuclear Instruments and Methods in Physics Research Section A*, vol. 601, pp. 54–65, mar 2009.

[144] A. Jablonski and C. J. Powell, “Relationships between electron inelastic mean free paths, effective attenuation lengths, and mean escape depths,” *Journal of Electron Spectroscopy and Related Phenomena*, vol. 100, pp. 137–160, oct 1999.

[145] S. Tanuma, C. J. Powell, and D. R. Penn, “Calculations of electron inelastic mean free paths for 31 materials,” *Surface and Interface Analysis*, vol. 11, pp. 577–589, aug 1988.

[146] J. Scofield, “Theoretical photoionization cross sections from 1 to 1500 keV.,” tech. rep., Divison of Technical Information Extension, U.S. Atomic Energy Commission, jan 1973.

[147] J. J. Yeh and I. Lindau, “Atomic subshell photoionization cross sections and asymmetry parameters: $1 \leq Z \leq 103$,” *Atomic Data and Nuclear Data Tables*, vol. 32, pp. 1–155, jan 1985.

[148] C. Kalha, N. K. Fernando, P. Bhatt, F. O. L. Johansson, A. Lindblad, H. Rensmo, L. Z. Medina, R. Lindblad, S. Siol, L. P. H. Jeurgens, C. Cancellieri, K. Rossnagel, K. Medjanik, G. Schönhense, M. Simon, A. X. Gray, S. Nemšák, P. Lömker, C. Schlueter, and A. Regoutz, “Hard x-ray photoelectron spectroscopy: a snapshot of the state-of-the-art in 2020,” *Journal of Physics: Condensed Matter*, vol. 33, p. 233001, jun 2021.

[149] S. Tougaard, “Practical guide to the use of backgrounds in quantitative XPS,” *Journal of Vacuum Science & Technology A: Vacuum, Surfaces, and Films*, vol. 39, p. 011201, dec 2020.

[150] S. Tougaard, “Quantitative analysis of the inelastic background in surface electron spectroscopy,” *Surface and Interface Analysis*, vol. 11, pp. 453–472, 1988.

[151] S. Tougaard, “Energy loss in XPS: Fundamental processes and applications for quantification, non-destructive depth profiling and 3D imaging,” *Journal of Electron Spectroscopy and Related Phenomena*, vol. 178-179, pp. 128–153, 2010.

[152] E. Gnacadja, N. Pauly, and S. Tougaard, “Universal inelastic electron scattering cross-section including extrinsic and intrinsic excitations in XPS,” *Surface and Interface Analysis*, vol. 52, pp. 413–421, 2020.

[153] A. Barrie and F. J. Street, “An Auger and X-ray photoelectron spectroscopic study of sodium metal and sodium oxide,” *Journal of Electron Spectroscopy and Related Phenomena*, vol. 7, pp. 1–31, jan 1975.

[154] G. H. Major, T. G. Avval, D. I. Patel, D. Shah, T. Roychowdhury, A. J. Barlow, P. J. Pigram, M. Greiner, V. Fernandez, A. Herrera-Gomez, and M. R. Linford, “A discussion of approaches for fitting asymmetric signals in X-ray photoelectron spectroscopy (XPS), noting the importance of Voigt-like peak shapes,” *Surface and Interface Analysis*, 2021.

[155] H. H. Brongersma, M. Draxler, M. de Ridder, and P. Bauer, “Surface composition analysis by low-energy ion scattering,” *Surface Science Reports*, vol. 62, pp. 63–109, mar 2007.

[156] H. H. Brongersma, “Low-energy ion scattering,” in *Characterization of Materials* (E. N. Kaufmann, ed.), John Wiley & Sons, 2012.

[157] B. M. J. Smets and T. P. A. Lommen, “Ion Beam Effects on Glass Surfaces,” *Journal of the American Ceramic Society*, vol. 65, pp. c80–c81, jun 1982.

[158] M. Kodama, S. Komiyama, A. Ohashi, N. Horikawa, K. Kawamura, and S. Hirai, “High-pressure in situ X-ray computed tomography and numerical simulation of sulfide solid electrolyte,” *Journal of Power Sources*, vol. 462, p. 228160, jun 2020.

[159] T. Famprikis, Ö. U. Kudu, J. A. Dawson, P. Canepa, F. Fauth, E. Suard, M. Zbiri, D. Dambournet, O. J. Borkiewicz, H. Bouyanfif, S. P. Emge, S. Cretu, J.-N. Chotard, C. P. Grey, W. G. Zeier, M. S. Islam, and C. Masquelier, “Under Pressure: Mechanochemical Effects on Structure and Ion Conduction in the Sodium-Ion Solid Electrolyte Na_3PS_4,” *Journal of the American Chemical Society*, vol. 142, pp. 18422–18436, oct 2020.

[160] A. P. Vadhva, J. Hu, M. Johnson, R. Stocker, M. Braglia, D. Brett, and A. Rettie, “Electrochemical Impedance Spectroscopy for All-Solid-State Batteries: Theory, Methods and Future Outlook,” *ChemElectroChem*, 2021.

[161] M. A. Danzer, "Generalized distribution of relaxation times analysis for the characterization of impedance spectra," *Batteries*, vol. 5, no. 3, pp. 1–16, 2019.

[162] M. Hahn, S. Schindler, L. C. Triebs, and M. A. Danzer, "Optimized process parameters for a reproducible distribution of relaxation times analysis of electrochemical systems," *Batteries*, vol. 5, no. 2, 2019.

[163] J. Macdonald, "Impedance spectroscopy," *Ann. Biomed. Eng.*, vol. 20, no. 3, pp. 289–305, 1992.

[164] A. Jain, S. P. Ong, G. Hautier, W. Chen, W. D. Richards, S. Dacek, S. Cholia, D. Gunter, D. Skinner, G. Ceder, and K. A. Persson, "Commentary: The materials project: A materials genome approach to accelerating materials innovation," jul 2013.

[165] Z. Deng, G. Sai Gautam, S. K. Kolli, J. N. Chotard, A. K. Cheetham, C. Masquelier, and P. Canepa, "Phase Behavior in Rhombohedral NaSiCON Electrolytes and Electrodes," *Chemistry of Materials*, vol. 32, pp. 7908–7920, sep 2020.

[166] D. Kramer and G. Ceder, "Tailoring the morphology of $LiCoO_2$: A first principles study," *Chemistry of Materials*, vol. 21, pp. 3799–3809, aug 2009.

[167] L. Wang, F. Zhou, Y. S. Meng, and G. Ceder, "First-principles study of surface properties of $LiFePO_4$: Surface energy, structure, Wulff shape, and surface redox potential," *Physical Review B - Condensed Matter and Materials Physics*, vol. 76, p. 165435, oct 2007.

[168] S. Naqash, Q. Ma, F. Tietz, and O. Guillon, "$Na_3Zr_2(SiO_4)_2(PO_4)$ prepared by a solution-assisted solid state reaction," *Solid State Ionics*, vol. 302, pp. 83–91, apr 2017.

[169] A. Jalalian-Khakshour, C. O. Phillips, L. Jackson, T. O. Dunlop, S. Margadonna, and D. Deganello, "Solid-state synthesis of NASICON ($Na_3Zr_2Si_2PO_{12}$) using nanoparticle precursors for optimisation of ionic conductivity," *Journal of Materials Science*, vol. 55, pp. 2291–2302, feb 2020.

[170] J. T. S. Irvine, D. C. Sinclair, and A. R. West, "Electroceramics: Characterization by Impedance Spectroscopy," *Advanced Materials*, vol. 2, pp. 132–138, mar 1990.

[171] R. A. Huggins, “Simple method to determine electronic and ionic components of the conductivity in mixed conductors a review,” *Ionics*, vol. 8, pp. 300–313, may 2002.

[172] M. Guin, S. Indris, M. Kaus, H. Ehrenberg, F. Tietz, and O. Guillon, “Stability of NASICON materials against water and CO_2 uptake,” *Solid State Ionics*, vol. 302, pp. 102–106, 2017.

[173] T. Krauskopf, B. Mogwitz, H. Hartmann, D. K. Singh, W. G. Zeier, and J. Janek, “The Fast Charge Transfer Kinetics of the Lithium Metal Anode on the Garnet-Type Solid Electrolyte $Li_{6.25}Al_{0.25}La_3Zr_2O_{12}$,” *Advanced Energy Materials*, p. 2000945, jun 2020.

[174] S. K. Otto, T. Fuchs, Y. Moryson, C. Lerch, B. Mogwitz, J. Sann, J. Janek, and A. Henss, “Storage of Lithium Metal: The Role of the Native Passivation Layer for the Anode Interface Resistance in Solid State Batteries,” *ACS Applied Energy Materials*, vol. 4, pp. 12798–12807, nov 2021.

[175] L. Cheng, E. J. Crumlin, W. Chen, R. Qiao, H. Hou, S. Franz Lux, V. Zorba, R. Russo, R. Kostecki, Z. Liu, K. Persson, W. Yang, J. Cabana, T. Richardson, G. Chen, and M. Doeff, “The origin of high electrolyte-electrode interfacial resistances in lithium cells containing garnet type solid electrolytes,” *Physical Chemistry Chemical Physics*, vol. 16, pp. 18294–18300, aug 2014.

[176] D. Klotz, A. Weber, and E. Ivers-tiffée, “Practical Guidelines for Reliable Electrochemical Characterization of Solid Oxide Fuel Cells,” *Electrochimica Acta*, vol. 227, pp. 110–126, 2017.

[177] Z. Zhang, S. Wenzel, Y. Zhu, J. Sann, L. Shen, J. Yang, X. Yao, Y.-S. Hu, C. Wolverton, H. Li, L. Chen, and J. Janek, “$Na_3Zr_2Si_2PO_{12}$: A Stable Na + -Ion Solid Electrolyte for Solid-State Batteries,” *ACS Applied Energy Materials*, vol. 19, p. 39, jul 2020.

[178] C. Powell and A. Jablonski, “The NIST Electron Effective-Attenuation-Length Database,” *Journal of Surface Analysis*, vol. 9, no. 3, pp. 322–325, 2002.

[179] J. Gibson, S. Narayanan, J. E. N. Swallow, P. K. Thakur, M. Pasta, T.-L. Lee, and R. S. Weatherup, “Gently Does It!: In Situ Preparation of Alkali Metal - Solid Electrolyte Interfaces for Photoelectron Spectroscopy,” *Faraday Discussions*, 2022.

[180] J. Janek, "Oscillating reactions at metal electrodes in solid electrolytes," *Solid State Ionics*, vol. 101-103, pp. 721–727, nov 1997.

[181] H. Xie, C. Yang, Y. Ren, S. Xu, T. R. Hamann, D. W. McOwen, E. D. Wachsman, and L. Hu, "Amorphous-Carbon-Coated 3D Solid Electrolyte for an Electro-Chemomechanically Stable Lithium Metal Anode in Solid-State Batteries," *Nano Letters*, vol. 21, pp. 6163–6170, jul 2021.

[182] O. J. Foust, *Sodium-NaK Engineering Handbook. Volume I. Sodium chemistry and physical properties.* 1972, jan 1972.

[183] I. D. Seymour and A. Aguadero, "Suppressing void formation in all-solid-state batteries: the role of interfacial adhesion on alkali metal vacancy transport," *Journal of Materials Chemistry A*, vol. 9, pp. 19901–19913, 2021.

[184] M. J. Rice and W. L. Roth, "Ionic transport in super ionic conductors: a theoretical model," *Journal of Solid State Chemistry*, vol. 4, pp. 294–310, mar 1972.

[185] M. Yang, Y. Liu, A. M. Nolan, and Y. Mo, "Interfacial Atomistic Mechanisms of Lithium Metal Stripping and Plating in Solid-State Batteries," *Advanced Materials*, p. 2008081, 2021.

[186] C. Ablitt, H. McCay, S. Craddock, L. Cooper, E. Reynolds, A. A. Mostofi, N. C. Bristowe, C. A. Murray, and M. S. Senn, "Tolerance Factor Control of Uniaxial Negative Thermal Expansion in a Layered Perovskite," *Chemistry of Materials*, vol. 32, pp. 605–610, jan 2020.